UNIVERSITÀ DEGLI STUDI DI MILANO - BICOCCA
Scuola di Dottorato di Scienze

Dottorato in Fisica e Astronomia, Ciclo XXII
Coordinatore: Prof. Claudio Destri

DISPLACEMENT DAMAGE INDUCED BY COSMIC RAYS IN SILICON DEVICES USING GEANT4 TOOLKIT FOR SPACE APPLICATIONS

Tutore: Prof. Massimo Gervasi
Correlatore: Dott. Pier Giorgio Rancoita

Tesi di: Cristina Consolandi
Matricola n. 708229

Anno Accademico 2008-2009

Contents

Introduction **1**

1 Space Radiation Environment **6**
1.1 Galactic Cosmic Rays 6
1.1.1 The Directional Spectrum 7
1.1.2 The Energy Spectrum 8
1.1.3 The Mass Spectrum 10
1.2 Solar Wind and Heliospheric Magnetic Field 14
1.2.1 The Modulation Effect 19
1.2.2 ISO 15390 Model for Galactic Cosmic Rays 22
1.3 The Earth's Magnetosphere and Trapped Particles 23

2 Electromagnetic Energy Loss **28**
2.1 Coulomb Scattering Process 28
2.1.1 Non-Relativistic Scattering 28
2.1.2 Relativistic Treatment of Scattering 34
2.2 Limits of Non-Relativistic and Relativistic Coulomb Scattering 41
2.3 Non-Relativistic Differential Scattering Cross Section 42
2.3.1 Unscreened Coulomb Potential 43
2.3.2 Universal Screening Potential 45
2.4 Relativistic Differential Cross Sections 46
2.5 Stopping Power 49
2.5.1 Nuclear Collision Energy-Loss 49
2.5.2 Electronic Collision Energy-Loss 51
2.5.3 Electronic Energy-Loss Fluctuations 52

3 Displacement Damage **57**
3.1 The Displacement Cascade 57
3.1.1 Displacement Damage Function 58
3.1.2 Damage Energy 60
3.2 Non-Ionizing Energy Loss 62

3.2.1 Neutrons NIEL . . . 64
3.2.2 Protons NIEL . . . 68
3.2.3 Heavy Nuclei NIEL . . . 69
3.2.4 Alpha Particles NIEL . . . 72
3.3 Defect Complexes . . . 73
3.4 Reduction of the Minority Carrier Lifetime After Irradiation . 76
3.5 Bipolar Junction Transistor (BJT) . . . 78

4 GEANT4-Based Development for NIEL and NIEL-Dose Calculation 85
4.1 Non-Relativistic ZBL NIEL Calculation . . . 85
4.2 Relativistic NIEL Calculation . . . 88
4.3 Total NIEL for Protons and Alpha Particles . . . 91
4.4 GEANT4 Simulation Toolkit . . . 92
4.4.1 GEANT4 Single Scattering Process . . . 93
4.4.2 Simulation Test of the GEANT4 Single Scattering Process . . . 94
4.4.3 Improved Implementation of the GEANT4 Single Scattering Process . . . 97
4.4.4 Simulation Results of the Upgraded GEANT4 Coulomb NIEL Fraction . . . 99
4.4.5 The ISO 15390 Model as a Primary Generator in GEANT4 101
4.5 NIEL-Dose Calculation . . . 102

5 The Carriers Transport Phenomena in Silicon 109
5.1 Equilibrium Carriers Statistics . . . 109
5.1.1 Carriers Concentration . . . 111
5.1.2 Intrinsic Material . . . 112
5.1.3 n-type and p-type Silicon . . . 113
5.1.4 Compensated Semiconductor . . . 118
5.1.5 Degenerate Semiconductors . . . 119
5.2 Generation and Recombination Processes . . . 120
5.3 Carriers Transport-Phenomena . . . 122
5.3.1 Resistivity and Mobility . . . 125
5.4 Scattering and Mobility . . . 129
5.4.1 Acoustic Phonon Scattering . . . 130
5.4.2 Ionized Impurity Scattering . . . 131
5.4.3 Neutral Impurity Scattering . . . 131
5.4.4 Semi-Empirical Relations for Carriers Mobility . . . 132
5.5 The Hall Effect . . . 134
5.5.1 The Hall Scattering Factor . . . 136

5.5.2 Hall Coefficient in Compensated Semiconductors 142

6 Experimental Results of the Hall Effect Measurements 143
6.1 Samples Characteristics and Irradiation Fluences 143
6.2 Experimental Setup and Method 146
6.3 Experimental Results of Non-Irradiated Samples 149
6.4 Temperature Scan of Irradiated Samples 151

Conclusions 156

A GEANT4 Coulomb NIEL 158

B The Silicon Structure 163
B.1 Covalent Bound and Crystal Structure 163
B.2 The Reciprocal Lattice and the Energy-Band Structure 166
B.3 The Effective Mass Approximation 168
B.4 Constant Energy Surfaces 171
B.5 Density of States 172

Introduction

In the space environment there are many kind of energetic particles of different origin. Protons are the most abundant but alpha particles, heavier nuclei, and electrons are also present. Abundances and energy spectra depend on the position inside the solar cavity and are strongly affected by the solar activity. The dominant radiation at energies above 30-50 MeV/nucleon is constituted by the Galactic Cosmic Rays (GCRs). They are composed mainly of protons and alpha particles ($\approx 98\%$), of a lesser amount of nuclei up to nickel and of an even lesser of heavier nuclei (atomic mass number A$\geq$ 60). These particles continuously enter the solar cavity and are isotropically distributed. At low energies from 1 MeV/nucleon up to about 30 MeV/nucleon, we find the so-called Anomalous Cosmic Rays (ACRs). They are ionized atoms of hydrogen, helium, nitrogen, oxygen, neon and carbon, coming from the interstellar medium. Neutral atoms penetrate inside the heliosphere and become ionized by the ultraviolet radiation coming from the Sun. As ionized particles, they follow the heliospheric magnetic field lines and may be accelerated by stochastic process or by shock waves [2].

Along their travel through the interplanetary space, GCRs can reach the Earth's magnetosphere, interact with the upper layers of the atmosphere and, finally, produce secondary particles like for example neutrons. Neutrons decay into protons (10 -100 MeV) and electrons (up to 10 MeV) which may became trapped particle in the Earth's radiation belts. Other phenomena like geomagnetic storms - i.e. large variations of the Earth's magnetosphere caused by the solar wind- may increase the electron population of the outer radiation belt. The expanding solar wind transports, with the heliospheric magnetic field, a constant flux of particles mostly composed by protons and electrons. In addition -during transient phenomena like solar flares which are explosive releases of energy, and coronal mass ejections, which are ejection of plasma material form the Sun- solar energetic particles (SEP) are produced in the energy range from few keV to several GeV [2].

The space radiation environment will be described in chapter 1 where particular attention will paid to GCRs because their fluxes constantly invest spacecrafts, satellite and all other materials present in the Space, and constitute an hazard for electronic components of the space missions. Due to their high energies, GCRs are capable of passing through the shielding material and to inflict permanent damage to electronic devices. In the same chapter,

a simplified description of the solar wind and of the solar cycles will be reported. The solar cycles modify the heliospheric magnetic field causing the modulation effect on the low energy part of the GCRs spectrum. In section 1.2.2 the ISO 15390 model will be described. This model is the reference one to estimate the radiation impact of GCRs on hardware and biological tissues. It is able to reproduce the modulation effect due to the 11 and the 22-years solar cycles. In addition, a brief description of the magnetosphere environment and of the trapped particles of the radiation belts will be given for completeness.

Charged energetic particles, like GCRs, lose energy while passing through matter by Coulomb interactions with electrons and atoms of the material. The scattering mechanism with electrons determines the *electronic collision* energy loss (see section 2.5.3). Electrons may be excited to an higher energy level or, if the transferred energy is enough, they may be emitted as δ-rays from the atom. The ionizing energy loss of the incident particle, is responsible of the absorbed dose D^{Ion} due to ionization processes.
In *nuclear collisions*, instead, the energy is released by the interactions with the target nuclei of the material. Part of this transferred energy can be dissipated inside the material by phonon vibrations but it can also be sufficient to displace the whole atom from its lattice position. This energy deposition is called Non-Ionizing-Energy-Loss (NIEL). The displaced atom is called *primary knock-on atom* (PKA). The PKA in turn may have sufficient energy to migrate inside the lattice and, by nuclear collisions, can displace other atoms which may create further displacements. The whole process is a cascade of atomic collisions which modify the bulk structure of the device. The NIEL, which is the fraction of energy lost by the incident particle that goes into displacement processes, is related to the absorbed NIEL-Dose D^{NIEL}.
The relative importance, of these two scattering mechanisms, depends on the energy of the incoming particle. Nuclear energy loss dominates for low energetic particles, while high energetic particles mostly lose energy by electronic collisions. For example, for protons of 1 GeV, D^{Ion} is three orders of magnitude greater than D^{NIEL}, while for heavy nuclei of tens MeV/nucleon, D^{Ion} exceeds D^{NIEL} by four orders of magnitudes [1]. Nevertheless the nuclear energy loss is important for the formation of defects inside the material. In facts, it is responsible of the displacement damage which is the typical cause of degradation for silicon devices and so it will be treated in detail in chapter 2.

The displacement damage is a cumulative process which creates disorder in the lattice structure of the material and can be quantified by the amount of NIEL as it will be explained in chapter 3. For the low part of the albedo particles that populate the space radiation environment, many simulation pro-

grams already perform the NIEL calculation in the non-relativistic regime. One example is the TRIM program (Transport of Radiation In Matter) which is able to simulate, in a two-dimensional approximation, the interaction of all type of incident ions in any kind of target material. This program reproduces the Coulomb scattering process in the non-relativistic regime up to 1 GeV/nucleon and it is able to simulate the nucleus screening effect, caused by electrons, which is relevant at low energies.

For high energetic protons and alpha particles, we know the NIEL value from literature which includes the nuclear NIEL contribution due to hadronic interactions, at energies up to 24 GeV and 1 GeV/nucleon respectively. For heavier nuclei there is a lack of information about the NIEL value at high energies. The knowledge of the displacement damage induced by heavy nuclei is of fundamental importance for the computation of the NIEL-Dose due to GCRs. In fact, even if heavy nuclei constitute the minority fraction of the GCRs spectrum, the displacement damage induced by a single heavy nucleus is much larger than the one induced by a proton with the same energy. As a consequence, the computation of the absorbed NIEL-Dose during space missions must include the heavy nuclei contribution.
From literature, it is possible to know the analytical Coulomb NIEL value for heavy nuclei only in the non-relativistic limit and at energies up to 1 GeV. As it will be explained in section 4.1 we performed a computational integration of the NIEL value which is based on the same screening theory and it is in agreement with the literature values in the same energy range (1 keV up to 1 GeV).

In addition we were able to extend the energy range for the NIEL computation. To calculate the NIEL, it is necessary to give an expression for the differential scattering cross section for energy transfer which depends on the specific interaction process. For heavy nuclei the displacement damage induced by Coulomb interactions is expected to be the relevant fraction for the NIEL computation (see sections 3.2.3 and 4.5). Therefore the Coulomb scattering process will be analyzed in details in section 2.1. First it will be treated in the non-relativistic limit (section 2.1.1) and then it will be described in the relativistic regime (section 2.1.2).

To get the Coulomb NIEL fraction for heavy nuclei we improved the already existing GEANT4 single scattering process. The original code was developed by the CERN GEANT4 team group for muons and hadrons simulations only. In section 4.4.3 we present a modification of the differential scattering cross section to extend the use of this code to heavier particles. The modified code allows one to compute the scattering probabilities in the high energy regime also for heavy nuclei. The results of the NIEL calculated by the GEANT4 improved simulation program are in good agreement with

the literature protons values. Thanks to the collaboration with the GEANT4 team, this modification of the source code was accepted and will be included in the GEANT4 release available from December 2009 [64].

In section 4.4.5, in addition, we present our work aimed to simulate the GCR fluxes by the use of GEANT4. We developed a code written in C++ language based the ISO 15390 model which was interfaced to the GEANT4 Particle Generator. This gives the possibility to have a particle generator in the GEANT4 framework which is able to reproduce the solar modulation effect on the GCRs spectrum. Fluxes of particles of this generator are presented for different periods of the solar activity. The knowledge of the GCRs fluxes, by the use of the ISO model, and of the NIEL values, obtained by the modified GEANT4 program, enables us to estimate the expected NIEL-Dose absorbed by a silicon sample during one year mission. As it will be explained in chapter 4, the calculation was performed considering two different periods of the Sun activity for particles in the energy range from 50 MeV/nucleon up to 10 GeV/nucleon. For proton and alpha particles we used the tabulated NIEL values taken from literature which include both Coulomb and Nuclear interactions. For all the other nuclei, we used the Coulomb NIEL fraction obtained from our computation.

During space missions, electronic devices undergo to constant fluxes of energetic particles which will enhance the absorbed NIEL-Dose. From a microscopic point of view, the crystal structure of the material results to be modified after irradiation. These modifications will cause the degradation of the electrical characteristics of the device. Point defects created during irradiation such as vacancies and interstitial atoms (called Frenkel pairs (FP)) may migrate inside the material and evolve into more stable defects in a relative small region of space. Vacancies can interact with impurity atoms, already present in the material, and form defect complexes. As it will be explained in section 3.3, defects complexes introduce discrete energy levels in the forbidden energy gap of the semiconductor. These levels act as trapping centers for conducting carriers which are removed from the conduction or the valance band according to the trapping center energy level. The carrier removal will lead to the increase of the resistivity of the semiconductor. In addition, deep energy levels are responsible for the reduction of carriers life-time (see 3.4) because electrons and holes are captured and re-emitted with a delay time. This mechanism is one of the main causes of degradation for all those devices which operate with a depleted region as solar cells, detectors and bipolar transistors. As it will be discussed in section 3.5, it is well known that the bipolar transistors gain is lowered after irradiation. The difference of the inverse of the gain, before and after irradiation, was found to have a linear dependence on the concentration of FPs. However, the radiation damage

is a complex phenomena which involves both ionization and non-ionization processes. Different parts of a device may be degraded by both mechanisms. For example, silicon devices which operate with an oxide layer are more subjected to ionization damage respect to the displacement one. It is then necessary to perform a separate investigation on the various components of a device by testing the radiation hardness of the bulk material which is typically employed as a substrate for the fabrication of all those devices used during space missions. For example, the base region of a bipolar transistor has a low resistivity (0.01 Ω cm) of both n and p-type, solar cells employ substrate semiconductors of resistivities in the range 10-1500 Ω cm, while detectors have high and very high silicon doped material (>1000 Ω cm).

For instance, in our laboratory, we performed Hall effect measurements on silicon bulk samples of different resistivities, irradiated with fast neutrons and high energy carbon ions [102]. In chapter 5 an introduction to the electronic characteristic of a non-irradiated semiconductor will be given. Subsequently the macroscopic variables such as the mobility and the resistivity of carriers will be derived (the fundamental structure of the non-irradiate silicon lattice crystal will be given in appendix B). In chapter 6 experimental results of temperature scans of the Hall coefficient, the resistivity and the Hall mobility from 300 K down to 11 K will be reported for both non-irradiated and irradiated silicon samples.

Chapter 1

Space Radiation Environment

In this chapter an introduction to the Space radiation environment will be given. Particular attention will be set to the most energetic particles which are the Galactic Cosmic Rays (GCRs). GCRs constitute an hazard for electronic components of the space missions, because they are capable of passing through the shielding material of spacecrafts and they are able to inflict permanent damage to the electronic devices. After that the attention will placed on the solar wind and on the solar cycles which modify the heliospheric magnetic field causing the modulation effect on the GCRs spectrum. In addition the ISO model which includes modulation effects, will be described. Since most of the space missions operate in the Earth's magnetosphere, a brief description of the magnetosphere environment and of the trapped particles in the radiation belts are also given for completeness.

1.1 Galactic Cosmic Rays

Galactic Cosmic Rays (GCRs) are high energetic charged particles that penetrate the heliosphere from the local interstellar space. They are fully ionized nuclei composed most of all by protons, a little part of alpha particles and a minimal fraction is made up with heavier nuclei and electrons. Most of them are relativistic and a few have ultra-relativistic energies extended up to 10^{20} eV. Their origin is not still well understood. Supernova explosion are the major acceleration sources of GCRs up to energies of the order of 10^{15} eV. Higher energetic particles ($> 10^{19}$ eV) may have Extragalactic origin. The three fundamental GCRs observable variables are the *directional spectrum* which gives information about the arrival direction, the *energy spectrum* which defines the energy differential flux and the *mass spectrum* which gives the composition.

1.1.1 The Directional Spectrum

Excluding the geomagnetic field effects, the GCRs angular distribution is isotropic. The number of particles ΔN, incident on a unit surface ΔS, per unit time Δt, within a unit solid angle $\Delta\Omega$ perpendicular to the surface is defined as the *intensity*:

$$\Phi \equiv \frac{\Delta N}{\Delta S \Delta t \Delta \Omega} \tag{1.1}$$

and it is uniform in all directions. This happens because the propagation of GCRs in our Galaxy is not rectilinear. GCRs continuously interact with the Galactic magnetic field irregularities which have the same dimensions of the particles gyroradius. As a consequence GCRs diffuse in all directions as in a scattering process.

A particle of charge Ze which moves in a magnetic field B is subjected to the Lorenz's force which, in Gaussian units, is equal to:

$$\mathbf{F} = \frac{Ze}{c}\mathbf{v} \times \mathbf{B} \tag{1.2}$$

If the particle moves with velocity v perpendicularly to the magnetic field line, the balance between the Lorenz's force and the centrifugal force can be simply written as:

$$\frac{mv^2}{r} = \frac{Ze}{c}vB \tag{1.3}$$

where m is the mass of the particle and r is the bending radius or gyroradius of the circular trajectory. From the (1.3) it possible to derive:

$$Br = \frac{pc}{Ze}. \tag{1.4}$$

where p is the momentum of the particle. The second term of this last equation is defined as the particle *magnetic rigidity*:

$$R \equiv \frac{pc}{Ze} \quad [\mathrm{V}] \tag{1.5}$$

which is a measure of the resistance that the particle opposes to B when the magnetic field bends its trajectory. For a relativistic particle the magnetic rigidity is the ratio between the particle kinetic energy and its charge. A useful relation to have an idea of the cosmic rays gyroradius is given by [3]:

$$R\ [\mathrm{V}] = 300B\ [\mathrm{Gauss}]\ r\ [\mathrm{cm}] \tag{1.6}$$

The Galactic magnetic field of our Galaxy, is estimated to be $\sim 3 \times 10^{-6}$ Gauss. If the particle rigidity is $< 10^{15}$ V then r is less than 1 pc (1 pc

$=3.08\times10^{18}$ cm) which is the typical dimension of a Supernova remnant; if $R \sim 10^{18}$ V then $r \sim 1$ kpc which is the dimension of the Galaxy Disk plus the Galactic Halo; if $R \sim 10^{21}$ V then $r \sim 1$ Mpc which is much larger than the Galaxy dimension. Particles of this limit kinetic energy are not affected by the Galactic magnetic field and so may leak out from the Galaxy. In principle for these particles it could be possible to directly know the source of production. Unfortunately particle of this energy are rare and so a detail study of their sources is difficult.

1.1.2 The Energy Spectrum

The energy spectrum of GCRs is described by the *differential intensity* or *differential flux* $\Phi(E)$ which gives the number of particles with energy between E and $E + dE$, observed per unit surface, time, solid angle and energy i.e.:

$$\Phi(E) \equiv \frac{dN}{dSdtd\Omega dE} \tag{1.7}$$

Neglecting the modulation effects, it is well described by a power low spectrum [7]:

$$\Phi(E) \propto E^{-\alpha} \tag{1.8}$$

where α is the differential spectral index. The integration of $\Phi(E)$, from a defined energy value, over the whole solid angle, gives the integral intensity :

$$\Phi(> E_0) = \int_{E_0}^{\infty} \Phi(E) dE d\Omega \tag{1.9}$$

that is the number of particles incident on a unit surface per unit time with energies greater than E_0. Typical values are $\Phi(> 10^{11}\text{eV}) = 1$ particle m^{-2} per-second; $\Phi(> 10^{15}\text{eV}) = 1$ particle m^{-2} per-year; $\Phi(> 10^{19}\text{eV}) = 1$ particle m^{-2} per-century.

The units of measurement for the flux depend on the units used for E which may be given in energy-per-nucleon or in energy-per-nucleus. Sometimes instead of the number of particles it is used the number of nucleons. Fluxes can also be given in particles per unit rigidity.
In this work the differential flux will be given in particle per energy-per-nucleon and the units of measurement will be:

$$\Phi(E) \quad \left[\frac{\text{N}^o \text{ of particles}}{\text{m}^2 \text{ s sr MeV/nucl}} \right] \tag{1.10}$$

The overall GCRs energy spectrum is reported in figure 1.1. The flux progressively diminishes with increasing particle energy with a spectral index

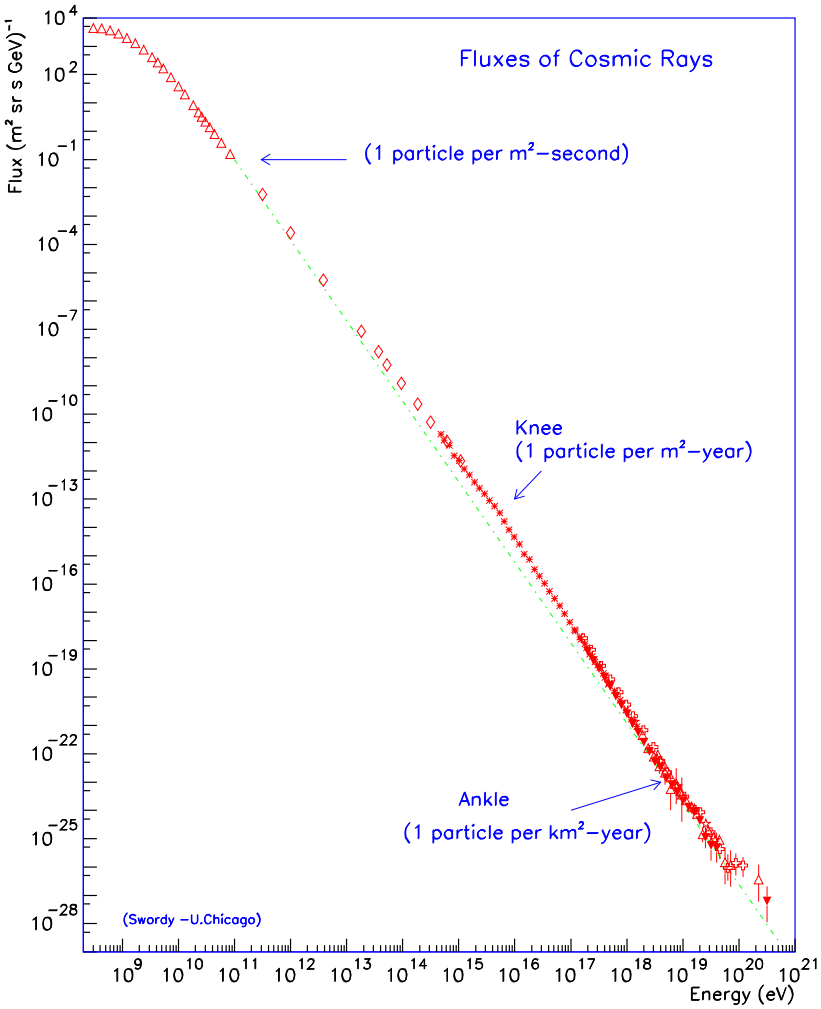

Figure 1.1: Overall Galactic Cosmic Ray Energy Spectrum [21] [20]

$\alpha = 2.7$ up to energies of the order of 10^{15} eV where the spectrum exhibits a change of slope ("knee") becoming steeper with a spectral index equal to $\alpha = 3.1$. This change of slope may be caused by the loss of efficiency of the acceleration mechanisms or even because of the leak out of particles from the Galaxy [4].

At energy of the order of 10^{19} eV the spectrum seems to recover the initial slope ("ankle") for a short energy range up to the GZK (Greisen-Zatsepin-Kuzmin [8]) cutoff at about 6×10^{19} eV where the interaction of cosmic rays with the photons of the Cosmic Microwave Background [3] is expected to be evident.

The power low spectrum, observed up to the knee region, may be well explain by the Fermi's acceleration mechanism [4]. This mechanism provides the acceleration of GCRs by shock waves that may follow supernova explosions. Qualitatively, every time that a particle crosses the shock wave front, it increases its energy for an amount proportional to the velocity of the wave front. It is possible to prove that this process ends with the production of accelerated particles which are distributed according to a power low distribution. The spectral index, obtained with the typical values of shock waves produced by a supernova explosion, is in agreement with the experimental value. Also the acceleration time, of the order of one month, is reasonable. The maximum kinetic energy achieved by this acceleration process is of the order of 10^{15} eV which may explain the change of slope at these energies.

At energies greater than 10^{19} eV the GCRs flux reaches so low values that an hypothetical Extragalactic component may become visible. Unfortunately particles of these energies are very rare and lose rapidly their energy by the interaction with the photons of the Cosmic Microwave Background (CMB). Primary protons produce pions on the blackbody photons and they lose energy via the Δ resonance [3]:

$$p + \gamma \rightarrow p + \pi^0 \tag{1.11}$$

$$p + \gamma \rightarrow n + \pi^+ \tag{1.12}$$

This effect, GZK, has been proposed by Greisen [8] in the 1966. The threshold proton energy for the photoproduction of pions with the CMB photons ($E_{CMB} \sim 1.1$ mV) is about 6×10^{19} eV. This is the estimation for the GZK cutoff of the GCR Energy spectrum.

At low energies (< 10 GeV), instead, the spectrum shows a prominent attenuation caused by the interaction of the GCRs with the magnetic field irregularities carried by the solar wind (Solar Wind Modulation). The solar modulation is an effect that causes the reduction of the GCRs flux at low energies. When the Solar activity reaches a maximum there is an increase of the solar wind which prevents less energetic particles to penetrate inside the eliosphere. This effect disappears above a few tens of GeV/nucleon that is when the gyroradius of the particle has the same order of magnitude of the heliosphere dimension 100 AU (1 Astronomical Unit $=1.5 \times 10^8$ km) assuming an average field of 0.1 nT.

1.1.3 The Mass Spectrum

The mass spectrum gives information about the GCRs composition. The nucleus fraction constitutes 99% of the total composition and the rest 1%

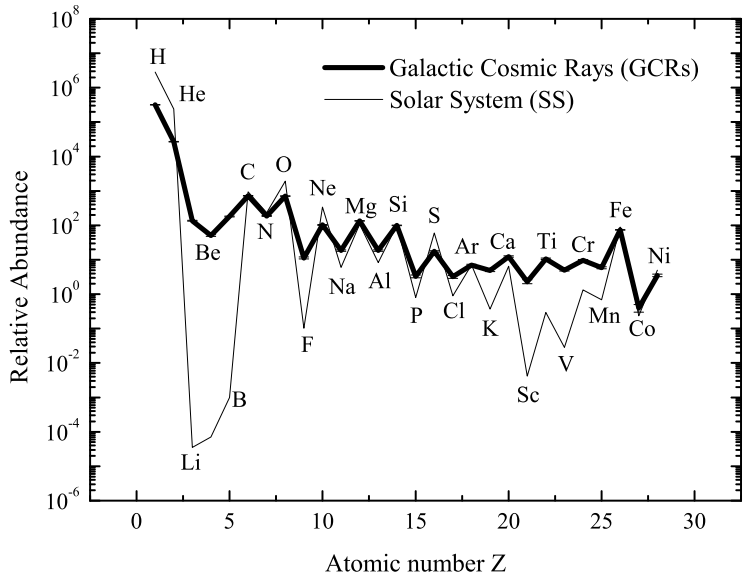

Figure 1.2: Relative abundance of elements in Galactic Cosmic Rays (GCRs) and in the Solar System (SS). The abundance of silicon is defined as 100 [19].

is made of electrons. Protons (H) are the 89% of the nucleus part, alpha particles (He) are the 10% the rest are heavier nuclei up to nickel (Z=92) while for $Z > 92$ the nuclei percentage is negligible. In figure 1.2 are reported the GCRs relative abundances which, in general, are compatible with a Solar-like source. Differences between the Solar System and the GCR relative abundances are visible for some nuclei. The GCRs deficit of H and He nuclei is probably caused by the difficulty to ionize very light atoms.

In the GCR mass spectrum there is also an excess of the light nuclei before carbon as lithium (Li), beryllium (Be), boron (B), and of the nuclei before iron as scandium (Sc), titanium (Ti), vanadium (V), chrome (Cr), manganese (Mn). These abundances are compatible with the production of secondary GCRs by spallation process. When the particles energies are of the order of GeV, an energetic "primary" light particle (H, He) may interact with a heavier atom of the interstellar gas (C, N,O ...Fe), and during the fragmentation process, lighter nuclei may be created as "secondary" GCR. The higher the secondary abundances are, the greater is the number of interactions. This can give important information about the interstellar medium

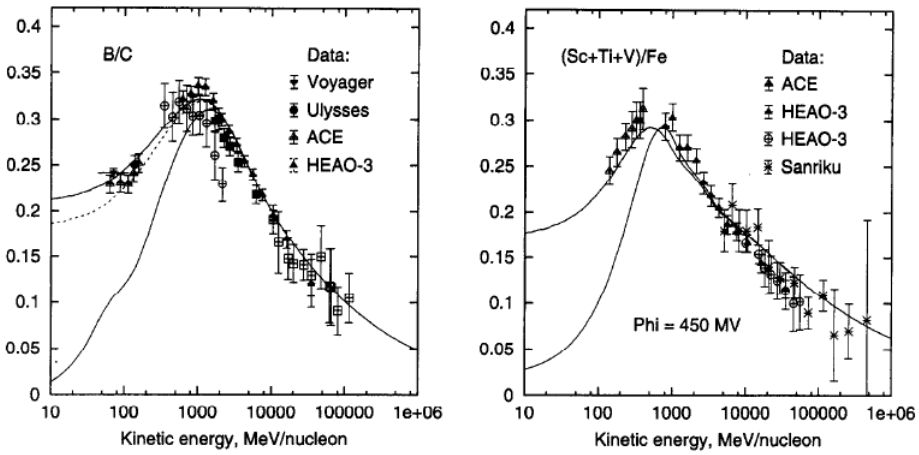

Figure 1.3: Ratio of "secondary" over "primary" GCRs. Left: B/C ratio; right: (Sc+Ti+V)/Fe ratio. Details are available at [5]

and, if the particle is unstable, can also give information about the lifetime of Cosmic Rays.

The ratio of "secondary" over "primary" N_{sec}/N_{prim}, for example, gives information about the quantity of matter traversed by cosmic rays. The mean free path of cosmic rays may be expressed by the mass thickness defined as:

$$x = \langle\rho\rangle l \quad [\mathrm{g/cm^2}] \tag{1.13}$$

where $\langle\rho\rangle$ is the mean density of the interstellar medium, and l is the distance traveled by the cosmic rays. The density number of particles in the interstellar medium is simply given by:

$$n = \frac{\langle\rho\rangle}{\langle m\rangle} \quad [\mathrm{cm^{-3}}] \tag{1.14}$$

where $\langle m\rangle$ is the mean mass of the interstellar medium. Qualitatively the N_{sec}/N_{prim} value is proportional to the cross section for secondary production σ_{sec}, and to the density number n, times the traveling distance:

$$\frac{N_{sec}}{N_{prim}} \propto \sigma_{sec} n l \propto \sigma_{sec} \frac{x}{\langle m\rangle} \tag{1.15}$$

This quantity is directly measured in experiments from which the mass thickness is estimated to be in the range $x = 6 - 10$ g/cm^2. Strong and

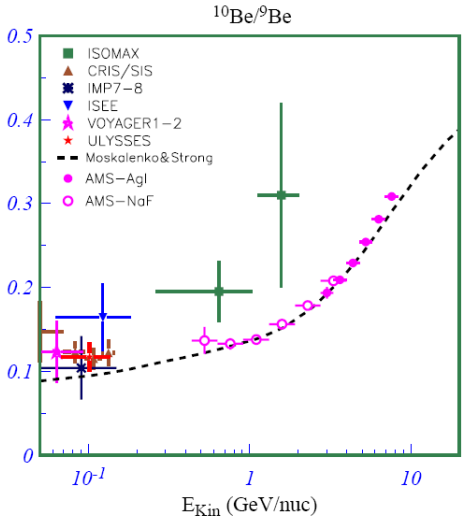

Figure 1.4: AMS-02 expected sensitivity on Be10/Be9 ratio [6]

Moscalenko [5] developed a code for the cosmic rays propagation using "secondary" over "primary" ratio. Their results of B/C and (Sc+Ti+V)/Fe ratios is compared with experimental data in figure 1.3.

The information about the lifetime of cosmic rays, may be obtained from "unstable"/"stable" isotopes ratio. By the equation (1.14), the mass thickness can also be rewritten as:

$$x = n\langle m\rangle l = n\langle m\rangle \ \beta c \ \tau_{life} \tag{1.16}$$

where βc is the velocity of the cosmic ray and τ_{life} is its the lifetime. In figure 1.4 is reported the ^{10}Be/^{9}Be ratio for experimental data and the corresponding excepted value for one year of observation with AMS-02 experiment [6]. From the fitting curves it is possible to estimate the density number as $n = 0.2$ cm^{-3}. By this result it is possible to deduce that cosmic rays spend much of their life in a medium of less density than the interstellar space, which may be, for example, the Halo of the Galaxy. The value of the number density n together with the mass thickness x, enables one to estimate the GCR mean lifetime as $\tau_{life} \sim 2 \times 10^7$ years.

In figure 1.5 are plotted the mayor components of primary cosmic rays nuclei of energies greater than 2 GeV/nucleon.

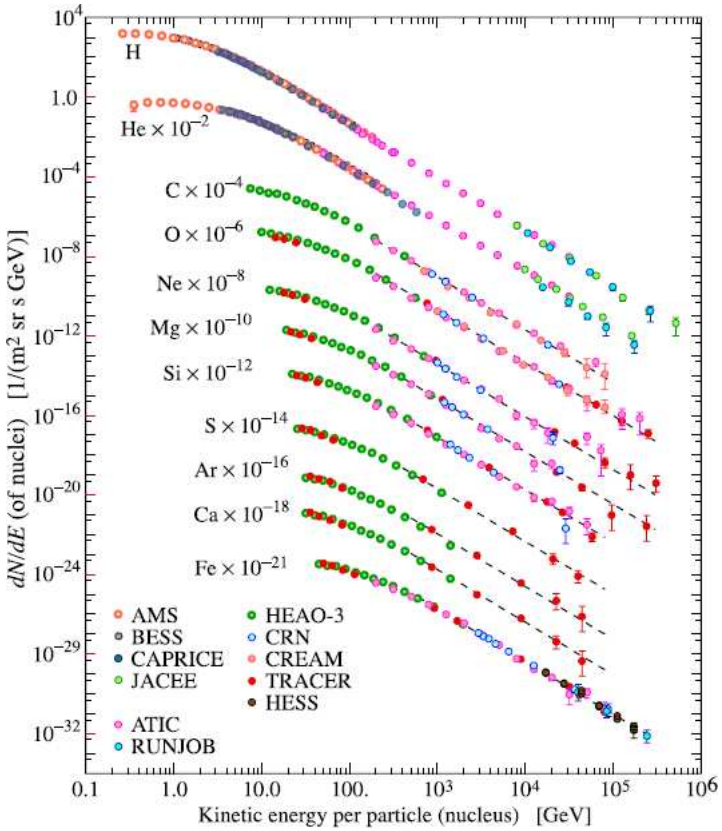

Figure 1.5: Mayor components of the primary cosmic rays [7]

1.2 Solar Wind and Heliospheric Magnetic Field

The solar wind is the extension into the interplanetary space of the *solar corona*, the outer region of the Sun's atmosphere. It is characterized by very high temperature (2×10^6 K) and low density (10^4-10^8 cm^{-3}) plasma made most of all by protons and electrons in equal measure.

The corona plasma is well described by the Magneto-Hydro-Dynamic theory (MHD) which enables one to obtain the hydrostatic solution of the coronal expansion in the interplanetary medium. The solar wind expands subsonically up to a distance of about 0.3 AU and then the expansion becames supersonic. The velocity of the solar wind was measured by the solar orbiter spacecraft *Ulysses* during different periods of the solar activity. Data were taken up to polar latitudes (80^o). At solar minimum, (see left side of figure 1.6) the solar wind fans out from the poles at an average speed of 750 km/s,

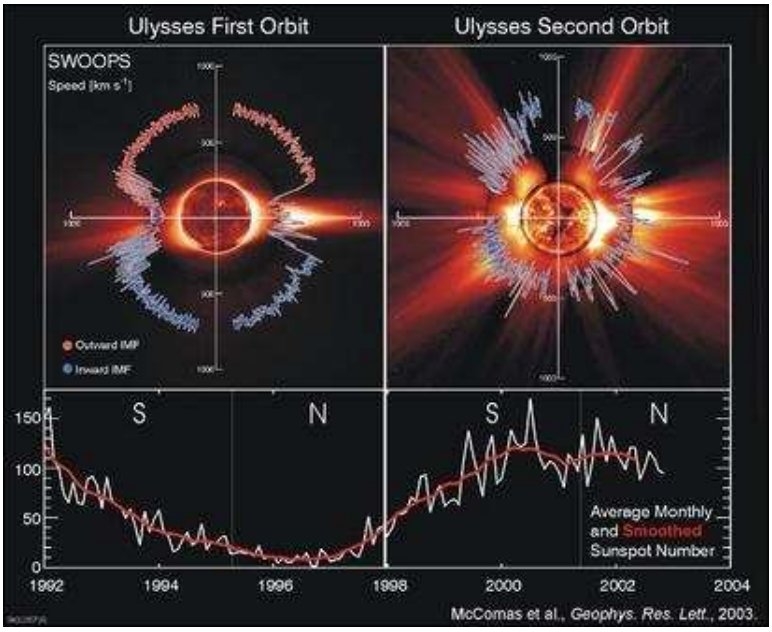

Figure 1.6: Solar wind speed as a function of latitude for Ulysses' first two orbits. Bottom: sunspot number over the period 1992-2003, declining phase of the solar minimum to the solar maximum [22].

much faster than the wind that emerges from the Sun's equatorial zone equal to 350 km/s. At solar maximum the solar wind is more irregular as shown in the right side of the same figure.

During the solar minimum the configuration of the Sun's magnetic field is well approximated by a dipole. The dipole configuration enables one to define the overall polarity of the Sun which is usually referred with the number A. If the northern hemisphere lines point outward the Sun, the polarity is defined positive ($A > 0$). In the opposite configuration the polarity is negative ($A < 0$).

The high corona temperature makes the plasma a very good conductor and, as a consequence, the Sun's magnetic file lines result to be frozen with the solar wind while it expands into the interplanetary space. Because of the solar rotation the geometry of the heliosphere magnetic file (HMF) lines basically follow an archimedean spiral (see left side of figure 1.7) but strongly depend on the solar activity. One of the consequences of the solar activity is the formation of spots over it surface at latitudes between 20^o-30^o. Sunspots are dark regions of relative low temperature plasma ($T \sim 4000$ K) with very strong local magnetic fields (up to 30 kG). Each sunspot is associated with another one of different polarity (inward-outward magnetic field) and

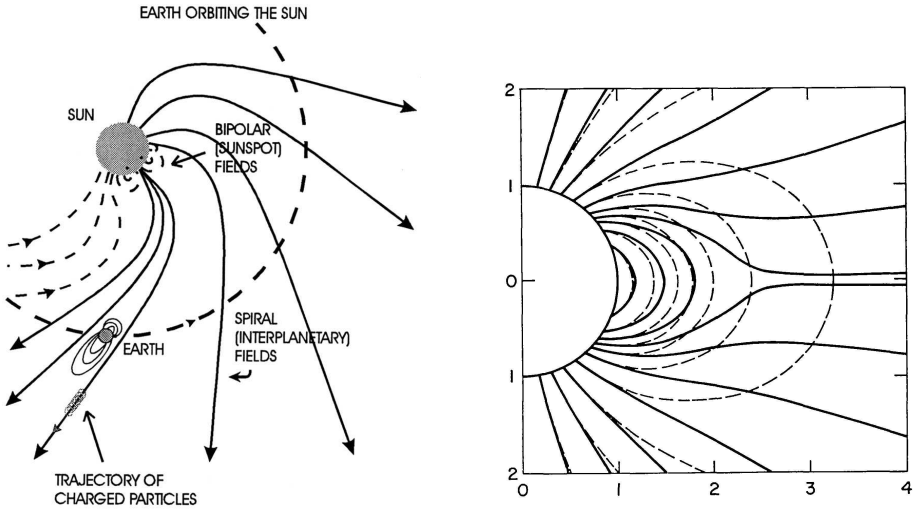

Figure 1.7: Left: interplanetary magnetic field lines. [27]. Right: Coronal Magnetic field line configuration during solar minimum; dashed lines refers to a pure dipole magnetic field [25].

together form a bipolar sunspot. The leading spot of the bipolar field has the same polarity as the solar hemisphere, while the trailing spot is of opposite polarity. Bipolar sunspots may form groups. The number of spots exhibit alternating periods of minimum and maximum which last about 11-years defining a solar cycle.

Sunspots have been monitored since the XVII century but the first solar cycle has been fixed in the period from 1755 to 1766 (see figure 1.8). At present (2009-2010) we are at the end of the 23^{rd} solar cycle. A useful quantity which enables one to control the solar activity is the sunspot index or *Wolf number* defined by [2]:

$$W = k(10g + f) \tag{1.17}$$

where f is the number of individual spots while g is the number of recognizable groups of sunspots and k is a correction factor accounting for the technological evolution of instruments. After each 11-year cycle the polarity of the Sun results to be reversed.

The reversal of the magnetic field lines follows a 22-years cycle which can be described by the Babcock's model [9] as a progression of distinct stages as shown in figure 1.9. The first stage starts with a solar minimum when the solar magnetic field can be described by an axis-symmetric dipole with a major poloidal component and a negligible toroidal one. This configuration is not stable because the Sun doesn't rotate as a rigid body but has a

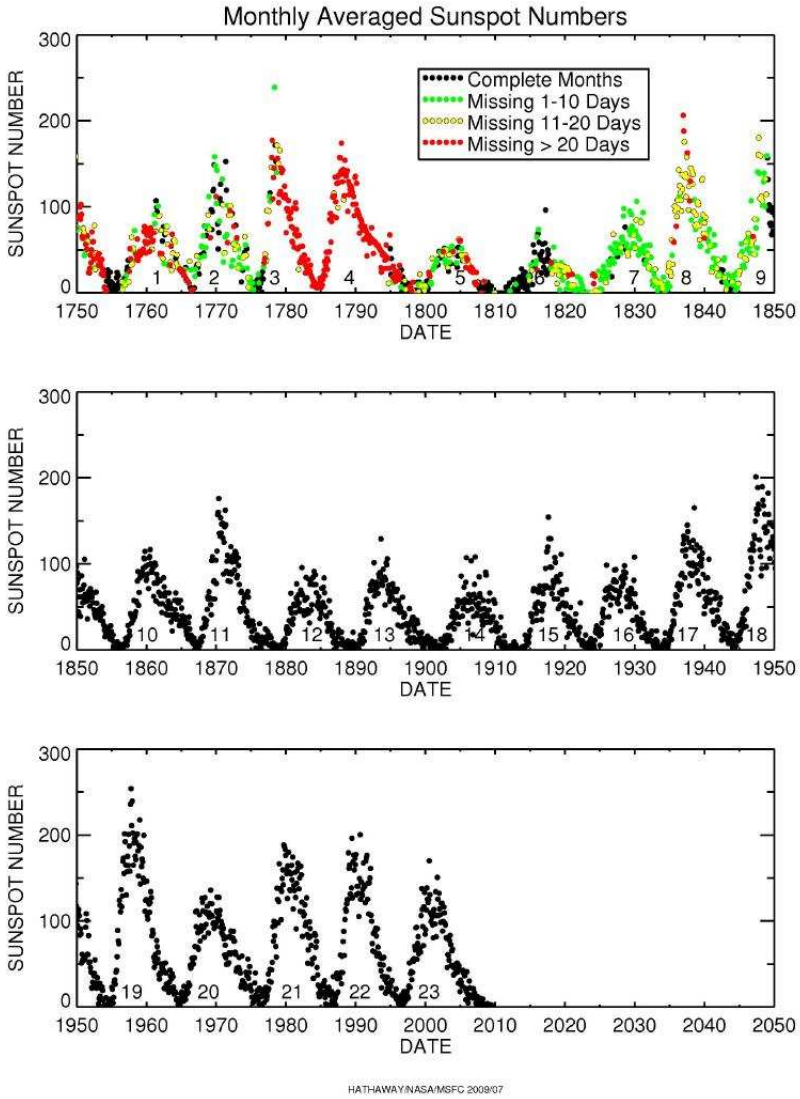

Figure 1.8: Monthly averages (updated 2009/07/01) of the sunspot numbers [23].

differential rotation: elements of fluid near the equator spin faster than the ones near the poles. As a consequence, the differential rotation makes the poloidal component progressively less important than the toroidal component which becomes the dominant one. The progressive intensification of the toroidal magnetic field causes the eruption of magnetic filed lines from the photosphere which appear as sunspots.

Sunspots of different polarity migrate towards opposite directions. The leading spots tend to migrate towards the equator, while the trailing spots

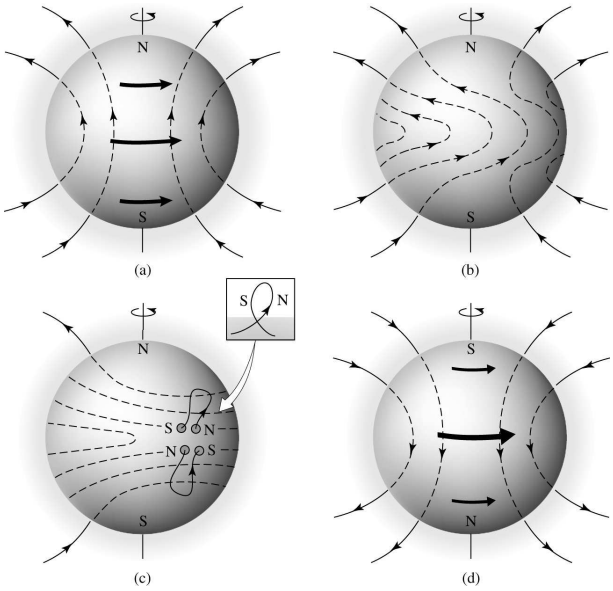

Figure 1.9: Schematic representation of the reversal magnetic field by the Babcock model. (a) Axis-symmetric poloidal magnetic field; (b) progressive growing of the toroidal magnetic field component due to the solar differential rotation; (c) formation of sunspots with closed magnetic field lines; (d) end of the cycle: the poloidal magnetic field is re-established with opposite polarity [24].

migrate towards the solar pole. At the equator the leading spots of each hemisphere cancel each other while at the poles the trailing spots neutralize the existing toroidal magnetic filed in favor of the poloidal component. The progressive formation and migration of sunspots continues until the solar dipole field results to be reversed.

The configuration of the Coronal magnetic field lines, during a solar minimum, is shown on the right side of figure 1.7. The pure dipole configuration is distorted because of the out going solar plasma. Magnetic field lines become open at relative low latitudes. Near the dipole equator the first open lines of each hemisphere can come quite close: since they have opposite direction the magnetic field must change sign rather suddenly. This implies the presence of a very high current density called heliospheric current sheet.

In addition, since the Sun's magnetic axis is tilted with respect to the solar rotation axes, the current sheet assumes a wavy form, similar to a ballerina's twirling skirt, while it expands into the interplanetary medium. The current sheet configuration varies according to the solar activity. The tilt angle increases progressively from a value of about 4^o-10^o during solar minimum to values which can exceed 75^o during solar maximum periods. Figure 1.10

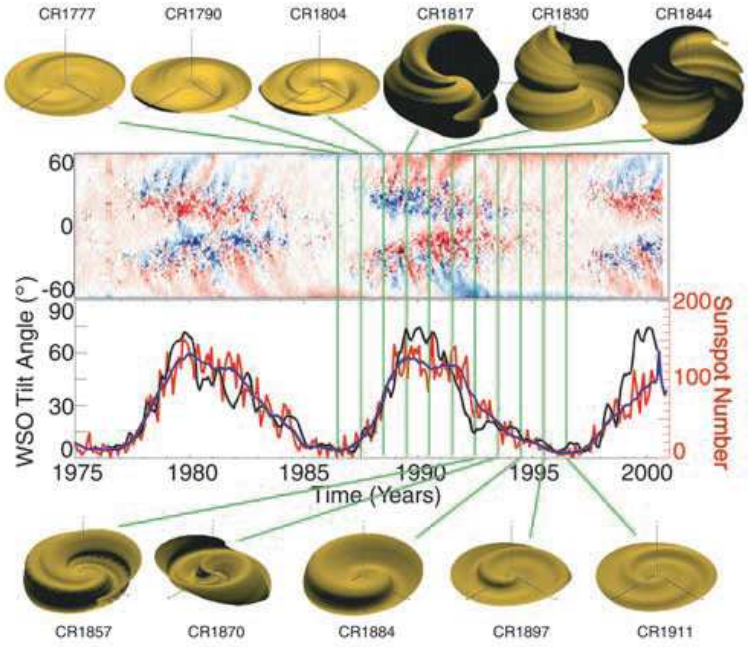

Figure 1.10: Evolution of the current sheet during the solar cycle 22. Upper central part: synoptic maps of the magnetic field lines; red and blue points indicate outward and inward polarity respectively. Lower central part: red and blue lines are monthly and yearly averaged values of sunspot number respectively [26].

represents a three-dimensional MHD model based on experimental data of the current sheet progressive evolution during the 22^{nd} solar cycle [26]. In the same figure, in the lower central part, it is reported the averaged value of the sunspot number and in the upper one it is shown the radial component of the magnetic field between $\pm 60^{o}$ Sun's latitudes. The current sheet brings an additive effect in the modulation of GCRs as it will be explained in next section.

1.2.1 The Modulation Effect

The modulation effect is the variation of the GCRs spectrum in relation to the solar activity. During solar maximum periods fluxes of low energetic particles are less abundant compare to the ones measured during solar minimum. The anti-correlation between solar minimum and maximum activity and particles fluxes is evident in the long record of the Climax neutron monitor[1] shown

[1]Neutrons are produced as secondary particles by the interaction of cosmic rays with the atoms of the earth atmosphere. Measures of neutron monitor enable to supervise the

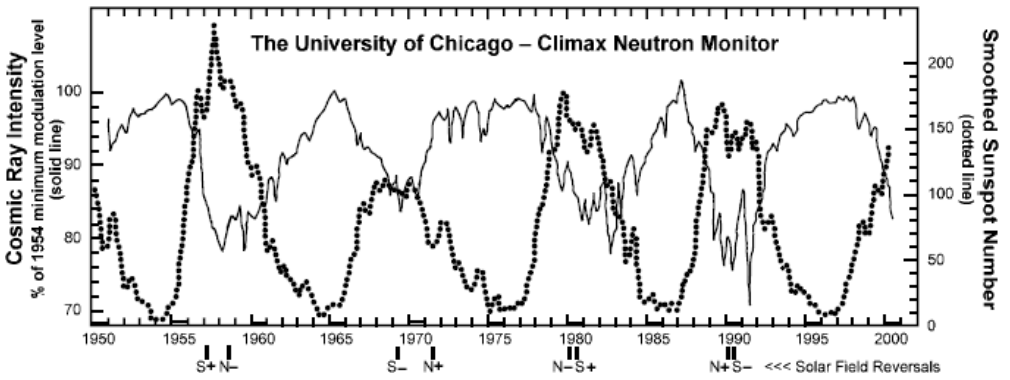

Figure 1.11: Continuous line: long term Climax neutron monitor observation; dashed line: smoothed sunspot number. Under the abscissa axis the reversal magnetic field polarity is reported [14].

in figure 1.11. The modulation effect can be explain by considering the propagation of GCRs in the heliosphere.

The basic theory of the cosmic rays propagation was developed in the sixteen's by Parker [10]. Cosmic rays that enter the heliosphere are subjected to a diffusion process caused by the small scale HMF irregularities, a convection plus a cooling process caused by the solar wind expansion and a drift process caused by curvatures and gradients of the HMF. The number density of particles having kinetic energy equal to T at time t in the position $\mathbf{r}$ inside the solar cavity, can be expressed by the quantity $U(\mathbf{r}, T, t)$. Its time variation is calculated by the Parker's transport equation which may be written, in a general form, as:

$$\frac{\partial U}{\partial t} = -\nabla\cdot(\mathbf{v}_{sw}U) + \frac{1}{3}(\nabla\cdot\mathbf{v}_{sw})\frac{\partial}{\partial T}(\alpha T U) + \nabla\cdot(\underline{\underline{\mathbf{k}}}^s\cdot\nabla U) - \nabla\cdot(\langle\mathbf{v}_d\rangle U) \quad (1.18)$$

where $\mathbf{v}_{sw}$ is the solar wind velocity, α is an energy dependent term which is $\alpha = 2$ for non-relativistic particles and $\alpha = 1$ for ultra-relativistic particles; the tensor $\underline{\underline{\mathbf{k}}}^s$ is the symmetric part of the diffusion tensor $\underline{\underline{\mathbf{k}}}$ which, in general, has the form:

$$\underline{\underline{\mathbf{k}}} = \begin{pmatrix} k_\perp & -k_A & 0 \\ k_A & k_\perp & 0 \\ 0 & 0 & k_\parallel \end{pmatrix} \quad (1.19)$$

where $k_\perp$ and $k_\parallel$ are the perpendicular and parallel components respect to the magnetic field direction; k_A is the antisymmetric tensor component which

cosmic ray fluxes. Data available at *http://ulysses.sr.unh.edu/NeutronMonitor/*

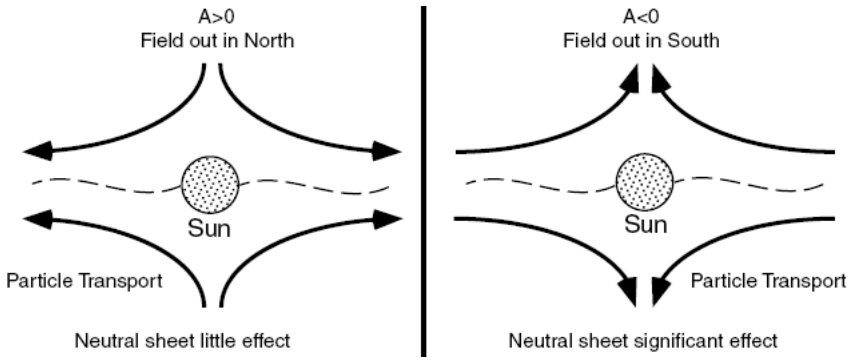

Figure 1.12: Drift direction of a positive charge particle according to the solar polarity magnetic field [14].

is responsible of the drift velocity whose mean value $\langle \mathbf{v}_d \rangle$ is present in the transport equation (5.40).

The first and the second terms of the (5.40) describe the convection of cosmic rays caused by the solar wind and the adiabatic energy loss of the particles because of the solar wind expansion, respectively; the third term represents the diffusion of particles along parallel and perpendicular directions of the HMF. The diffusion process is caused by the small-scale HMF irregularities which have typical dimensions of $10^5 - 10^7$ km. Assuming a magnetic field of few nT [1], these values correspond to the gyroradius dimension of a proton of about 100 MeV -10 GeV of kinetic energy, and so protons of this energies will be more affected by the diffusion process. The last term of equation (5.40) describes drift effects caused by HMF large-structures and dominates during solar minimum periods while can be neglected during maximum solar periods.

Convection and diffusion terms depend on the solar activity but are independent of the solar polarity. The drift term instead depends also on the solar polarity. Its direction is shown in figure 1.12 for a positive particle. When the Sun's polarity is positive $A > 0$, positive charged particles will propagate inside the heliosphere coming from the pole directions and will drift outward the heliosphere along the equator latitudes. In the opposite $A < 0$ configuration, cosmic rays will enter the heliosphere from the equatorial regions and will flow outside at polar latitudes. An additional drift effect, which is caused by the interaction of cosmic rays with the neutral sheet, is evident from the shape of the neutron monitor peaks recorded during solar minimum periods of opposite solar polarity. In positive periods ($A > 0$) particles come from the polar regions and the neutron monitor records almost flat peaks. In the reverse configuration ($A < 0$) sharply peaks are evident.

During negative periods, in facts, positive particles diffuse inward along equatorial regions where they encounter the neutral current sheet. Particles that cross the neutral sheet will experience magnetic fields of opposite polarity and this results to be a quite slow process compared with the one of inward propagation along the pole directions.

The net effect is visible on the cosmic ray density fluxes which are modulated during the 11-year cycle because of the minimum and maximum solar activity alternation and they show a further attenuation when the polarity is negative (22-years cycle).

1.2.2 ISO 15390 Model for Galactic Cosmic Rays

The ISO (International Organization of Standardization) 15390 model [15] is the standard for estimating the radiation impact of GCRs on hardware, biological and other materials in the space environment. It is based on the model of GCRs fluxes proposed by Nymmik [16]. It establishes the expected rigidity or energy spectra of GCRs in the near-Earth space, beyond the Earth's Magnetosphere. This model predicts fluxes of protons, electrons and nuclei up to $Z = 92$ in the energy range from 10 MeV/nucl to 100 GeV/nucl. It includes the modulation effect induced by the 11-year cycle of the solar activity and the 22-year reversal magnetic field cycle of the heliospheric magnetic field. The rigidity spectrum, for the i-th nucleus, is obtained by a semi-empirical relation calculated as:

$$\Phi_i(R,t) = \frac{C\beta_i^{\alpha_i}}{R^{\widetilde{\gamma}_i}} \left[\frac{R}{R + R_0(R,t)} \right]^{\Delta(R,t)} \tag{1.20}$$

β is the particle velocity in units of c, R is the rigidity of the particle expressed in GV; $\Delta_i(R,t)$, whose expression can be found in [15], is a dimensionless parameter which contains the dependence of the particle flux on the large-scale magnetic field polarity at time t; $R_0(R,t)$ is the modulation potential given by:

$$R_0(R,t) = 0.375 + 3 \times 10^{-4} \overline{W}_{t-\delta t}^{1.45} \tag{1.21}$$

where $\overline{W}_{t-\delta t}$ is the smoothed monthly *Wolf number* averaged over 12-months a sort of mean of the sunspots number calculated at time $t - \delta t$; the Wolf number is the only parameter of the model and it is calculated at the time δt before the measure. The lag time δt takes in to account the polarity of the solar cycle and depends also on the particle rigidity. The terms C_i, α_i and $\widetilde{\gamma}_i$ are the fitting coefficients of the experimental data for the i-th nucleus, calculated by the Monte Carlo method using the last-squares technique. Their

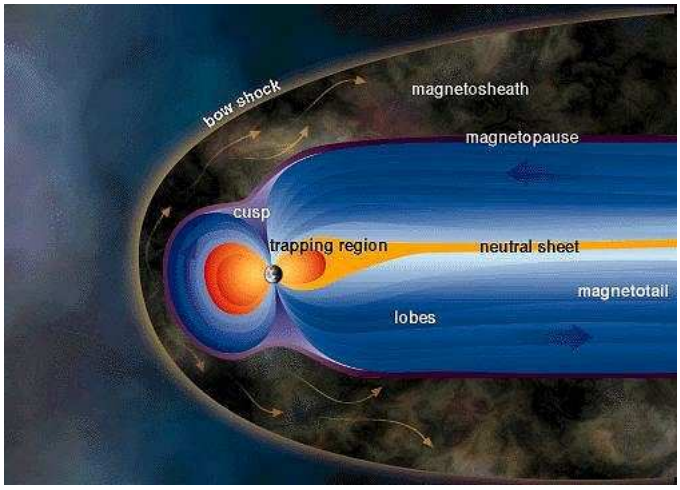

Figure 1.13: Artistic view of the Earth's magnetosphere.

values can be found in [15], [16] and their standard deviations determinate the error bars of the fluxes.

The energy spectra, derived from the (1.20), is given in units of [s m^2 sr MeV/nucl]$^{-1}$ and it is calculated by:

$$\Phi_i(E,t) = \Phi_i(R,t)\frac{A_i}{|Z_i|\beta} \times 10^{-3} \tag{1.22}$$

where A_i and Z_i are the mass and the atomic numbers of the particle.

1.3 The Earth's Magnetosphere and Trapped Particles

The *magnetosphere* is the region of space around the Earth where the dipolar Earth's magnetic field extends its effects. Its shape is influenced by the solar wind which constantly blows and transports the heliospheric magnetic field. The interaction between the high speed solar wind plasma and the Earth's magnetic field make it assumes a compressed form on the day-side and a stretched shape on the night-side. The day-side of the magnetosphere may vary with the solar activity changing its extension from 6 Re up to 10 Re while the night-side may extend to thousands of Re (Earth's radius, Re= 6371 km) [1].

In figure 1.13 it is reported an artistic view of the Earth's magnetosphere. A standing shock wave is expected to be formed in the boundary between

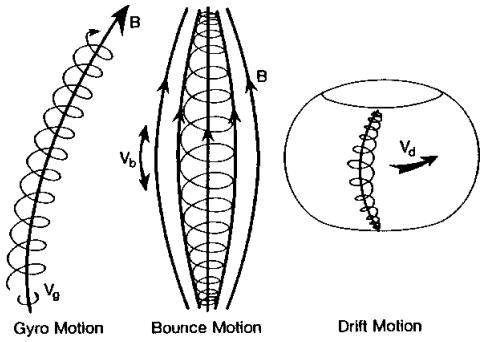

Figure 1.14: Decomposition of the motion of a trapped particle in the Earth's magnetosphere.

the supersonic solar wind and the magnetosphere [2]. The solar wind is decelerated in this *blow shock* and flows tangentially along the *magnetopause* forming a region called the *magnetosheath*. The magnetopause, which is the outmost boundary of the magnetosphere, partially prevents the solar plasma to penetrate the inner regions of the magnetosphere. Anyway the presence of a flowing plasma in the *low latitude boundary layer* (a thin region just under the magnetopause) indicates that the magnetopause doesn't act as a perfect shield. In the interface between the day and night -sides there are also two *polar cups* regions where the magnetosheath plasma extends deeper in the dense region of the atmosphere.
Along the night-side of the magnetosphere the magnetic field lines are highly stretched and become open forming the *magnetotail*. In this region there is the *plasma mantle* which comes from the plasma magnetosheath and extends almost parallel to the magnetic field lines. The division between north and south hemispheres is characterized by magnetic field lines of opposite polarity which come quite near each other in the magnetotail and they cause the formation of a neutral current sheet layer.

The inner regions of the magnetosphere are characterized by a bipolar magnetic field with closed field lines. In these regions there are the two *Van Allen radiation belts* divided by the *slot region*. The inner radiation belt extends in the range $1.5 - 2.4$ Re, while the outer radiation belt lies between $4.5 - 5$ Re. In these regions charged particles with rigidity lower than the *geomagnetic cut off* value R_{cut}, which depends on the geomagnetic latitude, result to be trapped by the magnetic field lines. The cut off value sets also the minimum value under which a particle can't penetrate inside the magnetosphere. This leads to an additional modulation effect in the low part of the cosmic ray spectrum observed inside the magnetosphere. The

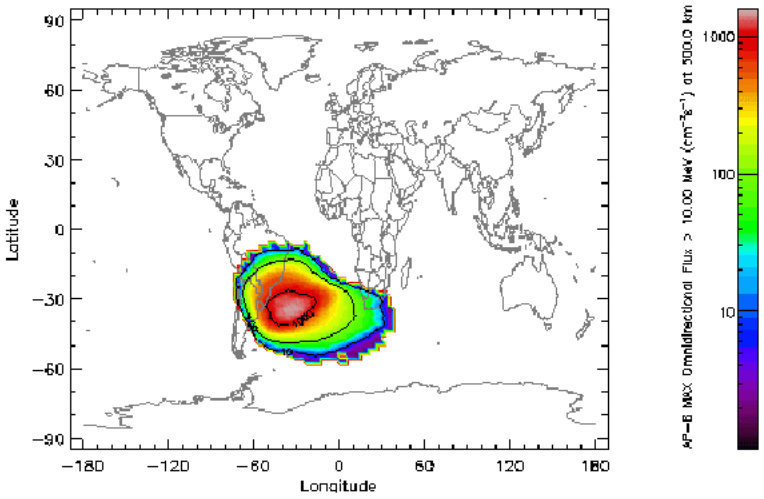

Figure 1.15: South Atlantic Anomaly. From AP-8 MAX (SPENVIS)[1]. Proton integral flux ($E > 10$ MeV) at 500 km goes from 1 to $\sim 2{\times}10^3$ cm^{-2} s^{-1} [28].

transport of GCRs through the magnetosphere may be done by the use of a *transmission function* which depends on the particle rigidity, latitude and declination of the observation point [1].

The motion of a trapped particle in the geomagnetic field can be decomposed in three components as represented in figure 1.14. The first component is the gyration of the particle around the magnetic field line following a helical orbit. While it gyrates, the particle reaches regions where the magnetic field is more intens. This causes a reflection of the particle which experiences the magnetic mirror force that makes it bouncing back-and-forth. In addition the geomagnetic field has a gradient in the perpendicular direction of the magnetic field lines that make the particles drift around the Earth. The drift motion usually takes from minutes to hours; the bounce motion seconds to minutes and the gyro motion milliseconds to seconds.

In the Low Earth's Orbits (LEO altitudes 100-1000 km [18]) where many space missions are present, there is the AMS-radiation belt. In this region quasi-trapped particles of energy up to few GeV/nucleon were observed by the AMS mission in the 1998. These particles are Secondary Cosmic Rays produced by the interaction of the primary GCRs with the upper layers of the atmosphere. In addition the LEO intersect the South Atlantic Anomaly (SAA) a region of space where the geomagnetic field is particularly week and so energetic particle may reach the altitude of about 500 km (see figure 1.15).

At higher altitudes (1000-36000 km) there are the *Medium Earth Orbits*

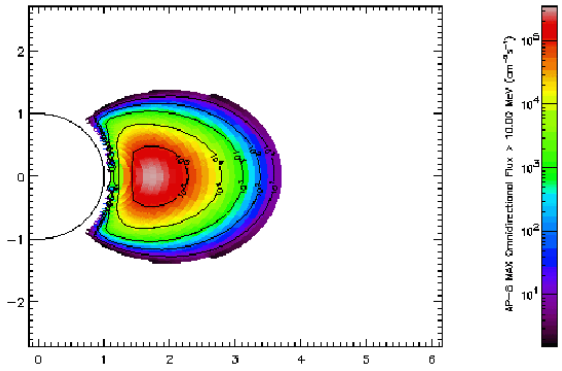

Figure 1.16: Trapped proton belt. From AP-8 MAX (SPENVIS)[1]. Proton integral fluxes ($E > 10$ MeV) go from 1 to $\sim 3{\times}10^5$ cm^{-2} s^{-1} [28].

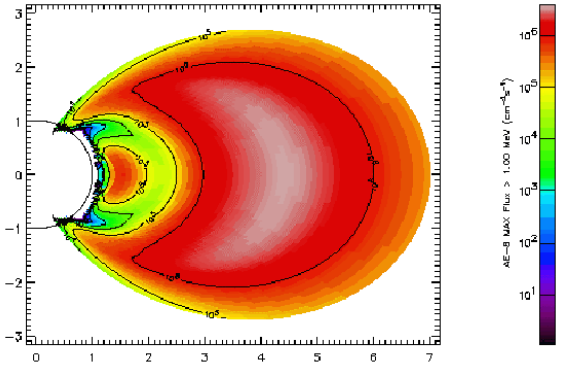

Figure 1.17: Trapped electron belt. From AE-8 MAX (SPENVIS)[1]. Electron integral fluxes ($E > 1$ MeV) go from 1 to $\sim 3{\times}\ 10^5$ cm^{-2} s^{-1} [28].

which intersect the inner radiation belt populated most of all by protons in the energy range 10 - 100 MeV (see figure 1.16) but there are also less energetic electrons. The population of this region is quite stable even if it can vary with the solar activity. These particles come most of all from the Cosmic Ray Albedo Decay. Neutrons are generated by the collision of cosmic rays with the atoms of the atmosphere. For example a proton with energy of 5 GeV produces about seven neutrons a fraction of which diffuses in the out direction of the magnetosphere where it decays in protons and electrons which become trapped particles [17].

[1]The AP-8 and AE-8 models consist of maps that contain omnidirectional, integral electron and proton fluxes in the energy range 0.04 MeV to 7 MeV for electrons and 0.1

At the altitude of 36000 km there is the *geostationary orbit* which is used for space communication satellites. This orbit intersects the outer radiation belt which contains most of all electrons of energies up to 10 MeV (see figure 1.17). These electrons are most of all the result of geomagnetic storms and so their density population fluctuates very often.

MeV to 400 MeV for protons in the Earth's radiation belts. The maps are based on data from more than 20 satellites [29].

Chapter 2

Electromagnetic Energy Loss

Charged energetic particles, like cosmic rays, lose energy while passing through matter by Coulomb interactions with the electrons and with the nuclei of the material. To calculate the energy loss it is necessary to determinate the differential scattering cross section for energy transfer which depends on the specific interaction potential $V(r)$. For charged particles, as cosmic rays, the Coulomb scattering process will be analyzed in details. Particular attention will be paid on the *nuclear collisions* mechanism which is responsible for the formation of defects inside the material. The electronic energy loss and its fluctuations will be also reported for completeness.

2.1 Coulomb Scattering Process

In this section elastic collisions between two particles will be considered. The collision is elastic if the total kinetic energy of the two particles remains the same before and after collision. The problem can be analyzed in three systems of reference: *relative*, *center of mass* and *laboratory system*. In the relative one the interaction is viewed by an observer fixed at the target position while the mass of the collision partner is equal to the *reduced mass*. The advantage of using this system consists in reducing the two particles problem into the interaction between a fixed scattering center and an effective particle of mass equal to the reduced mass.

2.1.1 Non-Relativistic Scattering

The scattering problem may be solved by introducing the position of the center of mass $\mathbf{R}$ and the relative position $\mathbf{r}$ of the two particles defined

as [30]:

$$\mathbf{R} = \frac{m_1\mathbf{r}_1 + m_2\mathbf{r}_2}{m_1 + m_2} = \frac{(m_1\mathbf{r}_1 + m_2\mathbf{r}_2)}{M} \tag{2.1}$$

$$\mathbf{r} = \mathbf{r}_1 - \mathbf{r}_2 \tag{2.2}$$

where m_1 and m_2 are the projectile and target particle masses respectively and $M = m_1 + m_2$. The two-body problem is separated into the motion of the center of mass $\mathbf{R}$, viewed from the laboratory system, and into the relative motion $\mathbf{r}$ which is the trajectory, viewed from the target particle, described by an effective particle with mass equal to the reduced mass μ whose non-relativistic expression is given by:

$$\mu \equiv \left(\frac{1}{m_1} + \frac{1}{m_2}\right)^{-1} = \frac{m_1 m_2}{m_1 + m_2} \tag{2.3}$$

The total energy of the system is equal to:

$$E_{tot} = \frac{1}{2}m_1\dot{\mathbf{r}}_1^{\,2} + \frac{1}{2}m_2\dot{\mathbf{r}}_2^{\,2} + V(r) = \frac{1}{2}M\dot{\mathbf{R}}^2 + \frac{1}{2}\mu\dot{\mathbf{r}}^2 + V(r) \tag{2.4}$$

where the first term on the right side of the equation is the kinetic energy of the center of mass and the sum of the other two terms defines the relative energy:

$$E_r = \frac{1}{2}\mu\dot{\mathbf{r}}^2 + V(r) \tag{2.5}$$

The motion of the center of mass, viewed from the laboratory system, is rectilinear uniform along a straight line. The relative motion instead may be described by the motion of the effective particle of mass μ which moves along a curved trajectory described by $\mathbf{r}$, in a fix plain as shown in figure 2.1. At large distances the relative energy is simply given by:

$$E_r = \frac{1}{2}\mu v^2 = E_1\frac{m_2}{m_1 + m_2} \tag{2.6}$$

where v is the relative velocity which is equal to projectile particle velocity v_1 if the target is at rest before scattering, and $E_1 = m_1 v_1^2/2$ is the kinetic energy of the projectile particle.

The relative motion may be obtained from the equation of motion written in polar coordinates (r, φ). Eliminating the φ coordinate it is possible to obtain the radial component of the relative velocity as [30]:

$$\dot{r} = \mp v\left\{1 - \frac{V(r)}{E_r} - \frac{b^2}{r^2}\right\}^{\frac{1}{2}} \tag{2.7}$$

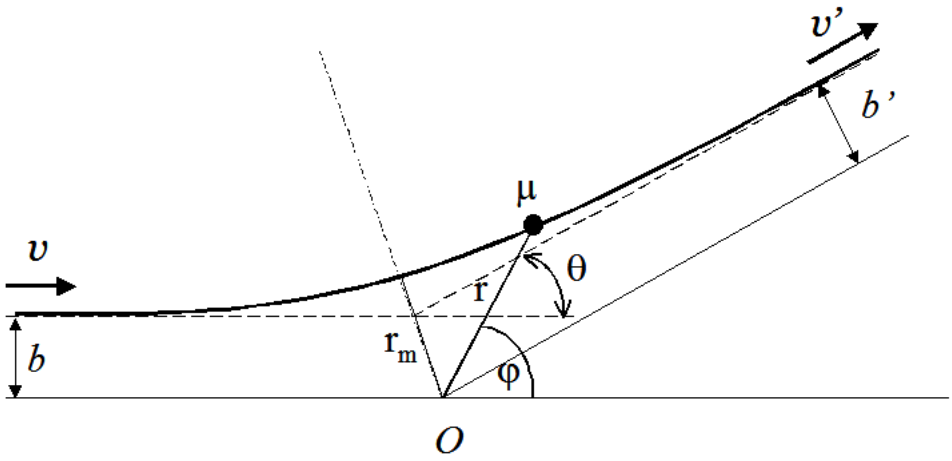

Figure 2.1: Scattering process in the relative frame of reference. $v = v'$ initial and final velocities; $b = b'$ initial and final impact parameters; r, φ polar coordinates; r_m distance of closest approach; θ scattering angle; μ reduced mass; O origin of the scattering center.

where b is the impact parameter. This expression enables one to obtain the distance of closest approach r_m by the equation:

$$0 = 1 - \frac{V(r_m)}{E_r} - \frac{b^2}{r_m^2} \tag{2.8}$$

that is when the radial velocity vanishes. The distance of closest approach depends on the impact parameter b and on the interaction potential $V(r)$.

The angle of deflection or *scattering angle* can be obtained from the equation of the trajectory and it is equal to [30]:

$$\theta = \pi - 2\int_{r_m}^{\infty} \frac{b}{r^2}\left\{1 - \frac{V(r)}{E_r} - \frac{b^2}{r^2}\right\}^{-\frac{1}{2}} dr. \tag{2.9}$$

It is important to say that for a given interaction potential the scattering angle depends only on the impact parameter b and on the relative energy E_r.

The scattering problem may be also solved in the center of mass (CM) system where the origin of the coordinate axis is fixed at the center of mass position:

$$\mathbf{R}_{CM} = \frac{m_1\mathbf{r}_{1CM} + m_2\mathbf{r}_{2CM}}{M} = 0 \tag{2.10}$$

where the CM index refers to the center of mass coordinate system.

The positions of the two particles in the CM system are related to the laboratory system $\mathbf{r}_1, \mathbf{r}_2$ coordinates, to the CM's position $\mathbf{R}$ (2.1), and to

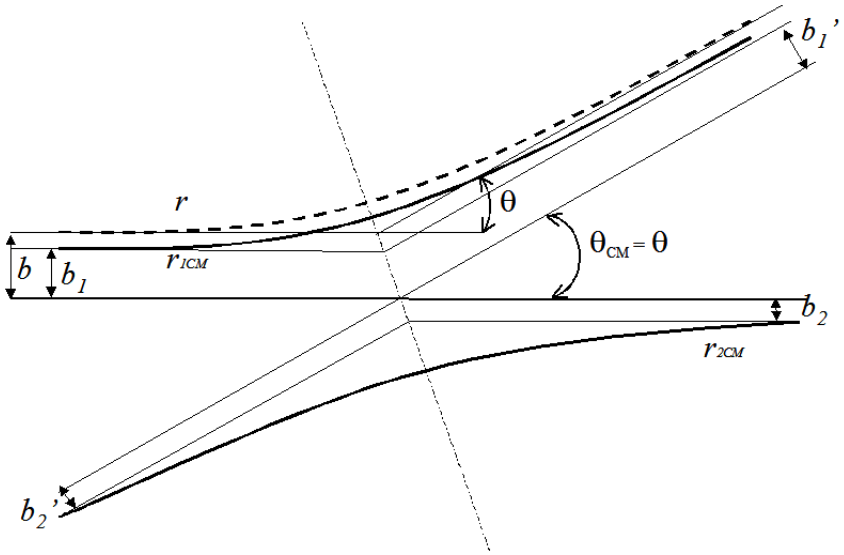

Figure 2.2: Scattering process in the center of mass frame; $\mathbf{r}$ trajectory of the relative motion; $\mathbf{r}_{1CM}$, $\mathbf{r}_{2CM}$ trajectories of the projectile and target; $b_i = b_i'$ initial and final impact parameter ($i = 1, 2$); $b = b_1 + b_2$ impact parameter in the relative frame of reference; θ scattering angle in the relative system; θ_{CM} scattering angle in the CM system.

the relative position $\mathbf{r}$ (2.2), by:

$$\mathbf{r}_{1CM} = \mathbf{r}_1 - \mathbf{R} = \frac{m_2}{M}\mathbf{r} \tag{2.11}$$

$$\mathbf{r}_{2CM} = \mathbf{r}_2 - \mathbf{R} = -\frac{m_1}{M}\mathbf{r} \tag{2.12}$$

An observer in the origin will see the two particles approaching each other before the collision and after the collision he will see them moving far away in opposite directions. The trajectories of the two particles will remain parallel before and after the collision, and since the relative velocity can also be written as $\dot{\mathbf{r}} = \dot{\mathbf{r}}_{1CM} - \dot{\mathbf{r}}_{2CM}$, the two trajectories will also be parallel to the relative one as shown in figure 2.2. This has the important consequence that the scattering angle of both particles in the center of mass system, is equal to the one of the effective particle in the relative frame of reference:

$$\theta_{1CM} = \theta_{2CM} \equiv \theta \tag{2.13}$$

which is given by the equation (2.9).

In the center of mass system the momentum and the energy are conserved and since the position of the CM is fixed (2.10) the total momentum is equal to zero:

$$M\dot{\mathbf{R}}_{CM} = m_1\dot{\mathbf{r}}_{1CM} + m_2\dot{\mathbf{r}}_{2CM} = 0 \tag{2.14}$$

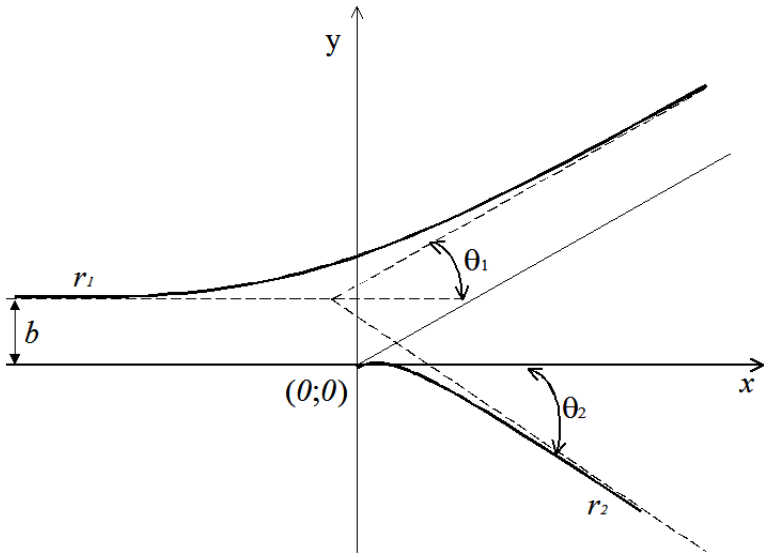

Figure 2.3: Scattering in the laboratory frame. $\mathbf{r}_1$, $\mathbf{r}_2$ projectile and target trajectories, b impact parameter; θ_1, θ_2 deflecting angles.

which implies that the momenta of the two particles are equal and opposite:

$$m_1 \dot{\mathbf{r}}_{1CM} = -m_2 \dot{\mathbf{r}}_{2CM} \tag{2.15}$$

By the use of the (2.11) with the reduced mass definition (2.3), it is possible to obtain:

$$m_1 \dot{\mathbf{r}}_{1CM} = \mu \dot{\mathbf{r}} \tag{2.16}$$

i.e. the momentum of the effective particle is equal to the momentum of the projectile particle in the CM system.

Once that the problem is solved in the center of mass system, all the quantities can be obtained in the laboratory system. The initial momenta of the two particles before collision can be obtained from the (2.11) and (2.12):

$$\mathbf{p}_1 = \mu \dot{\mathbf{r}} + m_1 \dot{\mathbf{R}} \tag{2.17}$$

$$\mathbf{p}_2 = -\mu \dot{\mathbf{r}} + m_2 \dot{\mathbf{R}} \tag{2.18}$$

The final momenta after collision $\mathbf{p}'_1$, $\mathbf{p}'_2$ can be obtained from the initial ones by eliminating the center of mass velocity and considering that the relative velocity remains unchanged after collision:

$$\mathbf{p}'_1 = \mu \dot{\mathbf{r}}' + \frac{m_1}{M}(\mathbf{p}_1 + \mathbf{p}_2) \tag{2.19}$$

$$\mathbf{p}'_2 = -\mu \dot{\mathbf{r}}' + \frac{m_2}{M}(\mathbf{p}_1 + \mathbf{p}_2). \tag{2.20}$$

where $\dot{\mathbf{r}}'$ is the relative velocity after scattering whose absolute value is equal to the one before scattering ($\dot{r}' = \dot{r}$). If the target is at rest before scattering ($\mathbf{p}_2 = 0$), then the x and y components of the momentum projectile particle after scattering are given by:

$$x) \quad p_1' \cos\theta_1 = \mu\dot{r}\cos\theta + \frac{m_1}{M}p_1 \tag{2.21}$$

$$y) \quad p_1' \sin\theta_1 = \mu\dot{r}\sin\theta \tag{2.22}$$

where θ_1 is the scattering angle of the projectile particle (in the laboratory system of reference). The ratio of the y component over the x one, together with the definition of the reduced mass and of the relative velocity (which in this case is $\dot{\mathbf{r}} = \dot{\mathbf{r}}_1$), enables one to obtain the scattering angle of the projectile particle in the laboratory system θ_1, as a function of the relative scattering angle θ i.e.:

$$\tan\theta_1 = \frac{\sin\theta}{\dfrac{m_1}{m_2} + \cos\theta} \tag{2.23}$$

The same can be done for the scattering angle of the target particle. The (2.20) can be decomposed as:

$$x) \qquad p_2' \cos\theta_2 = -\mu\dot{r}\cos\theta + \frac{m_2}{M}p_1 = \mu\dot{r}(1-\cos\theta) \tag{2.24}$$

$$y) \qquad -p_2' \sin\theta_2 = -\mu\dot{r}\sin\theta \tag{2.25}$$

where it has been considered that $p_1 = m_1\dot{r}_1 = m_1\dot{r}$. From the ratio of these last two equations it is possible to obtain:

$$\tan\theta_2 = \frac{\sin\theta}{1-\cos\theta} \tag{2.26}$$

or equivalently that $\theta_2 = (\pi - \theta)/2$.

The final kinetic energies of the projectile and of the target are simply given by $E_1' = p_1'^2/(2m_1)$, $E_2' = p_2'^2/(2m_2)$. If the target is initially at rest, then its kinetic energy after collision, denoted by T, can be calculated by squaring and summing the two equations (2.24), (2.25):

$$T \equiv E_2' = \frac{p_2'^2}{2m_2} = \frac{(\mu\dot{r})^2}{2m_2}[(1-\cos\theta)^2 + \sin\theta^2] = \frac{m_1 m_2}{M^2}E_1 2(1-\cos\theta) \tag{2.27}$$

and remembering that $2(1-\cos\theta) = 4\sin^2\frac{\theta}{2}$ the energy transferred by the projectile particle to the target one is equal to:

$$T = T_{max}\sin^2\frac{\theta}{2} \tag{2.28}$$

where T_{max} is the maximum energy that can be transferred during a single collision i.e.:

$$T_{max} = \frac{4m_1m_2}{M^2}E_1 \tag{2.29}$$

The scattering process in the laboratory system is schematized in figure 2.3.

2.1.2 Relativistic Treatment of Scattering

Cosmic rays are high energy particles thus the treatment described so far has to be generalized to a relativistic treatment of scattering. In any frame of reference a particle of rest mass m and velocity $\mathbf{v}$ has momentum equal to:

$$\mathbf{p} = m\mathbf{v}\gamma \tag{2.30}$$

where γ is:

$$\gamma = \frac{1}{\sqrt{1-\beta^2}} \tag{2.31}$$

and $\beta = |\mathbf{v}|/c$. The relativistic total energy is given by:

$$\mathscr{E} = mc^2\gamma \tag{2.32}$$

that can be also written as:

$$\mathscr{E} = mc^2 + E \tag{2.33}$$

where E is the kinetic energy of the particle which can be expressed by:

$$E = mc^2(\gamma - 1) \tag{2.34}$$

Another useful relation between total energy and momentum is:

$$\mathscr{E}^2 = (pc)^2 + (mc^2)^2 \tag{2.35}$$

which together with the (2.32) and the (2.31) enables one to write:

$$\frac{1}{\beta^2} = 1 + \left(\frac{mc^2}{pc}\right)^2 \tag{2.36}$$

The total energy $\mathscr{E}$ and the three components of the momentum $\mathbf{p}$ form the four-vector:

$$(a_1, a_2, a_3, a_4) = \left(p_x, p_y, p_z, \frac{\imath}{c}\mathscr{E}\right) \tag{2.37}$$

with $\imath = (-1)^{1/2}$. The Lorentz'e transformations between the laboratory frame of reference to another inertial frame, which moves with velocity V parallel to the x axis, are:

$$\begin{aligned} a_1 &= \frac{\overline{a}_1 - \imath(V/c)\overline{a}_4}{\sqrt{1 - V^2/c^2}} \\ a_2 &= \overline{a}_2 \\ a_3 &= \overline{a}_3 \\ a_4 &= \frac{\overline{a}_4 + \imath(V/c)\overline{a}_1}{\sqrt{1 - V^2/c^2}} \end{aligned} \tag{2.38}$$

where the $\overline{a}_i$ components refer to the moving frame of reference. If the center of mass moves with velocity V along the x axis, the transformations (2.38) enable one to pass from the center of mass system to the laboratory system and to obtain the energy-momentum components:

$$\begin{aligned} p_x &= \frac{p_{xCM} + (V/c^2)\mathscr{E}_{CM}}{\sqrt{1 - \beta_{cm}^2}} \\ p_y &= p_{yCM} \\ p_z &= p_{zCM} \\ \mathscr{E} &= \frac{\mathscr{E}_{CM} + V\ p_{xCM}}{\sqrt{1 - \beta_{cm}^2}} \end{aligned} \tag{2.39}$$

where $\beta_{cm} = V/c$ is the velocity of the center of mass viewed from the laboratory system. These latter relations can be used to deduce the coordinates of the four-vector in the center of mass system as a function of the laboratory system coordinates i.e.:

$$\begin{aligned} p_{xCM} &= \frac{p_x - (V/c^2)\mathscr{E}}{\sqrt{1 - \beta_{cm}^2}} \\ p_{yCM} &= p_y \\ p_{zCM} &= p_z \\ \mathscr{E}_{CM} &= \frac{\mathscr{E} - V\ p_x}{\sqrt{1 - \beta_{cm}^2}} \end{aligned} \tag{2.40}$$

During a scattering process of a projectile particle of rest mass m_1 which moves with velocity $\mathbf{v}_1$, and a target particle of rest mass m_2 initially at rest in the laboratory system ($\mathbf{p}_2 = 0$), the conservation of momentum and total energy are equal to:

$$\mathbf{p}_1 = \mathbf{p}_1' + \mathbf{p}_2' \tag{2.41}$$

$$\mathscr{E}_1 + \mathscr{E}_2 = \mathscr{E}_1' + \mathscr{E}_2' \tag{2.42}$$

where $\mathscr{E}_2 = m_2c^2$ and the primed quantities are momenta and total energies after scattering. If both particles before scattering are considered as a unique system of total energy $(\mathscr{E}_1 + \mathscr{E}_2)$ then from the relations (2.30) and (2.32) the total momentum is equal to:

$$\mathbf{p}_1 = \frac{\mathscr{E}_1 + \mathscr{E}_2}{c^2}\mathbf{V} \tag{2.43}$$

where $\mathbf{V}$ is the velocity of the center of mass seen from the laboratory system. The equation (2.43) is useful to deduce a relation between β_{cm}, the total energy of the system $\mathscr{E}$ and the momentum of the projectile particle p_1:

$$\beta_{cm}^2 = \frac{(p_1c)^2}{(\mathscr{E}_1 + m_2c^2)^2} = \frac{\mathscr{E}_1^2 - (m_1c^2)^2}{(\mathscr{E}_1 + m_2c^2)^2} \tag{2.44}$$

In the center of mass system, the conservation of total momentum and total energy are:

$$\mathbf{p}_{1CM} + \mathbf{p}_{2CM} = \mathbf{p}'_{1CM} + \mathbf{p}'_{2CM} \tag{2.45}$$
$$\mathscr{E}_{1CM} + \mathscr{E}_{2CM} = \mathscr{E}'_{1CM} + \mathscr{E}'_{2CM} \tag{2.46}$$

With the use of the transformations (2.40) and of the relation (2.43) it is possible to demonstrate that in the CM system the total momentum before and after scattering (2.45) is zero and, as a consequence, the two particles have equal momenta with opposite directions before and after scattering:

$$\mathbf{p}_{1CM} = -\mathbf{p}_{2CM} \tag{2.47}$$
$$\mathbf{p}'_{1CM} = -\mathbf{p}'_{2CM} \tag{2.48}$$

which is equivalent to say that their trajectories remain parallel during the scattering process as in the non-relativistic case. The use of the relation between total energy and momentum (2.35) for both particles before and after scattering together with the (2.46) leads to:

$$\mathscr{E}_{1CM} = \mathscr{E}'_{1CM}; \quad \mathscr{E}_{2CM} = \mathscr{E}'_{2CM} \tag{2.49}$$

or equivalently to:

$$\mathbf{p}_{1CM}^2 = \mathbf{p}_{1CM}'^2; \quad \mathbf{p}_{2CM}^2 = \mathbf{p}_{2CM}'^2 \tag{2.50}$$

that is the modulus of the momentum is the same before and after scattering for both particles. This last observation together with the (2.47) and (2.48) enable one to say that the scattering angle θ in the center of mass system

is the same for both particles as in the non-relativistic case. In addition the total energy of both particle is the same before and after scattering (2.49).

Before scattering the total energy and momentum of the target particle in the CM system can be obtain from the transformations (2.40) together with $\mathscr{E}_2 = m_2c^2$ and $p_2 = 0$:

$$\mathscr{E}_{2CM} = \frac{m_2c^2}{\sqrt{1-\beta_{cm}^2}} \tag{2.51}$$

$$\mathbf{p}_{2CM} = -\frac{m_2\mathbf{V}}{\sqrt{1-\beta_{cm}^2}}. \tag{2.52}$$

This latter relation implies that $\mathbf{v}_{2CM} = -\mathbf{V}$. After scattering the correspondent quantities can be deduced considering that the energy is the same before and after scattering (equation (2.49)) and that the momentum remains invariant in modulus (equation 2.50) while its components depends only on the scattering angle θ:

$$\mathscr{E}'_{2CM} = \frac{m_2c^2}{\sqrt{1-\beta_{cm}^2}} \tag{2.53}$$

$$\mathbf{p}'_{2CM} = -\frac{m_2V}{\sqrt{1-\beta_{cm}^2}}(\cos\theta, \sin\theta, 0) \tag{2.54}$$

For the projectile particle the momentum before and after scattering are simply achieved considering the equations (2.47) and (2.48) $\mathbf{p}'_{1CM} = -\mathbf{p}'_{2CM}$. The total energy before and after scattering are:

$$\mathscr{E}_{1CM} = \mathscr{E}'_{1CM} = \sqrt{(p'_{1CM}c)^2 + (m_1c^2)^2} \tag{2.55}$$

$$= \sqrt{\frac{(m_2cV)^2}{1-\beta_{cm}^2} + (m_1c^2)^2} \tag{2.56}$$

where it has been considered the relation (2.35) and the transformations (2.40).

Once that the problem is solved in the center of mass system, the final quantities in the laboratory system can be obtained from the transformations (2.39). The total energy of the target particle after scattering is equal to:

$$\mathscr{E}'_2 = m_2c^2\frac{1-\beta_{cm}^2\cos\theta}{1-\beta_{cm}^2} \tag{2.57}$$

where the x component of the momentum (2.54) has been used. The (2.57) can be rewritten substituting the β_{cm}^2 given by (2.44):

$$\mathscr{E}'_2 = m_2c^2 + \frac{m_2c^2\left[\mathscr{E}_1^2 - (m_1c^2)^2\right]}{(m_1c^2)^2 + (m_2c^2)^2 + 2\mathscr{E}_1m_2c^2}(1-\cos\theta) \tag{2.58}$$

which, by the use of $(1-\cos\theta) = 2\sin^2(\theta/2)$, becomes:

$$\mathscr{E}_2' = m_2c^2 + \frac{2m_2c^2\left[\mathscr{E}_1^2 - (m_1c^2)^2\right]}{(m_1c^2)^2 + (m_2c^2)^2 + 2\mathscr{E}_1 m_2c^2}\sin^2\frac{\theta}{2} \tag{2.59}$$

Since $\mathscr{E}_2' = m_2c^2 + E_2'$ where E_2' is the kinetic energy of the target after scattering which is equal to the second term on the right side of the (2.59) it is possible to write the kinetic energy transferred to the target particle after scattering as $T \equiv E_2'$:

$$T = T_{max}\sin^2\frac{\theta}{2} \tag{2.60}$$

where T_{max} is the relativistic maximum kinetic energy that can be transferred during the single collision:

$$T_{max} = \frac{2m_2c^2\left[\mathscr{E}_1^2 - (m_1c^2)^2\right]}{(m_1c^2)^2 + (m_2c^2)^2 + 2\mathscr{E}_1 m_2c^2} \tag{2.61}$$

The denominator of the (2.61) is equal to the square of the total center of mass energy $\mathscr{E}_{cm}$, when the target particle is at rest:

$$\mathscr{E}_{cm} = \sqrt{(m_1c^2)^2 + (m_2c^2)^2 + 2\mathscr{E}_1 m_2c^2} \tag{2.62}$$

The maximum energy T_{max} can be written in a more compact form as a function of the initial kinetic energy of the projectile particle E_1. The second term at numerator of the (2.61), which is equal to $(p_1c)^2$ can be rewritten as:

$$\mathscr{E}_1^2 - (m_1c^2)^2 = E_1^2 + 2m_1c^2E_1 = E_1(E_1 + 2m_1c^2) \tag{2.63}$$

The denominator of the (2.61) assumes the form:

$$\begin{aligned}(m_1c^2)^2 + (m_2c^2)^2 + 2\mathscr{E}_1 m_2c^2 &= (m_1c^2 + m_2c^2)^2 + 2m_2c^2(\mathscr{E}_1 - m_1c^2)\\ &= (m_1c^2 + m_2c^2)^2 + 2m_2c^2E_1\end{aligned}$$

With these two last equations the (2.61) becomes:

$$T_{max} = \frac{2E_1(E_1 + 2m_1c^2)}{\left(1 + \dfrac{m_1}{m_2}\right)^2 m_2c^2 + 2E_1} \tag{2.64}$$

The final total energy of the projectile particle can by obtained from the conservation of total energy (2.42) together with the expression of $\mathscr{E}_2'$ given by (2.58):

$$\mathscr{E}_1' = \mathscr{E}_1 + \mathscr{E}_2 - \mathscr{E}_2' = \mathscr{E}_1 - \frac{m_2c^2\left[\mathscr{E}_1^2 - (m_1c^2)^2\right]}{(m_1c^2)^2 + (m_2c^2)^2 + 2\mathscr{E}_1 m_2c^2}(1-\cos\theta) \tag{2.65}$$

The three coordinates of the final momentum of the target particle are obtained from the transformations (2.39) together with (2.54) where $\mathscr{E}'_{2CM}$ is given by the (2.53):

$$\begin{aligned} p'_{2x} &= \frac{m_2 V}{1-\beta_{cm}^2}(1-\cos\theta) \\ p'_{2y} &= -\frac{m_2 V}{\sqrt{1-\beta_{cm}^2}}\sin\theta \\ p'_{2z} &= 0 \end{aligned}$$

The correspondent quantities for the projectile particle are obtained considering that $\mathbf{p}'_{1CM} = -\mathbf{p}'_{2CM}$, together with $\mathscr{E}'_{1CM}$ given by (2.56):

$$\begin{aligned} p'_{1x} &= \frac{V}{1-\beta_{cm}^2}\left(m_2\cos\theta + \sqrt{m_2^2\beta_{cm}^2 + m_1^2(1-\beta_{cm}^2)}\right) \\ p'_{1y} &= \frac{m_2 V}{\sqrt{1-\beta_{cm}^2}}\sin\theta \\ p'_{1z} &= 0 \end{aligned}$$

All these quantities solve the kinematic scattering problem considering only the conservation laws of total energy and total momentum.

The Coulomb scattering problem may be also solved in the relative frame of reference whit the introduction of an effective particle of mass equal to the reduced mass of the system. The relative momentum $\mathbf{p}_r$, which is associated to the effective particle, is equal to:

$$\mathbf{p}_r = \mu_r \mathbf{v}_r \gamma_r \tag{2.66}$$

where $\mathbf{v}_r$ is the relative velocity and μ_r is the relativistic reduced mass which can be written by the Todorov's definition as [41] [39]:

$$\mu_r \equiv \frac{m_1 m_2 c^2}{\mathscr{E}_{cm}} \tag{2.67}$$

where $\mathscr{E}_{cm}$ is the total center of mass energy defined as:

$$\mathscr{E}_{cm} \equiv \sqrt{(\mathscr{E}_1 + \mathscr{E}_2)^2 - (\mathbf{p}_1 + \mathbf{p}_2)^2} \tag{2.68}$$

If, before scattering, the target particle is at rest in the laboratory system then $\mathscr{E}_{cm}$ is given by equation (2.62) The effective particle total energy $\mathscr{E}_r = \mu_r c^2$, can also be written as [41]:

$$\mathscr{E}_r = \frac{\mathscr{E}_{cm}^2 - (m_1 c^2)^2 - (m_2 c^2)^2}{2\mathscr{E}_{cm}} \tag{2.69}$$

As in the non-relativistic case, the relative momentum is equal to the momentum of the incoming particle calculated in the CM system i.e.:

$$\mathbf{p}_r \equiv \mathbf{p}_{1CM} = -\mathbf{p}_{2CM} \tag{2.70}$$

which implies that the scattering angle of the effective particle is equal to the one of the two colliding partners calculated in the CM system, as in the non-relativistic treatment, i.e.:

$$\theta = \theta_{1CM} = \theta_{2CM} \tag{2.71}$$

The total center of mass energy can be written equivalently as [39]:

$$\mathscr{E}_{cm} = Mc^2 + E_k \tag{2.72}$$

where E_k is the total kinetic energy of the system. If $E_k \ll Mc^2$, the relativistic reduced mass approaches the non-relativistic one μ whose expression was given in equation (2.3), i.e.

$$\mu_r = \frac{m_1 m_2 c^2}{\mathscr{E}_{cm}} \rightarrow \mu = \frac{m_1 m_2}{M} \quad \left(\text{for } \frac{\mathscr{E}_{cm}}{c^2} \rightarrow M\right)$$

In addition when the rest mass of the incoming particle m_1 is much smaller than the target rest mass m_2, the reduced mass μ_r approaches m_1. This can be seen considering the equations (2.67) and (2.62) together with the condition $m_1 \ll m_2$, i.e.:

$$\begin{aligned}
\frac{1}{\mu_r^2} &= \frac{\mathscr{E}_{cm}^2}{(m_1 m_2 c^2)^2} = \frac{(m_1c^2)^2 + (m_2c^2)^2 + 2\mathscr{E}_1 m_2 c^2}{(m_1 m_2 c^2)^2} \simeq \\
&\simeq \frac{(m_2c^2)^2 + 2\mathscr{E}_1 m_2 c^2}{(m_1 m_2 c^2)^2} = \frac{1 + 2\dfrac{\mathscr{E}_1}{m_2c^2}}{m_1^2} = \\
&= \frac{1 + 2\dfrac{m_1}{m_2}\gamma_1}{m_1^2} \simeq \frac{1}{m_1^2}
\end{aligned} \tag{2.73}$$

As a consequence, also the effective particle velocity β_r approaches the velocity of the incoming particle calculated in the CM system β_{1CM}. This can be demonstrated remembering that $\mathbf{p}_r \equiv \mathbf{p}_{1CM}$ (equation (2.70)) and considering the equation (2.36) with $m_1 \ll m_2$ (i.e. $\mu_r \simeq m_1$):

$$\begin{aligned}
\frac{1}{\beta_r^2} &= 1 + \left(\frac{\mu_r c^2}{p_r c}\right)^2 = 1 + \left(\frac{\mu_r c^2}{p_{1CM} c}\right)^2 \simeq \\
&\simeq 1 + \left(\frac{m_1 c^2}{p_{1CM} c}\right)^2 = \frac{1}{\beta_{1CM}^2}
\end{aligned} \tag{2.74}$$

The reduced mass treatment is necessary when the mass of the incoming particle is not negligible compared to the target one.

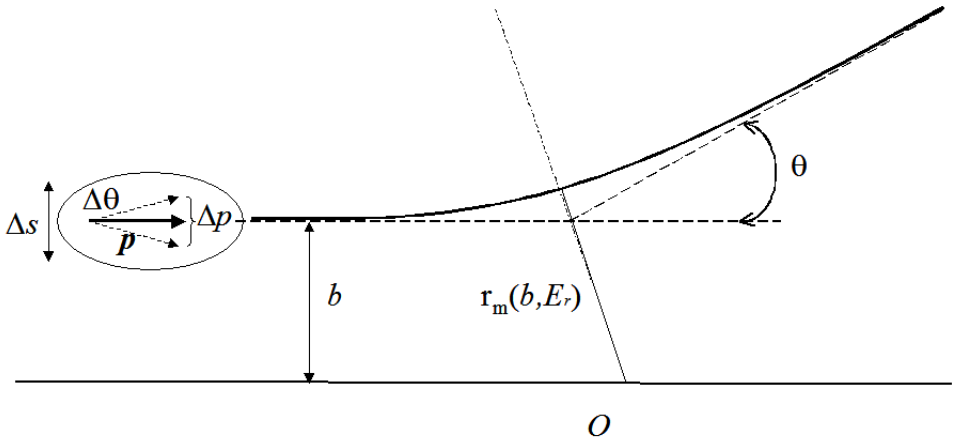

Figure 2.4: Schematic representation of the wave packet during a scattering process in the relative frame of reference. Δs width of the wave packet; $\Delta\theta$ uncertainty in the direction; $\mathbf{p}$ wave packet momentum; Δp uncertainty in the momentum; b impact parameter; $r_m(b, E_r)$ distance of closest approach; θ scattering angle.

2.2 Limits of Non-Relativistic and Relativistic Coulomb Scattering

The non-relativistic and the relativistic scattering processes described so far employ particles, scattering angles and trajectories. These classical concepts however are no longer appropriate when the Heisenberg's uncertainty principle becomes important [30].

In the quantal description a particle is represented by a wave packet of width equal to Δs and of group velocity equal to the incident particle velocity v. The spread of the momentum Δp may be estimated by the uncertainty principle:

$$\Delta p \Delta s \simeq h \tag{2.75}$$

where h is Planck's constant. Figure 2.4 gives an idea of this wave packet. A non-quantal description is possible when Δs is negligible compared to the distance of closest approach r_m:

$$\Delta s \ll r_m(b, E_r) \tag{2.76}$$

where r_m, in general, is a function of the impact parameter b and of the relative energy E_r. The (2.76) condition is equivalent to give a condition to the momentum uncertainty:

$$\Delta p \gg \frac{h}{r_m(b, E_r)} \tag{2.77}$$

In addition the uncertainty of the momentum leads to the uncertainty of the angular spread of the wave packet $\Delta\theta$ which has to be negligible compared to the scattering angle θ:

$$\Delta\theta \simeq \frac{\Delta p}{p} \ll \theta \tag{2.78}$$

Combining the (2.77) with the (2.78) it is possible to obtain a condition for the scattering angle:

$$\theta \gg \frac{h}{p\ r_m(b, E_r)}. \tag{2.79}$$

For too small scattering angles, which correspond to large impact parameters, a quantal description of the scattering process is necessary [30]. This condition gives also a lower limit in the energy transferred T_{min} which has to be used in the computation of the stopping power:

$$T_{min} = T_{max} \sin^2 \frac{\theta_{min}}{2} \tag{2.80}$$

One example is the unscreened Coulomb potential which goes to zero for $b \to \infty$. In fact, the differential scattering cross section, obtained from the unscreened Coulomb potential, diverges for very small scattering angles, as a consequence the stopping power doesn't have a finite value. On the contrary, if the Coulomb potential is screened, the lower energy limit T_{min} may be set to zero without problems because the scattering cross section doesn't diverge.

2.3 Non-Relativistic Differential Scattering Cross Section

During irradiation experiments or in the space environment, the problem of scattering becomes more complex because all the target atoms of the material are subjected to fluxes of many projectile particles. As a consequence there will be many scattering angles and impact parameters which depend on the interaction potential (see equation (2.9)). In this case the problem may be described introducing the *differential cross section* $d\sigma(\theta)/d\Omega$ in the relative frame of reference. Inside the material all the target atoms may be considered fixed and, for simplicity, the projectile particles have homogeneous flux given by $\phi = nv$ where n is the number density of projectile particles and v is their velocity. The number of particle incident per unit time within the interval $[b; b+db]$ of the impact parameter b, must be equal to the number of particles emerging after collision within the solid angle $d\Omega$ i.e.:

$$\phi\ 2\pi b\ db = \phi\ \frac{d\sigma(\theta)}{d\Omega} d\Omega \tag{2.81}$$

Considering that $d\Omega = 2\pi \sin\theta d\theta$ it is possible to obtain the relation between differential the cross section and the impact parameter:

$$\frac{d\sigma(\theta)}{d\Omega} = \frac{b}{\sin\theta}\left|\frac{db}{d\theta}\right| \tag{2.82}$$

where the absolute value is taken because $db/d\theta$ is often negative while $d\sigma(\theta)/d\Omega$ is define positive.

2.3.1 Unscreened Coulomb Potential

The differential scattering cross section can be easily obtained for the unscreened Coulomb potential, where the effect of the electrons on the term $Z_1 Z_2 e^2$ is not considered:

$$V(r) = \frac{Z_1 Z_2 e^2}{r} \tag{2.83}$$

With this potential the integration of the scattering angle (2.9) gives the result [30]:

$$\sin\frac{\theta}{2} = \frac{\dfrac{Z_1 Z_2 e^2}{2bE_r}}{\left[1 + \left(\dfrac{Z_1 Z_2 e^2}{2bE_r}\right)^2\right]^{\frac{1}{2}}} \tag{2.84}$$

from which it is possible to obtain a simple relation between the scattering angle and the impact parameter:

$$b = \frac{1}{2}\frac{Z_1 Z_2 e^2}{E_r}\frac{1}{\tan\frac{\theta}{2}} \tag{2.85}$$

so that:

$$\left|\frac{db}{d\theta}\right| = \frac{1}{4}\frac{Z_1 Z_2 e^2}{E_r}\frac{1}{\sin^2\frac{\theta}{2}} \tag{2.86}$$

The differential cross section (2.82) is given by:

$$\frac{d\sigma(\theta)}{d\Omega} = \left(\frac{Z_1 Z_2 e^2}{4E_r}\right)^2 \frac{1}{\sin^4\frac{\theta}{2}} \tag{2.87}$$

or, by substituting the E_r expression (2.6), it can be written as:

$$\frac{d\sigma(\theta)}{d\Omega} = \left(\frac{Z_1 Z_2 e^2}{2\mu c^2 \beta}\right)^2 \frac{1}{\sin^4\frac{\theta}{2}} \tag{2.88}$$

The differential cross section may be also given as a function of the kinetic energies. Since the energy transferred to the target particle is a unique function of the scattering angle (see (2.28)), the number of particles that have transferred a kinetic energy T to the target atoms must be equal to:

$$\frac{d\sigma(T, E_1)}{dT} dT = \frac{d\sigma(\theta)}{d\Omega} d\Omega \tag{2.89}$$

where $d\sigma(T, E_1)/dT$ is the *differential cross section for energy transfer*. Differentiating the (2.28) leads to:

$$dT = T_{max} \sin\frac{\theta}{2} \cos\frac{\theta}{2}\, d\theta = \frac{T_{max}}{2} \sin\theta\, d\theta \tag{2.90}$$

where T_{max} is given by (2.29). Substituting the (2.90) in the (2.89) and remembering that $d\Omega = 2\pi \sin\theta d\theta$, leads to:

$$\frac{d\sigma(T, E_1)}{dT} = \frac{d\sigma(\theta)}{d\Omega} \frac{4\pi}{T_{max}} \tag{2.91}$$

Substituting the $d\sigma(\theta)/d\Omega$ given by (2.87) and considering that:

$$\sin^4\frac{\theta}{2} = \left(\frac{T}{T_{max}}\right)^2 \tag{2.92}$$

gives an expression for the (2.91) which becomes:

$$\frac{d\sigma(T, E_1)}{dT} = 4\pi \left(\frac{Z_1 Z_2 e^2}{4E_r}\right)^2 \frac{T_{max}}{T^2} \tag{2.93}$$

Substituting in the (2.93) the E_r expression given by the first equation of the (2.6) it is possible to obtain:

$$\frac{d\sigma(T, E_1)}{dT} = \pi \left(\frac{Z_1 Z_2 e^2}{\mu c^2\ \beta^2}\right)^2 \frac{T_{max}}{T^2} \tag{2.94}$$

The $d\sigma(T, E_1)/dT$ may by also written as a function of the incoming particle kinetic energy E_1 by substituting in the (2.93) the T_{max} expression given by (2.29) and the E_r one given by the second equation of (2.6):

$$\frac{d\sigma(T, E_1)}{dT} = \pi \frac{m_1}{m_2} \frac{(Z_1 Z_2 e^2)^2}{E_1} \frac{1}{T^2} \tag{2.95}$$

which is the classical *Rutherford differential cross section.*

2.3.2 Universal Screening Potential

Inside the material, however, the interaction potential is not simply given by the Coulomb potential (2.83) because the atomic electrons screen the nucleus charge. The *screened Coulomb* potential may by expressed as:

$$V(r) = \frac{Z_1 Z_2 e^2}{r}\chi(r) \tag{2.96}$$

where $\chi(r)$ is the *screening function* which depends on the atom model, that is on the electrons charge distribution. Many analytical forms of the screening function can be found in literature which are based on the Thomas-Fermi model. The Thomas-Fermi model assumes that electrons can be treated like an ideal gas uniformly distributed inside the potential well of the positive charge nucleus. These models, however, simplify the problem because they don't consider the shell structure of the atom.

Zeigler, Biersack and Littmark (ZBL), instead, used a model in which electrons are spherically symmetric distributed around the nucleus. ZBL performed the screening function calculation for a large set of target and projectile particles. Their numerical result leads to the *universal screening function* given by [1]:

$$\begin{aligned}\chi(x)_U \;\simeq\; & 0.01818\exp(-3.2x) \\ & +0.5099\exp(-0.9423x) \\ & +0.2802\exp(-0.4028x) \\ & +0.02817\exp(-0.2016x)\end{aligned} \tag{2.97}$$

where $x = r/a_U$ is the reduced radius and a_U is the *universal screening length* given by:

$$a_U = \left(\frac{9\pi^2}{128}\right)^{1/3}\frac{a_0}{(Z_1^{0.23}+Z_2^{0.23})} \simeq \frac{0.88534\ a_0}{(Z_1^{0.23}+Z_2^{0.23})} \tag{2.98}$$

and $a_0 = \hbar^2/m_e e^2 = 5.29\times10^{-9}$cm is the Bhor radius.
The differential scattering cross section for the universal screened potential doesn't have an analytical expression but must be solved numerically. Lindhard Nielsen and Scharff (1968) introduced the one parameter differential scattering cross section which, in reduce notations, can be written as [31]:

$$\frac{d\sigma(T,E_1)}{dT}dT = -\frac{\pi a_U^2}{2}\frac{f(t^{\frac{1}{2}})}{t^{\frac{3}{2}}}dt \tag{2.99}$$

where t is a dimensionless parameter given by:

$$t = \epsilon^2\frac{T}{T_{max}} \tag{2.100}$$

and ϵ is the ZBL reduce energy:

$$\epsilon = \frac{a_U}{Z_1 Z_2 e^2}\left(\frac{m_2}{m_1 + m_2}\right) E_1 \tag{2.101}$$

the term $f(t^{\frac{1}{2}})$ is referred to as the Thomas-Fermi scattering function.

Littmark and Ziegler (1981), by mans of a spline fit, gave a quite complex expression for the $f(t^{\frac{1}{2}})$ function [32]. A simplified analytical form was given by Nastasi et al. (1996) i.e.:

$$f(t^{\frac{1}{2}}) = \lambda t^{\frac{1}{2}-m}[1 + (2\lambda t^{1-m})^q]^{-\frac{1}{q}}. \tag{2.102}$$

For the universal ZBL potential Nastasi et al. [33] gave the following values of the fitting parameters: $\lambda = 5.012$, $m = 0.203$, $q = 0.413$, in the range $10^{-6} \leq t^{1/2} \leq 10^4$. This expression of the Thomas-Fermi scattering function was also used by Messenger et al. (2003) [50] to compute the Non-Ionizing-Energy-Loss for heavy nuclei, as it will be explained in sections 3.2.3 and 4.1.

2.4 Relativistic Differential Cross Sections

To determine the scattering angle and, as a consequence, the differential cross section, it is necessary to solve the equation of motion inside which the proper interaction potential must be inserted. For a detail calculation in the relativistic regime the delay time interaction between the two particles must be taken into account because of the finite propagation velocity of the electromagnetic signal. The definition of the differential cross section, instead, remains the same as in the non-relativistic limit because of its statistical nature. The value of the differential cross section which was used (Jun et al. [34]) for the calculation of the displacement damage caused by protons in the space environment, was derived from the well known electron differential cross section. The relativistic differential scattering cross section for electrons (mass m_e and velocity v_e), with a target atom of mass m_2, was calculated by Darwin (reference in [30]):

$$\frac{d\sigma(\theta)}{d\Omega}\Big|_{DR} = (1 - \beta_e^2)\frac{d\sigma(\theta)}{d\Omega}\Big|_{R} \tag{2.103}$$

$$\gamma_e = \frac{1}{\sqrt{1 - \beta_e^2}} \tag{2.104}$$

where $d\sigma(\theta)_R/d\Omega$ is the non-relativistic Rutherford cross section given by the (2.88):

$$\frac{d\sigma(\theta)}{d\Omega}\Big|_R \simeq \left(\frac{Z_2 e^2}{2m_e v_e^2}\right)^2 \frac{1}{\sin^4\frac{\theta}{2}} \tag{2.105}$$

where it has been considered that $\mu \simeq m_e$, since $m_e \ll m_2$. The (2.103) is then equal to:

$$\frac{d\sigma(\theta)}{d\Omega}\Big|_{DR} = \left(\frac{Z_2 e^2}{2m_e c^2\ \beta_e^2\gamma_e}\right)^2 \frac{1}{\sin^4\frac{\theta}{2}} \tag{2.106}$$

By the use of the transformation (2.91) and of the (2.92), the DR differential cross section (2.106) can be written as:

$$\frac{d\sigma(T, E_1)}{dT}\Big|_{DR} = \pi\left(\frac{Z_2 e^2}{m_e c^2\ \beta_e^2\gamma_e}\right)^2 \frac{T_{max}}{T^2} \tag{2.107}$$

The maximum energy transferred by an electron can be calculated by the (2.64):

$$T_{max} \simeq \frac{E_e(E_e + 2m_e c^2)}{m_2 c^2 + 2E_e}$$

where $E_e \equiv E_1$ is the kinetic energy of the incoming electron, and it has been considered that $m_1 \equiv m_e \ll m_2$.

This result was extended in the quantal case by Mott (reference in [30]) who calculated the quantal cross section for electrons scattering with a target nucleus of charge $Z_2 e$. The resulting infinite series was fitted by McKinley and Feshbach (reference in [30]) who gave the following analytical function which is valid for elements of $Z_2 \leq 30$:

$$\frac{d\sigma(\theta)}{d\Omega}\Big|_{McF} = \frac{d\sigma(\theta)}{d\Omega}\Big|_R \left[1 - \beta_e^2 \sin^2\frac{\theta}{2} + Z_2\alpha\beta_e\pi \sin\frac{\theta}{2}\left(1 - \sin^2\frac{\theta}{2}\right)\right] \tag{2.108}$$

where $d\sigma(\theta)_{DR}/d\Omega$ is given by the (2.103) and $\alpha = e^2/(\hbar c)$ is the *finite structure constant*. The same approximated function can be used to obtained the differential scattering cross section for energy transferred by incident electrons [30]:

$$\frac{d\sigma(T, E_1)}{dT}\Big|_{McF} = \frac{d\sigma(T, E_1)_{DR}}{dT}\left[1 - \beta_e^2\frac{T}{T_{max}} + Z_2\alpha\beta_e\pi\sqrt{\frac{T}{T_{max}}}\left(1 - \sqrt{\frac{T}{T_{max}}}\right)\right] \tag{2.109}$$

This expression of the differential cross section was derived without considering the radiative energy loss of electrons and considering the nucleus as a point like particle during scattering.

Seitz [38] proposed to use this last expression to calculate the differential cross section for incident protons and light incident nuclei of charge $Z_1 e$, providing that the incident particle has mass $m_1 \ll m_2$. The general differential cross section for energy transfer, for light incoming particles, is then equal to [38], [35]:

$$\frac{d\sigma(T,E_1)}{dT}\Big|_{Seitz} = \pi\left(\frac{Z_1 Z_2 e^2}{m_1 c^2\ \beta^2\gamma}\right)^2 \frac{T_{max}}{T^2}\left[1-\beta^2\frac{T}{T_{max}}+Z_2\alpha\beta\pi\sqrt{\frac{T}{T_{max}}}\left(1-\sqrt{\frac{T}{T_{max}}}\right)\right] \tag{2.110}$$

This is also the expression that was used by Jun et al. [34], [35] to calculate the Coulomb fraction of the displacement damage induced by protons on silicon materials for space applications.

Another relativistic differential cross section is given by Starusziewicz and Zalewski (SZ) who solved the relativistic Coulomb scattering problem in the relative frame of reference. Their relativistic differential cross section is equal to [40]:

$$\frac{d\sigma(\theta)}{d\Omega}\Big|_{SZ} = \left(\frac{\mathscr{E}_r Z_1 Z_2 e^2}{2(p_r c)^2}\right)^2 \frac{1}{\sin^4\frac{\theta}{2}} \tag{2.111}$$

where the term $\mathscr{E}_r$ is the effective particle total energy. This differential cross section may be also written as:

$$\frac{d\sigma(\theta)}{d\Omega}\Big|_{SZ} = \left(\frac{Z_1 Z_2 e^2}{2\mu c^2\beta_r^2\gamma_r}\right)^2 \frac{1}{\sin^4\frac{\theta}{2}} \tag{2.112}$$

where it has been considered that the total energy of the effective particle is $\mathscr{E}_r = \mu_r c^2\gamma_r$ and that the quantity $(p_r c)^2$ may by written as:

$$(p_r c)^2 = (\mu_r c^2\beta_r\gamma_r)^2 \tag{2.113}$$

Since $\sin^4(\theta/2) = (1-\cos\theta)^2/4$, another form for the (2.112) is:

$$\frac{d\sigma(\theta)}{d\Omega}\Big|_{SZ} = \left(\frac{Z_1 Z_2 e^2}{p_r c\ \beta_r}\right)^2 \frac{1}{(1-\cos\theta)^2} \tag{2.114}$$

The differential cross section (2.112) can also be written as a function of the kinetic energy of the recoil target T and of the incident particle E_1 as:

$$\frac{d\sigma(T,E_1)}{dT}\Big|_{SZ} = \pi\left(\frac{Z_1 Z_2 e^2}{\mu_r c^2\beta_r^2\gamma_r}\right)^2 \frac{T_{max}}{T^2} \tag{2.115}$$

which has the same form of the relativistic differential scattering cross section for electrons given by Darwin, i.e. equation (2.107), and of the one given by Seitz, i.e. equation (2.110), except for the terms in parenthesis.

2.5 Stopping Power

A projectile particle of initial kinetic energy E_1 losses energy while traversing a target material by collision processes with electrons and atoms. The total energy loss per unit path length is given by the sum of these two scattering mechanisms:

$$-\frac{dE}{dx}\Big|_{tot} = -\frac{dE}{dx}\Big|_{e} - \frac{dE}{dx}\Big|_{n} \tag{2.116}$$

where the indexes e and n refers to electron and nuclear collision respectively. The average energy loss for each process $i = e, n$ is calculated by the integral [33]:

$$-\frac{dE}{dx}\Big|_{i} = N \int_{T_{min}}^{T_{max}} T \frac{d\sigma(T, E_1)}{dT} dT \tag{2.117}$$

where N is the density number of targets which can be equal to the electron density $Z_2 N_A \rho / A_2$, or to the atom density $N_A \rho / A_2$ of the material according to the scattering mechanism; $d\sigma(T, E_1)/dT$ is the differential scattering cross section for energy transfer; T is the kinetic energy transferred to the target particle. The integral has to be performed from a minimum kinetic energy T_{min} to the maximum energy that can be transferred by a single collision T_{max}.

2.5.1 Nuclear Collision Energy-Loss

The evaluation of the nuclear collision energy loss is usually performed by the use of the *stopping cross section* defined as [33]:

$$S_n(E_1) \equiv \frac{1}{N}\frac{dE}{dx}\Big|_{n} = \int_{T_{min}}^{T_{max}} T \frac{d\sigma(T, E_1)}{dT} dT \tag{2.118}$$

where $N = N_A \rho / A_2$. The nuclear stopping cross section $S_n(E_1)$ can be written in the reduce notation as $S_n(\epsilon)$ [33]. i.e.:

$$S_n(\epsilon) = \frac{\epsilon}{\pi a_U^2 E_1} \left(\frac{M^2}{4 m_1 m_2} \right) S_n(E_1) \tag{2.119}$$

where ϵ is the ZBL reduce energy given by (2.101) and a_U is the universal screening length given by (2.98). Substituting the (2.118) in the (2.119) leads to:

$$S_n(\epsilon) = \frac{\epsilon}{\pi a_U^2 E_1} \left(\frac{M^2}{4 m_1 m_2} \right) \int_{0}^{T_{max}} T \frac{d\sigma(T, E_1)}{dT} dT \tag{2.120}$$

where the minimum kinetic energy was set to zero ($T_{min} = 0$) [33]. The kinetic energy transferred to the target is given by (2.28) and the differential cross section may be given as a function of the scattering angle $d\sigma(T, E_1) = d\sigma(\theta)$. In addition, since the scattering angle is a function of the impact parameter b (2.82), it is convenient to use $d\sigma(\theta) = 2\pi b\ db$, so that the equation (2.120) can be written as:

$$S_n(\epsilon) = \frac{\epsilon}{a_U^2} \int_0^\infty \sin^2\left(\frac{\theta}{2}\right) 2b\ db \tag{2.121}$$

where the integration is performed over all possible impact parameters.
Zeigler, Biersack and Littmark deduced the nuclear universal stopping power by performing the integral (2.121). They first numerically evaluated the scattering angles by the integration of the (2.9) inside which the potential expression $V(r)$ is given by the screened Coulomb potential (2.96) with screening function $\chi(x)_U$ equal to (2.97). They also gave the curve that fits the numerical results which is equal to [1]:

$$\text{if } \epsilon \leq 30; \quad S_n(\epsilon) = \frac{\ln(1 + 1.1383\epsilon)}{2(\epsilon + 0.01321\epsilon^{0.21116} + 0.19593\epsilon^{0.5})} \tag{2.122}$$

$$\text{if } \epsilon > 30; \quad S_n(\epsilon) = \frac{ln(\epsilon)}{2\epsilon} \tag{2.123}$$

The first fitting function (2.122) gives the stopping cross section for low energy particles for which the collisions become less penetrating and the interaction potential must be screened by electrons. The second equation, instead, (2.123) gives results in the high energy range where the screening effects are less important. In this case the interaction involves the inner parts of the atom and so the differential cross section tend to the unscreened Rutherford one (2.93).

The universal nuclear stopping power can then be written as [1]:

$$-\left.\frac{dE}{dx}\right|_{nU} = 5.1053 \times 10^3 \frac{\rho Z_1 Z_2}{A_2(Z_1^{0.23} + Z_2^{0.23})} \left(\frac{m_2}{M}\right) S_n(\epsilon) \tag{2.124}$$

where the numerical constant is given in order to express the stopping power in MeV cm^{-1}. In figure 2.5 the universal $S_n(\epsilon)$ stopping cross section is reported with four other screening functions. All curves overlap for $\epsilon > 10$ which means that the screening effects can be neglected at high energies. Deviations arise in the low energy part of the plot where differences in the screening functions become evident.

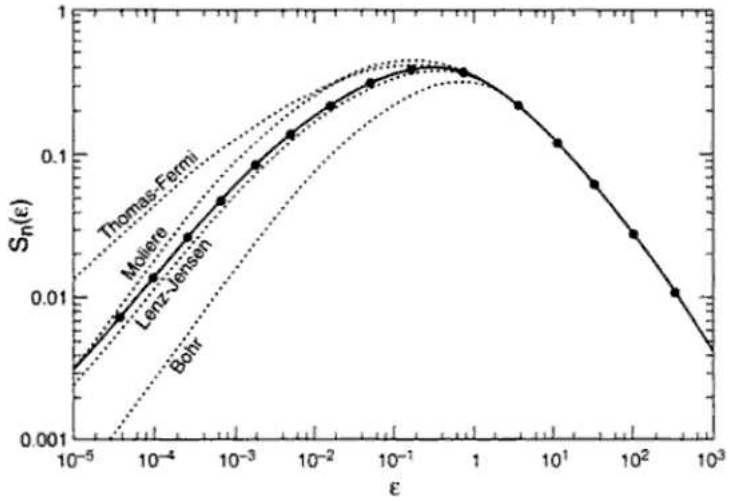

Figure 2.5: Universal stopping cross section in reduced notation compared with four other non-relativistic calculations [33].

It has to be remarked however that the universal stopping power was calculated in the non-relativistic limit. To evaluate the nuclear collision energy loss by the integral (2.117) in the relativistic regime, it is necessary to use one of the differential scattering cross sections given in section 2.4 which however don't consider screening effects.

2.5.2 Electronic Collision Energy-Loss

The electronic energy loss formula for an incoming relativistic particle of velocity $v = \beta c$ and charge $Z_1 e$ is given by [1]:

$$-\left.\frac{dE}{dx}\right|_e = \frac{2\pi N_A e^4}{m_e c^2}\frac{Z_2 Z_1^2 \rho}{A\ \beta^2}\left\{\ln\left[\frac{2m_e c^2\beta^2 T_{max}}{I^2(1-\beta^2)}\right] - 2\beta^2 - \delta - U\right\} \qquad (2.125)$$

where T_{max} is the maximum kinetic energy that can be transferred by a single collision, $I \simeq 11.5 Z_2$ eV is the mean excitation energy of the medium, δ is the *density effect* correction term which becomes important for high velocities, and U is the *shell correction* term which is important for low velocity incoming particles.

The first two terms in parenthesis are the result of the mean energy loss during the scattering process with free electrons (Bethe-Bloch formula) which is a good approximation when the velocity of the incoming particle is greater than the velocity of atomic electrons. As the velocity of the incident particle

decreases the contribution to energy loss caused by the inner shell electrons decreases progressively. The non participation of the inner shell electrons to the collision process is considered by adding the shell correction term U whose expression can be found in ICRU[1] Report 49 [42].

When the velocity of the incident particle approaches the relativistic regime its passage through matter influences the atoms of the medium which tend to become polarized. The density effect correction term takes into account this effect with the reduction of the stopping power due to the polarization of the medium; its expression can be found in [1].

High order correction terms may be added inside the brackets of the stopping power formula [43]:

$$F = G - S + 2(Z_1 L_1 + Z_1^2 L_2) \tag{2.126}$$

where G is the *Mott* correction term which describes the close-collisions and become important at large velocities and for high Z_1; S is the *finite size correction* term which takes into account the space distribution of charge of the projectile particle which becomes visible at energies above few hundred GeV; L_1 is the *Barkas* correction term which describes distant collisions where the stopping power of a negative particle is larger than the one of a positive particle of same velocity and mass. L_2 is the *Bloch* correction term which becomes important for low velocities. In this case the electrons can't be considered free and so the interaction with the nuclei of the material must be included.

2.5.3 Electronic Energy-Loss Fluctuations

The stopping power formula (2.125) gives the mean value of the energy lost by electronic collision of a charged particle when it passes through a medium. Anyway the stopping power has a statistical nature because for each scattering process different amount of energy may be transferred to the atomic electrons. This effect may be taken into account by calculating the distribution function for the energy loss.

The probability that a particle of a given energy E loses a total amount of energy in the range Δ and $\Delta + d\Delta$ traversing a material of thickness x is defined as the energy loss fluctuation function or straggling function $f(x, \Delta)$. The first computation of this distribution function was done by Landau [44]. He considered that an incoming particle of energy E has a given probability per unit length denoted as ω, to loss an amount of energy T by a single collision. He supposed that the total energy lost by the incoming particle is

[1]International Commission on Radiation Units and Measurements

smaller than the incoming particle energy ($\Delta \ll E_1$) and so the probability ω depends only on T. By means of the transport equation he considered that the variation of the distribution function on a length dx is equal to the collision integral:

$$\frac{\partial f(x,\Delta)}{\partial x} = \int_0^\infty \omega(T)[f(x,\Delta - T) - f(x,\Delta)]dT \tag{2.127}$$

which gives the difference between the number of particles that enter and those that live the energy interval $[\Delta;\ \Delta + d\Delta]$. By means of the Laplace's transformation he gave the solution:

$$f(x,\Delta)_L = \frac{1}{2\pi\imath}\int_{\sigma-\imath\infty}^{\sigma+\imath\infty} e^{\Big(p\Delta - x\int_0^\infty \omega(T)[1-e^{-pT}]dT\Big)}dp \tag{2.128}$$

where p is the conjugate variable of the transferred energy for the Laplace's transformation, and σ is a positive quantity fixed for the integral computation. This is a general expression which depends on the differential collision probability function $\omega(T)$. The computation of the integral in the exponential term of (2.128) was done by Landau which used the expression:

$$\omega(T) = \frac{2\pi N_A e^4}{m_e c^2}\frac{Z_2 Z_1^2 \rho}{A\ \beta^2}\frac{1}{T^2} \tag{2.129}$$

which is valid when the energy loss is much smaller than the maximum energy ($T \ll T_{max}$). This is a good approximation for thin absorbers. The collision probability per unit path length may be rewritten as:

$$\omega(T) = \frac{\xi}{x}\frac{1}{T^2} \tag{2.130}$$

where ξ is the Landau's width quantity which is defining as:

$$\xi = \left(\frac{2\pi N_A e^4}{m_e c^2}\right)\frac{Z_2 Z_1^2 \rho}{A\ \beta^2}x = 0.1535\frac{Z_2 Z_1^2 \rho}{A\ \beta^2}x \quad \text{[MeV]} \tag{2.131}$$

After the change of variable $\xi p = u$, Landau gave the solution for the distribution function:

$$f(x,\Delta)_L = \frac{\varphi(\lambda)}{\xi} \tag{2.132}$$

$$\varphi(\lambda) = \frac{1}{2\pi\imath}\int_{\sigma-\imath\infty}^{\sigma+\imath\infty} e^{u\ln u - \lambda u}du \tag{2.133}$$

$$\lambda = \frac{\Delta}{\xi} - \Big(\ln\frac{\xi}{T'} + 1 - C_E\Big) \tag{2.134}$$

where $C_E = 0.577215$ is the Euler's constant, and the energy T' is defined so that:

$$\ln T' = -\ln\left[\frac{2m_e c^2\beta^2}{I^2(1-\beta^2)}\right] + \beta^2. \tag{2.135}$$

Vavilov [45] gave a more general solution to the distribution function and performed the integral calculation up to the maximum energy T_{max}. He used the Rutherford macroscopic differential collision probability:

$$\omega(T) = \frac{\xi}{x}\frac{1}{T^2}\left(1 - \beta^2\frac{T}{T_{max}}\right) \tag{2.136}$$

which is valid for particles of spin equal to zero [1]. Vavilov used the following expression for the mean transferred energy:

$$\langle\Delta\rangle = \xi\left(\ln\left[\frac{2m_e c^2\beta^2 T_{max}}{I^2(1-\beta^2)}\right] - 2\beta^2\right) \tag{2.137}$$

in which all the correction terms were neglected, and he obtained the expression for the universal parameter λ:

$$\lambda = \frac{\Delta}{\xi} - \left(\ln\frac{\xi}{T_{max}} + \frac{\langle\Delta\rangle}{\xi} - \beta^2 + 1 - C_E\right) \tag{2.138}$$

$$= \frac{\Delta - \langle\Delta\rangle}{\xi} - \left[\ln\frac{\xi}{T_{max}} - \beta^2 + 1 - C_E\right] \tag{2.139}$$

The Vavilov's solution is equal to the Landau's one when $\xi \ll T_{max}$. The Landau-Vavilov solution has a maximum when the λ parameter is equal to:

$$\lambda_0 = -0.229 \tag{2.140}$$

and the Full Width Half Maximum is about:

$$FWHM \simeq 4.02\ \xi. \tag{2.141}$$

The λ_0 value enables one to obtain the more probable value for the total energy loss:

$$\Delta_{mp} = \langle\Delta\rangle + \xi\left[\ln\frac{\xi}{T_{max}} - \beta^2 + 1 - C_e + \lambda_0\right] \tag{2.142}$$

Since the terms in parenthesis of the above relation are negative, the more probable value is shifted towards lower energies respect to the mean energy loss value. As a consequence the Landau-Vavilov distribution function has

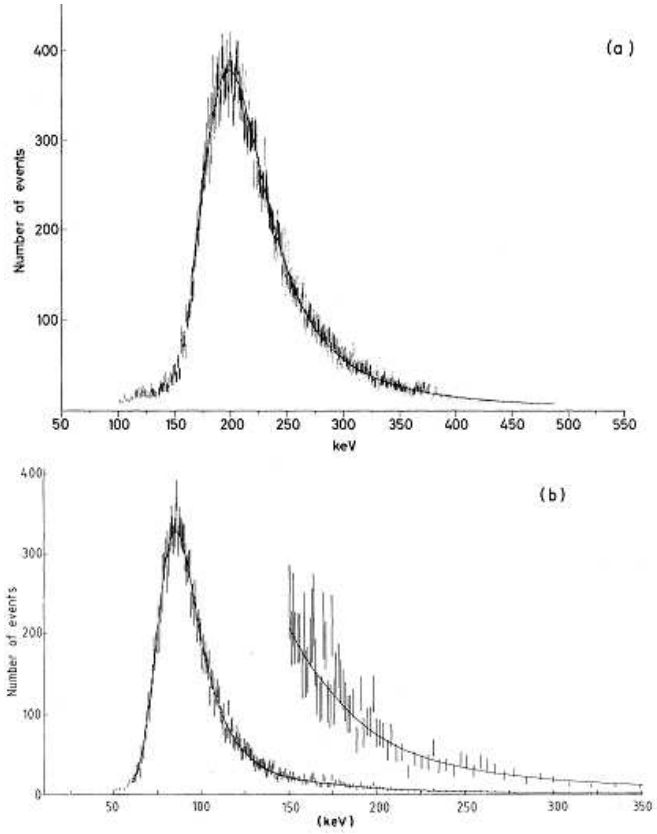

Figure 2.6: Energy loss spectra of (a) 0.736 GeV/c and (b) 115 GeV/c protons. Continuous lines are the fitting curves of the experimental data. In figure (b) a magnification of the tail is reported [46].

an asymmetric shape with a long tail that extends towards high energies. This tail is due most of all to fast δ-rays.

In thick absorbers the Landau solution is no longer valid and when $\xi \gg T_{max}$, the Landau-Vavilov's distribution function becomes almost a gaussian function:

$$f(x,\Delta)_V \simeq \frac{1}{\sqrt{2\pi}\sigma_V} \exp - \frac{(\Delta - \langle\Delta\rangle)^2}{2\sigma_V^2} \tag{2.143}$$

where the standard deviation is equal to:

$$\sigma_V = \sqrt{\xi T_{max}\Big(1 - \frac{\beta^2}{2}\Big)}. \tag{2.144}$$

Anyway the Landau-Vavilov solution obtained above for thin absorbers ($\xi \ll T_{max}$) deviates from experimental results [46]. This happens because the

differential collision probability used for the calculation doesn't consider shell order corrections and all the computation is done considering the electrons as free particles. This is true in the limit of close collision when the kinetic energy transferred to the electron is greater than their binding energy. But for distant collisions the differential collision probability must be modified in order to take into account the electrons binding energy. Making this considerations the modified energy loss distribution may be expressed as the convolution of a Gaussian function with a Landau-Vavilov solution [1]:

$$f(x,\Delta) = \frac{1}{\sigma\sqrt{2\pi}}\int_{-\infty}^{+\infty} f(x,\Delta')_L \times \exp\left[\frac{-(\Delta-\Delta')^2}{2\sigma^2}\right]d\Delta' \quad (2.145)$$

$$\sigma = \sqrt{\frac{8}{3}\xi\sum_i I_i\frac{Z_i}{Z_2}\ln\left(\frac{2m_ec^2\beta^2}{I_i}\right)} \quad (2.146)$$

where Z_i is the effective number of electrons in the i-th shell, I_i is the ionization potential of the i-th shell. The sum is performed over the shells that satisfy the condition $I_i < 2m_ec^2\beta^2$. The modified solution (2.145) was compared with experimental results by Hancock and collaborators [46]. They used a thin silicon detector (~ 300 μm) and they measured the energy loss of protons and pions in the momentum range 0.7 to 115 GeV/c. Deviation from the theoretical distribution function are expected to be observed in the tail because of the lack of δ-rays. In figure 2.6 are reported the experimental results with the fitting function (2.145) for protons of two different energies. The fitting parameters ξ (2.131), Δ_{mp} (2.142) and σ (2.146) are in good agreement with the expected ones. The effective most-probable energy loss of the overall distribution results to be shifted towards higher energy values of about 3% respect to the Landau-Vavilov parameter Δ_{mp} because of the Gaussian function contribution.

Chapter 3

Displacement Damage

In this chapter the displacement process and the consequent collision cascade will be described. Afterward the Non-Ionizing Energy Loss will be defined and its tabulated values for different particles will be given. In addition an overview of the crystal defects induced after irradiation and an example of device degradation will be given.

3.1 The Displacement Cascade

When a cosmic ray passes through a silicon device, it can transfer to the target nuclei of the material an amount of energy sufficient to displace the whole atoms from their lattice positions. The atoms directly displaced by the incident particle are called *primary knock-on atoms* (PKAs). A target atom is displaced form its lattice position only if the incident particle transfers an amount of energy greater than a threshold value T_d. If the transferred energy is less than T_d the target atom will not move from its lattice position but will lose the additional kinetic energy by phonon vibrations sharing its energy with the crystal lattice. When, instead, the transferred kinetic energy is greater than T_d a vacancy-interstitial defect called *Frenkel-pair* is formed.

The minimum energy that the recoiling target must have in order to live its lattice position, is not uniform in all directions but depends on the direction of the recoiling target particle that is on the scattering angle [33]. Different orientations in the crystal lattice have different energies of displacement barrier and so the threshold energy is distributed in an interval from a minimum to a maximum energy value. For the silicon material this interval ranges from 13 eV to 33 eV [1]. To simplify the problem, the different orientations of the lattice crystal are usually not considered and a displacement energy T_d is fixed. For silicon this value is generally taken equal to 20 eV, 21

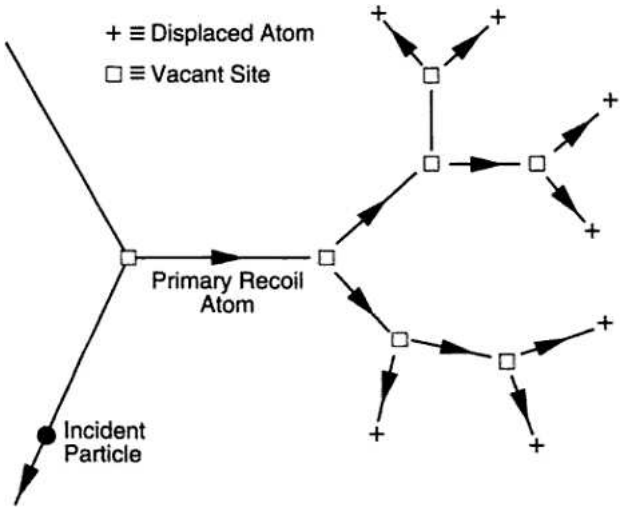

Figure 3.1: Schematic representation of the collision cascade caused by a PKA which was displaced by an incident particle [33].

eV or 25 eV.

When a Frenkel-pair is formed the PKA leaves behind a vacancy, and migrates inside the material. According to its initial kinetic energy T, it will travel a certain distance as a projectile particle before coming at rest as an interstitial. If $T \gg T_d$ the PKA will lose its energy by electronic and nuclear collisions and will be able to produce secondary displacements which in turn may produce furthers displacements in a collision cascade. This process may be described by the binary-collision approximation in which the interaction involves only two atoms. For mono-atomic materials, as silicon, the collision process, started by the PKA, involves identical atoms and so atomic and mass number of the projectile and the target are equal.

3.1.1 Displacement Damage Function

In a collision cascade starting from a PKA of kinetic energy T the mean number of displacements $\langle N_d(T) \rangle$ is called *displacement damage function* which is a measure of the Frenkel-pairs number. The displacement damage function was firstly calculated by Kinchin and Pease (1955) [47]. In their model the interaction potential between the PKAs and the target atoms of the material is assumed to be equal to the hard-sphere potential. The hard-sphere potential is a useful approximation for nearly head-on collision in which the scattering angle approaches π and the impact parameter b approaches zero.

The hard-sphere potential is equal to zero when the two particles are far

apart and rises to infinity for a distance less than the one of closest approach so that the two particles are considered impenetrable. At the distance of closed approach r_m the hard-sphere potential is equal to the relative energy of the two particles (2.6) with identical masses [33]:

$$V(r_m) = E_r = \frac{T}{2} \tag{3.1}$$

where T is the kinetic energy of the PKA and r_m is simply given by the sum of the two atoms radii. The impact parameter may be obtained by the integration of the scattering angle relation (2.9) from r_m to infinity in which the interaction potential is zero. The result is [30]:

$$b = r_m \cos\frac{\theta}{2} \tag{3.2}$$

which enables one to calculate the hard-sphere differential cross section together with the equation (2.82):

$$\frac{d\sigma(\theta)}{d\Omega} = \frac{b}{\sin\theta}\left|\frac{db}{d\theta}\right| = \frac{r_m^2}{4}$$

By the use of the (2.91) the hard-sphere differential cross section for energy transfer may be obtained:

$$\frac{d\sigma(T'', T)}{dT''} = \frac{\pi r_m^2}{T_{max}} \tag{3.3}$$

where T'' is the kinetic energy transferred to the secondary target atom and T_{max} is given by the (2.29) which, for identical particles, is equal to the projectile PKA kinetic energy ($T_{max} \equiv T$). The total scattering cross section may be computed by the integral:

$$\sigma(T) = \int_0^T \frac{d\sigma(T'', T)}{dT''} dT'' = \int_0^T \frac{\pi r_m^2}{T} dT'' = \pi r_m^2 \tag{3.4}$$

This enables one to calculate the probability for a PKA of energy T to produce a secondary recoiling atom of energy between T'' and $T'' + dT''$ for the hard-sphere potential [33]:

$$P(T'', T)dT'' = \frac{1}{\sigma(T)} \frac{d\sigma(T'', T)}{dT''} dT'' = \frac{dT''}{T} \tag{3.5}$$

In a collision cascade starting from a projectile particle of kinetic energy $T > 2T_d$ the mean number of displacements $\langle N_d(T) \rangle$ may be calculated by:

$$\langle N_d(T) \rangle = \int_0^T N_d(T) P(T'', T) dT'' = \int_0^T N_d(T) \frac{dT''}{T} \tag{3.6}$$

In addition Kinchin and Pease considered that particles lose energy only by nuclear collisions while electronic collisions are not taken into account. When a secondary target atom receives a kinetic energy less than T_d it is not displaced from its lattice site. Atoms that receive an amount of energy in the range between T_d and $2T_d$ are displaced but do not contribute in further displacements. With this simplified model Kinchin and Pease were able to give a linear relation between the displacement damage function and the initial kinetic energy of the PKA [47]:

$$\langle N_d(T) \rangle = \frac{T}{2T_d} \tag{3.7}$$

This calculation, however, overestimates the number of displaced atoms because atoms slow down only by the hard-sphere interaction potential and the electronic energy loss is not considered.

3.1.2 Damage Energy

Robinson and Torrens [48] improved the collision cascade model of Kinchin and Pease by introducing the electronic energy loss process and by the use of a more realistic interatomic potential. The interatomic potential used by Robinson and Torrens is the screened Coulomb potential (2.96) with screening function given by the Molière's approximation of the Thomas-Fermi model, given by:

$$\chi(x) = 0.35 \exp(-0.3x) + 0.55 \exp(-1.2x) + 0.10 \exp(-6x) \tag{3.8}$$

where $x = r/a_F$ and a_F is the screening length proposed by Firsov:

$$a_F = \left(\frac{9\pi^2}{128} \right)^{1/3} \frac{a_0}{(Z_1^{1/2} + Z_2^{1/2})^{2/3}} \tag{3.9}$$

where a_0 is the Bohr radius. To perform a more realistic calculation of the displacement damage function, Robinson and Torrens introduced the inelastic energy loss due to electronic collisions. The inelastic collision occurs when a certain amount of energy Q is spent for electronic transitions. In this case the total kinetic energy of the two interacting atoms after collision is less than the initial kinetic energy of the incoming atom. The conservation of energy implies that [30]:

$$T = T' + T'' + Q \tag{3.10}$$

where T and T' are the kinetic energies of the PKA atom before and after collision respectively, T'' is the kinetic energy of the target atom after collision and Q is the energy spent in electronic excitation which may also be sufficient to ionize the target atom. The energy Q may also be spent into the exchange of atomic electrons between the two interacting atoms. Since the PKA will lose all its energy during the cascade process and it will come at rest inside the material, the energy lost only in elastic collisions is given by:

$$\nu(T) = T - Q \tag{3.11}$$

which is called *damage energy*. Since the cross section for PKA production is inversely proportional to the square of the transferred kinetic energy ($d\sigma(T, E)/dT \propto T^{-2}$) low energy recoils are favorite also for relativistic incoming projectile as cosmic rays. As a consequence the PKAs can be described non-relativistically. For low energy particles the electronic energy loss for the calculation of Q in the (3.11) is no longer given by the Bethe-Bloch formula (2.125). In fact, when the velocity of the moving particle is less than the Bohr electron velocity, electrons of the target atom can't receive energy by direct collision with the slow incoming particle [33].

Firsov proposed a model for the calculation of electronic energy loss at low energies. In his model, Firsov represented the interaction between two atoms as an exchange of momentum which involves electron capture. During the scattering process the two atoms are considered to be fused in a quasi-molecule compound [33]. In this approximation electrons can pass from the target to the incoming atom which results to be slow down.

Other authors like Lindhard and Sharff proposed another model for the electronic energy loss in the low energy range. The main difference between the Firsov's and Lindhard-Sharff model is the form of the screening interatomic potential. The inelastic energy loss Q of a single collision proposed by Robinson and Torrens is a modification of the Firsov's model. Anyway Norgett et al. [49] pointed out that the amount of displacement damage calculated with the Firsov's model is similar in magnitude to the prediction obtained by the use of the Lindhard-Sharff model.

At present the damage function commonly used for the displacement damage calculation is obtained by the Robinson's analytical approximation of the Lindhard-Sharff model which, for mono-atomic material, may be expressed

as [50] [1]:

$$\begin{aligned} \nu(T) &= \frac{T}{1 + k_d g(\epsilon_d)} && (3.12) \\ k_d &= 0.1334 Z^{2/3} m^{-1/2} && (3.13) \\ g(\epsilon_d) &= \epsilon_d + 0.40244 \epsilon_d^{3/4} + 3.4008 \epsilon_d^{1/6} && (3.14) \\ \epsilon_d &= 0.01014 Z^{-7/2} T && (3.15) \end{aligned}$$

where k_d is the electronic energy-loss factor of Lindhard-Sharff model in reduced notation, ϵ_d is the reduced energy, m and Z are mass and atomic number of the material and T is the kinetic energy of the PKA.

With the use of this damage energy it is possible to calculate the *modified Kinchin and Pease displacement damage function*:

$$\langle N_d(T) \rangle = \begin{cases} 0 & \text{if } \nu(T) < T_d \\ 1 & \text{if } T_d \leq \nu(T) < 2T_d/\xi \\ \dfrac{\xi \nu(T)}{2T_d} & \text{if } \nu(T) \geq 2T_d/\xi \end{cases} \tag{3.16}$$

where $\nu(T)$ is equal to the amount of energy that goes in elastic nuclear collisions given by the (3.12) and the coefficient ξ is the *displacement efficiency* which depends on the interaction potential and it does not depend on the initial kinetic energy T. Analytical calculation and computer simulation suggest a value of $\xi = 0.8$.

3.2 Non-Ionizing Energy Loss

The Non-Ionizing Energy Loss (NIEL) is the energy deposited inside the material which goes into displacement process or into phonon vibrations. If it is calculated from the threshold displacement energy value T_d it is a useful tool to quantify the cumulative displacement damage induced by an incident particle inside the material. It is the equivalent quantity of the displacement damage as the stopping power is for the total ionizing dose (TID). In analogy with the stopping power given by:

$$-\frac{dE}{dx} = N \int_{T_{min}}^{T_{max}} T \frac{d\sigma(T, E)}{dT} dT$$

where E is the kinetic energy of the incident particle, N is the density number of targets, the NIEL is given by the fraction of the deposited energy that goes

only into displacement processes:

$$NIEL(E) \equiv -\frac{dE}{dx}\Big|_{displacement} = N \int_{T_d}^{T_{max}} TL(T) \frac{d\sigma(T,E)}{dT} dT \qquad (3.17)$$

where in this case $N = N_A\rho/A_2$ (with ρ and A_2 density and atomic mass number of the target respectively) and $L(T)$ is the fraction of the recoil energy T that goes into displacement processes, which accounts for the collision cascade and it is called *damage efficiency* or Lindhard correction:

$$L(T) = \frac{\nu(T)}{T} \qquad (3.18)$$

where $\nu(T)$ is given by the equation (3.12). The NIEL is expressed in energy per unit path length, usually in MeV/cm or in MeV cm^2/g if it is divided by the mass density ρ of the material.

According to the type and energy of the incident particle the total NIEL is given by the sum of different contributes which depend on the differential cross section of the specific process. The cumulative cross section may be written as [53]:

$$\frac{d\sigma(T,E)}{dT} = \frac{d\sigma(T,E)}{dT}\Big|_{Coul} + \frac{d\sigma(T,E)}{dT}\Big|_{Hadr\ el} + \frac{d\sigma(T,E)}{dT}\Big|_{Hadr\ inel} \qquad (3.19)$$

where the term on the right side, denoted with *Coul*, gives the Coulomb scattering contribution to NIEL; the second and the third terms, indexed by *Hadr el* and *Hadr inel*, are the differential cross sections for energy transferred due to hadronic interactions of the incident particle with the target nucleus. They are nuclear elastic and inelastic collision processes and they are relevant at high energies (see section 3.2.3).

In nuclear elastic collision processes the charge and the number of nucleons remains unchanged after collision [54]. In nuclear inelastic collisions, instead, the incident nucleus may be absorbed by the target nucleus which can have sufficient energy to start an intranuclear cascade followed by the evaporation process. In this case there is a change in the atomic number of the target nucleus after collision. In the intranuclear cascade the target nucleus may eject particles of energy up to the incident one. After that the residual nucleus is left in an exited state and evaporates by emitting nucleons of energy from 10 MeV to 15 MeV [54]. The damage induced by secondary particles coming from this nuclear cascade and from the evaporation processes are generally not included in the NIEL calculation because they account only for the one per cent of the total damage [54].

If the incident particles are distributed according to a spectral fluence function $\Phi(E)$ expressed in MeV^{-1} cm^{-2}, then each particle of energy E will lose a non-ionizing energy $NIEL(E)$ so that the total damage energy deposited per unit volume of material can be calculated as:

$$E_{dis} = \int_{E_{min}}^{E_{max}} NIEL(E)\ \Phi(E)dE \quad \left[\frac{\mathrm{MeV}}{\mathrm{cm}^3}\right] \tag{3.20}$$

where NIEL is expressed in MeV/cm and E_{min} and E_{max} are the minimum and maximum kinetic energies of the incident particles distribution.

By the energy density E_{dis} and the modified Kinchin-Pease relation (3.16) it is possible to estimate the number of Frenkel-pairs generated by a generic distribution of incident particles soon after irradiation:

$$FP = \frac{\xi E_{dis}}{2T_d} \tag{3.21}$$

which is a measure of the damage induced inside the lattice crystal. Once that the number of Frenkel-pairs is calculated by the (3.21), it is possible to compare the effects of the displacement damage on the electronic devices induced by different kind of particles. In addition the NIEL absorbed Dose is simply given by:

$$D^{NIEL} = \frac{E_{dis}}{6.24 \times 10^9 \rho} \quad [\mathrm{Gy}] \tag{3.22}$$

where the numerical constant is the conversion factor from MeV/g to J/kg which is equal to a *Gray* (Gy). The NIEL induced by neutrons, protons and heavy nuclei are given in the following sub-sections.

3.2.1 Neutrons NIEL

Neutrons are an important tool to understand the displacement damage because they interact only by nuclear elastic and inelastic processes. In addition our experimental measurements, which will be examined in chapter 6, are performed on silicon bulk samples irradiated with neutrons. Thermal (~ 0.025 eV) and fast (> 10 keV) neutrons are produced in the nuclear fission reactors according to a spectral fluence distribution $\Phi(E)$ obtained by the time intrgal [1]:

$$\Phi(E) = \int \Phi(E,t)dt \quad [\mathrm{MeV}^{-1}\ \mathrm{cm}^{-2}] \tag{3.23}$$

where $\Phi(E,t)$ is the neutron spectral flux given in MeV^{-1} cm^{-2} s^{-1}. The total neutron fluence is computed by the energy integral:

$$\Phi_n = \int_{E_{min}}^{E_{max}} \Phi(E)dE \quad [\mathrm{cm}^{-2}] \tag{3.24}$$

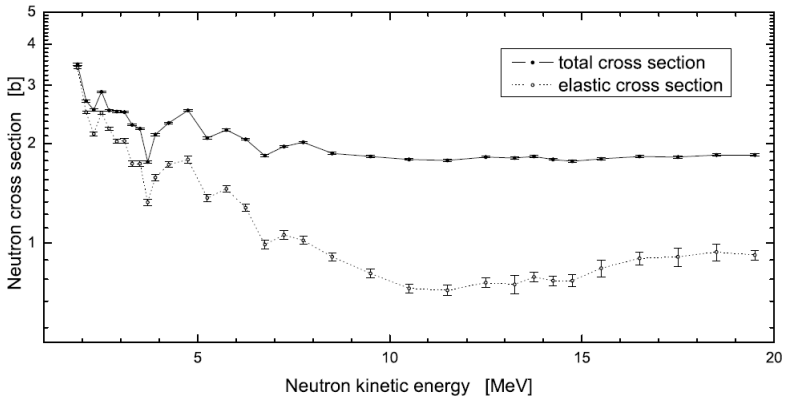

Figure 3.2: Total and elastic neutron cross section in silicon material [1].

Only neutrons exceeding 10 keV are relevant in the displacement damage computation, so that, in general, $E_{min} = 10$ keV. Usually the E_{max} value for a fission reactor does not exceed 15 MeV [1].

For neutrons up to 1 MeV [30], the elastic collision is the most likely process to produce displacement [1]. Since the elastic differential cross section for energy transfer results to be independent on the kinetic energy T transferred to the target atom, the scattering process may be described by the use of the hard-sphere potential. All transferred kinetic energies from zero to the maximum value T_{max}, given by (2.64) with $E_1 \equiv E$, are equally probable and the mean value is equal to $T_{max}/2$.

For neutrons with energies above the resonance peaks the elastic cross section decrease and the inelastic process which leads to nuclear interactions such as $(n, 2n)$, (n, p), (n, α), (n, d), becomes dominant. The total cross section, in the energy range from 1.75 MeV up to 20 MeV is reported in figure 3.2 together with the elastic component [1].

The displacement damage induced by both elastic and inelastic processes may be calculated by the use of the *displacement kerma function* or *damage function* $D(E)$ expressed in MeV cm^{-2} and defined as [52] [1]:

$$D(E) = \sum_k \sigma_k(E) \int_{T_d}^{T_{max}} \nu_k(T) P_k(T, E) dT \tag{3.25}$$

where:

$$\sigma_k(E) = \int \frac{d\sigma_k(T, E)}{dT} dT \tag{3.26}$$

is the integral cross section for the k-th reaction; $\nu_k(T)$ is the damage energy which is given by the Robinson's analytical approximation given in equation

(3.12), and $P_k(T,E)dT$ is the probability for a particle of kinetic energy E to produce a recoil of kinetic energy between T and $T+dT$ for the k-th reaction:

$$P_k(T,E)dT = \frac{1}{\sigma_k(E)}\frac{d\sigma_k(T,E)}{dT}dT \tag{3.27}$$

where $d\sigma_k(T,E)/dT$ is the differential cross section for energy transfer of the k-th reaction. It is possible to demonstrate that the displacement kerma function $D(E)$ is proportional to the NIEL. By the use of the (3.27) the displacement kerma function, given by equation (3.25), can be also written as:

$$D(E) = \sum_k \int_{T_d}^{T_{max}} \nu_k(T)\frac{d\sigma_k(T,E)}{dT}dT \tag{3.28}$$

and since $\nu_k(T) = TL(T)$ (see equation (3.18)), $D(E)$ is given by:

$$D(E) = \sum_k \int_{T_d}^{T_{max}} TL_k(T)\frac{d\sigma_k(T,E)}{dT}dT \tag{3.29}$$

By these manipulations, the $D(E)$ has the same form of the total NIEL given by equation (3.17) inside which $d\sigma(T,E)/dT$ is given by the sum (3.19) where, in this case, the Coulomb differential cross section is not included. The relation between $D(E)$ and NIEL is then simply given by:

$$NIEL(E) = ND(E) \tag{3.30}$$

Values of neutrons $D(E)$, and the corresponding NIEL, in silicon material are reported in figure 3.3 which may be found in literature [1] from 0.001 eV to 10 TeV.

The neutrons displacement energy density is calculated by:

$$E_{dis} = N\int_{E_{min}}^{E_{max}} D(E)\ \Phi(E)dE \quad \left[\frac{\mathrm{MeV}}{\mathrm{cm}^3}\right] \tag{3.31}$$

where E_{max} and E_{min} are the maximum and minimum energies of the spectral fluence. The displacement damage induced by neutrons distributed according to a generical spectral fluence $\Phi(E)$ may be normalized with the one induced by mono-energetic neutrons of 1 MeV with fluence $\Phi_n^{1\mathrm{MeV}}$ by the use of a proportional constant κ called *hardness factor*:

$$\Phi_n^{1\mathrm{MeV}} = \kappa\Phi_n \tag{3.32}$$

where Φ_n is computed by the (3.24). The hardness factor may be calculated equating the quantity E_{dis} induced by a generic fluence Φ_n, to the equivalent value $E_{dis}|_{1\mathrm{MeV}}$ produced by the 1 MeV neutrons fluence $\Phi_n^{1\mathrm{MeV}}$, that is:

$$E_{dis}|_{1\mathrm{MeV}} = E_{dis} \tag{3.33}$$

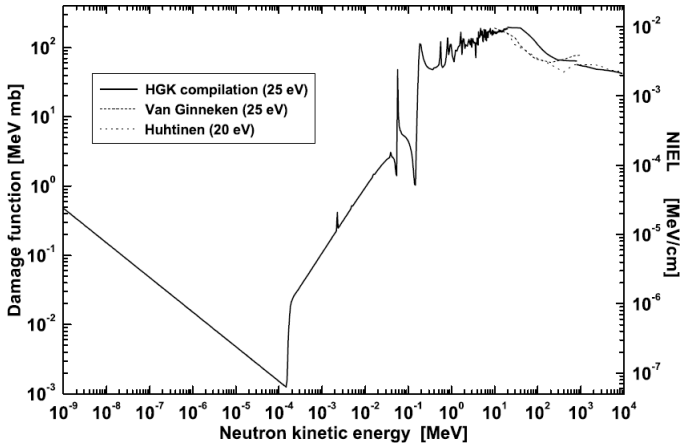

Figure 3.3: Damage function and corresponding NIEL values for neutrons in silicon material [1]. The HGK compilation is available on-line at [56] with $T_d = 25$ eV. Van Ginneken $T_d = 25$ eV [59]. Huhtinen $T_d = 20$ eV [57]

where $E_{dis}|_{1\text{MeV}} = ND(1\text{MeV})\Phi_n^{1\text{MeV}}$ and E_{dis} is calculated by the expression (3.31). The (3.33) is then equal to:

$$D(1\text{MeV})\Phi_n^{1\text{MeV}} = \int_{E_{min}}^{E_{max}} D(E)\ \Phi(E)dE \tag{3.34}$$

where $D(1\text{MeV}) = 95$ MeV mb is the ASTM standard[1]. From the (3.34) it is possible to write:

$$\Phi_n^{1\text{MeV}} = \int_{E_{min}}^{E_{max}} \frac{D(E)}{D(1\text{MeV})}\ \Phi(E)dE \tag{3.35}$$

By the use of the (3.32) it is possible to obtain the hardness factor where Φ_n is given by (3.24):

$$\kappa = \frac{\Phi_n^{1\text{MeV}}}{\int_{E_{min}}^{E_{max}} \Phi(E)dE} = \frac{\int_{E_{min}}^{E_{max}} \frac{D(E)}{D(1\text{MeV})}\ \Phi(E)dE}{\int_{E_{min}}^{E_{max}} \Phi(E)dE} \tag{3.36}$$

which enables one to compare the total displacement damage induced by different fission reactors facilities each characterized by a specific κ.

[1]Standard practice of characterizing neutron energy fluence spectra in terms of equivalence mono-energetic fluence for radiation hardness testing electronics [1]

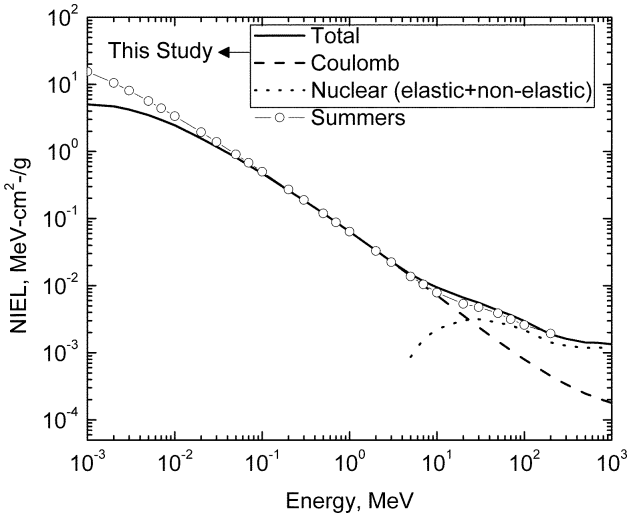

Figure 3.4: Jun et al. [34] proton NIEL in silicon. Energy range 1keV-1 GeV, The Coulomb contribution is calculated by the use of the ZBL screened potential for $E < 50$ MeV and by the relativistic differential cross section (2.110) for $E \geq 50$ MeV. Nuclear elastic and inelastic contributions are included. Summers et al. [60]

3.2.2 Protons NIEL

Protons, as all charged particles, cause displacement damage by Coulomb interactions with the target nuclei. In addition, at high energy, nuclear elastic and inelastic collisions may occur and increase the total NIEL.

In literature the total proton NIEL in silicon was tabulated by Jun et al. [35], [34] in the energy range from 200 eV to 1 GeV, calculated with a threshold displacement energy $T_d = 21$ eV. Their results are reported in 3.4 together with the Summers et al. [60] values, in the energy range from 1 keV to 1 GeV. It is possible to see deviations form the non-relativistic unscreened Coulomb potential both at low and high energies. At low energies Jun et al. assumed a screened Coulomb potential with the ZBL universal screening function which is given by (2.97). At higher energies they used the unscreened Coulomb differential cross section given by the equation (2.110). Nuclear elastic collisions are relevant above 20 MeV (50% of the total NIEL) while the inelastic processes are expected to be relevant at energies greater than 100 MeV [54]. To compute the nuclear elastic and inelastic cross section, the same authors developed a transport code (MCNPX) which uses the cross section of Barashenkov and Polanski [24] for the calculation of the PKAs kinetic energies.

Huhtinen [57] extended the proton NIEL calculation in a silicon material

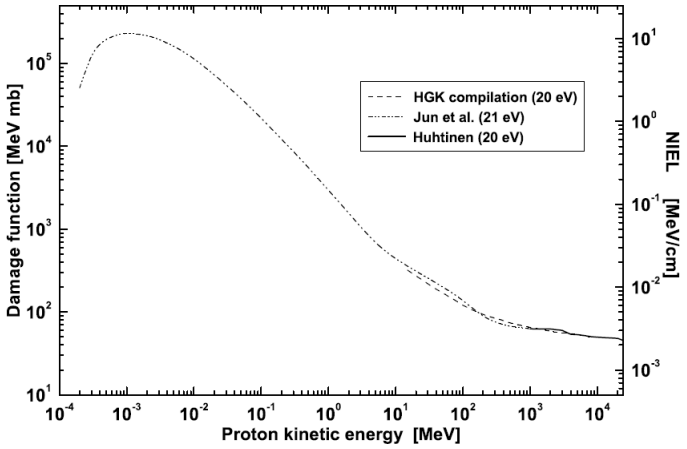

Figure 3.5: Damage function and corresponding NIEL values for protons in the energy range from 2 eV to 24 GeV in silicon [1]. In the HGK compilation a threshold displacement energy equal to 20 eV is used [56]. Data taken from Jun et al. [34] assumed $T_d = 21$ eV. Huhtinen values are calculated with $T_d = 20$ eV [57].

up to 24 GeV. In his work a displacement threshold energy equal to 20 eV was assumed.

In fig 3.5 are reported the values tabulated by these authors for the proton NIEL in silicon material and the related damage function $D(E)$, in the energy range from 2 eV up to 24 GeV [1]. In the same figure are also reported the HGK compilation values for proton kinetic energies in the range from 15 MeV to 9 GeV available on line at [56].

3.2.3 Heavy Nuclei NIEL

The Coulomb NIEL fraction was calculated in the non-relativistic regime by Messenger et al. [50] for protons, alpha particles and heavy ions in the energy range from 0.1 keV to 1 GeV. In their work the analytical computation of NIEL was obtained by means of the integral (3.17) with the use of the one parameter differential scattering cross section reported in section 2.3.2 (equation (2.99)). The integral was performed from the threshold energy of displacement, fixed at $T_d = 21$ eV, up to the maximum energy that can be transferred during a single collision T_{max} which in this case is equal to the non-relativistic value (equation (2.29)).

In figure 3.6 are reported the Messenger et al. [50] results of the NIEL computation for different particles incident on a silicon material. In this work however the relativistic corrections, which in this energy range are necessary at least for protons and alpha particles, were not considered.

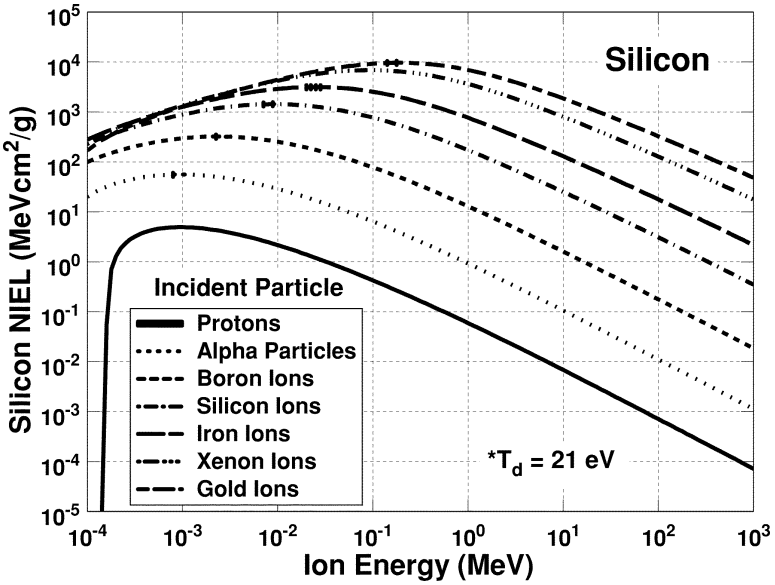

Figure 3.6: Results taken from Messenger et al. [50], of NIEL calculation for different incoming ions in the energy range 100 eV- 1 GeV in silicon material.

Unfortunately in literature there is a lack of the NIEL calculation for heavy nuclei at higher energies which is important for the calculation of the displacement damage induced by cosmic rays. In addition, since cosmic rays are relativistic particles, nuclear interactions may become relevant after a certain energy. An estimation of the energy at which the Coulomb and the nuclear processes have the same NIEL value may be found in [1]. In this estimation the total cross section for nuclear interactions is considered, to a first approximation, to be proportional to the square of the sum of the geometrical radii of the interacting nuclei:

$$\sigma_{Nucl} \propto (R_2 + R_1)^2 \propto (A_2^{1/3} + A_1^{1/3})^2 \tag{3.37}$$

where the indexes 2 and 1 refers to the target and the incident nucleus respectively. The total Coulomb cross section is considered to be proportional to $(Z_1 Z_2)^2$ where Z_1 is the atomic number of the incident nucleus and Z_2 is the one of the target. To take into account the relativistic contraction of the region of space in which the electric field is maximum, $(Z_1 Z_2)^2$ is divided by the velocity of the incoming nucleus multiplied by the particle Lorentz's

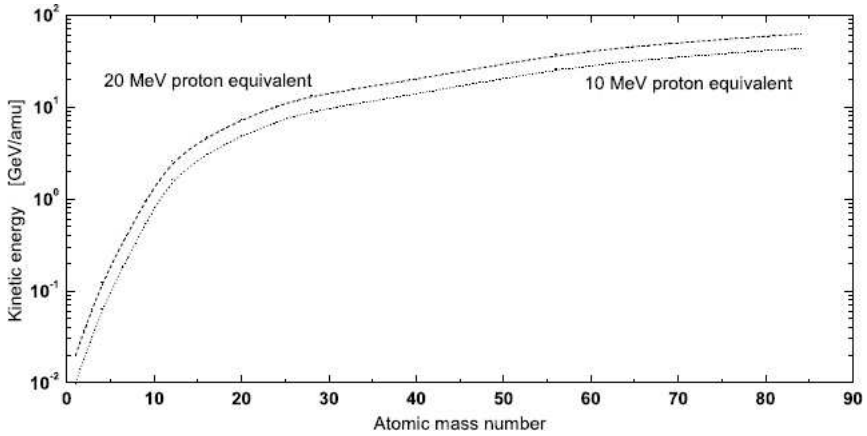

Figure 3.7: Kinetic energies at which the nuclear interactions are expected give the same NIEL contribution as the coulomb one as a function of the atomic mass number [1]. The upper curve is calculated considering 20 MeV equivalent proton kinetic energy, the lower is for 10 MeV.

factor[2]:

$$\sigma_{Coul} \propto \frac{(Z_2 Z_1)^2}{\beta_1 \gamma_1} \propto \frac{(Z_2 Z_1)^2}{\sqrt{\gamma_1^2 - 1}} \tag{3.38}$$

The ratio of these two cross sections may be written as:

$$\frac{\sigma_{Coul}}{\sigma_{Nucl}} \propto \left(\frac{Z_2 Z_1}{A_2^{1/3} + A_1^{1/3}} \right)^2 \frac{1}{\sqrt{\gamma_1^2 - 1}} = \frac{S_{2,1}}{\sqrt{\gamma_1^2 - 1}} \tag{3.39}$$

As already said in section 3.2.2, for protons of kinetic energy above 20 MeV nuclear interactions are relevant in the total computation of NIEL. For protons of 20 MeV the ratio of the two cross sections written above is approximatively one. For heavier nuclei the equivalent kinetic energy at which the ratio (3.39) is approximatively one, may be calculated by:

$$\frac{S_{2,1}}{\sqrt{\gamma_1^2 - 1}} \approx \frac{S_{2,p}}{\sqrt{\gamma_{p,20MeV}^2 - 1}} \tag{3.40}$$

where the term on the left side is calculated for a generic nucleus (index 1) and the one on the right side is obtained for protons of kinetic energy equal to 20 MeV (index p). From the relation (3.40) it is possible to obtain the

[2]The collision time is proportional to $1/(v\gamma)$ where v is the velocity of the incident particle and γ is its Lorentz factor.

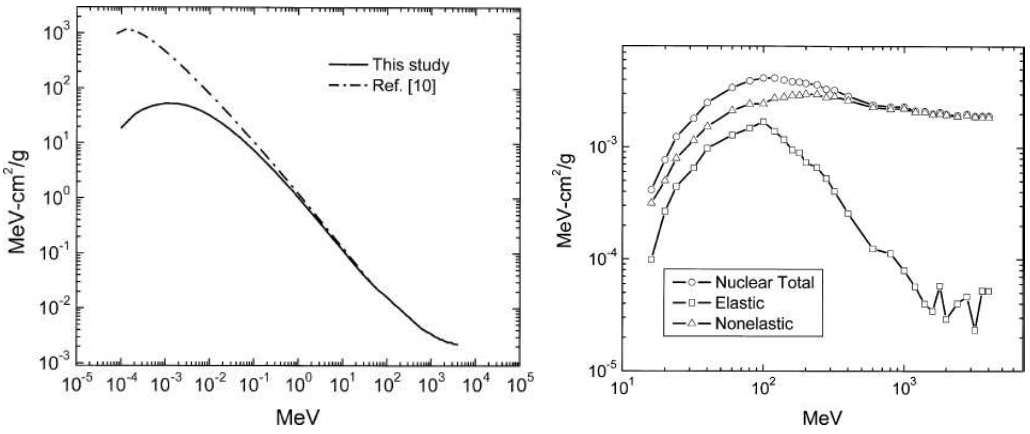

Figure 3.8: Right: Alpha NIEL value where the header "This study" refers to non-relativistic screened Coulomb NIEL value plus nuclear interactions [36] and the heather "Ref. [10]" refers to [51] where the Coulomb potential is not screened. Left: Alpha NIEL due to nuclear interactions: nuclear elastic, inelastic and total [36].

equivalent nucleus Lorentz's factor:

$$\gamma_1 = \sqrt{(\gamma_{p,20MeV}^2 - 1)\left(\frac{S_{2,1}}{S_{2,p}}\right)^2 + 1} \tag{3.41}$$

where $\gamma_{p,20MeV}$ is the proton Lorentz's factor calculated for a kinetic energy of 20 MeV, $S_{2,1}$ and $S_{2,p}$ are the proportional constants given in the (3.39) for a generic incident nucleus and a proton respectively. The result of this computation is reported in figure 3.7 for a silicon target material as a function of the atomic mass number of the incident nucleus. The two curves correspond to 10 MeV and 20 MeV equivalent proton kinetic energies for which nuclear interactions account for 15% and 50% of the total NIEL respectively. The kinetic energy is expressed in GeV/amu (atomic mass unit). For alpha particles the equivalent kinetic energy is about 120 MeV/amu, for lithium it is about 420 MeV/amu and for beryllium it is about 940 MeV/amu [1]. For heavier nuclei the equivalent kinetic energy exceeds 1 GeV/amu.

3.2.4 Alpha Particles NIEL

The same authors who performed the proton NIEL calculation, Jun et al. [34] extended their work also for alpha particles [36]. The total alpha NIEL values are tabulated from 10 eV/nucl up to 1 GeV/nucl by Jun et al. [36]. In their study authors used the Coulomb NIEL component in the non-relativistic regime calculated by Messenger et al. [50] whose values were already reported

in figure 3.6. The nuclear contribution to the NIEL value for alpha particles was calculated with the same transport code (MCNPX) which was used for protons. The total NIEL accounting for Coulomb process plus nuclear interactions is reported on the left side of figure 3.8. On the right side of the same figure, the nuclear interaction contribution to NIEL is reported alone.

3.3 Defect Complexes

From a microscopic point of view the crystal lattice of the material results to be modified in the region of space where the incident cosmic ray has passed. Vacancies and interstitial atoms created during irradiation may migrate inside the material and form cluster of defects in a relative small region of space or can interact with impurity atoms already present in the material and form defect complexes.

Defect complexes, in fact, are the result of the rearrangement of the primary point defects generated after irradiation. Because of the thermal agitation the primary point defects, which are vacancies (V) and interstitial atoms (I), are free to migrate inside the material. Their activation energies range between 18-45 meV [1] and depend on the type and on the resistivity of the semiconductor. Inside the cluster most of these primary defects will spontaneously anneal by the filling process of a vacancy with an interstitial ($V + I$). It was calculated that the filling process occurs with a probability of more than 90% inside the cluster [57]. This spontaneous anneal reduces the initial Frenkel-pairs number calculated by the equation (3.21) which is the estimated value soon after irradiation.

The remaining vacancies will interact with already present impurity atoms of the material or with other vacancies by forming new types of defect complexes which are more stable defects.
Stable defects will introduce in the forbidden energy gap of the semiconductor discrete energy levels which may act as trapping centers for conducting carriers. This mechanism is called carrier removal and will lead to the increase of the resistivity of the bulk material. In addition electrons and holes are captured and re-emitted with a delay time causing the reduction of the carriers life time. For example this mechanism is one of the main causes of degradation of bipolar transistors for which the gain results to be lowered after irradiation (see section 3.5).
If the energy levels introduced by defect complexes lie close to the mid-gap energy level, then they will act as generation-recombination centers. The enhancement of the recombination-generation process, for example, will cause an increase of the reverse bias current of silicon detectors which will increase

the noise level of the detector signal (for generation-recombination process see 5.2).

One stable defect is the divacancy center called $G7$-center, which is formed by the reaction:

$$V + V \rightarrow V_2 \tag{3.42}$$

The divacancy may have four charge states ranging from double negative to positive which introduce discrete levels $E_c - 0.23$, $E_c - 0.39$ and $E_v + 0.21$ [58].

Another stable defect is the vacancy-dopant complex called E-center, in which the vacancy atom interacts with a dopant atom removing its dopant function. For example in a n-type material, doped with phosphorus atoms (P), the reaction:

$$V + \mathrm{P} \rightarrow V\mathrm{P} \tag{3.43}$$

will cause the formation of an E-center which introduces a level of energy $E_c - 0.44$. The direct consequence is the reduction of the effective doping concentration (N_{eff}).

Another candidate for the reduction of the effective doping concentration is the divacancy-oxygen complex [57]. The divacancy complex may interact with an impurity Oxygen atom and form the V_2O complex by:

$$V_2 + O \rightarrow V_2O \tag{3.44}$$

Other defect complexes like V_2 and V_3 are suppose to decrease the N_{eff} value. The effective doping concentration is given by the difference between the donor and the acceptor concentrations. A simple relation which may explain the donor removal is [57]

$$N_{eff} = |[P] - f_1[V_2O] - f_2[V_2] - f_3[V_3]| \tag{3.45}$$

where the brackets [ ] indicate the concentration of the corresponding quantity, and f_i are coefficients which express the electron occupancies of the acceptor states.

To prevent the donor removal process it has been proposed to add Oxygen impurity atoms during the growing process of the semiconductor bulk. This will enhance the formation of the defect vacancy-oxygen by:

$$V + O \rightarrow VO \tag{3.46}$$

which has no important influences on the electrical properties of the silicon material. The VO formation should diminish the (3.42) reaction and as a consequence also the (3.44) one. This should strongly suppress the N_{eff} reduction as can be seen from experimental results [62] reported in figure

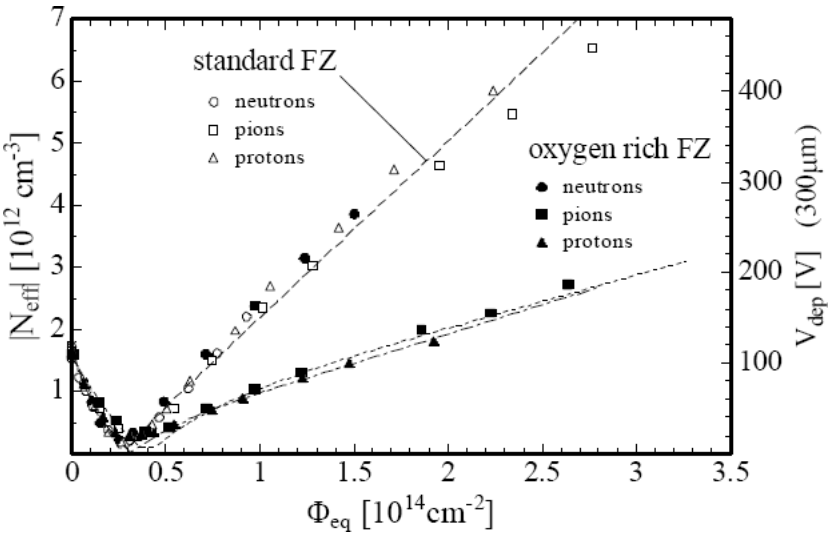

Figure 3.9: N_{eff} dependence on the accumulated 1 MeV neutron equivalent fluence for standard and oxygen enriched FZ silicon irradiated with reactor neutrons, 23 GeV protons and 192 MeV pions [62].

3.9 where the N_{eff} concentration, as a function of 1 MeV neutron equivalent fluence, is reported for standard and oxygen enriched silicon diodes. At low fluences the decrease of N_{eff} is dominated by the donor removal process which causes a decrease in the full depletion voltage[3], as can be seen from the right-side axis of figure 3.9. The N_{eff} value reaches its minimum when the donor concentration is exhausted or compensated by irradiation-induced acceptors. At this irradiation level the conduction type of the material changes from n- to p-type. The slope of a linear line fit beyond the inversion point is called β value and represents the introduction rate of deep acceptors. The oxygen enriched material presents a much lower β value compare to the standard silicon one.

The effective doping concentration decreases with increasing irradiation fluence until it reaches the level of complete compensation. At this stage the semiconductor acts almost like an insulator. With further increasing of the irradiation fluence the effective doping concentration become of opposite type. This effect was observed both for n-type and p-type materials irradiated with different kind of particles [61], [1].
The change of the effective conductivity type may be analyzed by the Hall effect which enables one to define the type and concentration of the majority

[3]The voltage which is necessary apply in order to deplete the device for the normal diode operation.

carriers. Experimental results of the Hall effect performed on silicon bulk samples irradiated with neutrons and carbon ions will be given in chapter 6 .

It has to be remark, however, that for heavily irradiated samples the conduction type is not well defined as in the case of a non-irradiated sample. This happens because even if an heavily irradiated sample approaches the intrinsic concentration level it is very different from an intrinsic semiconductor. An intrinsic semiconductor is suppose to have an almost perfect crystal lattice with very few impurity atoms. A heavily defected material, instead has a lot of impurities rearranged as defect complexes and in addition the crystal lattice doesn't have a perfect structure.

3.4 Reduction of the Minority Carrier Lifetime After Irradiation

One important quantity, which varies after irradiation, is the minority carrier lifetime. The carrier lifetime is reduced by the irradiation process which causes the formation of recombination centers within the forbidden band gap of the semiconductor. The *recombination carrier lifetime*, or *minority carrier lifetime*, is defined as:

$$\tau_m = \frac{1}{\sigma_m v_{th} N_t} \tag{3.47}$$

where the index m refers to minority carriers which can be electrons or holes according to the semiconductor type, N_t is the concentration of recombination centers before irradiation, σ_m is the relative capture cross section and v_{th} is the thermal velocity of carriers. After irradiation the minority carrier lifetime varies because of the increase of the concentration of recombination centers in the forbidden energy gap of the semiconductor. The recombination rate of minority carriers after irradiation, $1/\tau'_m$, is given by the non-irradiated one, $1/\tau_m$, plus a rate introduced after irradiation:

$$\frac{1}{\tau'_m} = \frac{1}{\tau_m} + \sigma_m v_{th} N'_t \tag{3.48}$$

where N'_t is the concentration of recombination centers which are created after irradiation. The N'_t value is related to the energy deposited by displacement process and it can be estimated to be:

$$N'_t = N \int_{E_{min}}^{E_{max}} \sigma(E)\phi(E)dE \tag{3.49}$$

where N is the target density number, $\phi(E)$ is the incident spectral fluence and

$$\sigma(E) = \int_{T_{min}}^{T_{max}} \frac{d\sigma(T,E)}{dT} dT \tag{3.50}$$

is the integral of the differential cross section for energy transfer for an incident particle of energy E. The averaged value of $\sigma(E)$ may be computed by:

$$\langle\sigma\rangle = \frac{\int_{E_{min}}^{E_{max}} \sigma(E)\phi(E)dE}{\int_{E_{min}}^{E_{max}} \phi(E)dE} = \frac{\int_{E_{min}}^{E_{max}} \sigma(E)\phi(E)dE}{\phi} \tag{3.51}$$

where ϕ is the irradiation fluence. From this last expression it is possible to write the equation (3.49) as:

$$N_t' = N\langle\sigma\rangle\phi \tag{3.52}$$

Inserting this last expression of N_t' in the (3.48) leads to:

$$\frac{1}{\tau_m'} = \frac{1}{\tau_m} + \sigma_m v_{th} N\langle\sigma\rangle\phi. \tag{3.53}$$

The multiplicative term of the irradiation fluence is define as the inverse of the lifetime damage coefficient K (sec cm^{-2}):

$$\frac{1}{K} \equiv \sigma_m v_{th} N\langle\sigma\rangle \tag{3.54}$$

which leads to an important relation between the variation of the reciprocal minority carrier lifetime and the irradiation fluence:

$$\Delta\left(\frac{1}{\tau_m}\right) \equiv \frac{1}{\tau_m'} - \frac{1}{\tau_m} = \frac{\phi}{K} \tag{3.55}$$

The concentration of recombination centers N_t' is proportional to the density energy deposited by displacement processes E_{dis} which is computed by the equation (3.20) and it is related to the Frenkel-pairs concentration FP by the equation (3.21). This consideration enables one to write:

$$E_{dis} \propto N_t' = \gamma_{dis} FP \tag{3.56}$$

where the γ_{dis} coefficient is the proportionality constant. By the use of the (3.56), the right side of the equation (3.55) can be written as

$$\frac{\phi}{K} = \sigma_m v_{th} N_t' = \sigma_m v_{th} \gamma_{dis} FP = \lambda FP \tag{3.57}$$

where it has been introduced the parameter $\lambda = \sigma_m v_{th} \gamma_{dis}$ which does not depend on the incident particle type. The (3.55) can then be rewritten as:

$$\Delta\left(\frac{1}{\tau_m}\right) = \lambda F P \tag{3.58}$$

which gives a relation between the difference of the recombination rates before and after irradiation as a function of the FP concentration.

3.5 Bipolar Junction Transistor (BJT)

A bipolar junction transistor is a device which acts as a current or as a voltage amplifier according to the configuration mode, in which both charges, electrons and holes, participate to conduction. It is made up of two semiconductor junctions and it can be of *npn* or of *pnp* type. The three semiconductors regions are called emitter (E), base (B) and collector (C). In the active mode operation, the E-B junction is forward biased while the B-C one is reversed. The E region of the device is heavily doped with a concentration that may exceed 10^{20} cm^{-3} and so it has a very low resistance. The B region has a low resistance too, but not less then 0.01 Ω cm which corresponds to a doping concentration of 10^{18} cm^{-3}. The C region, instead, has a lower doping concentration of about 10^{16} cm^{-3}.

The *pnp* type[4] transistor currents are schematically reported in figure 3.10. The emitter current, I_{E}, is set up by the hole current $I_{\mathrm{E}p}$ which flows form E to B and by the electron current $I_{\mathrm{E}n}$ given by electrons flowing form B to E. Since E is heavily doped and the E-B junction is forward biased, there will be a great injection of holes form E to B. Inside the base, which is a n-type semiconductor, holes become of minority type. The base width is usually very narrow so that the major fraction of holes are able to reach the C region. This is true if the recombination rate inside the base is low. The B-C junction instead is reversed biased and, as a consequence, the C current I_{C} is given by the holes coming form the emitter which didn't recombine inside the base (denoted as the hole current $I_{\mathrm{C}p}$) plus an electron current $I_{\mathrm{C}n}$ which is given by the electrons flowing from C to B. The $I_{\mathrm{C}n}$ current is also known as leakage current and it is made up by the electrons thermally generated inside the collector region. The base current I_{B} is set up of three components: $I_{\mathrm{E}n}$, $I_{\mathrm{C}n}$ and the $I_{\mathrm{BB}}(= I_{\mathrm{E}p} - I_{\mathrm{C}p})$ current which is the current that is generated from the base contact in order to supply the electrons inside

[4]For a *npn* type the issue is analogous but with opposite charge.

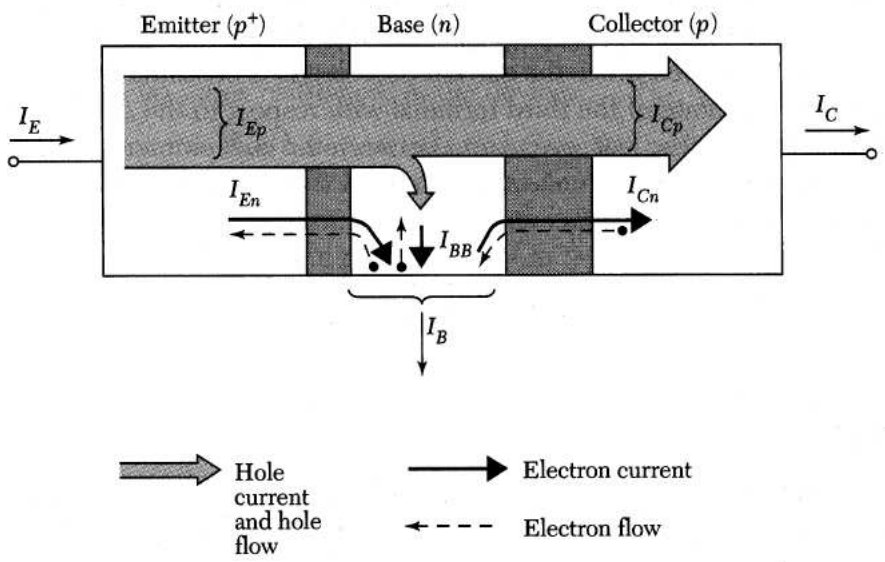

Figure 3.10: Various current components in a *pnp* transistor under active mode of operation [76].

the base which had recombined with the holes. In summary it is possible to write [76]:

$$\begin{aligned} I_{\mathrm{E}} &= I_{\mathrm{E}p} + I_{\mathrm{E}n} && (3.59)\\ I_{\mathrm{C}} &= I_{\mathrm{C}p} + I_{\mathrm{C}n} && (3.60)\\ I_{\mathrm{B}} &= I_{\mathrm{E}} - I_{\mathrm{C}} = I_{\mathrm{E}n} + (I_{\mathrm{E}p} - I_{\mathrm{C}p}) - I_{\mathrm{C}n} && (3.61)\\ &= I_{\mathrm{E}n} + I_{\mathrm{BB}} - I_{\mathrm{C}n} \end{aligned}$$

In many applications, a bipolar transistor is set in the common emitter configuration where B acts as input, C as output and E is common to both base and collector. The emitter is usually tied to the ground reference as reported in figure 3.11. In this configuration the current gain is define as [75]:

$$\beta \equiv \frac{\partial I_{\mathrm{C}}}{\partial I_{\mathrm{B}}} \tag{3.62}$$

Since the total collector current is given by $I_{\mathrm{C}} = I_{\mathrm{E}} - I_{\mathrm{B}}$, the current gain can be written as:

$$\beta = \frac{\partial I_{\mathrm{E}}}{\partial I_{\mathrm{B}}} - 1 = \frac{\partial I_{\mathrm{E}}}{\partial I_{\mathrm{C}}}\frac{\partial I_{\mathrm{C}}}{\partial I_{\mathrm{B}}} - 1 = \frac{1}{\alpha}\beta - 1 = \frac{\alpha}{1-\alpha} \tag{3.63}$$

where α is the amplification gain in the common emitter configuration defined

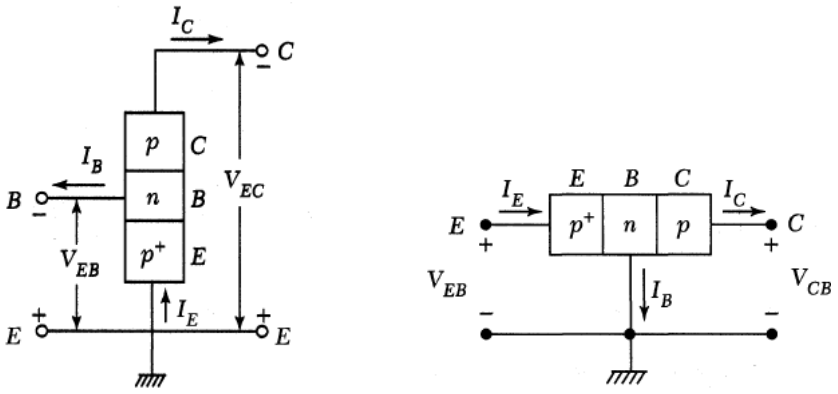

Figure 3.11: (Left) Common emitter and (right) common base configuration of a *pnp* bipolar transistor. [76].

as [75]:

$$\alpha \equiv \frac{\partial I_{\mathrm{C}}}{\partial I_{\mathrm{E}}} = \frac{\partial I_{\mathrm{E}p}}{\partial I_{\mathrm{E}}} \frac{\partial I_{\mathrm{C}p}}{\partial I_{\mathrm{E}p}} \frac{\partial I_{\mathrm{C}}}{\partial I_{\mathrm{C}p}} = \gamma \alpha_T M \tag{3.64}$$

$$\gamma = \frac{\partial I_{\mathrm{E}p}}{\partial I_{\mathrm{E}}} \tag{3.65}$$

$$\alpha_T = \frac{\partial I_{\mathrm{C}p}}{\partial I_{\mathrm{E}p}} \tag{3.66}$$

$$M = \frac{\partial I_{\mathrm{C}}}{\partial I_{\mathrm{C}p}} \tag{3.67}$$

where γ is the emitter efficiency, α_T is the base transport factor and M is the collector multiplication factor. Considering the equation (3.59) the efficiency is equal to:

$$\gamma = \frac{\partial I_{\mathrm{E}p}}{\partial I_{\mathrm{E}}} = 1 - \frac{\partial I_{\mathrm{E}n}}{\partial I_{\mathrm{E}}} \simeq 1 \tag{3.68}$$

i.e. $\gamma \simeq 1$, because the $I_{\mathrm{E}n}$ current is generally very low compared to the total I_{E} current because the E region is heavily doped. Considering the (3.60), the collector multiplication factor is equal to:

$$M = \frac{\partial I_{\mathrm{C}}}{\partial I_{\mathrm{C}p}} = 1 + \frac{\partial I_{\mathrm{C}n}}{\partial I_{\mathrm{C}}} \simeq 1 \tag{3.69}$$

i.e. $M \simeq 1$, because the leakage current $I_{\mathrm{C}n}$ is generally very low. By these considerations it is possible to say that $\alpha \simeq \alpha_T$ and the current gain (3.75) can be rewritten as:

$$\beta \simeq \frac{\alpha_T}{1 - \alpha_T} \tag{3.70}$$

As can be seen from equation (3.66), the base transport factor gives a measure of the minority carriers which are able to reach the collector region. It is possible to demonstrate [61] that this quantity may be approximated by the expression:

$$\alpha_T \simeq 1 - \frac{\tau_{tr}}{\tau_p} \tag{3.71}$$

where τ_{tr} is the minority carriers transit time across the base and τ_p is the minority carrier lifetime in the base (holes if the base is of n-type). If the depth of the quasi-neutral base region is much smaller than the diffusion length of the minority carriers inside the base, then the transit time will be much smaller than the minority carrier life so that $\tau_{tr}/\tau_p \ll 1$. Inserting the (3.71) expression in the (3.70) relation, the current gain becomes:

$$\beta \simeq \frac{\tau_p}{\tau_{tr}} - 1 \simeq \frac{\tau_p}{\tau_{tr}} \tag{3.72}$$

which is valid for a non-irradiated bipolar transistor. The minority carriers transit time across the base is the major component of the emitter to collector delay time τ_d so that $\tau_d \simeq \tau_{tr}$. In addition the delay time is related to the cutoff frequency f_T by the relation:

$$f_T = \frac{1}{2\pi\tau_d} \simeq \frac{1}{2\pi\tau_{tr}}. \tag{3.73}$$

The cutoff frequency is the frequency at which the bipolar transistor current gain is equal to unity. By this last approximation (3.73) the minority carriers transit time can be quantified by $\tau_{tr} \simeq 1/2\pi f_T$, and so the current gain can be written as:

$$\beta \simeq 2\pi f_T \tau_p = \omega_T \tau_p \tag{3.74}$$

where ω_T is the angular cutoff frequency which is supposed not to vary with irradiation. If, after irradiation, the transistor still retains a significant current gain ($\beta' > 3$) it is possible to write the variation of the reciprocal current gain as:

$$\Delta\left(\frac{1}{\beta}\right) \equiv \frac{1}{\beta'} - \frac{1}{\beta} \simeq \frac{1}{\omega_T \tau'_p} - \frac{1}{\omega_T \tau_p} = \frac{1}{\omega_T}\Delta\left(\frac{1}{\tau_p}\right) \tag{3.75}$$

The variation of the reciprocal minority carrier lifetime was derived in the relation (3.55) which can be substituted in the equation (3.75) to obtain the Messenger-Spratt equation:

$$\Delta\left(\frac{1}{\beta}\right) = \frac{\phi}{\omega_T K} \tag{3.76}$$

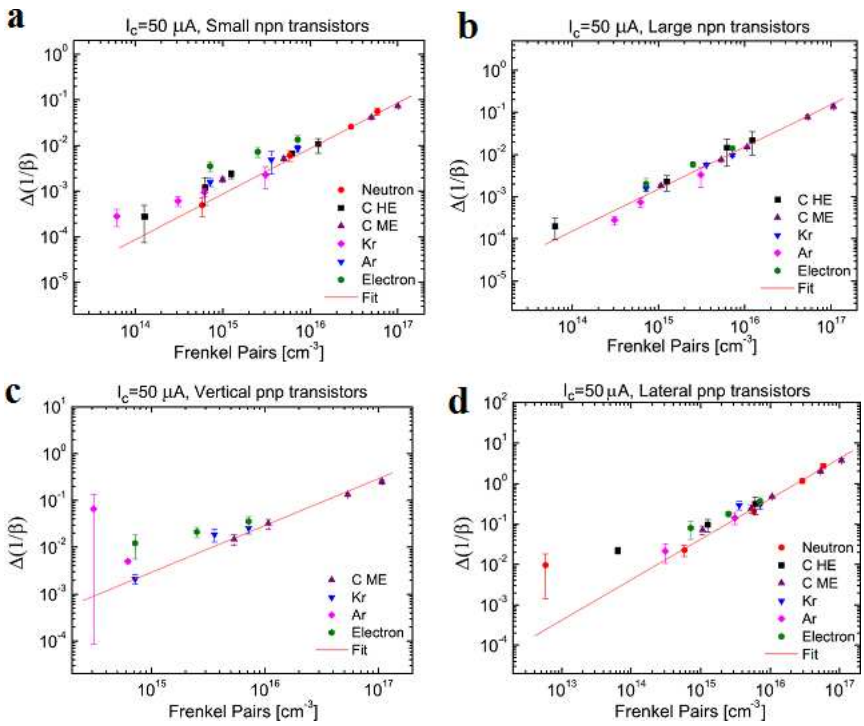

Figure 3.12: Linear dependence of the quantity $\Delta(1/\beta)$ as a function of FP concentration for different type of bipolar transistors (**a**) small emitter area *npn* type; (**b**) large emitter area *npn* type; (**c**) vertical *pnp* type; (**d**) lateral *pnp* type. All measurements are performed with a constant current $I_C = 50$ μA [76].

where K is the lifetime damage coefficient. To get a relation independent on the incoming particle type, it is convenient to use the (3.58) relation between the difference of the reciprocal minority carrier lifetime and the FP concentration. This leads to the modified Messenger-Spratt equation:

$$\Delta\left(\frac{1}{\beta}\right) = \frac{\lambda}{\omega_T} FP \tag{3.77}$$

This linear dependence on the FP concentration was experimentally observed [63] and data are reported in figure 3.12 for different kind of incident particles. The linearity does not depend on the incident particle type and starts for a FP concentration of about 10^{15} cm^{-3} which corresponds to a NIEL dose of $\sim$5 Gy.

The proportionality constant is equal to:

$$k(I_C) = \frac{\lambda}{\omega_T} \tag{3.78}$$

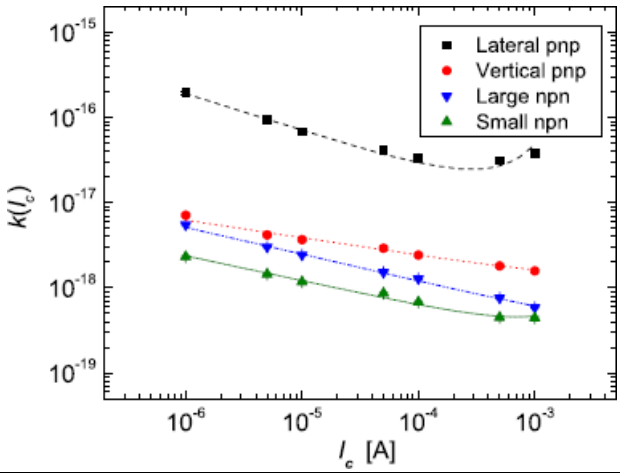

Type of transistor	a	b	n
npn 50 µm × 50 µm	5.91×10^{-22}	9.0×10^{-3}	−0.32
npn 5 µm × 5 µm	5.24×10^{-23}	1.3×10^{-3}	−0.30
pnp lateral	1.74×10^{-22}	3.7×10^{-4}	−0.43
pnp vertical	2.17×10^{-21}	6.0×10^{-3}	−0.21

Figure 3.13: Top: Dependence of the parameter $k(I_C)$ on the collector current, I_C, for large and small emitter area region *npn* transistors; same parameter for vertical and lateral *pnp* transistors. Bottom: fitting coefficient of equation (3.79) [63].

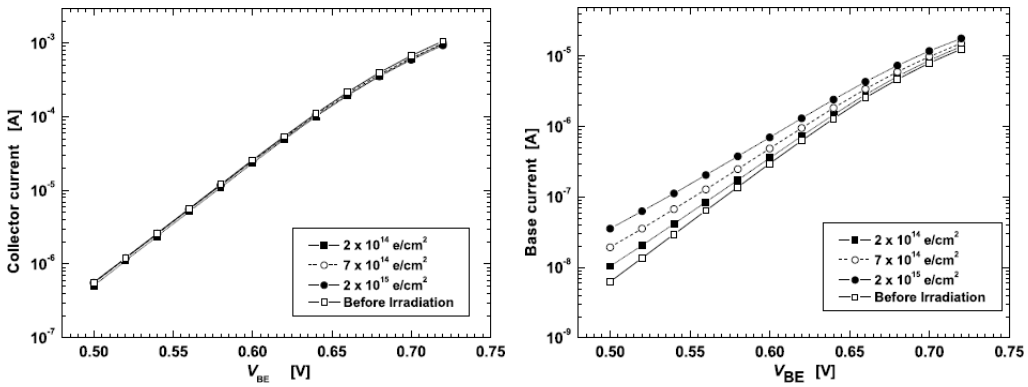

Figure 3.14: (Right) Collector current, I_C and (left) base current, I_B. Dependence on V_{BE} at 25 °C. The data are for *npn* transistor with large emitter area region of 50 μm × 50 μm before and after the irradiation with electrons [63].

and it depends on the collector current I_C, on the emitter area (small or large) and on the transistor type (*npn* or *pnp*). A semi-empirical relation is

also given [63]:

$$k(I_C) = \frac{a[\exp(I_C/b) - 1]}{I_C^{(1-n)}} \tag{3.79}$$

which, for low currents $I_C < 100$ μA, reduces to:

$$k(I_C) = \frac{a}{b} I_C^n \tag{3.80}$$

Fitting curves and coefficient values are reported in figure 3.13 for different kind of bipolar transistors. In the same work, the behavior of I_C and I_B currents were investigated and results are reported in figure 3.14 as a function of the B-E voltage for transistors of large emitter area irradiated with electrons. While the I_C current is only sightly affected by the irradiation, the I_B one exhibits large variations after irradiation.

Chapter 4

GEANT4-Based Development for NIEL and NIEL-Dose Calculation

In this chapter an improved implementation of the GEANT4 single scattering process will be described [64]. This modification enables one to correctly simulate the Coulomb NIEL fraction for all nuclei of the GCRs spectrum. Simulations were performed in the energy range from 20 MeV/nucleon up to 10 GeV/nucleon and the results were compared with a computational integration of the NIEL which makes use of the relativistic differential cross sections reported in section 2.4. In order to have the NIEL value for the entire energy range of the space environment, a computational integration was performed also at low energies where screening effects are important.

In addition, to simulate the GCRs fluxes by the GEANT4 toolkit, the ISO 15390 model was introduced as a particle generator in GEANT4. Knowing the GCRs ISO fluxes and the NIEL values enables us to calculate the NIEL-Dose absorbed by a silicon sample during both solar maximum and solar minimum periods.

4.1 Non-Relativistic ZBL NIEL Calculation

We performed the calculation of the ZBL NIEL by the use of the ROOT program. The NIEL calculated by the ZBL universal stopping power, as reported in section 2.3.2, is the reference value in the non-relativistic regime and when potential screening effects are important. We performed the same work as Messenger et al. [50] (see section 3.2.3 and figure 3.6). The NIEL is

obtained by the integration of:

$$NIEL(E)\big|_{ZBL} = N \int_{T_d}^{T_{max}} TL(T) \frac{d\sigma(T,E)}{dT}\Big|_{ZBL} dT. \tag{4.1}$$

where E is the kinetic energy of the incoming particle, T is the one of the recoiling target, N is the target atom density, $L(L)$ is the damage efficiency or Lindhard correction, given by equation (3.18)

$$L(T) = \frac{\nu(T)}{T} \tag{4.2}$$

where $\nu(T)$ is given by the equation (3.12):

$$\nu(T) = \frac{T}{1 + k_d g(\epsilon_d)}$$

and the related coefficients are given by the equations (3.13), (3.14) and (3.15):

$$\begin{aligned} k_d &= 0.1334 Z^{2/3} m_2^{-1/2} \\ g(\epsilon_d) &= \epsilon_d + 0.40244 \epsilon_d^{3/4} + 3.4008 \epsilon_d^{1/6} \\ \epsilon_d &= 0.01014 Z_2^{-7/2} T \end{aligned}$$

where Z_2 is the atomic number of the target. The lower limit of integration was set as $T_d = 21$ eV, while T_{max} is the non-relativistic maximum energy that can be transferred during a single collision whose expression is given by equation (2.29)

$$T_{max} = \frac{4 m_1 m_2}{(m_1 + m_2)^2} E.$$

where m_1 and m_2 are the projectile and target rest masses respectively. For the integration of the equation (4.1), the ZBL differential cross section, given by (2.99), was used, i.e.

$$\frac{d\sigma(T,E)}{dT}\Big|_{ZBL} dT = -\frac{\pi a_U^2}{2} \frac{f(t^{\frac{1}{2}})}{t^{\frac{3}{2}}} dt \tag{4.3}$$

which is obtained by the screened Coulomb potential with the universal screening function $\chi(x)_U$ given by (2.97); a_U is the universal screening length given by (2.98). The function $f(t^{\frac{1}{2}})$ is given by equation (2.102):

$$f(t^{\frac{1}{2}}) = \lambda t^{\frac{1}{2}-m} [1 + (2\lambda t^{1-m})^q]^{-\frac{1}{q}}$$

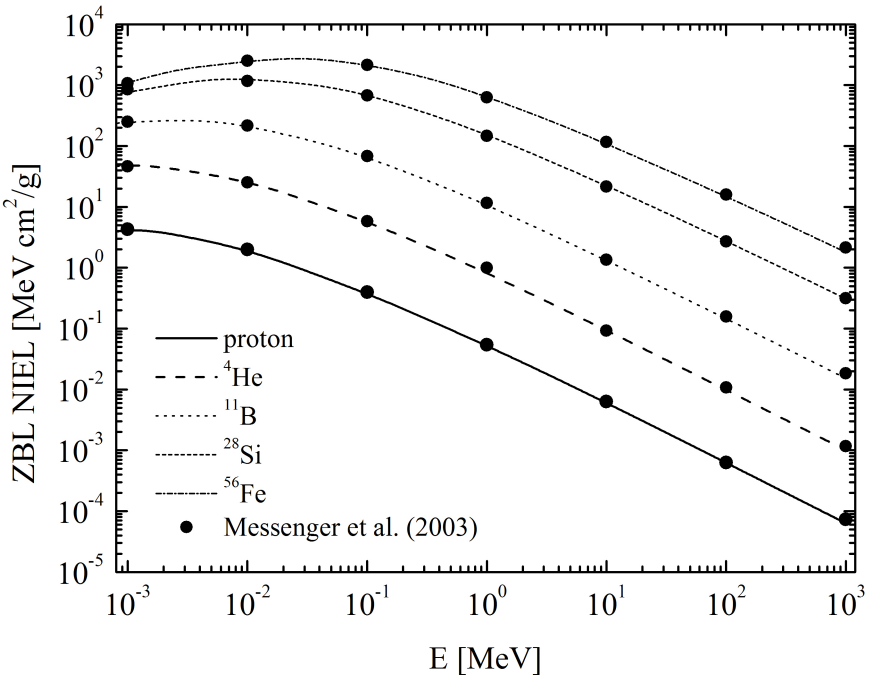

Figure 4.1: ZBL NIEL values for different incoming nuclei in a silicon material. The curves are obtained by the integration of the equation (4.1) while the dots are taken from [50].

where t is the dimensionless parameter given by equation (2.100):

$$t = \epsilon^2 \frac{T}{T_{max}} \tag{4.4}$$

and ϵ is the ZBL reduce energy given by (2.101)

$$\epsilon = \frac{a_U}{Z_1 Z_2 e^2} \left(\frac{m_2}{m_1 + m_2} \right) E \tag{4.5}$$

where Z_1 and Z_2 are the atomic numbers of projectile and target respectively. The results of the NIEL computation for different incoming nuclei in a silicon material, are reported in figure 4.1. The energy range of the incident particles was set from 1 keV up to 1 GeV. The NIEL values obtained by this work are in good agreement with those performed by Messenger at al. [50] which are also reported in the same figure.

4.2 Relativistic NIEL Calculation

We performed the NIEL integral by the use of the two relativistic differential cross sections given in section 2.4 in order to extend the Coulomb NIEL fraction to higher energies which are necessary for GCRs. Also in this case the NIEL is computed by

$$NIEL(E)\big|_{rel} = N \int_{T_d}^{T_{max}} TL(T) \frac{d\sigma(T,E)}{dT}\Big|_{rel} dT \tag{4.6}$$

where as already said, N is the target atom density and $L(T)$ is the Lindhard correction term. The integral was performed from $T_d = 21$ eV up to the maximum energy that can be transferred during a single collision T_{max} whose relativistic expression is given by equation (2.64):

$$T_{max} = \frac{2E(E + 2m_1c^2)}{\left(1 + \frac{m_1}{m_2}\right)^2 m_2c^2 + 2E}$$

where E is the kinetic energy of the incoming particle in the laboratory frame of reference.

The first differential cross section is the one proposed by Starusziewicz and Zalewski (SZ), which is equal to the (2.115)

$$\frac{d\sigma(T,E)}{dT}\Big|_{SZ} = \pi \left(\frac{Z_1 Z_2 e^2}{\mu_r c^2 \beta_r^2 \gamma_r} \right)^2 \frac{T_{max}}{T^2} \tag{4.7}$$

where μ_r is the relativistic reduced mass that was defined in equation (2.67); the effective particle velocity β_r can be computed by the use of the relation (2.36) :

$$\frac{1}{\beta_r^2} = 1 + \left(\frac{\mu_r c^2}{p_r c} \right)^2 \tag{4.8}$$

where as already said, the relative momentum $\mathbf{p}_r$ is equal to the momentum of the incoming particle calculated in the CM system (see equation (2.70)).

In figure 4.2 are reported the ZBL NIEL values from 1 keV/nucleon up to 1 GeV/nucl and the ones obtained by the relativistic differential cross section SZ calculated in the range 20 MeV/nucl-10 GeV/nucl. Different incoming nuclei are reported. At 20 MeV/nucleon, for light nuclei as protons and alpha particles, the variation between these two curves is of few %, for medium nuclei, as ^{27}Al, it is about 19% and it is slightly larger than that for heavy nuclei. However at 1 GeV/nucelon, which is the upper limit of the TRIM simulation program [98], for all nuclei the non-relativistic ZBL

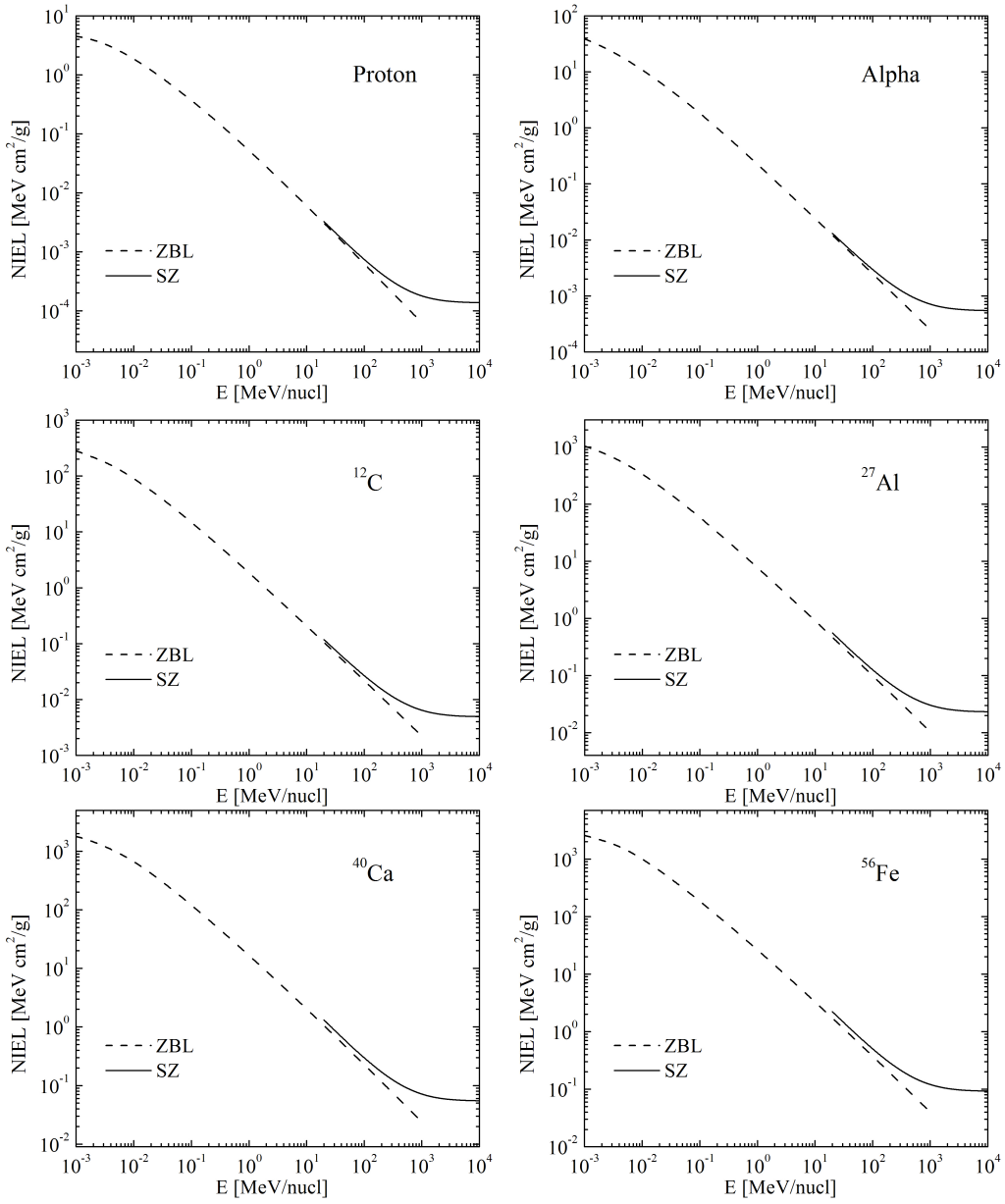

Figure 4.2: ZBL NIEL values from 1 keV/nucl up 1GeV/nucl (dashed lines) and NIEL values from 20 MeV/nucl to 10 GeV/nucl (solid lines) computed with the relativistic differential cross section (4.7).

treatment gives a NIEL value which is about a factor of 3 lower than the one obtained with the relativistic treatment.

Another relativistic differential cross section is given by Seitz (see equa-

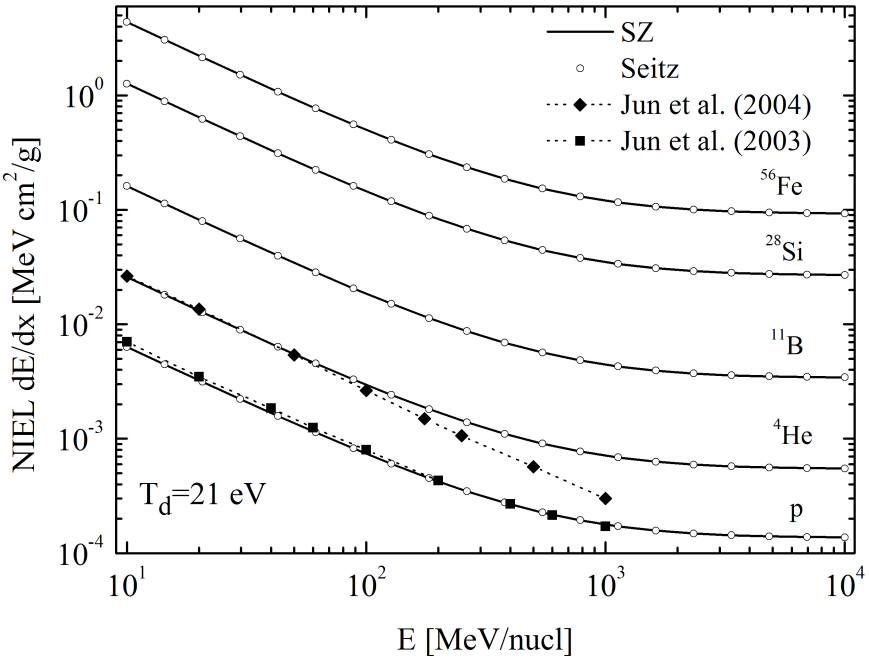

Figure 4.3: Coulomb NIEL value results from the computational integration of equation 4.6. Solid lines are obtained by the use of the relativistic differential cross section of equation (4.7) while circles are with the equation (4.9) (Jun et al. (2004) [36] and Jun et al. (2003) [34]).

tion (2.110)). To extend the use of this cross section for heavy nuclei, it was re-written with the introduction of the relativistic reduced mass, as:

$$\frac{d\sigma(T,E)}{dT}\Big|_{Seitz} = \pi\left(\frac{Z_1 Z_2 e^2}{\mu_r c^2\ \beta_r^2\gamma_r}\right)^2 \frac{T_{max}}{T^2} F(T,E) \tag{4.9}$$

where the $F(T,E)$ term is given by:

$$F(T,E) = 1 - \beta_r^2 \frac{T}{T_{max}} + Z_2\alpha\beta_r\pi\sqrt{\frac{T}{T_{max}}}\left(1-\sqrt{\frac{T}{T_{max}}}\right) \tag{4.10}$$

This differential cross section was already used by Jun et al. [35] [34] to treat the relativistic Coulomb interactions of protons in silicon. In this case $m_1 \ll m_2$, as a consequence μ_r reduces to the proton rest mass and β_r to the speed of the incoming proton in the CM reference system (see equations (2.73) and (2.74)).

The NIEL values obtained with these two relativistic differential cross sections (SZ and *Seits*) are reported in figure 4.3 for some nuclei in a silicon

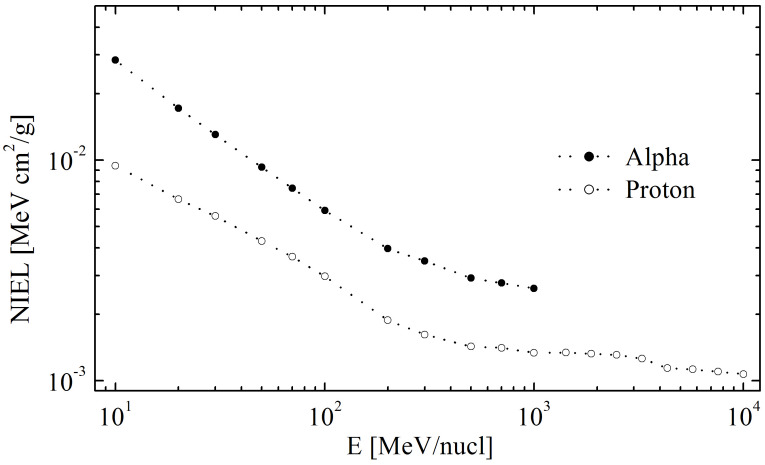

Figure 4.4: Total (Coulomb plus nuclear) NIEL for protons and alpha particles (for details se text in section (4.3)). Dotted lines are to guide the eye.

material. In this figure E ranges from 10 MeV/nucleon to 10 GeV/nucleon. In the same figure the Jun et al. Coulomb NIEL values for protons [34] and alpha particles [36] are also reported. The agreement with the Jun's protons values is good and our results are also analogous to the alpha ones in the lower energy part of the plot. We remember that the Jun's et al. alpha Coulomb NIEL values were obtained by the non-relativistic ZBL treatment. From this figure it is possible to see that relativistic corrections are necessary for energies greater than about 70 MeV/nucleon.

In addition form this analysis emerges that the two differential cross sections, given by (4.7) and (4.9), are almost equal i.e.

$$\frac{d\sigma(T,E)}{dT}\Big|_{Seitz} \simeq \frac{d\sigma(T,E)}{dT}\Big|_{SZ}. \tag{4.11}$$

This means that $F(T,E) \simeq 1$ for all energies E and for all incoming nuclei. Since the tow cross sections give the same results, from here on only the SZ (4.7) will be considered.

4.3 Total NIEL for Protons and Alpha Particles

In previous sections only the Coulomb NIEL fraction was considered. However, for protons and alpha particles it is necessary to include also the nuclear NIEL fraction due to hadronic interactions.

For protons, in figure 4.4, are reported the Jun's el al. [34] values form 10 MeV up to 1 GeV and the Huhtinen's [57] ones from greater energies. For alpha particles, in the same figure, the total NIEL is given by the sum of the nuclear NIEL fraction taken from Jun et al. [36] and the Coulomb NIEL fraction obtained by our relativistic calculation.

4.4 GEANT4 Simulation Toolkit

GEANT4 is a simulation program which reproduces the interaction of elementary particles with matter. It was projected to simulate experiments in particle physics, nuclear physics, for accelerator design and for space application, which is the field of our interest.
GEANT4 is an object-oriented program, written in C++ language, which enables the user to chose between a vast set of models for the same physical process. In addition the user has the possibility to understand all the *classes* in the source code, to personalize her/his own program and to suggest new implementations with a debug working, as we have done [64].

Inside the program it is possible to construct the desired three-dimensional geometry, to define the material of the device under test and to simulate the environment of interest. All set of known particles may be generated in the energy range from eV to TeV. During the simulation, the particles are transported inside the *world*[1] and all physical processes are contemporaneously active. Each process proposes a *step* length which depends on the cross section of the specific interaction. Each step is continuously updated during the simulation and the one chosen by the Monte Carlo program is always the smallest of the proposed ones. In this way, processes of different probabilities may be simulated all in a time.

Each simulated particle, with all its physical processes, constitutes an *event*. A set of events -i.e. a specific number of incident particles of given energies - is called a *run*. During the *run*, primary particles may produce secondary ones - i.e. δ-rays or PKAs - by the interaction with matter. The user has the possibility to *stop-and-kill* secondary particles or to generate them according to a specific threshold energy T_d. The stopping power of a charged particle is divided in two parts:

$$-\frac{dE}{dx} = \int_0^{T_d} T \frac{d\sigma(T,E)}{dT} dT + \int_{T_d}^{T_{max}} T \frac{d\sigma(T,E)}{dT} dT \qquad (4.12)$$

[1] In GEANT4 it is possible to construct the space where all the interactions take place, i.e. the *world*, both as a box or as a sphere.

where the first term is the *continuous* energy loss which goes form zero to the T_d value and it is considered deposited inside the material while the second term is the *discrete* energy loss which goes from T_d to the maximum energy that can be transferred during a single collision and it is spent for secondary particles production.

In addition there is the possibility for the user to activate an option which allows the production of secondary particles even if they have kinetic energies under threshold. This is very important when secondary particles are produced near the material boundary and have sufficient energy to escape from the material. In this way the energy lost by the incident particle is differentiated from the one deposited inside the material and the secondary particle may be transported for longer distances if the material is immerse in a thin medium.

4.4.1 GEANT4 Single Scattering Process

The single elastic scattering process, already existing in the GEANT4 code, was developed to simulate the Coulomb scattering process of incident muons and hadrons with target atoms of the material [70]. It is an alternative to the multiple scattering process which gives information only on the scattering angular deviation but not on the energy loss of the incident particle. The single scattering, instead, simulates every single interaction and it has the advantage to give information about the energy transferred to the target atom T, which is of fundamental importance for the NIEL calculation. However this has the disadvantage to significantly increase the number of steps which corresponds to pure CPU[2] performances.

The basic theory of this scattering process is based on the Wentzel's model [71] which is suitable for light particles ($m_1 \ll m_2$) of charge $Z_1 e$ incident on atomic nuclei of charge $Z_2 e$. The potential of the model is equal to:

$$V(r) = \frac{Z_1 Z_2 e^2}{r} \exp\left(-r/a_{TF}\right) \tag{4.13}$$

which is a simplified version of a screening potential with screening length a_{TF} given by the Thomas-Fermi expression:

$$a_{TF} = \frac{0.885 a_0}{Z_2^{1/3}} \tag{4.14}$$

where a_0 is the Bohr radius. By the use of this potential, the differential

[2]Central Processing Unit

scattering cross section is given by:

$$\left.\frac{d\sigma(\theta)}{d\Omega}\right|_W = \left(\frac{Z_1 Z_2 e^2}{pc\ \beta}\right)^2 \frac{1}{(2A_s + 1 - \cos\theta)^2} \tag{4.15}$$

where p and β are the momentum and the velocity of the incident particle, calculated in the CM system, while A_s is the screening parameter taken from the Molier's and Bethe's work [72]:

$$A_s = \left(\frac{\hbar}{2p\ a_{TF}}\right)^2 \left[1.13 + 3.767\left(\frac{\alpha Z_2}{\beta}\right)^2\right]. \tag{4.16}$$

It has to be observed that at relativistic energies the screening term A_s has negligible effects and this differential cross section reduces to the SZ one as can be seen when this latter is expressed in the form given by the equation (2.114). The differential scattering cross section of the GEANT4 code is obtained by the Wentzel's cross section (4.15) multiplied by a form factor taken from Butkevick [73]:

$$\left.\frac{d\sigma(\theta)}{d\Omega}\right|_{G4} = \left.\frac{d\sigma(\theta)}{d\Omega}\right|_W \left(\frac{1}{(1 + (qR_N)^2/12)^2} + \frac{1}{Z_2}\right) \tag{4.17}$$

where q is the momentum transferred to the target nucleus and R_N is the target nucleus size. The first term of the form factor takes into account nuclear size effects and dominates at high energies while the second term takes into account the atomic effects of the scattering off electrons and it is important at lower energies.

This differential cross section gives satisfactory results for muons incident on a 1.5 mm aluminium foil as can by seen from figure 4.5 where the probability of the GEANT4 single scattering model is compared to the GEANT4 multiple scattering one and to experimental data.

4.4.2 Simulation Test of the GEANT4 Single Scattering Process

The single scattering model was tested with different nuclei incident on a silicon target material[3]. The original GENAT4 single scattering process was programmed to give secondary particles only for transferred kinetic energies greater than a threshold value (for silicon material it was equal to 2.24 keV). In origin this threshold value was calculated by the product of the mean

[3]The geant4.9.1.p03 version was used.

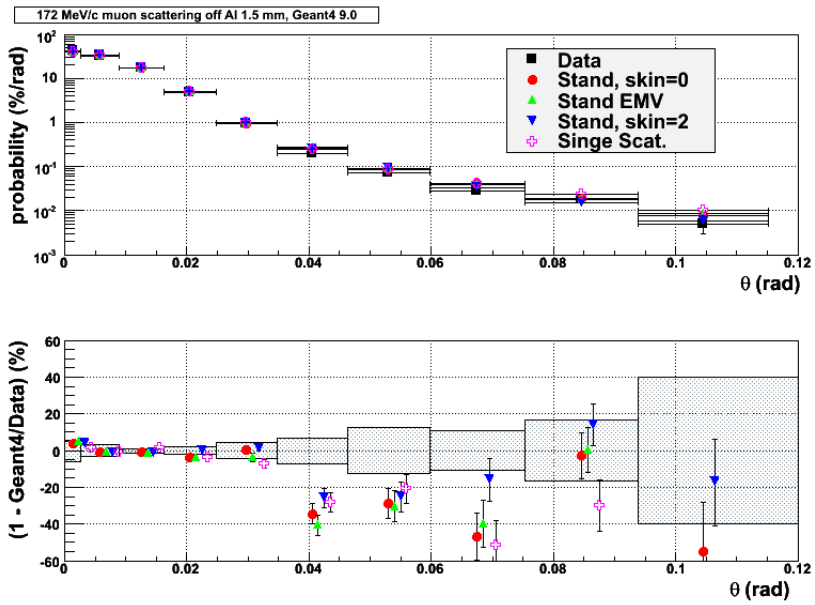

Figure 4.5: Picture taken from [70]. Scattering of 172 MeV/c muons in 1.5 mm Aluminium foil. Data values [74] are black squares. Colored markers corresponds to different options of multiple scattering (Stand) and single scattering (Single Scat.). The bottom graphic represents the relative difference between GEANT4 simulation results and data values in percent; dashed areas are one standard deviation from data.

excitation energy of the material (174 eV for silicon) times the atomic number Z_2. With the GEANT4 team authorization, this part of the code was modified in order to have secondary particles of a desired threshold energy. For our present test, this value was set equal to $T_d = 0.5$ eV in order to check the lower part of the recoiling spectrum. The device under test was a squared of silicon (1×1) cm^2. The thickness of the target was fixed according to the type and energy of the incident particle in order to have approximatively 20% probability to have one interaction.

The expected probability to have an interaction, as a function of the kinetic energy transferred to the target atom, was calculated by:

$$p(T) = x \frac{N_A \rho}{A_2} \int_{T_d}^{T} \left. \frac{d\sigma}{dT'} \right|_{Ruth} dT' \tag{4.18}$$

where x is the target thickness, N_A is the Avogadro's constant, ρ is the target density and A_2 is the target atomic mass number. To simplify the problem, the energies of the incident particles were chosen in the non-relativistic range in order to use the Rutherford's differential cross section (2.94). By solving

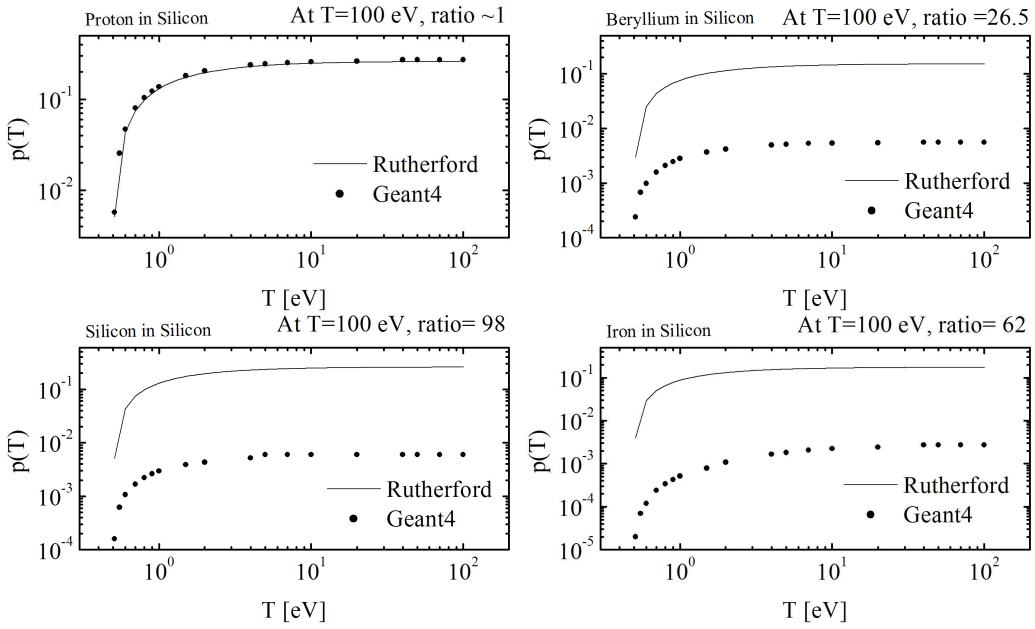

Figure 4.6: Probability of interaction as a function of the kinetic energy transferred to the target atom. Comparison of the GEANT4 simulation with the Classical Rutherford value calculated by equation (4.19).

the integral (4.18), for a silicon target, the following relation is obtained:

$$p(T) = 48.1 \frac{Z_1^2}{\beta^2} \frac{(T - T_d)}{T T_d} x \tag{4.19}$$

During the simulation, secondary silicon particles (PKAs) were stored and their total number, as a function of T, were calculated and compared to the analytical value (4.19). Different projectiles were considered and the results for some nuclei (protons 100 MeV , ^{9}Be 1 GeV, ^{28}Si 1 GeV, ^{56}Fe 1 GeV) are plotted in figure 4.6. Protons values were in good agreement with the expected ones, but the heavier nuclei had probabilities underestimated.

A value of $T = 100$ eV was fixed, where the curves are saturated, and the ratios between theory and simulation were calculated. Result are reported in the same figure. As can be seen from these results the differential cross section (4.17) was suitable for light particles but not for heavy nuclei. Since we are interested in the scattering process involving heavy nuclei, particular attention was given to solve this problem.

4.4.3 Improved Implementation of the GEANT4 Single Scattering Process

The original GEANT4 differential cross section (4.17) may be written in a more compacted form as:

$$\left.\frac{d\sigma(\theta)}{d\Omega}\right|_{G4} = \left(\frac{Z_1 Z_2 e^2}{p_{1CM} c \beta_{1CM}}\right)^2 F(\theta, q) \tag{4.20}$$

where it has been underlined that the momentum is calculated in the center of mass system (CM). The velocity of the incident particle in the CM system β_{1CM} is obtained by

$$\frac{1}{\beta_{1CM}^2} = 1 + \left(\frac{m_1 c^2}{p_{1CM} c}\right)^2 \tag{4.21}$$

The function $F(\theta, q)$ contains all terms related to the scattering angle, to the form factor and to the screening effects. Since $c p_{1CM} = m_1 c^2 \beta_{1CM} \gamma_{1CM}$, the GEANT4 cross section (4.20) can be also written as:

$$\left.\frac{d\sigma(\theta)}{d\Omega}\right|_{G4} = \left(\frac{Z_1 Z_2 e^2}{m_1 c^2 \ \beta_{1CM}^2 \gamma_{1CM}}\right)^2 F(\theta, q) \tag{4.22}$$

As previously said, this differential cross section works well when the mass of the incoming particle, m_1 is much smaller than the target one m_2. This means that this differential cross section is suitable when the target particle can be considered at rest during the scattering interaction. If the mass of the incoming particle is no longer negligible compared to the mass of target atom, then the introduction of the reduce mass is necessary as already said in section 2.1.2. The differential cross section has to be calculated in the relative frame of reference where instead of two particles we have one effective particle of reduced mass μ_r given by equation (2.67). The scattering angle of the effective particle is equal to the one of the incoming particle calculated in the CM system (see equation (2.71)) and, as a consequence, the angular part of the differential cross section, contained in the function $F(\theta, q)$, doesn't change. The screening term A_s, given by equation (4.16), contains the particle momentum and velocity and so it becomes:

$$A_s = \left(\frac{\hbar}{2 p_r \ a_{TF}}\right)^2 \left[1.13 + 3.767 \left(\frac{\alpha Z_2}{\beta_r}\right)^2\right] \tag{4.23}$$

where p_r is the modulus of the relative momentum and β_r is the relative velocity (see equations (2.66) and (4.8)). In addition the relative momentum

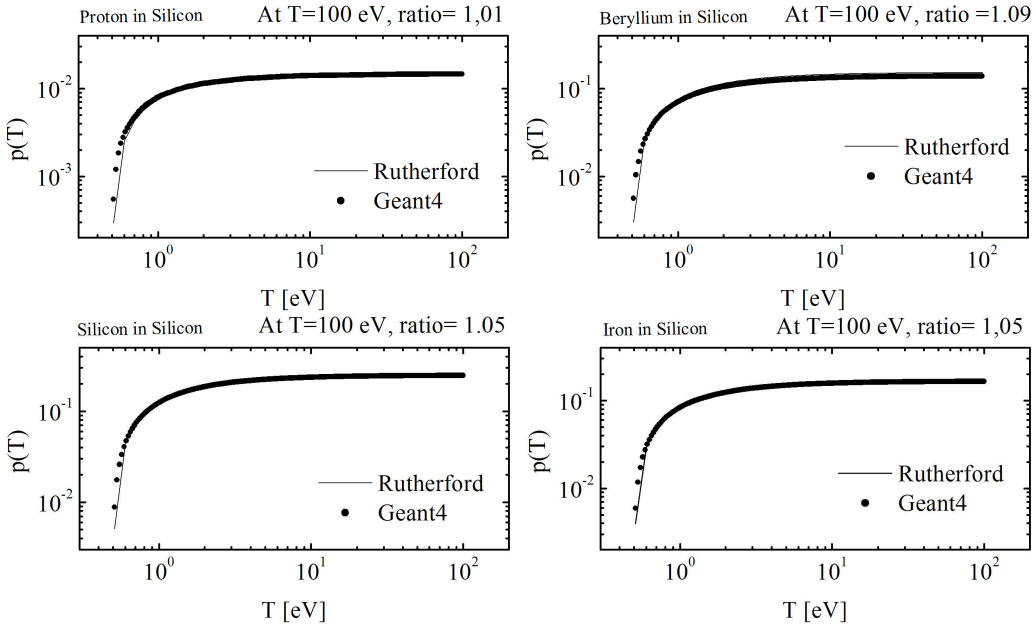

Figure 4.7: Same as figure 4.6 after the introduction of the reduced mass μ_r as explained in section 4.4.3

is equal to the one of the incoming particle in the CM system as it was underlined in equation (2.70). By these considerations the differential cross section for the Coulomb scattering becomes:

$$\frac{d\sigma(\theta)}{d\Omega} = \left(\frac{Z_1 Z_2 e^2}{\mu_r c^2 \ \beta_r^2 \gamma_r} \right)^2 F(\theta, q) \tag{4.24}$$

where β_r is calculated by the (4.8).

To test this cross section, we modified the code and performed the same simulation as previously done. New results are presented in figure 4.7 for the same particles of figure 4.6. Scattering probabilities are in good agrement with the expected values (equation (4.19)) with a ratio theoretical-simulation of about 1 for all incoming particles. This modification gives us the correct number of recoiled targets, that is the number of primary knock-on atoms (PKAs).

4.4.4 Simulation Results of the Upgraded GEANT4 Coulomb NIEL Fraction

With the GEANT4 modified differential cross section (4.24) it was possible to perform the simulation of the Coulomb NIEL fraction for all nuclei (numerical values are listed in appendix A). The mean NIEL value within a *run* is computed by:

$$NIEL(E)_{G4} = \left(\frac{\sum_{ij} T_{ij} L(T_{ij})}{N_{events}} \right) \frac{1}{\langle \Delta x \rangle \rho} \quad [\text{MeV cm}^2/\text{g}] \tag{4.25}$$

where E is the kinetic energy of the incident particle, N_{events} is the total number of *events* (the number of incident particles was usually set equal to 10^5), T_{ij} is the kinetic energy of the i-th PKA generated by the j-th primary particle, $L(T_{ij})$ is the damage efficiency (as usual computed by the (4.2)); the sum is performed over both the total number of PKAs (index i) and the total number of *events* (index j); $\rho = 2.33$ g/cm^3 is the silicon density; $\langle \Delta x \rangle$ is the mean material thickness crossed by the primary particles i.e.:

$$\langle \Delta x \rangle = \frac{\sum_j \Delta x_j}{N_{events}} \tag{4.26}$$

where Δx_j is the one crossed by the j-th particle. The term in brackets of the (4.25) is the mean energy loss which goes into displacement processes i.e.:

$$\langle \Delta E \rangle|_{displ} = \frac{\sum_{ij} T_{ij} L(T_{ij})}{N_{events}} = \frac{\sum_j \Delta E_j|_{displ}}{N_{events}} \tag{4.27}$$

where $\Delta E_j|_{displ}$ is the one lost by the j-th particle i.e.

$$\Delta E_j|_{disp} = \sum_i T_{ij} L(T_{ij}) \tag{4.28}$$

By this considerations the equation (4.25) assumes a more familiar form:

$$NIEL(E)_{G4} = \frac{1}{\rho} \frac{\langle \Delta E \rangle|_{displ}}{\langle \Delta x \rangle} \tag{4.29}$$

In order to have the NIEL value for a specific kinetic energy E, the thickness Δx_j of the *j-event* is fixed by the condition:

$$\frac{\Delta E_j|_{tot}}{E} \simeq 10^{-3} \tag{4.30}$$

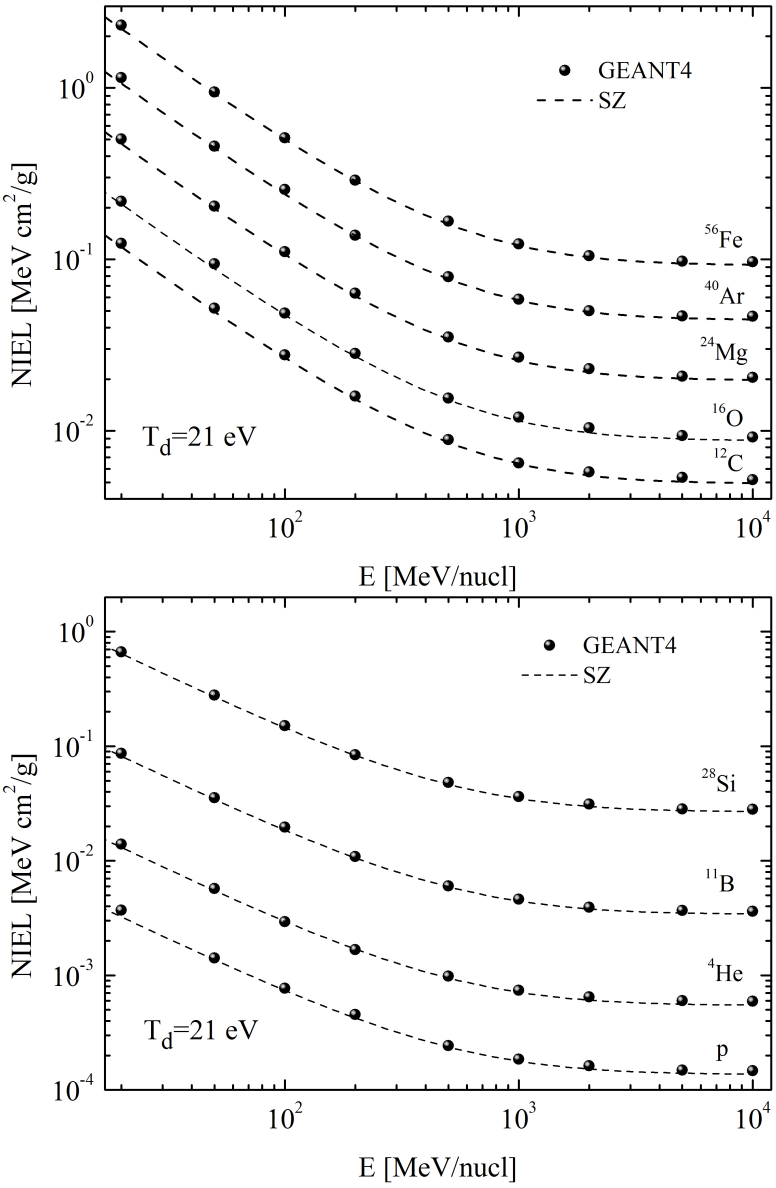

Figure 4.8: GEANT4 upgraded simulation results of the Coulomb NIEL fraction for different incoming particles on a silicon target in comparison with the computational integration performed by the use of the SZ differential cross section (4.7).

where $\Delta E_j|_{tot}$ is the total energy lost[4] by the j-th particle after a thickness Δx_j and E is its initial kinetic energy. When the condition (4.30) is fulfilled the incident particle is *stopped-and-killed* and the related Δx_j value is got.

[4]Most of all by electronic collision processes.

In this way the incident particle loses only the 0.1% of its kinetic energy[5] (i.e. E is almost constant). During the simulation only PKAs of energies greater than the threshold value for displacement, which was fixed at $T_d = 21$ eV, were generated.

Results of the simulation, for different incoming nuclei, are reported in figure 4.8. In the same figure the NIEL values obtained by the computational integration of the (4.6) by the use of the SZ differential cross section (4.7) are also reported. The agreement of these two methods is good.

4.4.5 The ISO 15390 Model as a Primary Generator in GEANT4

We developed a code, written in C++ language, based on the ISO 15390 model which, as already said in section 1.2.2, is the standard for estimating the radiation damage on electrical devices. It is based on the Nymmik's work [16] which is aimed to give the expected fluxes of GCRs in different periods of the solar activity. The flux $\Phi_i(E,t)$ of the i-th nucleus is calculate by the equation (1.22) and it is given in units of [s m^2 sr MeV/nucl]$^{-1}$.

An example of the code output is reported in figure 4.9 for some nuclei in the energy range from 20 MeV/nucleon to 10 GeV/nucleon. For each nucleus the two curves correspond to the fluxes which are expected in two different solar periods: in the year 2010 the fluxes will reach their maximum and in the year 2013 they will be at the minimum values. The next maximum of the solar activity is expected in the year 2012 but, due to the finite velocity of propagation of the solar wind, the minimum of the fluxes is expected about one year later ($\sim$ 15 months is the delay time for the Nymmik model during maximum periods [15]).

This code was interfaced to the GEANT4 particle generator in order to have particles distributed according to the ISO fluxes. Inside the *Primary Generator Action*, which is the GEANT4 class aimed to generate particles, we wrote a code where it is necessary to fix the energy range of the spectrum, the type of particle and the year and the month of interest. The total energy range is divided into intervals, and in each interval ΔE_j, the number of particles N_j which have to be generated is calculated starting from the Nymmik's flux $\Phi_i(E_j,t)$ value calculated at the cental energy E_j of the interval as:

$$N_j(\Delta E_j) = \Phi_i(E_j,t) \times \Delta E_j \times \Delta t \times \Delta S \times 4\pi \tag{4.31}$$

[5]For low kinetic energies and light particles the value was set at 1% in order to increase the statistics of PKAs while for heavier particles, which produce a grater number of PKAs, it was decreased at 0.01% to improve the CPU performances.

where Δt is the time interval, and ΔS is the surface element. These quantities may be varied in order to increase the statistics. The total number of particle is simply given by the sum of the N_j. In order to generate particles of different energies, for each interval the kinetic energy is chosen randomly between the maximum $E_{max,j}$ and the minimum value $E_{min,j}$. The particle direction of generation is chosen randomly too.

To test this particle generator, we performed a simulation for two different solar periods and for different nuclei. A 3-D spherical world was constructed where particle were shotted in random directions as can be seen from figure 4.10. In this plot the (x, y, z) space coordinates of generation are reported.

The energy interval of the primary particles was set from 20 MeV/nucleon to 10 GeV/nucleon and at the end of the simulation, the initial kinetic energies were stored. The histogram reconstruction of the distribution of these energies is reported in figure 4.11 for protons, alpha particles, carbon and iron nuclei. As wanted the fluxes of the particles generated by GEANT4 overlap to the Nymmik's ones.

4.5 NIEL-Dose Calculation

With the ISO model and the NIEL values, it was possible to estimate the expected NIEL-Dose absorbed by a silicon sample during one year mission due to GCRs. The NIEL-Dose can be calculated by (3.22):

$$D^{NIEL} = \frac{E_{dis}}{6.24 \times 10^9 \rho} \quad [\text{Gy}] \tag{4.32}$$

where ρ is the target density (for silicon $\rho = 2.33$ g/cm^3) and the numerical constant is the conversion factor from MeV/g to J/kg which is a *Gray* (Gy). E_{dis} is the energy density deposited by the incident particle in displacement processes which is obtained by means of (3.20):

$$E_{dis} = \int_{E_{min}}^{E_{max}} NIEL(E)\ \Phi(E) dE \quad \left[\frac{\text{MeV}}{\text{cm}^3}\right] \tag{4.33}$$

In this case the NIEL is given in units of MeV/cm, $\Phi(E)$ is the spectral fluence given in 1/(MeV cm^2) with minimum and maximum kinetic energies ranging form E_{min} to E_{max}. If the NIEL is given in units of MeV cm^2/g, then the (4.33) becomes:

$$E_{dis} = \rho \int_{E_{min}}^{E_{max}} NIEL(E)\ \Phi(E) dE \tag{4.34}$$

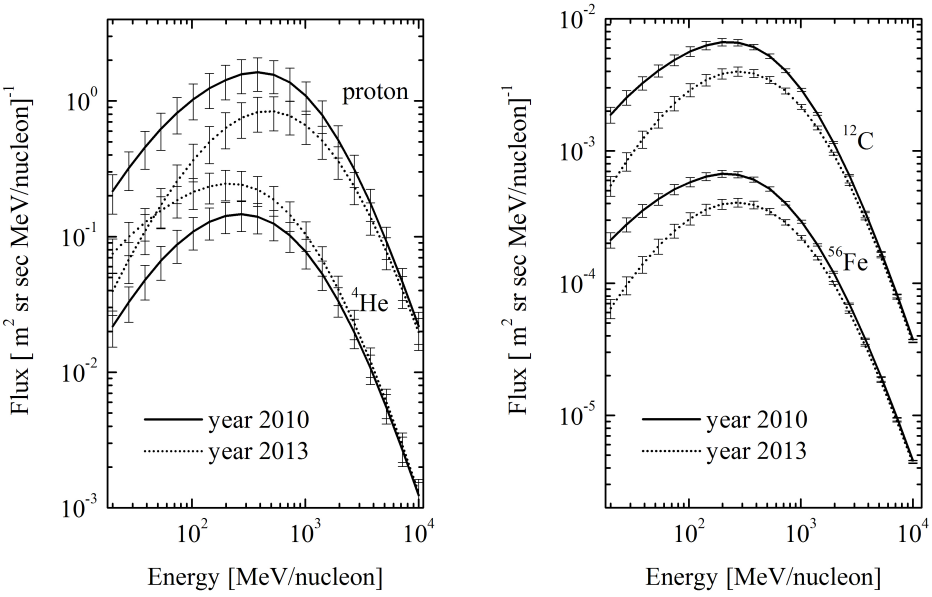

Figure 4.9: Expected GCRs fluxes -ISO model- in two different periods of the solar activity for protons, alpha particle, carbon, and iron nuclei. The curves are obtained with the code based on the Nymmik's model [16]

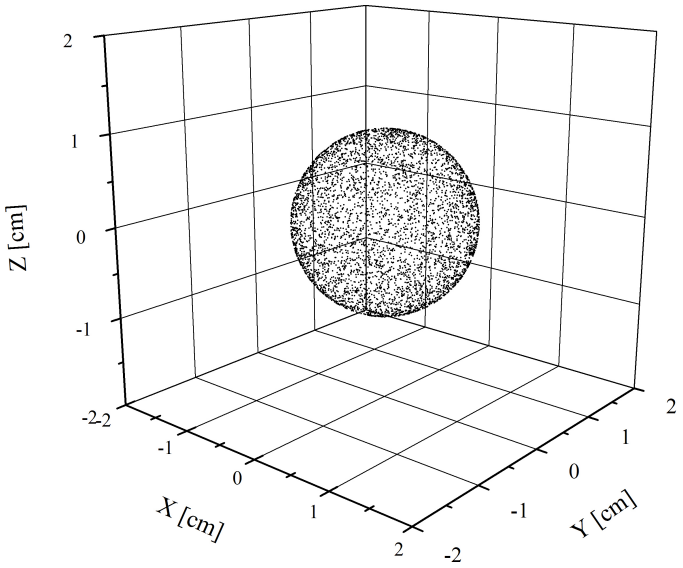

Figure 4.10: Scatter plot of the (x, y, z) space coordinates of the GEANT4 particle generator.

Substituting this latter expression of E_{dis} in the (4.32), the NIEL-Dose may be written as:

$$D^{NIEL} = \int_{E_{min}}^{E_{max}} D^{NIEL}(E)dE \tag{4.35}$$

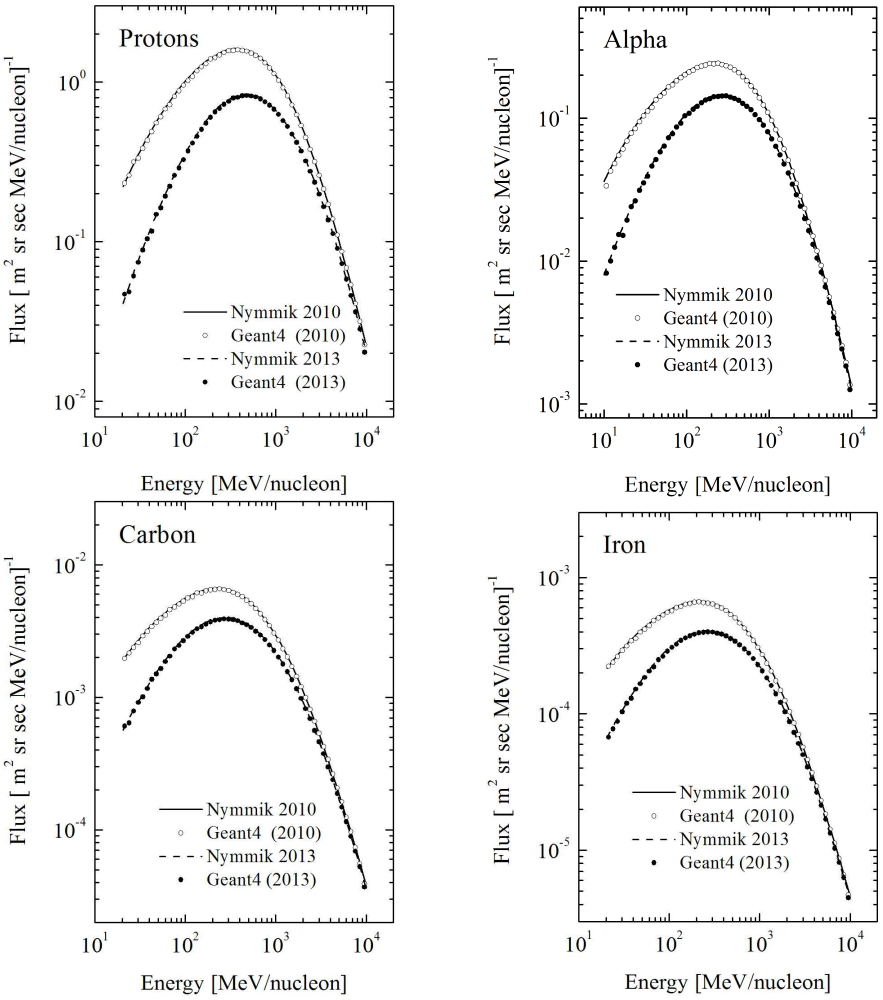

Figure 4.11: Histogram reconstruction of the GCRs fluxes generated by GEANT4 in comparison with the Nymmik's spectrum performed in two different periods of the solar activity.

where the term $D^{NIEL}(E)$ is the NIEL spectral dose:

$$D^{NIEL}(E) = \frac{NIEL(E)\ \Phi(E)}{6.24 \times 10^9} \tag{4.36}$$

The spectral fluence $\Phi_i(E)$, for the i-th nucleus, is obtained by the integration of the ISO GCRs flux over time, and over the entire solid angle i.e:

$$\Phi_i(E) = \int_{\Delta t} \int_{4\pi} \Phi_i(E,t) dt d\Omega \tag{4.37}$$

where $\Phi_i(E,t)$ is given by (1.22).

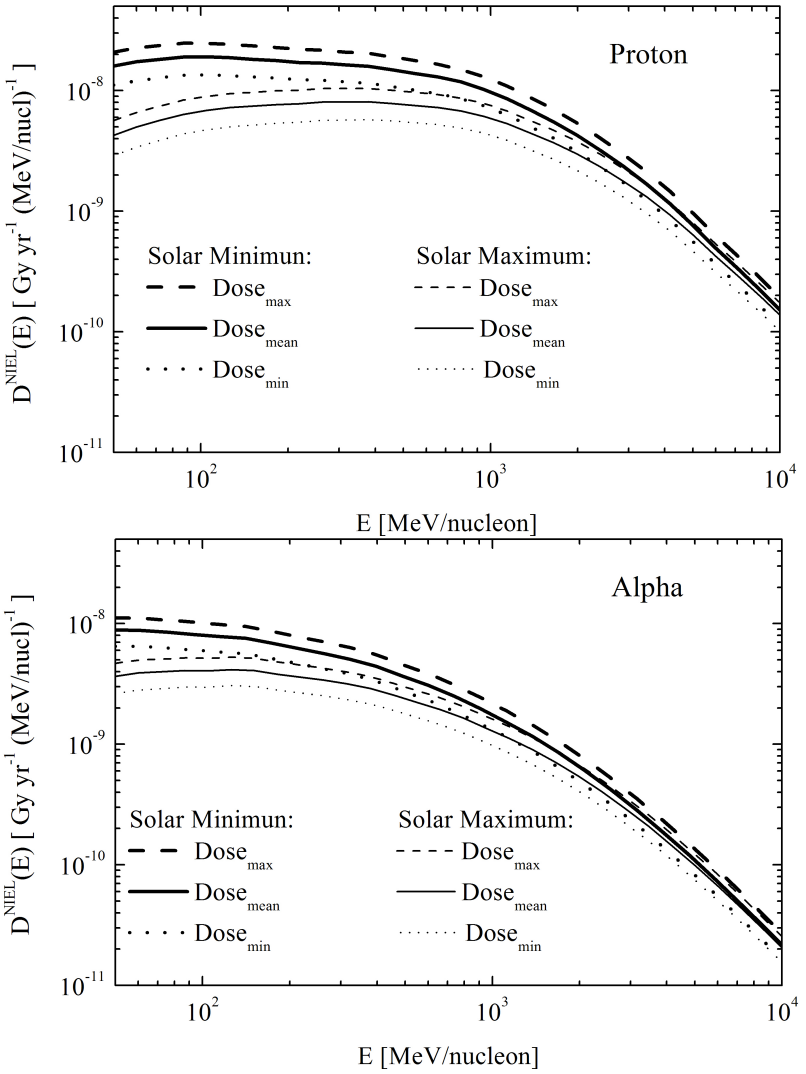

Figure 4.12: Spectral NIEL-Dose for protons (top) and alpha particles (bottom). Thick lines refers to a typical solar minimum period while thin lines to a maximum one. For each solar period the dashed lines are the $D^{NIEL}max(E)$, the solid ones are the mean spectral NIEL-Doses, while the dotted ones are the $D^{NIEL}_{min}(E)$ values.

The NIEL-Dose calculation was performed for two periods of the solar activity. To simplify the problem, the spectral fluence of the i-nucleus was approximated by:

$$\Phi_i(E) \simeq 4\pi\Phi_i(E,t)\Delta t \tag{4.38}$$

where Δt is the time interval which corresponds to one year mission ($\sim \pi\times10^7$ s) and $\Phi_i(E,t)$ to a typical flux which depends on the solar activity. For a

solar maximum period the ISO flux of the year 2013 was considered, while for a solar minimum period the one of the year 2010 was taken. By the use of the (4.38) the spectral dose (4.39) for the i-th nucleus is computed by:

$$D_i^{NIEL}(E) = \eta \; NIEL_i(E)\Phi_i(E,t) \quad \left[\frac{\text{Gy}}{\text{yr MeV/nucleon}}\right] \tag{4.39}$$

where η is the numerical coefficient equal to 6.33×10^{-2}. The spectral NIEL-Dose, in the range from 50 MeV/nucleon to 10 GeV/nucleon, is reported in figure 4.12 for protons and alpha particles where the $NIEL_i(E)$ values correspond to the total NIEL (Coulomb plus nuclear) reported in figure 4.4. For alpha particles the nuclear NIEL values are available only up to 1 GeV/nucleon. For greater energies ($>$ 1 GeV/nucl) the alpha NIEL behavior is expected to be similar to the proton one which is almost constant from 1 GeV/nucleon up to 10 GeV/nucleon. To a first approximation it is therefore possible to consider the alpha NIEL value almost constant in the same energy range. This approximation should not affect the NIEL-Dose calculation since the greatest uncertainties of this computation comes from the fluxes. For each solar period, in facts, the maximum and minimum spectral NIEL-Dose are calculate by:

$$D_{max,i}^{NIEL}(E) = \eta \; NIEL_i(E)\big(\Phi_i(E,t) + \sigma_{\Phi_i(E,t)}\big) \tag{4.40}$$

$$D_{min,i}^{NIEL}(E) = \eta \; NIEL_i(E)\big(\Phi_i(E,t) - \sigma_{\Phi_i(E,t)}\big) \tag{4.41}$$

where $\sigma_{\Phi_i(E,t)}$ is the ISO flux standard deviation whose expression can be found in [15]. In figure 4.12 dashed lines correspond to $D_{max,i}^{NIEL}(E)$, the solid ones are the mean values obtained by the (4.39) while the dotted ones are the $D_{min,i}^{NIEL}(E)$ values. Thick lines correspond to the solar minimum period and the thin lines correspond to the solar maximum one.

The spectral NIEL-Dose was obtained also for all the other nuclei of the GCRs spectrum. Since the GEANT4 NIEL simulation gives the same results as the analytical computation obtained by means of the differential cross section SZ (4.7) (see figure 4.8) this latter was used to simplify the computational integration of the NIEL-Dose. It has to be noted that even if the nuclear NIEL fraction was not considered in this computation it should not significantly affect the overall estimation of the NIEL-Dose. In facts, as it was explained in section 3.2.3, the nuclear contribution to the total NIEL is expected to be greater than 50% at energies above 440 MeV/amu and 940 MeV/amu for lithium and beryllium respectively. However, these nuclei have low relative abundances as can be seen from figure 1.2. For all the other nuclei the nuclear contribution should be important only for energies greater than 1 GeV/nucleon where the GCRs fluxes decrease. In addition as

Nucleus	(A,Z)	Solar Minimum: D^{NIEL}	$\pm\sigma_{D^{NIEL}}$	Solar Maximum: D^{NIEL}	$\pm\sigma_{D^{NIEL}}$
He	(2,4)	5.97	1.49	4.14	1.04
Li	(7,3)	1.74×10^{-2}	0.49×10^{-2}	1.18×10^{-2}	0.34×10^{-2}
Be	(9,4)	1.66×10^{-2}	0.46×10^{-2}	1.14×10^{-2}	0.32×10^{-2}
B	(11,5)	9.38×10^{-2}	1.75×10^{-2}	6.36×10^{-2}	1.22×10^{-2}
C	(12,6)	4.77×10^{-1}	0.85×10^{-1}	3.15×10^{-1}	0.58×10^{-1}
N	(14,7)	1.67×10^{-1}	0.31×10^{-1}	1.12×10^{-1}	0.22×10^{-1}
O	(16,8)	7.75×10^{-1}	1.27×10^{-1}	5.15×10^{-1}	0.87×10^{-1}
F	(19,9)	2.20×10^{-2}	0.66×10^{-2}	1.52×10^{-2}	0.46×10^{-2}
Ne	(20,10)	2.15×10^{-1}	0.46×10^{-1}	1.42×10^{-1}	0.31×10^{-1}
Na	(23,11)	6.34×10^{-2}	1.63×10^{-2}	4.17×10^{-2}	1.09×10^{-2}
Mg	(24,12)	3.15×10^{-1}	0.62×10^{-1}	2.15×10^{-1}	0.43×10^{-1}
Al	(27,13)	7.56×10^{-2}	1.78×10^{-2}	5.13×10^{-2}	1.22×10^{-2}
Si	(28,14)	3.91×10^{-1}	0.78×10^{-1}	2.60×10^{-1}	0.53×10^{-1}
P	(31,15)	2.11×10^{-2}	0.41×10^{-2}	1.44×10^{-2}	0.28×10^{-2}
S	(32,16)	1.00×10^{-1}	0.21×10^{-1}	6.71×10^{-2}	1.40×10^{-2}
Cl	(35,17)	2.44×10^{-2}	0.62×10^{-2}	1.67×10^{-2}	0.43×10^{-2}
Ar	(40,18)	5.00×10^{-2}	0.90×10^{-2}	3.48×10^{-2}	0.64×10^{-2}
K	(39,19)	4.11×10^{-2}	0.70×10^{-2}	2.81×10^{-2}	0.49×10^{-2}
Ca	(40,20)	1.22×10^{-1}	0.21×10^{-1}	7.96×10^{-2}	1.44×10^{-2}
Sc	(45,21)	2.64×10^{-2}	0.45×10^{-2}	1.77×10^{-2}	0.31×10^{-2}
Ti	(48,22)	9.89×10^{-2}	1.80×10^{-2}	6.65×10^{-2}	1.24×10^{-2}
V	(51,23)	5.82×10^{-2}	1.09×10^{-2}	3.89×10^{-2}	0.75×10^{-2}
Cr	(52,24)	1.27×10^{-1}	0.22×10^{-1}	8.42×10^{-2}	1.53×10^{-2}
Mn	(55,25)	8.28×10^{-2}	1.78×10^{-2}	5.62×10^{-2}	1.23×10^{-2}
Fe	(56,26)	9.15×10^{-1}	1.54×10^{-1}	6.18×10^{-1}	1.07×10^{-1}
Co	(59,27)	6.92×10^{-3}	6.20×10^{-3}	4.98×10^{-3}	4.46×10^{-3}
Ni	(59,28)	4.72×10^{-2}	0.98×10^{-2}	3.26×10^{-2}	0.69×10^{-2}
Nuclei Total		10.32	$\pm$1.51	7.05	$\pm$1.05
Protons		27.27	$\pm$7.44	16.76	$\pm$4.63

Table 4.1: NIEL-Dose values D^{NIEL} and uncertainties $\sigma_{D^{NIEL}}$, in units of μGy/yr, for all the nuclei of the GCRs spectrum. Values are obtained for typical solar minimum (3-th and 4-th columns) and solar maximum periods (5-th and 6-th columns). The integration was performed from 50 MeV/nucleon up to 10 GeV/nucleon.

it can be seen from the spectral NIEL-dose curves, the major contribution of the NIEL-Dose computation comes from the integration in the energy range from 50 MeV/nucleon up to about 2 GeV/nucleon.

The integral NIEL-Dose (4.35), for each nucleus, was performed for the minimum energy $E_{min} = 50$ MeV/nucleon above which the GCRs are the dominant radiation of the space environment, up to $E_{max} = 10$ GeV/nucleon where fluxes decrease of about two orders of magnitude respect to the maximum flux value. The standard deviation of the integral NIEL-Dose for all the nuclei, from alpha particles to nickel, was computed by:

$$\sigma_{D^{NIEL}} = \sqrt{\sum_i \left(\sigma_{D^{NIEL},i}\right)^2} \tag{4.42}$$

where the standard deviation of the i-th nucleus was obtained as:

$$\sigma_{D^{NIEL},i} = \frac{D^{NIEL}_{max,i} - D^{NIEL}_{min,i}}{2} \tag{4.43}$$

The upper $D^{NIEL}_{max,i}$, and the lower $D^{NIEL}_{min,i}$ NIEL-Dose values are computed by means of the integration of the maximum (4.40) and the minimum (4.41) spectral NIEL-Doses i.e.:

$$D^{NIEL}_{max,i} = \int_{E_{min}}^{E_{max}} D^{NIEL}_{max,i}(E)dE \tag{4.44}$$

$$D^{NIEL}_{min,i} = \int_{E_{min}}^{E_{max}} D^{NIEL}_{min,i}(E)dE \tag{4.45}$$

Results of the computation are listed in table 4.1 for typical solar minimum and solar maximum periods. We obtained that the total NIEL-Dose, for all nuclei from alpha to nickel, is 37.8% and 42% of the protons one during the minimum and the maximum solar periods respectively. In addition it has to be noted that the NIEL-Dose strongly depends on the ISO flux model which brings an uncertainty of about 27.5% for the protons value, while for the overall nuclei it is about 14.5%.

Chapter 5

The Carriers Transport Phenomena in Silicon

In this chapter an introduction to the carriers transport phenomena of a semiconductor is given. For our interest, and also for simplicity, only silicon will be considered. Some macroscopic variables such as the mobility and the resistivity will be derived. In addition the Hall effect theory will be described. Since radiation damage is a complex phenomena, it is necessary to know the normal carriers behavior (in a non-irradiated sample) in order to underline the major differences which arise after irradiation. Some fundamental notions of the silicon structure are reported in appendix B.

5.1 Equilibrium Carriers Statistics

Silicon is an indirect (see B.1) semiconductor with an energy separation of the valance from the conduction band - forbidden energy gap E_g- of about 1.124 eV at room temperature.

In this section the carriers distribution at thermal equilibrium in the two bands are given as a function of temperature and doping concentration. The carriers concentration out of equilibrium[1] considered in section 5.2. The presence of electrical external sources, in facts, modify the equilibrium carriers statistics. In addition, defects induced after irradiation may increase the recombination process.

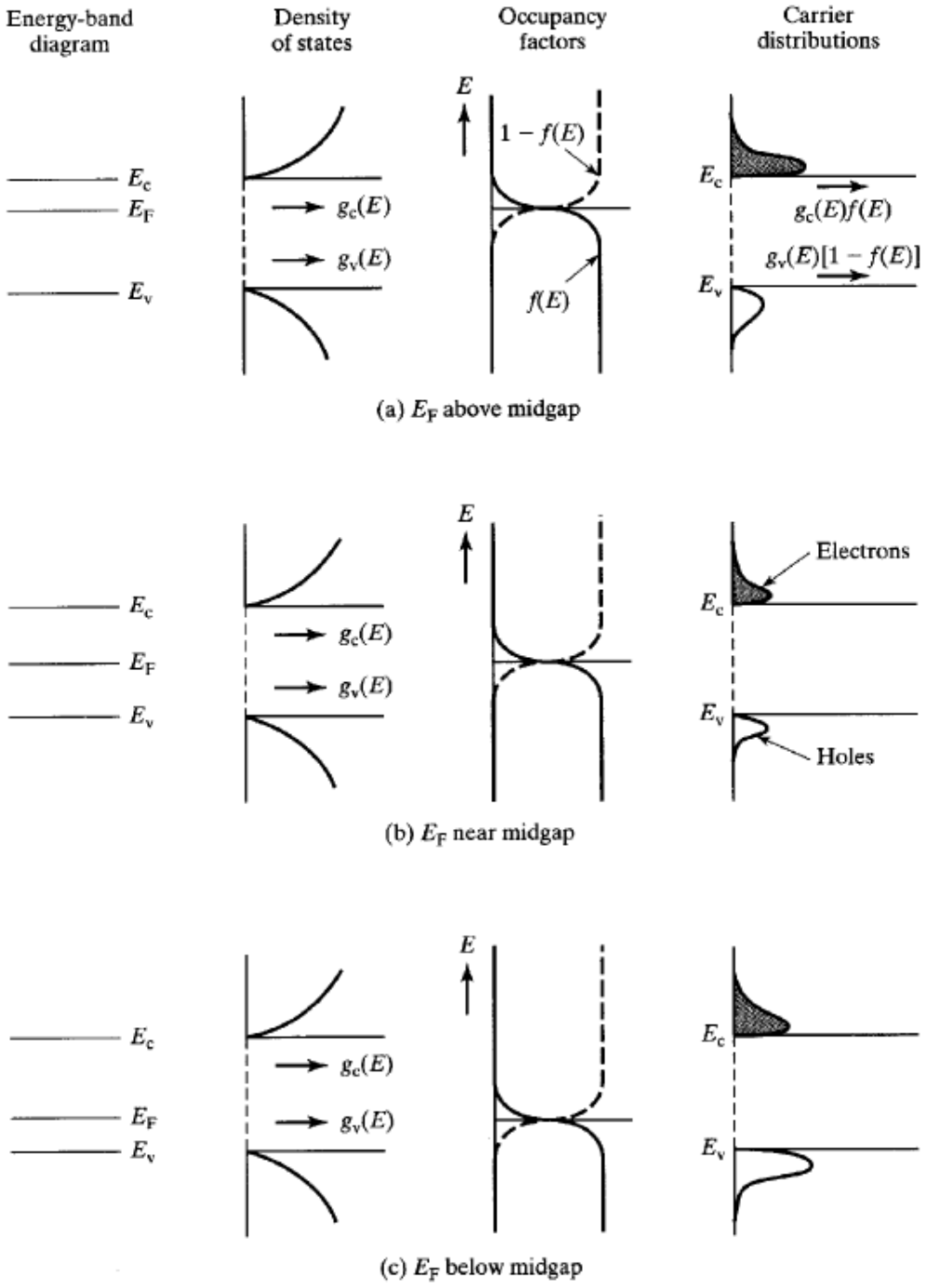

Figure 5.1: Carrier distribution in respective bands when the Fermi level is (a) above (b) near and (c) below mid-gap respectively. In each case there are also shown: the energy-band diagram, the density of states and the occupancy factor [78].

5.1.1 Carriers Concentration

The carriers concentration of electrons in the conduction band and of holes[2] in the valance band, can be obtained by [78]:

$$n(T) = \int_{E_c}^{E_{top}} g_c(E) f(E;T) dE \tag{5.1}$$

$$p(T) = \int_{E_{bottom}}^{E_v} g_v(E)[1 - f(E;T)] dE \tag{5.2}$$

where T is the equilibrium temperature, $n(T)$ and $p(T)$ refer to electrons and holes respectively. The integral (5.1) is computed from the bottom of the conduction band E_c to the top value E_{top}, and the integral (5.2) is computed from the bottom of the valance band E_{bottom} to the top value E_v (see figure 5.1). The terms $g_c(E)$ and $g_v(E)$ are the density of states available in the conduction and in the valance band respectively which are given by equations (B.24) and (B.25). The term $f(E;T)$ is the Fermi-Dirac probability distribution function which gives the probability at temperature T for the state of energy E to be occupied by an electron and its expression is:

$$f(E;T) = \frac{1}{1 + e^{(E-E_F)/k_B T}} \tag{5.3}$$

where k_B is the Boltzmann's constant and E_F is the Fermi energy level.

For non-degenerate semiconductors, the Fermi energy level lies in the forbidden energy gap and its position varies according to the carriers population. When the electrons carrier population overcomes the holes one, E_F lies in the upper half of the band gap. When the reverse is true, E_F is positioned below the mid-gap. When both types of carriers have similar concentrations, the Fermi energy level lies near the mid-gap energy which is called *intrinsic energy level* and it is denoted by E_i.

If the energy E is far from the Fermi energy, i.e. $|E - E_F| > 3k_B T$, the Fermi-Dirac distribution function can be approximated by a Maxwell-Boltzmann type function [78]:

$$f(E;T) \simeq \exp\left[-(E - E_F)/k_B T\right] \tag{5.4}$$

$$1 - f(E;T) \simeq \exp\left[-(E_F - E)/k_B T\right] \tag{5.5}$$

which can be used for electrons ($E > E_F$) and holes ($E < E_F$) respectively. By this approximation and by the use of the equations (B.24) and (B.25) for

[1] Out of equilibrium the generation and recombination processes re-establish the equilibrium condition.

[2] Holes unoccupied electron states are See section B.3 for the holes concept.

the density of sates, it is possible integrate the expressions (5.1) and (5.2) and to obtain the carriers concentrations as:

$$n(T) = N_c \exp\left[-(E_c - E_F)/k_B T\right] \tag{5.6}$$
$$p(T) = N_v \exp\left[-(E_F - E_v)/k_B T\right] \tag{5.7}$$

where for the integration it was considered that $E_{tom} \to +\infty$ and $E_{bottom} \to -\infty$. The numbers N_c and N_v are the effective density of states for conduction and valence band respectively, which are equal to [78]:

$$N_c = 2\left(\frac{2\pi m^*_{de} k_B T}{h^2}\right)^{3/2} \tag{5.8}$$

$$N_v = 2\left(\frac{2\pi m^*_{dh} k_B T}{h^2}\right)^{3/2} \tag{5.9}$$

where m^*_{de} and m^*_{dh} are the density of state effective masses whose expressions are given in equations (B.28) and (B.30). For silicon, at room temperature, the effective density of states are equal to $N_c = 7.28 \times 10^{19}$ cm^{-3}, $N_v = 1.05 \times 10^{19}$ cm^{-3} [75].

In figure 5.1 are reported the Energy-band diagrams, the density of states functions, the occupancy factors - i.e. $g_c(E)f(E;T)$ and $g_v(E)[1 - f(E;T)]$- and the carrier distributions as a function of the Fermi energy level position. The three represented positions are: $E_F > E_i$, $E_F = E_i$ and $E_F < E_i$. In all three cases, as the energy increases in the conduction band or diminishes in the valance band, the carrier distributions are zero at the band edges then increase rapidly and reach a peak close to E_c or E_v afterward they decay to zero In essence the carriers are distributed near the band edges within few $k_B T$.

5.1.2 Intrinsic Material

A semiconductor with a very low level of impurity atoms concentration is called *intrinsic*. Because of thermal agitation, electrons continuously move from the valance to the conduction band, leaving behind a hole. The reverse process, called *recombination*, takes place as well. At a given equilibrium temperature, for the charge neutrality condition the mean number of electrons in the conduction band is equal to the holes one in the valance band. This value is defined as the intrinsic concentration n_i:

$$n(T) = p(T) = n_i(T). \tag{5.10}$$

By equating the carriers concentrations given by (5.6) and (5.7) it is possible to obtain the position of the Fermi energy level, for an intrinsic semiconductor, i.e.:

$$E_F = \frac{E_c + E_v}{2} - \frac{k_B T}{2} \ln\left(\frac{N_c}{N_v}\right) \tag{5.11}$$

where $(E_c + E_v)/2 = E_g/2$. At room temperature $k_B T = 0.026$ eV and for silicon $\ln(N_c/N_v) \simeq 0.9$, then the Fermi energy level is approximatively equal to the intrinsic energy level $E_i = E_g/2$.
To get an expression for the intrinsic concentration as a function of temperature, it is convenient to consider the product $n(T)p(T) = n_i^2(T)$, where the carriers concentrations are given by the relations (5.6) and (5.7), i.e.:

$$n_i(T) = \sqrt{N_c N_v} \exp\left[-\frac{(E_g/2)}{k_B T}\right] \tag{5.12}$$

$$\propto T^{3/2} \exp\left[-\frac{(E_g/2)}{k_B T}\right]. \tag{5.13}$$

This latter expression underlines the dependence of the intrinsic concentration on temperature ($T^{3/2}$) and on the energy band gap E_g. At $T = 300$ K for silicon $E_g = 1.124$ eV and $n_i = 1.45 \times 10^{10}$ cm^{-3} [75].

5.1.3 n-type and p-type Silicon

The relative population of carriers in bands, can be varied by doping the semiconductor with a specific concentration and type of impurity atoms. For silicon (IV group element) it is performed by adding atoms of the V or III group; phosphorus (P) or boron (B) are generally used. The V group element is called *donor* atom because it has one more electron available for conduction in respect to silicon. The semiconductor becomes a n-type material. The III group element, instead, is an *acceptor* atom since it has one less electron in the conduction band; in this case the semiconductor becomes a p-type material. Impurity atoms in the crystal structure introduce discrete energy levels inside the forbidden band gap. Ionization energies, respect to E_c and E_v levels, of some impurity atoms are reported in figure 5.2. Donor and acceptor atoms introduce shallow levels, denoted by E_d and E_a, which lie close to the conduction and the valance band respectively. The ionization energy depends on the dopant atom: it varies form 10's meV to 100's meV; for example it is 0.046 eV for the donor P and it is 0.044 eV for the acceptor B. These levels are partially or totally ionized according to the equilibrium temperature.

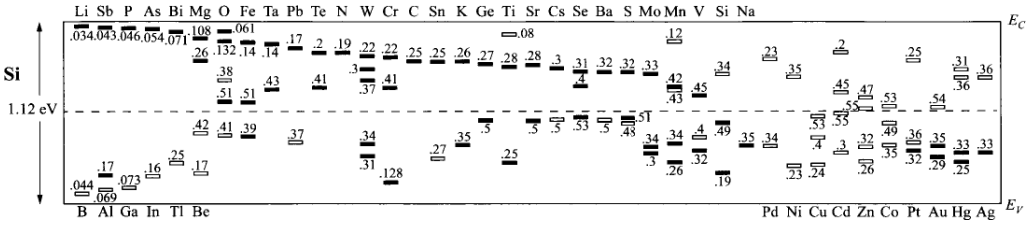

Figure 5.2: Ionization energy of various impurities atoms in silicon [76].

A qualitative description of the free carrier concentration as a function of temperature, is now given for a non-degenerate semiconductor [76].
The donors and acceptors concentration of atoms are denoted by N_d and N_a, while $n_d(T)$ and $p_a(T)$ represent the electrons and the holes concentrations as a function of temperature, which are yielded by donors and acceptors respectively. In addition, thermally generated carriers may be present with a concentration given by the intrinsic one $n_i(T)$. The total electrons and holes concentration for a n-type and a p-type semiconductor, are given by the sum of the dopant plus the intrinsic contribution:

$$n(T) = n_d(T) + n_i(T) \qquad (n\text{-type}) \tag{5.14}$$
$$p(T) = p_a(T) + n_i(T) \qquad (p\text{-type}) \tag{5.15}$$

which are valid for a n-type and a p-type respectively.

Low Temperatures.
If the temperature approaches the *absolute zero* there is no thermal energy to ionize dopant atoms or to excite electrons from the valance to the conduction band. As a consequence there are no free carriers for conduction and the carrier concentration is null, i.e.:

$$n(T \to 0) = 0 \qquad (n\text{-type}) \tag{5.16}$$
$$p(T \to 0) = 0 \qquad (p\text{-type}) \tag{5.17}$$

For $T \neq 0$ in the *low temperatures* regime, the intrinsic contribution the to carriers concentration is still null $n_i(T) = 0$. Only a small fraction of dopant atoms is ionized and so the relations (5.14) and (5.15) become:

$$n(T) \simeq n_d(T) < N_d \qquad (n\text{-type}) \tag{5.18}$$
$$p(T) \simeq p_a(T) < N_a. \qquad (p\text{-type}) \tag{5.19}$$

To find the position of the Fermi energy level for a n-type semiconductor, the quantity $[1 - f(E_d; T)]N_d$ which is the number of ionized donors atoms, has

to be equal to the concentration of electrons in the conduction band given by equation (5.6). For the p-type semiconductor, the number of acceptor atoms occupied by electrons, $f(E_a;T)N_a$, has to be equal to the holes concentration given by equation (5.7). Then, assuming the Fermi-Dirac approximations (5.4) and (5.5), the position of the Fermi energy level is:

$$E_F = \frac{E_c + E_d}{2} + \frac{k_B T}{2} \ln\left(\frac{N_d}{N_c}\right) \qquad (n\text{-type}) \tag{5.20}$$

$$E_F = \frac{E_v + E_a}{2} - \frac{k_B T}{2} \ln\left(\frac{N_a}{N_v}\right) \qquad (p\text{-type}) \tag{5.21}$$

For a non-degenerate semiconductor, the dopant concentration is negligible in comparison to the effective density of states ($N_d \ll N_c$ or $N_a \ll N_v$) and so at low temperatures the Fermi energy level is positioned between the bottom of the conduction band and the donor energy level for a n-type semiconductor or between the top of the valance band and the acceptor energy level for a p-type material i.e.:

$$E_F \simeq \frac{E_c + E_d}{2} \qquad (n\text{-type}) \tag{5.22}$$

$$E_F \simeq \frac{E_v + E_a}{2} \qquad (p\text{-type}) \tag{5.23}$$

To obtain the carrier concentration, at low temperatures, E_F given by relations (5.20) and (5.21) have to be substituted in (5.6) and (5.7) respectively:

$$n(T) = \sqrt{N_c N_d}\exp\left[-\frac{(E_c - E_d)/2}{k_B T}\right] \qquad (n\text{-type}) \tag{5.24}$$

$$p(T) = \sqrt{N_v N_a}\exp\left[-\frac{(E_a - E_v)/2}{k_B T}\right] \qquad (p\text{-type}) \tag{5.25}$$

These are the concentrations of carriers in the **freeze out region** where the majority of them are bound to dopant atoms.

Intermediate Temperatures.

As the temperature increases, more and more electrons have thermal energies greater than the dopant ionization energy and so the number or free carriers in the bands increases.

At *intermediate temperatures*, all dopants atoms are ionized ($n_d(T) \equiv N_d$ or $p_a(T) \equiv N_a$). If the thermal energy is less than the band gap energy E_g, the intrinsic concentration is still negligible respect to the dopant concentration

($n_i(T) \ll N_d$ or $n_i(T) \ll N_a$). The carriers concentrations ((5.14) and (5.15)) are almost equal to the dopants contribution:

$$n(T) \simeq n_d(T) = N_d \quad (n\text{-type}) \tag{5.26}$$
$$p(T) \simeq p_a(T) = N_a \quad (p\text{-type}) \tag{5.27}$$

The position of the Fermi energy level is obtained by equating the (5.6) and (5.7) to the corresponding concentration of dopant atoms (equations (5.26) and (5.27)). The Fermi energy level relations are then given by:

$$E_F = E_c - k_B T \ln\left(\frac{N_c}{N_d}\right) \quad (n\text{-type}) \tag{5.28}$$
$$E_F = E_v + k_B T \ln\left(\frac{N_v}{N_a}\right) \quad (p\text{-type}) \tag{5.29}$$

In this temperature interval, called **extrinsic region**, the carriers concentration remains almost constant and the Fermi energy level lies just under E_c or above E_v and it depends on the dopant concentration (N_d or N_a) and on temperature.

High Temperatures

When the thermal energy reaches and, as the temperature increases, overcomes the band gap energy, the contribution of the intrinsic carriers $n_i(T)$ to the total number of free carriers is no more negligible. In this case is it necessary to distinguish between the majority carriers concentration (electrons n_n for a n-type or holes p_p for a p-type), and the minority carriers concentration (p_n in a n-type or n_p in a p-type) induced by thermal excitation of electrons from the valance to the conduction band. In the *high temperature* regime the majority carrier concentrations ((5.14) and (5.15)) are given by:

$$n_n(T) = N_d + n_i(T) \quad (n\text{-type}) \tag{5.30}$$
$$p_p(T) = N_a + n_i(T) \quad (p\text{-type}) \tag{5.31}$$

while the minority ones are:

$$p_n = n_i(T) \quad (n\text{-type}) \tag{5.32}$$
$$n_p = n_i(T) \quad (p\text{-type}) \tag{5.33}$$

As the temperature increases further on, the **intrinsic regime temperature** is reached and $n_i(T)$ dominates over the dopant contribution. The Fermi energy level approaches the intrinsic energy level E_i in the mid-gap

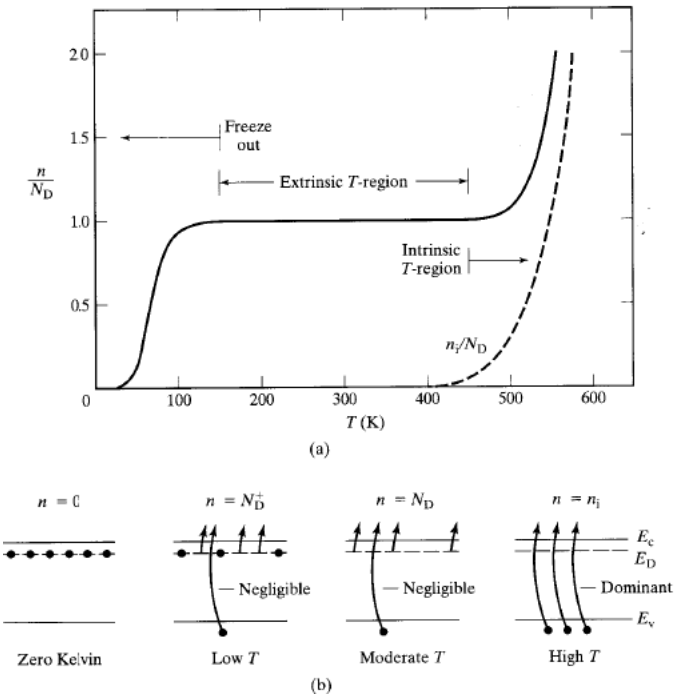

Figure 5.3: (a) Temperature dependence of the majority carriers concentration for a n-type silicon doped with a phosphorus dopant concentration $N_D = 10^{15} cm^{-3}$. The dashed line n_i/N_D is included for comparison (b) Qualitative band gap diagram for different temperature regimes. [78].

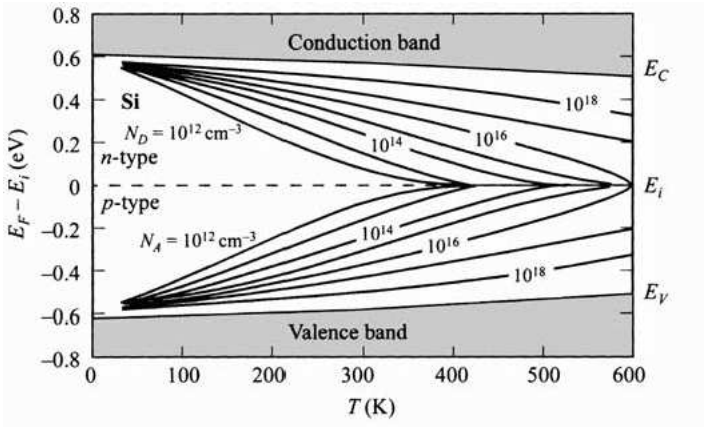

Figure 5.4: Fermi level for silicon as a function of temperature and impurity concentration [76].

(see equation (5.11)).

An example of the typical behavior of the $n(T)/N_d$ ratio as a function of temperature is reported in fig 5.3 for a n-type silicon doped with a phosphorus concentration $N_d = 10^{15} cm^{-3}$. **Freeze out**, **extrinsic** and **intrinsic** regions are distinguishable. The schematic energy band diagram and carriers population of donor level is also reported in the bottom of the same figure.

In figure 5.4 the positioning of the Fermi energy level, as a function of temperature, is presented for n-type and p-type silicon. Different curves refers to different concentrations of dopant atoms. As the temperature increases E_F shifts towards the mid-gap energy value; at a fix temperature the lowest dopant concentration has E_F closer to E_i.

5.1.4 Compensated Semiconductor

In real materials, both type of carriers are simultaneously present. An appropriate degree of doping atoms may change the relative concentration of electrons and holes. Semiconductor doped with both donor N_d and acceptor N_a atoms, are called *compensated*.
At thermal equilibrium holes and electrons concentrations satisfy the *mass action law*:

$$pn = n_i^2 \tag{5.34}$$

which is valid for all types of semiconductors.
In compensated materials, the dopant with the greatest concentration determines the conductivity type. For the charge neutrality condition, the total number of positive charges must be equal to the total number of negative ones, i.e.:

$$n + N_a = p + N_d \tag{5.35}$$

The total impurity concentration is equal to $|N_d - N_a|$ and, in general, it is greater than n_i. At intermediate temperatures, the carriers concentrations are given by:

$$n \simeq N_d - N_a \; ; \quad p = \frac{n_i^2}{n} \qquad (\text{if } N_d > N_a) \tag{5.36}$$

$$p \simeq N_a - N_d \; ; \quad n = \frac{n_i^2}{p} \qquad (\text{if } N_a > N_d) \tag{5.37}$$

where the mass action law (5.34) was considered. The position of the Fermi energy level becomes:

$$E_F = E_c - k_B T \ln\left(\frac{N_c}{N_d - N_a}\right) \quad \text{if } N_d > N_a \tag{5.38}$$

$$E_F = E_v + k_B T \ln\left(\frac{N_v}{N_a - N_d}\right) \quad \text{if } N_a > N_d \tag{5.39}$$

When $N_d = N_a$ the semiconductor is totaly compensated and the Fermi energy level is no longer given by the (5.38) or (5.39). In this case E_F shifts to the intrinsic level energy E_i in the center of the gap. The majority carriers concentration becomes equal to the minority one and the semiconductor behaves as an intrinsic material.

5.1.5 Degenerate Semiconductors

When the doping concentration is no longer negligible respect to the effective density of states concentration, the semiconductor is called *degenerate*. For silicon the critical doping concentration is about 1.3×10^{18} cm^{-3} for n-type P doped and 6.2×10^{18} cm^{-3} for p-type B doped [75]. For non-degenerate semiconductors, the dopant atoms can be considered decoupled as a consequence they form discrete energy levels in the forbidden energy gap. With increasing doping concentration, the distance between dopant atoms decreases and the atoms wave functions overlap. If N_d is the dopant concentration, the energy level associated with each dopant atom is N_d-fold degenerate. The overlapping of the wave functions causes the splitting of the N_d-fold degenerate energy levels, and brings to the formation of a impurity band [78].

For a very high doping concentration, the impurity band can intersect the conduction or the valance band according to the type of dopant. Since the dopant atoms are randomly distributed the edge of the conduction or valance band exhibits a tail [78] [75]. The tail is schematically represented in figure 5.5 where the density of states function for $T = 0$ is reported. It is possible to see the progressively reduction of the ionization energy with increasing dopant concentration. This has the important consequence that the **freeze-out region** of the carriers concentration **disappears** [75]. As a consequence the Fermi energy level progressively approaches the conduction band (or the valance band in the case of acceptor atoms) with increasing doping concentration. For very high doping, it can even lie in the conduction band (on in the valance one). In this case the semiconductor behaves almost like a metal. In addition the Fermi-Dirac distribution function can't be approximated by the Boltzmann one i.e. the relations (5.4) and (5.5) are

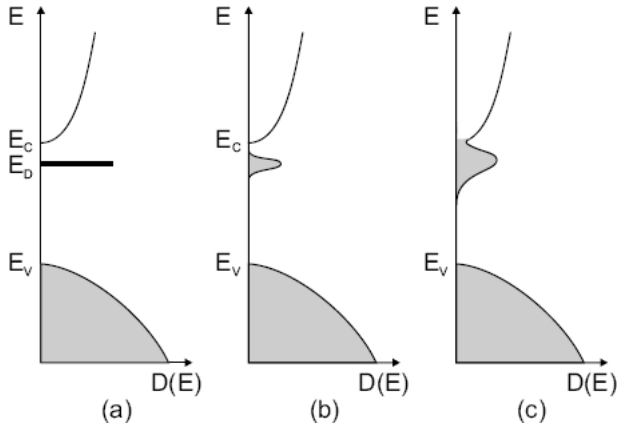

Figure 5.5: Formation of a (donor) impurity band. (a) with a small doping concentration the dopant energy level (E_D) is well defined, (b) increasing doping and development of an impurity band (c) the dopant band overlaps to the conduction band for high impurity concentration. The shaded areas indicate populated states at $T = 0$ K. $D(E)$ is the density of states [75].

no longer valid. The carriers concentration, as a function of temperature, are usually obtained by numerical integrations of the relations (5.1) and (5.2) [78]. However the majority carriers concentration in the **extrinsic temperature region** is still given by the doping concentration [78] i.e. $n \cong N_d$ for a n-type or $p \cong N_a$ for a p-type.

5.2 Generation and Recombination Processes

When the equilibrium concentration of carriers is disturbed by external sources, generation and recombination processes restore the equilibrium condition given by the mass action law (5.34).

If $np > n_i^2$, *injection* case, electrons tend to recombine with holes by making a transition from the conduction to the valance band. This is the band to band transition which is typical of direct semiconductors.

Since silicon is an indirect semiconductor, the band-to-band recombination is not favorite. Instead the dominant transition mechanism is the indirect recombination precess via discrete deep energy levels which act like traps within the band-gap. This is called single level recombination process. In this case electrons and holes captured with a rate given by the appropriate capture cross section (σ_n and σ_p). If the traps concentration is equal to N_t and E_t is their energy level, then the net transition rate U can be calculated

by [76]:

$$U = \frac{\sigma_p \sigma_n v_{th} N_t (pn - n_i^2)}{\sigma_p \left[p + n_i \exp\left(\frac{E_i - E_t}{k_B T} \right) \right] + \sigma_n \left[n + n_i \exp\left(\frac{E_i - E_t}{k_B T} \right) \right]} \tag{5.40}$$

where v_{th} is the thermal velocity of carriers ($\simeq 10^7$ cm/s), and E_i is the intrinsic energy level. The net transition rate is the difference between the recombination rate and the injection rate. The proportionality term $(pn - n_i^2)$ gives a measure of the out-equilibrium level of the material. The maximum value of U is achieved when $E_t = E_i$ that is when the trap level lies in the middle of the band-gap. Under this latter condition, the (5.40) can be rewritten as:

$$U = \frac{\sigma_p \sigma_n v_{th} N_t (pn - n_i^2)}{\sigma_p (p + n_i) + \sigma_n (n + n_i)} \tag{5.41}$$

In a n-type material, under low-level injection (i.e. the injected carriers satisfy the condition: $\Delta p = \Delta n \ll N_d$), the carriers densities become:

$$n_n = n_{n0} + \Delta n \simeq n_{n0} \approx N_d \tag{5.42}$$

$$p_n = p_{n0} + \Delta p \ll n_n \tag{5.43}$$

where n_{n0} and p_{n0} are the majority and minority carriers concentrations at equilibrium (i.e. $n_{n0} p_{n0} = n_i^2$), and N_d is the concentration of donor atoms. Substituting of the (5.42) and (5.43) inside the (5.41) with the condition $p_n \ll n_n$, it is possible to obtain that the *recombination carrier lifetime* is equal to the minority carriers lifetime. The net recombination rate, in facts, is given by:

$$U \simeq \frac{\Delta p}{\tau_p} \tag{5.44}$$

where τ_p is *minority carrier lifetime* defined as:

$$\tau_p = \frac{1}{\sigma_p v_{th} N_t} \tag{5.45}$$

For a p-type material the issue is analogous and the minority carriers lifetime is given by:

$$\tau_n = \frac{1}{\sigma_n v_{th} N_t} \tag{5.46}$$

The recombination carrier lifetime is the time spent by carriers (electrons and holes) within the bands (conduction and valance) before they being trapped by discrete deep levels inside the band-gap. The order of magnitude ranges

from 10^{-9} sec up to 10^{-4} sec and it depends to the concentration of levels inside the band-gap N_t. The carriers lifetime may be reduced by adding impurity atoms or by the irradiation process (see 3.3). The displacement damage, in facts, causes the formation of defects inside the crystal which introduce deep levels in the forbidden energy gap. It has to be remarked however, that while in the first case impurity atoms are added during the semiconductor fabrication in order to change the electrical response of the material, in the second case the irradiation creates unwished deep levels which degrades the device performances as it was explained in sections 3.3 and 3.5.

When carriers are below their equilibrium value $np < n_i^2$, a spontaneous thermal transition of an electron from the valance to the conduction band takes place. This thermal generation process restores the carriers equilibrium condition. The generation rate is equal to:

$$U = -\frac{\sigma_p \sigma_n v_{th} N_t n_i}{\sigma_p[1 + p/n_i] + \sigma_n[1 + n/n_i]} \equiv -\frac{n_i}{\tau_g} \tag{5.47}$$

where τ_g is the *generation carrier lifetime* which is given by:

$$\tau_g = \left(1 + \frac{n}{n_i}\right)\tau_p + \left(1 + \frac{p}{n_i}\right)\tau_n \tag{5.48}$$

where τ_p and τ_n are the holes and electrons lifetime respectively. According to the carriers concentration (n and p), the generation lifetime may be much longer than the recombination lifetime. The minimum value of τ_g is approximatively twice the recombination lifetime and it is reach when both p and n are smaller than n_i, that is when the semiconductor is intrinsic or heavily compensated.

5.3 Carriers Transport-Phenomena

The motion of free carriers under the influence of an external force is now considered. When an electric field $\mathbf{E}$ is applied to a silicon sample, the force $\mathbf{F} = \pm e\mathbf{E}$ accelerates carriers in the same or in the opposite direction according to their sign and generates the drift current.
Since the motion takes place inside the material, the acceleration process is always broken by collision mechanisms. The more relevant collision processes involve scattering of carriers with lattice phonons, ionized impurity atoms and neutral impurity atoms. Because of scattering, the motion of the single electron (or hole) is very complex. To describe it, a distribution function $f(\mathbf{k}; \mathbf{r}; t)$ is used which gives the probability, at a time t, to find the charge at position $\mathbf{r}$ with wave vector $\mathbf{k}$.

The time evolution of the distribution function under the influence of an external force $\mathbf{F}$, is given by the Boltzmann transport equation [79]:

$$\frac{\partial f}{\partial t} + \mathbf{v} \cdot \overrightarrow{\nabla}_{\mathbf{r}} f + \frac{\mathbf{F}}{\hbar} \cdot \overrightarrow{\nabla}_{\mathbf{k}} f = \left(\frac{df}{dt} \right)_{coll} \tag{5.49}$$

where $\mathbf{v}$ is the charge velocity. The distribution function varies during time because of the particles drift, the momentum variation due to the acceleration process and because of collisions inside the material.

If after collision the energy variation of the charge is small, a simple expression to the collision term may be given:

$$\left(\frac{df}{dt} \right)_{coll} = -\frac{f - f_0}{\tau} \tag{5.50}$$

where f_0 is the thermal equilibrium distribution function (Fermi-Dirac (5.3)), and τ is the *relaxation time* of the collision.

The relaxation time depends on the particle energy and on the specific scattering mechanism and it is different for electrons and holes. The typical order of magnitude is of 10^{-14} sec. To understand qualitatively its general meaning for simplicity it is considered not to vary with time. When the external force $\mathbf{F}$ is removed at time $t = 0$, a simple integration of (5.50) gives the shift of the distribution function $\Delta f = f - f_0$ at time $t > 0$:

$$\Delta f = \Delta f_{t=0} \exp\left(-\frac{t}{\tau} \right) \tag{5.51}$$

where $\Delta f_{t=0}$ is the shift at time $t = 0$. The relaxation time τ represents the decay constant with which the distribution function f recovers towards the thermal equilibrium one f_0.

If the external force is weak and if the distribution function is not far from equilibrium, the distribution function may by expanded in Taylor's series stopped at the first order, i.e.:

$$f \simeq f_0 + f_1 \tag{5.52}$$

where f_1 represents the effect of the external force and, since the force is supposed to weak, $f_1 \ll f_0$.

In a uniform crystal and in the steady state condition, the Boltzmann transport equation can be simplified and solved to give an expression to f. The uniform condition implies that the term $\overrightarrow{\nabla}_{\mathbf{r}} f = 0$, and in the steady state condition ($\partial f / \partial t = 0$) the (5.49) reduces to:

$$\frac{\mathbf{F}}{\hbar} \cdot \overrightarrow{\nabla}_{\mathbf{k}} f = -\frac{f - f_0}{\tau} \equiv -\frac{f_1}{\tau} \tag{5.53}$$

where τ is the specific relaxation time which depends on the particular scattering process.

Considering a n-type material the application of an electric field along the x direction, induces a force $F_x = -eE_x$ acting on free electrons. In this case the equation (5.53) becomes:

$$\frac{eE_x}{\hbar}\frac{\partial f}{\partial k_x} = \frac{f_1}{\tau} \tag{5.54}$$

Assuming an isotropic effective mass m^* the charges energy is given by:

$$E = \frac{\hbar^2 k^2}{2m^*}. \tag{5.55}$$

This enables to write:

$$\frac{\partial f}{\partial k_x} = \frac{\partial f}{\partial E}\frac{\partial E}{\partial k_x} = \frac{\partial f}{\partial E}\hbar v_x \tag{5.56}$$

where v_x is the velocity of the electrons in the x direction which is equal to:

$$v_x = \frac{\hbar k_x}{m^*} \tag{5.57}$$

Substituting the partial derivative (5.56) in the (5.54) and remembering that $f_0 \gg f_1$, a simple expression for the f_1 can be derived:

$$f_1 = eE_x\tau v_x\frac{\partial f_0}{\partial E} \tag{5.58}$$

Since f_0 is the Fermi-Dirac distribution function (5.3), its partial derivative is equal to:

$$\frac{\partial f_0}{\partial E} = -\frac{f_0(1-f_0)}{k_B T} \tag{5.59}$$

The electrons distribution function for a uniform lattice crystal under the influence of a week electric field acting along the x direction is then given by:

$$f = f_0 - eE_x\tau v_x\frac{f_0(1-f_0)}{k_B T}. \tag{5.60}$$

By means of the distribution function all physical quantities such as the drift velocity, the current density, the mobility and the resistivity can be calculated. For a p-type, where holes are majority carriers, the method is completely analogous.

5.3.1 Resistivity and Mobility

In a n-type semiconductor the current density, which arises when an electric field is applied in the x direction, is given by:

$$J_x = -en\langle v_x \rangle \tag{5.61}$$

where n is the electrons concentration and $\langle v_x \rangle$ is the mean drift velocity. The mean drift velocity can be computed by:

$$\langle v_x \rangle = \frac{\int v_x f d^3\mathbf{k}}{\int f d^3\mathbf{k}} \tag{5.62}$$

where the integral is extended over the entire wave vector space. Since $f_1 \ll f_0$ the integral at the denominator can be replaced by the integral of the thermal equilibrium distribution function f_0.

For **non-degenerate semiconductor** the thermal equilibrium function is $f_0 \ll 1$ then $(1 - f_0) \simeq 1$ so that the distribution function becomes:

$$f \simeq f_0 - eE_x \tau v_x \frac{f_0}{k_B T}. \tag{5.63}$$

Substituting this expression of f in term at the numerator of the (5.62) it is possible to write:

$$\langle v_x \rangle = \frac{\int v_x f_0 d^3\mathbf{k}}{\int f_0 d^3\mathbf{k}} - \frac{eE_x}{3k_B T} \frac{\int \tau v^2 f_0 d^3\mathbf{k}}{\int f_0 d^3\mathbf{k}}. \tag{5.64}$$

The first integral does not contain terms of the external force: it is the mean velocity in the x direction at thermal equilibrium condition which is zero[3]. Considering the change of variable:

$$d^3\mathbf{k} = 4\pi k^2 dk \propto E^{1/2} dE \tag{5.65}$$

the second term on the right side of the (5.64) can be rewritten as:

$$\langle v_x \rangle = -\frac{2eE_x}{3k_B T m^*} \frac{\int_0^\infty \tau E^{3/2} f_0 dE}{\int_0^\infty E^{1/2} f_0 dE} \tag{5.66}$$

[3]Positive and negative values are equally probable

where the E-k relation given by (5.55) and the v-k one ($v = \hbar k/m^*$) were used.
The f_0 function for non-degenerate semiconductor can be approximated by the Boltzmann distribution function (5.4). As a consequence the denominator term of the (5.66) can be rewritten with the use of the integration by parts:

$$\int_0^\infty E^{3/2} f_0 dE = \frac{3}{2} k_B T \int_0^\infty E^{1/2} f_0 dE \tag{5.67}$$

Substituting this last expression in the (5.66), the average velocity of the electrons is obtained as:

$$\langle v_x \rangle = -\frac{e\langle \tau \rangle}{m^*} E_x. \tag{5.68}$$

where $\langle \tau \rangle$ is the *average over energy* of the relaxation time. This average is computed as:

$$\langle \tau \rangle = \frac{\displaystyle\int_0^\infty \tau E^{3/2} f_0 dE}{\displaystyle\int_0^\infty E^{3/2} f_0 dE} \tag{5.69}$$

which is a measure of the scattering rate that is the average time between collision events (the mean free time).
The proportionality term between the drift velocity and the electric field is the drift mobility:

$$\mu = \frac{e\langle \tau \rangle}{m^*} \tag{5.70}$$

which depends on the mean free time $\langle \tau \rangle$. The effective mass m^* that has to be used to compute the mobility is the *conductivity effective mass* which is denoted by m_c^* and for electrons is given by [80]:

$$\frac{1}{m_{ce}^*} = \frac{1}{3}\left(\frac{1}{m_l^*} + \frac{2}{m_t^*}\right) \tag{5.71}$$

where m_l^* and m_t^* are longitudinal and transversal effective masses of the elliptical constant energy surface (see B.4). For holes the conductivity effective mass is given by:

$$\frac{1}{m_{ch}^*} = \frac{1}{3}\left(\frac{1}{m_{hh}^*} + \frac{1}{m_{lh}^*} + \frac{1}{m_{so}^*}\right) \tag{5.72}$$

where the subscript h, l and so refers to heavy hole, light hole and split-off valance band respectively[4].

[4]The conductivity effective mass, in practise, is a mean value of the charge effective mass when it moves on the energy surface of the corresponding band.

By substituting the $\langle v_x \rangle$ expression in the (5.61), the generalized Ohm's low is obtained:

$$J_x = \sigma E_x \tag{5.73}$$

where σ is the conductivity which is equal to:

$$\sigma = \frac{ne^2\langle\tau\rangle}{m^*} = en\mu. \tag{5.74}$$

The resistivity is simply given by the inverse of the conductivity:

$$\rho = \frac{1}{\sigma} = \frac{1}{en\mu}. \tag{5.75}$$

Analogous expressions for the holes resistivity and mobility can be derive.

For **compensated semiconductors**, the expressions of the total density of current and of the resistivity are given by:

$$J_x = J_e + J_h = \sigma E_x \tag{5.76}$$

$$\rho \equiv \frac{1}{\sigma} = \frac{1}{e(n\mu_e + p\mu_h)} \tag{5.77}$$

where μ_e and μ_h are electrons and holes mobilities which depend on the scattering mechanisms.

In **degenerate semiconductors**, the Fermi energy level E_F is located in the conduction band for a n-type material. As a consequence the term given by the (5.59) assumes a significant value only in vicinity of the Fermi energy level [79]. This means that the value $\partial f_0/\partial E$ can be considered as a Dirac δ-function. In addition the following relations hold [79]:

$$f_0 \simeq 1 \quad (\text{if } E \leq E_F) \tag{5.78}$$

$$f_0 \simeq 0 \quad (\text{if } E > E_F) \tag{5.79}$$

Considering the relations (5.58), (5.59) and (5.60), the electrons distribution function can be written in the more general form as:

$$f = f_0 + eE_x\tau v_x \frac{\partial f_0}{\partial E}. \tag{5.80}$$

Also in this case f_1, which is the second term of this latter expression, satisfies the condition $f_1 \ll f_0$ because the electric field E_x is supposed to be weak. The mean value of the velocity in the direction of the electric field, for a non-degenerate semiconductor, was computed by the relation (5.64). In this case it assumes the form:

$$\langle v_x \rangle = \frac{eE_x}{3} \frac{\int \tau v^2 \frac{\partial f_0}{\partial E} d^3\mathbf{k}}{\int f_0 d^3\mathbf{k}} \tag{5.81}$$

Making use of the change of variables (5.65) and of the relations $E = \hbar^2 k^2/(2m^*)$ and $v = \hbar k/m^*$, the (5.81) becomes:

$$\langle v_x \rangle = \frac{2eE_x}{3m^*} \frac{\int_0^\infty \tau E^{3/2} \frac{\partial f_0}{\partial E} dE}{\int_0^\infty E^{1/2} f_0 dE} \tag{5.82}$$

By means of the previous considerations, the denominator term can be computed as [79]:

$$\int_0^\infty E^{1/2} f_0 dE \simeq \int_0^\infty E^{1/2} dE = \frac{2}{3} E_F^{3/2} \tag{5.83}$$

while the numerator can be approximated by [79]:

$$\int_0^\infty \tau E^{3/2} \frac{\partial f_0}{\partial E} dE \simeq -\tau(E_F) E_F^{3/2} \tag{5.84}$$

The mean velocity (5.82) becomes:

$$\langle v_x \rangle = -\frac{e\tau(E_F)}{m^*} E_x \tag{5.85}$$

The mobility μ is then equal to:

$$\mu = \frac{e\tau(E_F)}{m^*} \tag{5.86}$$

In this case the relaxation time depends only on the energy of the Fermi level. By means of the (5.85) it is possible to write the current density as [79]:

$$J_x = \frac{e^2 n \tau(E_F)}{m^*} E_x = \sigma E_x \tag{5.87}$$

where σ is the conductivity which is equal to:

$$\sigma = \frac{e^2 n \tau(E_F)}{m^*} = en\mu \tag{5.88}$$

The resistivity is then simply given by:

$$\rho = \frac{1}{en\mu}. \tag{5.89}$$

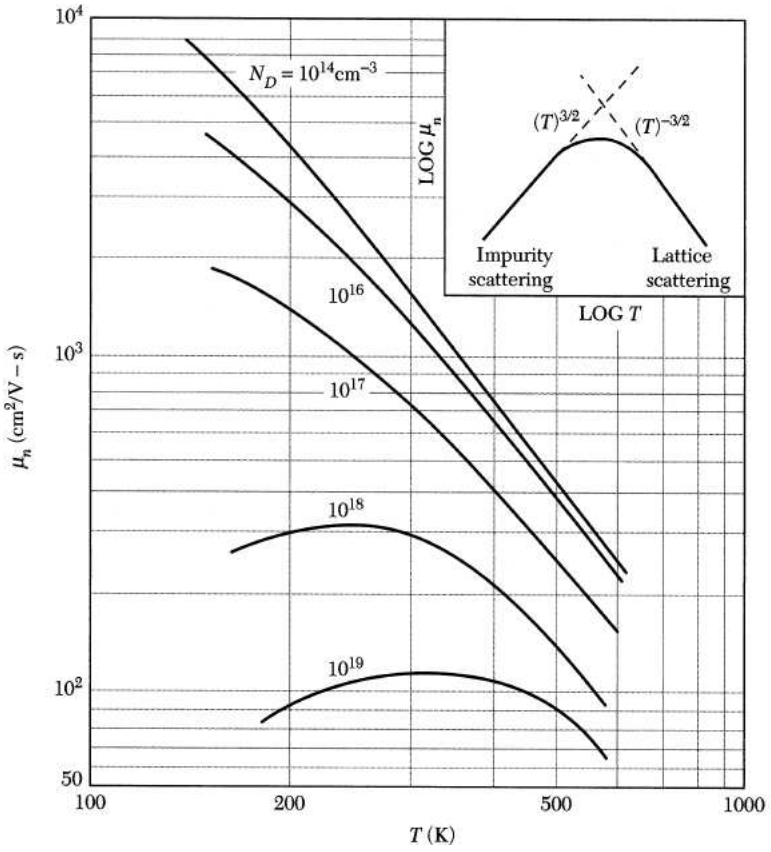

Figure 5.6: The temperature behavior of the electron mobility in a silicon sample for different donor concentrations

5.4 Scattering and Mobility

The collision mechanism involves different scattering processes. The more important are acoustic phonon scattering which dominates at high temperatures, and scattering with impurity atoms which can be ionized or neutral according to the temperature. Impurity atoms are always present inside the material. At low temperatures the scattering of impurity atoms dominates over the acoustic phonon scattering. The temperature behavior of the electron mobility for a silicon sample is reported in figure 5.6 for different donor concentrations. In the same figure the theoretical dependence on temperature for a pure lattice and a pure phonon scattering process are also reported.

The carriers mobility depends on every scattering process. Its total ex-

pression is given by:

$$\mu_{tot} = \frac{e\langle\tau_{tot}\rangle}{m_c^*} \tag{5.90}$$

where the total relaxation time τ_{tot} is computed as:

$$\frac{1}{\tau_{tot}} = \sum_i \frac{1}{\tau_i} \tag{5.91}$$

and the sum is extended to the all possible scattering mechanisms.

5.4.1 Acoustic Phonon Scattering

Carriers, moving inside the material, are scattered by phonons induced by lattice vibrations. This mechanism can be described by the deformation potential theory which quantifies the energy change of an electron due to the crystal lattice deformation. The variation of the energy band, δE, is supposed to be proportional to the variation of the crystal volume δV which is induced by the acoustic deformation [79]:

$$\delta E = D_{ac}\frac{\delta V}{V} \tag{5.92}$$

where D_{ca} is the deformation potential. The relaxation time for acoustic phonon scattering is given by [79]:

$$\tau_{ac} = \frac{2\pi\hbar^4\rho_c v_s^2}{(2m_d^*)^{2/3}D_{ac}^2\ k_B T}E^{-1/2} \tag{5.93}$$

where ρ_c is the crystal density and v_s is the velocity of sound, m_d^* is the density of state effective mass (see equations (B.28) and (B.30)). Making use of this expression for the relaxation time and of the relation (5.69), it is possible to compute the mean free time for acoustic scattering, $\langle\tau_{ac}\rangle$. The mobility definition is then given by [79]:

$$\mu_{ac} = \frac{2^{3/2}\pi^{1/2}e\hbar^4\rho_c v_s}{3m_d^{*3/2}m_c^* D_{ac}^2}(k_B T)^{-3/2} \tag{5.94}$$

where the temperature dependence indicates that the mobility decreases with increasing temperature ($T^{-3/2}$ see figure 5.6). Relations (5.93) and (5.94) are valid for both type of carriers with $m_d^* = m_{de}^*$ and $m_c^* = m_{ce}^*$ for electrons or $m_d^* = m_{dh}^*$ and $m_c^* = m_{ch}^*$ for holes.

5.4.2 Ionized Impurity Scattering

Semiconductors contain may impurity atoms which can be donors, acceptors or unwished atoms. At ordinary temperatures, the impurity atoms result to be ionized. The ionized atoms produce a Coulomb potential which deviated the electrons and holes trajectories. The relaxation time for the Coulomb scattering of electrons was deriver by Conwell and Wiesskopf [81] and subsequently it was redefined by *Brooks and Herring* [82] which took into account the screening effect of the Coulomb potential by inner electrons. The *Brooks-Herring* formula is [80], [79]:

$$\tau_{BH} = \frac{16\pi\epsilon^2(2m^*)^{1/2}}{Z^2e^4N_I}E^{3/2}\left[\log(1+\xi)-\frac{\xi}{1+\xi}\right]^{-1} \tag{5.95}$$

$$\xi = \frac{8\epsilon m^* k_B T}{\hbar^2 e^2 n}E \tag{5.96}$$

where ϵ is the dielectric constant of the semiconductor, Z is the charge of the impurity atom and N_I is the impurity atom concentration. The electron mobility for the *Brooks-Herring* formula is derived by computing the integral (5.69) which was simplified by setting the E term in the logarithmic expression equal to $3k_BT$ (when $E = 3k_BT$ the relaxation time (5.95) assumes its maximum value). The expression for the mobility is then given by [79]:

$$\mu_{BH} = \frac{64(\pi)^{1/2}\epsilon^2}{Z^2e^3N_Im^{*1/2}}(2k_BT)^{3/2}\left[\log(1+\xi_0)-\frac{\xi_0}{1+\xi_0}\right]^{-1} \tag{5.97}$$

$$\xi_0 = \frac{24\epsilon m^*(k_BT)^2}{\hbar^2e^2n} \tag{5.98}$$

where the temperature dependence indicates that the mobility increases with increasing temperature ($T^{3/2}$ see figure 5.6).

5.4.3 Neutral Impurity Scattering

At low temperatures, donor and acceptor atoms are no longer ionized and behave as neutral impurity atoms. As a consequence the contribution to the Coulomb scattering is null.
The wave function of the electron captured by the impurity atom extends over a distance which is grater than the lattice constant. This distance is the Bohr effective radius a_I and it is equal to [83]:

$$a_I = \frac{\epsilon/\epsilon_0}{m^*/m}a_0 \tag{5.99}$$

where a_0 is the Bohr radius. The scattering cross section for electron-neutral atom interaction has been derived by Erginsoy [84] who gave an approximated expression for the total scattering cross section i.e.:

$$\sigma_I = \frac{20a_I}{k} \tag{5.100}$$

which is valid for $ka_I \leq 0.5$.
If n_I is the density of neutral impurity atoms then the mean free path between collisions is equal to:

$$l_I = \frac{1}{n_I \sigma_I} \tag{5.101}$$

which gives a time between successive collision equal to [83]:

$$\tau_I = \frac{l_I}{v} = \frac{1}{n_I \sigma_I} \frac{m^*}{\hbar k} \tag{5.102}$$

$$= \frac{m^*}{\hbar 20 a_I} \frac{1}{n_I} \tag{5.103}$$

By using this relaxation time, the mobility of electrons is simply given by:

$$\mu_I = \frac{e}{\hbar 20 a_I} \frac{1}{n_I} \tag{5.104}$$

which is inversely proportional to the neutral impurity atom concentration n_I.

5.4.4 Semi-Empirical Relations for Carriers Mobility

The electrons and hales mobilities experimental data can be found in literature for different doping concentration, as a function of temperature [85].
Arora et al. [86] derived semi-empirical relations for the electrons and holes mobilities by fitting experimental data. In the temperature interval where acoustic phonon scattering dominates, they proposed the following fitting curves for the lattice scattering mobilities:

$$\mu_{Le} = 8.56 \times 10^8 T^{-2.33} \quad [200 - 500] \text{ K} \tag{5.105}$$

$$\mu_{Lh} = 1.58 \times 10^8 T^{-2.23} \quad [150 - 400] \text{ K} \tag{5.106}$$

which are valid for electrons and holes respectively.
Using the *Brooks-Herring* formula (5.95) Arora derived the ionized scattering

mobility for a n-type material as:

$$\mu_{Ie} = \frac{7.3 \times 10^{17}}{F(\xi_0) N_I} T^{3/2} \tag{5.107}$$

$$F(\xi_0) = \log(1+\xi_0) - \frac{\xi_0}{1+\xi_0} \tag{5.108}$$

$$\xi_0 = \frac{1.52 \times 10^{15}}{n'} T^2 \tag{5.109}$$

$$n' = n\left(2 - \frac{n}{N_d}\right) \tag{5.110}$$

where N_d is the donor concentration, and N_I is the ionized impurity one. A similar expression of the ionized scattering mobility was given for a p-type material:

$$\mu_{Ih} = \frac{5.6 \times 10^{17}}{F(\xi_0) N_I} T^{3/2} \tag{5.111}$$

$$\xi_0 = \frac{2.5 \times 10^{15}}{p'} T^2 \tag{5.112}$$

$$p' = p\left(2 - \frac{p}{N_a}\right) \tag{5.113}$$

where N_a is the acceptor atom concentration.
The total mobility could be obtained simply by applying the *Matthiessen*'s rule:

$$\mu = \left(\frac{1}{\mu_L} + \frac{1}{\mu_I}\right)^{-1} \tag{5.114}$$

but experimental data don't follow this relation demonstrating that the two scattering mechanisms are not fully independent. Arora gave the following empirical relations for total electrons and holes mobilities as a function of temperature and dopant concentration [86]:

$$\mu_e = 88\ T_o^{-0.57} + \frac{7.4 \times 10^8\ T^{-2.33}}{1 + \left[N_d/(1.26 \times 10^{17}\ T_o^{2.4})\right] 0.88\ T_o^{-0.146}} \tag{5.115}$$

$$\mu_h = 54.3\ T_o^{-0.57} + \frac{1.36 \times 10^8\ T^{-2.23}}{1 + \left[N_a/(2.35 \times 10^{17}\ T_o^{2.4})\right] 0.88\ T_o^{-0.146}} \tag{5.116}$$

$$T_o = \frac{T}{300}$$

These curves were derived from the fit of data in the temperature range $[250 - 500]$ K and for doping concentration up to 10^{20} cm^{-3}.

An alternative empirical relation to model both scattering mechanisms, was proposed by *Caughey* and *Thomas* for electron and hole mobilities [87]:

$$\mu = \mu_{min} + \frac{\mu_{pho} - \mu_{min}}{1 + (N/N_{ref})^{\gamma}} \tag{5.117}$$

where μ_{pho} is the acoustic phonon scattering mobility, and the experimental values for the fitting parameters can be find in [80]:

$$\begin{aligned}
\mu_{min\ e} &= (197.17 - 45.505\ \log(T)) && (5.118)\\
\mu_{min\ h} &= (110.90 - 25.597\ \log(T)) && (5.119)\\
N_{ref\ e} &= 1.12 \times 10^{17}\ T_o^{3.2} && (5.120)\\
N_{ref\ h} &= 2.23 \times 10^{17}\ T_o^{3.2} && (5.121)\\
\gamma_e &= \gamma_h = 0.72\ T_o^{0.065} && (5.122)
\end{aligned}$$

which are valid in the temperature range $[4.2 - 300]$ K and for doping concentrations up to 10^{19} cm^{-3}.

The computation of the mobility in presence of acoustic phonon scattering as it was derived by equation (5.94), is quite difficult because the phonons energies and the energies of the electrons inside the crystal have to be known. A mathematical method to compute μ_{pho} was proposed by *Sha* [88], [80]:

$$\mu_{pho} = \left(\frac{T_o^{\alpha}}{\mu_{0a}} + \frac{T_o^{\beta}}{\mu_{0b}} \right)^{-1} \tag{5.123}$$

where for electrons $\mu_{0ae} = 4195\text{cm}^2/(\text{V s})$, $\mu_{0be} = 2153\text{cm}^2/(\text{V s})$, $\alpha_e = 1.5$, $\beta_e = 3.13$,and for holes $\mu_{0ah} = 2502\text{cm}^2/(\text{V s})$, $\mu_{0bh} = 591\text{cm}^2/(\text{V s})$, $\alpha_h = 1.5$, $\beta_h = 3.25$.

5.5 The Hall Effect

When an electric fiend and a magnetic field are applied to a conductor in perpendicular directions to each other, inside the material there is the generation of another electric field oriented in the third perpendicular direction. This phenomena is called *Hall effect* and it is often used to measure the electrical characteristics of a semiconductor. Under the assumption that (1) the sample is infinitely long (2) the effective mass is isotropic, and (3) all electrons have the same velocity and constant relaxation time, a qualitative idea of the Hall effect can be given [90]. A n-type semiconductor is considered first; for a p-type one the issue is analogous.

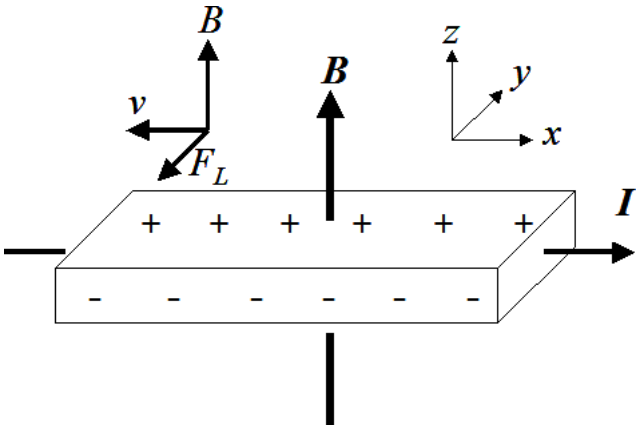

Figure 5.7: Scheme of the Hall effect geometry for electrons moving carriers inside an ideal infinite sample. Positive (+) and negative (-) signs refer to charge accumulation on the y sample direction.

When an electric field is applied to a n-type sample, inside the material flows a density of current $\mathbf{J}$ and the conductive electrons move with drift velocity $\mathbf{v}$. In addition when a magnetic field $\mathbf{B}$ is applied, electrons experience the Lorentz's force $\mathbf{F}_L = -\mathbf{ev} \times \mathbf{B}$. If the current flows in the positive x direction, and the magnetic field is in the z direction, electrons will be accelerated by the Lorentz's force $F_{L,y} = -e(-v_x)B_z$ in the -y direction, as shown in figure 5.7. In this way electrons will move on the -y side of the sample leaving in the $+y$ side immobile positive charges (donors). Because of this charge accumulation, an electric field E_y, oriented in the -y direction, will be induced. This electric field, called *Hall Field*, will prevent further accumulation of negative charges on the -y side of the sample and, in the steady state condition, it will balance the Lorentz's force $F_{L,y} + (-e)E_y = 0$. The Hall Field is given by:

$$E_y = \frac{F_{L,y}}{e} = v_x B_z = -\frac{J_x B_z}{ne} \tag{5.124}$$

or equivalently:

$$E_y = R_H J_x B_z \tag{5.125}$$

where the proportionality term between the induced electric field E_y and the term $J_x B_z$ is the *Hall coefficient* defined as:

$$R_H = -\frac{1}{ne}. \tag{5.126}$$

With the appropriate signs convention it is possible to obtain the *Hall coefficient* also for a p-type semiconduct as:

$$R_H = \frac{1}{pe}. \tag{5.127}$$

The Hall coefficient is inversely proportional to the carriers concentration and indicates the type of conducting carriers by the sign.

This simplified description was derived with the hypothesis that the relaxation time does not depend on the particle energy. If the energy dependence of the relaxation time is considered, then for a n-type sample the Hall coefficient is equal to [90]:

$$R_H = -\frac{r_H}{ne}. \tag{5.128}$$

where r_H is the Hall scattering factor which depends on the overall relaxation time and as a consequence, depends on every scattering process. The r_H values are given in literature [82], [89], [94] for different temperatures and ionized impurity concentration. It will be discussed in section 5.5.1.

R_H can be derived from experimental measurements. If w and t are the width and the thickness of the sample under test, then the current which flows inside of it, is $I_x = J_x wt$. The Hall voltage, which is given by $V_H = E_y w$ with E_y expressed by the (5.125), is equal to:

$$V_H = \frac{R_H}{t} I_x B_z. \tag{5.129}$$

By measuring the Hall voltage, R_H is obtained. If with experimental techniques the resistivity of the sample is measured too, then the (5.75) enables one to obtain the *Hall mobility* which is define as:

$$\mu_H \equiv \frac{|R_H|}{\rho} = r_H \mu. \tag{5.130}$$

The hall mobility differs from the (drift) mobility μ by the Hall scattering factor.

5.5.1 The Hall Scattering Factor

Inside the material, the equation of motion of a single electron under the influence of an electric and a magnetic field, is [79]:

$$m^* \frac{d\mathbf{v}}{dt} + m^* \frac{\mathbf{v}}{\tau} = -e(\mathbf{E} + \mathbf{v} \times \mathbf{B}) \tag{5.131}$$

where the relaxation time τ is considered to be constant so that $\langle\tau\rangle = \tau$ and the effective mass m^* is supposed to be isotropic. In the steady state condition, the particle velocity can be computed by:

$$\mathbf{v} = -\frac{e\tau}{m^*}(\mathbf{E} + \mathbf{v} \times \mathbf{B}) \tag{5.132}$$

In general, if the electric field is in the x direction and the magnetic field is oriented along the z axis, the motion of the electron has a drift component along the -x direction superimposed on an orbital motion which takes place in the xy plane[5]. The angular frequency of the orbital motion is equal to the *cyclotron frequency* defined as:

$$\omega_c \equiv \frac{eB_z}{m^*}. \tag{5.133}$$

However an electron inside the material will be continuously scattered by the collision processes which deviates its trajectory. The relaxation time is related to the electron mobility by (5.70) and so it is possible to obtain the relation:

$$\omega_c\tau = \mu B_z \tag{5.134}$$

which enables to distinguish between high and low external magnetic file conditions. If the electron is scattered with relaxation time shorter compared to the time taken to complete the cyclotron orbit, then the orbital motion will be disturbed and the trajectory will be more similar the one of a random walk along the -x direction. On the contrary, if the relaxation time is long, the electron completes many orbits before been scattered. These set the low and high magnetic file conditions:

$$\omega_c\tau = \mu B_z \ll 1 \quad (\text{low } \mathbf{B}) \tag{5.135}$$

$$\omega_c\tau = \mu B_z \gg 1 \quad (\text{high } \mathbf{B}) \tag{5.136}$$

under which different values of the Hall coefficient are obtained[6].

From the equation (5.132) it is possible to derive the components of the velocity and since $\mathbf{J} = -en\mathbf{v}$ the ones of the current density are obtained

[5]The orbital motion is induced by the Lorentz's force.

[6]The high $\mathbf{B}$ condition is achieved for magnetic fields grater than about 100 kGauss

too, i.e. [79]:

$$J_x = \frac{ne^2}{m^*}\left[\frac{\tau}{1+\omega_c^2\tau^2}E_x - \frac{\omega_c\tau^2}{1+\omega_c^2\tau^2}E_y\right] \tag{5.137}$$

$$J_y = \frac{ne^2}{m^*}\left[\frac{\omega_c\tau^2}{1+\omega_c^2\tau^2}E_x + \frac{\tau}{1+\omega_c^2\tau^2}E_y\right] \tag{5.138}$$

$$J_z = \frac{ne^2}{m^*}\tau E_z \tag{5.139}$$

Equations (5.137) and (5.138) can be written in the more compacted form as:

$$J_x = \sigma_{xx}E_x + \sigma_{xy}E_y \tag{5.140}$$

$$J_y = \sigma_{yx}E_x + \sigma_{yy}E_y. \tag{5.141}$$

These last expression together with the (5.139) enable one to write the generalized Ohm's low:

$$\mathbf{J} = \underline{\underline{\boldsymbol{\sigma}}}\mathbf{E} \tag{5.142}$$

where $\underline{\underline{\boldsymbol{\sigma}}}$ is the conductivity tensor which is equal to [75] [79]:

$$\underline{\underline{\boldsymbol{\sigma}}} = \begin{pmatrix} \sigma_{xx} & \sigma_{xy} & 0 \\ \sigma_{yx} & \sigma_{yy} & 0 \\ 0 & 0 & \sigma_{zz} \end{pmatrix} \tag{5.143}$$

The components of the conductivity tensor are equal to [79]:

$$\sigma_{xx} = \sigma_{yy} = \frac{ne^2}{m^*}\frac{\tau}{1+\omega_c^2\tau^2} \tag{5.144}$$

$$\sigma_{xy} = -\sigma_{yx} = -\frac{ne^2}{m^*}\frac{\omega_c\tau^2}{1+\omega_c^2\tau^2} \tag{5.145}$$

$$\sigma_{zz} = \frac{ne^2}{m^*}\tau. \tag{5.146}$$

With these expressions it is possible to obtain a relation between the Hall coefficient and the conductivity tensor components. The condition to measure the Hall coefficient is to impose $J_y = 0$. Using equations (5.140) and (5.141) it is possible to get:

$$J_x = \frac{\sigma_{xx}^2 + \sigma_{xy}^2}{\sigma_{xx}}E_x \tag{5.147}$$

$$E_y = \frac{\sigma_{xy}}{\sigma_{xx}}E_x \tag{5.148}$$

which can be substituted in the (5.125) to obtain [79]:

$$R_H = \frac{\sigma_{xy}}{\sigma_{xx}^2 + \sigma_{xy}^2} \frac{1}{B_z} \tag{5.149}$$

The sign of R_H is defined by the σ_{xy} component of the conductivity tensor[7] given by the equation (5.145).

This result is for one electron. Inside the material, however, there are many conductive electrons which have different velocities and relaxation times. If electrons are distributed according to a known distribution function f, it is possible to derive an expression analogous to the (5.149) by the calculation of the mean value of the velocity components. This enables to get the expression for the Hall coefficient valid for an arbitrary magnetic field strength oriented along the z axis:

$$R_H = \frac{\langle \sigma_{xy} \rangle}{\langle \sigma_{xx} \rangle^2 + \langle \sigma_{xy} \rangle^2} \frac{1}{B_z} \tag{5.150}$$

where average $\langle\ \rangle$ is taken over carriers energy (see equation (5.69)).
Whit some manipulation, it is possible to obtain the general expression of the Hall coefficient and of the scattering factor [79]:

$$R_H = -\frac{r_H}{en} \tag{5.151}$$

$$r_H = \frac{\left\langle \dfrac{\tau^2}{1+\omega_c^2\tau^2} \right\rangle}{\left\langle \dfrac{\tau}{1+\omega_c^2\tau^2} \right\rangle^2 + \omega_c^2 \left\langle \dfrac{\tau^2}{1+\omega_c^2\tau^2} \right\rangle^2}. \tag{5.152}$$

In the limit of high magnetic field $\omega_c\tau \gg 1$, and so $r_H \simeq 1$. For a n-type material, the Hall coefficient reduces to:

$$R_H \simeq -\frac{1}{ne} \quad \text{(high } \mathbf{B}\text{)}. \tag{5.153}$$

In the low magnetic field limit $\omega_c\tau \ll 1$, the Hall coefficient and the scattering factor become:

$$R_H = -\frac{r_H}{ne} \quad \text{(low } \mathbf{B}\text{)} \tag{5.154}$$

$$r_H \simeq \frac{\langle \tau^2 \rangle}{\langle \tau \rangle^2} \tag{5.155}$$

[7] For a p-type material the result is analogous but the effective mass m^* is the hole one and the sign of σ_{xy} is positive.

where the average is computed by means of (5.69). An analogous expression can be obtained for a p-type material. Since the relaxation time depends on the effective mass of the particle, electrons end holes have different Hall scattering factors.

To calculate r_H it is necessary to know the distribution function f of the charges and the energy dependence of the relaxation time. If f is equal to the Boltzmann distribution function (equation 5.4) and $\tau = aE^{-s}$, then the Hall scattering factor can be computed by [90] [79]:

$$r_H = \frac{\Gamma(\frac{5}{2} - 2s)\Gamma(\frac{5}{2})}{[\Gamma(\frac{5}{2} - s)]^2} \tag{5.156}$$

where Γ is the gamma function defined as:

$$\Gamma(p) = \int_0^\infty x^{(p-1)} e^{-x} dx \tag{5.157}$$

with properties: $\Gamma(p+1) = p\Gamma(p)$; if p is an integer then $\Gamma(p+1) = p!$, if $p = 1/2$ then $\Gamma(1/2) = \sqrt{\pi}$.
If the scattering process is the acoustic phonon scattering, then $s = 1/2$ and the r_H expression given by the (5.156) is equal to:

$$r_H = \frac{3\pi}{8} = 1.18 \tag{5.158}$$

very close to 1 and so the Hall mobility is almost equal the drift mobility.
For ionized impurity scattering $s = -3/2$ and so the Hall scattering factors is equal to:

$$r_H = \frac{315\pi}{512} = 1.93 \ . \tag{5.159}$$

In this case the Hall mobility is almost twice the drift one. For the non ionizing scattering process the relaxation time is energy independent, so $s = 0$ gives $r_H = 1$.

In general all scattering processes are contemporaneously present, as a consequence the Hall scattering factor assumes an intermediate value which will be closer to the dominant scattering mechanism and will vary with temperature. The Hall scattering factor can be experimentally determined from the ratio between the R_H measured in the low **B** condition and the one obtained in the high **B** condition. In figures 5.8 and 5.9 are reported the experimental and the theoretical r_H values as a function of temperature and of donors concentration for a n-type semiconductor.

For a degenerate semiconductor the relaxation time doesn't have to be mean over energy, $\langle\rangle$, because the term $\partial f_0/\partial E$ in the distribution function

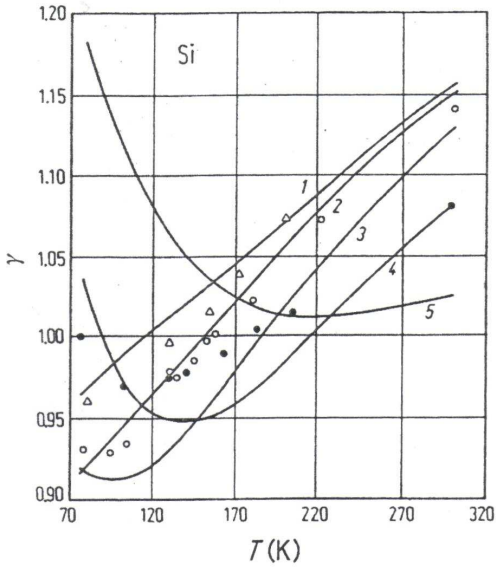

Figure 5.8: Hall scattering factor (γ) versus temperature (T) for n-type silicon. Experimental data (N_I is the ionized impurity concentration):$\triangle$ ($N_I = 2 \times 10^{13}$ cm^{-3}); $\circ$ ($N_I = 1.5 \times 10^{14}$ cm^{-3}); $\bullet$ ($N_I = 4.6 \times 10^{15}$ cm^{-3}). Theoretical lines: 1 ($N_I = 1 \times 10^{13}$ cm^{-3}); 2 ($N_I = 1 \times 10^{14}$ cm^{-3}); 3 ($N_I = 1 \times 10^{15}$ cm^{-3}); 4 ($N_I = 1 \times 10^{16}$ cm^{-3});5 ($N_I = 1 \times 10^{17}$ cm^{-3}) [85], [96]

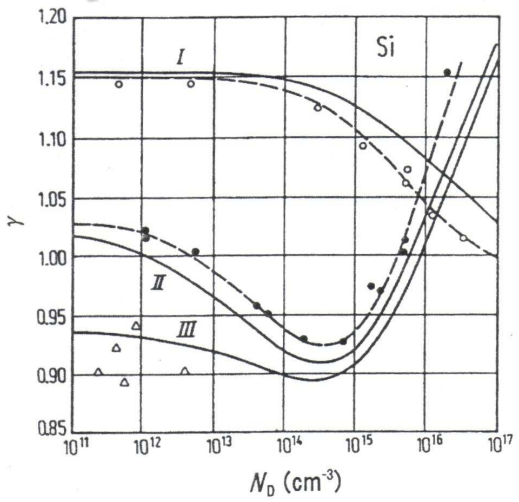

Figure 5.9: Hall scattering factor (γ) versus impurity concentration N_D for n-type silicon. Experimental data:$\bullet$ ($T = 77$ K); $\circ$ ($T = 300$ K); $\triangle$ ($T = 77$ K, low mobility sample). Theoretical lines: I ($T = 300$ K); II ($T = 77$ K); III ($T = 77$ K, additional neutral impurities with 6×10^{16} cm^{-3}) [95] [94]

assumes a significant value only near the Fermi energy level (see equation (5.84)). As a consequence the Hall scattering factor is almost equal to unity ($r_H \simeq 1$) and the Hall mobility can be considered equal to the drift one. The Hall factor is then simply given by $R_H = -1/en$ or by $R_H = 1/ep$ according to the doping type. In addition, since the carriers concentration is equal to the one of dopant atoms for all temperatures, the Hall coefficient is expected to be almost constant with temperature.

5.5.2 Hall Coefficient in Compensated Semiconductors

For a compensated semiconductor the general expression for the Hall coefficient is given by [79] [75]:

$$R_H = \frac{\langle\sigma_{xy}\rangle_p + \langle\sigma_{xy}\rangle_n}{[\langle\sigma_{xx}\rangle_p + \langle\sigma_{xx}\rangle_n]^2 + [\langle\sigma_{xy}\rangle_p + \langle\sigma_{xy}\rangle_n]^2 B_z} \tag{5.160}$$

where p and n indexes refer to electrons and holes which can be of majority or of minority type according to the level of compensation. In the limit of low magnetic field, the (5.160) reduces to [76]:

$$R_H = \frac{p\mu_h^2 r_{Hh} - n\mu_e^2 r_{He}}{e(p\mu_h + n\mu_e)^2} \quad (\text{low } \mathbf{B}) \tag{5.161}$$

where $r_{Hh},\ \mu_h$ and $r_{He},\ \mu_e$ are the Hall scattering factors and mobilities for holes and electrons respectively. The sign of the Hall coefficient depends on the numerator term. According to the relative doping concentration of donors and acceptors atoms, the sign may be positive or negative.

Chapter 6

Experimental Results of the Hall Effect Measurements

In this chapter experimental results of the Hall effect are reported [102]. We performed measurements on silicon bulk samples of different resistivities which are usually employed as substrates for the fabrication of devices used during space missions. Measurements were performed before and after irradiation with neutrons and carbon ions. Temperature scans from 300 K down to 11 K of the Hall coefficient, the resistivity and the Hall mobility are reported.

6.1 Samples Characteristics and Irradiation Fluences

Our samples are silicon bulk of n-type doped with phosphorus (P) and of p-type doped with boron (B) of different resistivities. They are squares with a surface area of 1 cm^2 and they have a thickness of 400 μm.
The resistivities before irradiation can be classified in:

- very-low (0.01 Ω cm)
- low (56 Ω cm)
- medium (157 Ω cm)
- high (2500 Ω cm)
- very-high (7000 Ω cm)

Type	ρ	N_{dopant}	Irradiated with
p	0.01	$\sim 1 \times 10^{19}$	Carbon ions
n	0.01	$\sim 5 \times 10^{18}$	Carbon ions
n	56	$\sim 8 \times 10^{13}$	Neutrons
n	157	$\sim 3 \times 10^{13}$	Neutrons
n	2500	$\sim 2 \times 10^{12}$	Neutrons
n	7000	$\sim 7 \times 10^{11}$	Carbon ions

Table 6.1: Type, doping concentration and resistivity of the silicon bulk samples before irradiation with the corresponding irradiation particles. The resistivity ρ is given in units of Ω cm; the doping concentration N_{dopant} is given in units of cm^{-3}.

The corresponding doping concentrations N_d and N_a were calculated at $T =$ 300 K by means of the relation (5.75):

$$N_d \simeq \frac{1}{e\rho\mu_e} \quad ; \quad N_a \simeq \frac{1}{e\rho\mu_h} \tag{6.1}$$

where it was considered than at this temperature the carriers concentrations are $n \simeq N_d$ and $p \simeq N_a$ (see section 5.1.3). For this computation the electrons and the holes mobilities were calculated by means of the semi-empirical formulas of Arora et al. [86] which were reported in equations (5.115) and (5.116). The resistivities and the doping concentrations before irradiation are listen in table 6.1 with the corresponding particles of irradiation.

Low, medium and high resistivities samples, in addition, contain an oxygen concentration of 6.4×10^{17} cm^{-3}, 4.7×10^{17} cm^{-3} and 0.7×10^{17} cm^{-3} respectively. The oxygen enrichment should diminish the reduction of the effective doping concentration N_{eff} after irradiation, as was explained in section 3.3. Very-low resistivities samples are degenerate semiconductors with a doping concentration of about $N_a \simeq 10^{19}$ cm^{-3} and $N_d \simeq 5 \times 10^{18}$ cm^{-3} for p and n-type respectively. For these samples, as was explained in section 5.1.5, the carriers concentration is almost equal to the doping concentration for all temperatures. Very-high resistivities samples have a doping concentration of about $N_d \simeq 7 \times 10^{11}$ cm^{-3} not far from the silicon intrinsic carriers concentration (as reported in section 5.1.2, $n_i = 1.45 \times 10^{10}$ cm^{-3})

Low, medium and high resistivities samples were irradiated with fast neutrons at the $\Sigma\Sigma$-facility of Bucarest [100]. The neutrons energy range was 10 keV - 18 MeV, and the mean energy value was about 0.827 MeV. The irradiation flux was $3.385\times$ 10^9 n cm^{-2} s^{-1}. The obtained fluences were in the range form 6.1×10^{11} n/cm^2 to 1.0×10^{15} n/cm^2. The Frenkel-pairs (FP)

concentration can be estimated by means of equation (3.21) i.e.:

$$FP = \frac{\xi E_{dis}}{2T_d} \tag{6.2}$$

where $\xi = 0.8$, T_d is the threshold displacement energy and E_{dis} is the neutron displacement energy density which is given in equation (3.31). By the use of the ASTM standard, $D(1\text{MeV}) = 95 \times 10^{-27}$ MeV cm^2, and of the relation (3.35), the displacement energy density can be computed by:

$$E_{dis} = N \int_{E_{min}}^{E_{max}} D(E)\ \Phi(E) dE = N D(1\text{MeV}) \Phi_n^{1\text{MeV}} \tag{6.3}$$

where $N = 5.01 \times 10^{22}$ is the silicon atom density. The term $\Phi_n^{1\text{MeV}}$ is the 1 MeV neutron equivalent fluence which is related to the neutron fluence Φ_n of the $\Sigma\Sigma$ reactor by means of the equation (3.32) i.e.:

$$\Phi_n^{1\text{MeV}} = \kappa \Phi_n \tag{6.4}$$

where $\kappa \simeq 0.704$ is the hardness parameter of the $\Sigma\Sigma$ reactor [100]. By means of this last relation, the (6.3) can be written as:

$$E_{dis} = N D(\text{MeV}) \kappa \Phi_n \tag{6.5}$$

Substituting this last expression of E_{dis} in the FP equation (6.2) with a displacement threshold energy $T_d = 25$ eV, it is possible to obtain:

$$FP \simeq 54.7\ \Phi_n \quad [\text{cm}^{-3}] \tag{6.6}$$

Very-low and very-high resistivities samples were irradiated by carbons ions of energy 1.14 GeV (95 MeV/nucleon). This irradiation took place at the GANIL facility near Caen. Six fluences were obtained in the range from 5.4×10^{10} to 1.0×10^{13} ions/cm^2. The concentration of FP for this irradiation fluences were previously calculated by Codegoni et al. [101] by means of the Monte Carlo simulation code TRIM [98]. Assuming a threshold energy of $T_d = 25$ eV, they obtained:

$$FP \simeq 1.2 \times 10^3\ \Phi_{^{12}C} \quad [\text{cm}^{-3}] \tag{6.7}$$

where $\Phi_{^{12}C}$ is the carbon irradiation fluence.

In addition, by means of the NIEL-Dose equation (3.22) and of the FP one given by (6.2), it is also possible to calculated the absorbed NIEL-Dose for theses FP concentrations i.e.:

$$D^{NIEL} = \frac{FP \times 2T_d}{6.24 \times 10^9 \xi \rho_{Si}} \ \ [\text{Gy}] \tag{6.8}$$

where $\rho_{Si} = 2.33$ g/cm^3 is the silicon density. Values of the neutrons and of the carbons fluences together with the FP concentrations and the NIEL-Dose are listed in table 6.2.

Neutrons			Carbon ions		
Φ_n	FP	D^{NIEL}	$\Phi_{^{12}C}$	FP	D^{NIEL}
n cm^{-2}	cm^{-3}	Gy	ion cm^{-2}	cm^{-3}	Gy
6.1×10^{11}	3.3×10^{13}	0.142	5.4×10^{10}	6.4×10^{13}	0.275
1.3×10^{12}	7.1×10^{13}	0.305	1.1×10^{11}	1.3×10^{14}	0.559
3.0×10^{12}	1.6×10^{14}	0.688	5.1×10^{11}	6.3×10^{14}	2.71
1.1×10^{13}	6.0×10^{14}	2.58	1.0×10^{12}	1.2×10^{15}	5.16
4.5×10^{13}	2.5×10^{15}	10.8	5.0×10^{12}	6.2×10^{15}	26.7
1.1×10^{14}	6.0×10^{15}	25.8	1.0×10^{13}	1.2×10^{16}	51.6
1.1×10^{15}	5.5×10^{16}	236			

Table 6.2: Fluences, FP concentrations and absorbed NIEL-Doses induced by neutrons and carbon ions.

6.2 Experimental Setup and Method

The samples were mounted on a fiberglass base covered on both sides with a copper layer. The electrical-insulation and the thermal conduction were guarantied by a thermal-conducting glue suitable for low temperatures. Four Ohmic contacts were made at the corners of the sample with ultrasonic thermal-compression bonding by means of an Heavy Wire Bonder (Orthodyne Model 20). An aluminium-silicon[1] wire, with a diameter of 100 μm, was used.

All measurements were performed using a constant current source (DC mode) with power supplied by a generator current (Keithley 220). An electrometer was used to control the current which flows inside the sample (Keithley 617). The potential difference between contacts was measured by means of a digital multimeter with high input impedance (>10 G ohm) (Keithley 196). All these instruments were connected with the sample by an Hall Effect Card (Keithley 7065) that controlled all the contacts of the circuit. The magnetic field, for the Hall coefficient measurements, was supplied by an electromagnet (Oxford instrument) capable of generating 3000 Gauss, of both polarities. The samples were mounted on the could-finger of a cryostat (ADP) which is able to reach a minimum temperature of 11 K. The temperature was kept constant by a temperature indicator-controller (Scientific Instruments Model 5500). The experimental setup was connected to a data acquisition system developed in the `LabView 8.0` environment. Experimental setup and pictures of instruments are reported in figure 6.1.

[1] Al 99%, Si 1%.

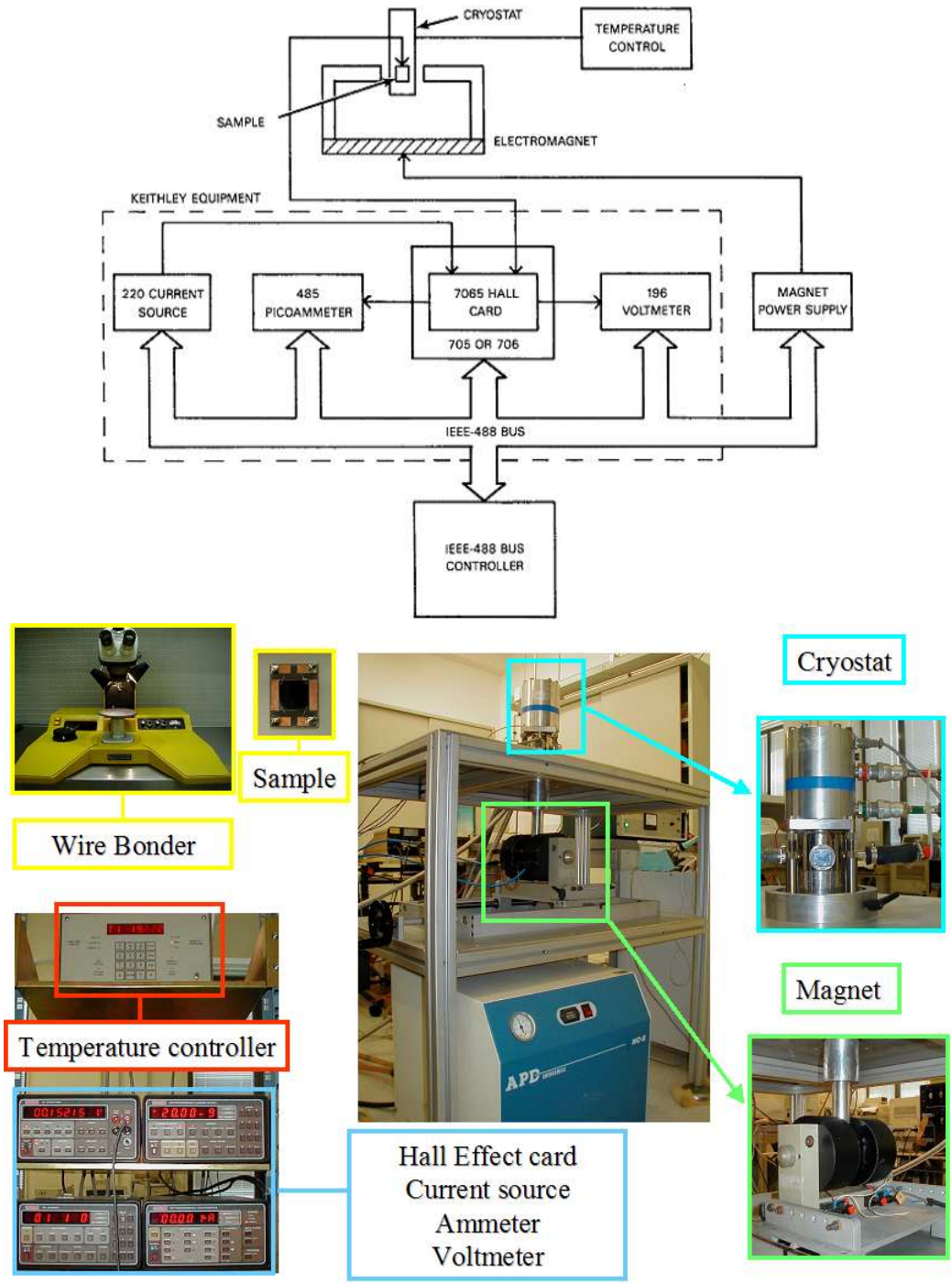

Figure 6.1: Top: schematic representation of the Hall effect setup. Bottom: Pictures of instruments.

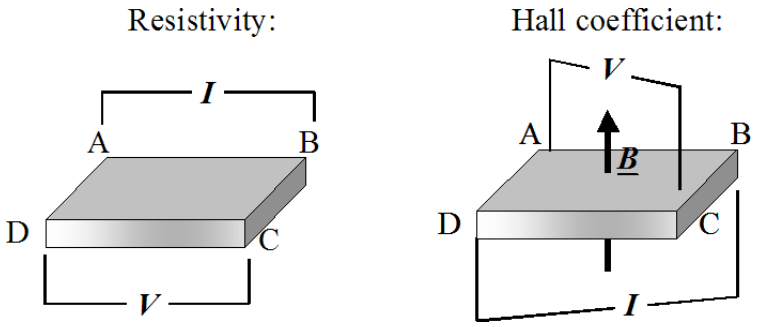

Figure 6.2: Schematically representation of voltages and currents for resistivity and Hall coefficient measurements.

The sample is schematically represented in figure 6.2 where the four contacts are labeled as A, B, C and D. To perform the resistivity measurements, we used the Van der Pauw method [90] which enables one to compute the ρ value as:

$$\rho = \frac{\pi t}{\ln 2}\left[\frac{R_{BA,CD} + R_{BC,DA}}{2}\right] f \tag{6.9}$$

where t is the sample thickness, $R_{BA,CD}$ and $R_{BC,DA}$ are the resistances computed by:

$$R_{BA,CD} = \frac{V_{CD}}{I_{BA}} \quad ; \quad R_{BC,DA} = \frac{V_{DA}}{I_{BC}} \tag{6.10}$$

where V_{CD} is the measured voltage between the contacts CD when in the other two, BA, it is applied the current I_{BA}. For the voltage V_{DA} and the current I_{BC} the issue is the same. The term f is a geometrical factor which depends on the measured resistances and it is computed by [90]:

$$\frac{Q-1}{Q+1} = \frac{f}{\ln 2}\cosh^{-1}\left(\frac{1}{2}\exp\left\{\frac{\ln 2}{f}\right\}\right) \tag{6.11}$$

with $Q = R_{BA,CD}/R_{BC,DA}$. The ρ measurement was performed with reversed current too and the mean value was taken.

To perform the Hall coefficient measurements the sample is immerse in a magnetic field which is perpendicular to the sample surface. We measure the voltage which arises at one diagonal of the sample when a current flows through the other diagonal as shown in figure 6.2.

The numerical value of the Hall coefficient is computed by:

$$R_{H_{AC,DB}} = \frac{V_{AC}t}{I_{DB}B} \quad ; \quad R_{H_{DB,AC}} = \frac{V_{DB}t}{I_{AC}B} \tag{6.12}$$

where B is the magnetic field strength (3000 Gauss) and V_{AC} is the voltage of the diagonal AC when the current I_{DB} flows along the other diagonal (DB). For the $R_{H_{DB,AC}}$ value the issue is the same. In addition the same measurements were performed with reversed current and reversed polarity of B. The final value of the Hall coefficient R_H is obtained by the mean of these eight measurements.

The Hall mobility μ_H, is defined as the ratio of the absolute value of the Hall coefficient and of the resistivity:

$$\mu_H = \frac{|R_H|}{\rho}. \tag{6.13}$$

From the condition (5.135) it is possible to see that our measures are performed in the low magnetic field regime. Assuming the electrons mobility calculated with Arora's formula at $T = 300$ K, $\mu_e \sim 1330$ cm^2/(Vs), and $B = 3000 \times 10^{-8}$ Wb/cm^2, we have:

$$\mu_e B \sim 1.33 \times 10^3 \times 3 \times 10^{-5} \simeq 0.04 \ll 1 \tag{6.14}$$

As already said in section 5.5.1, for a n-type non-degenerate sample, in the limit of low magnetic field, the Hall coefficient and the resistivity are [93]:

$$R_H = -\frac{r_H}{en} \ ; \ \rho = \frac{1}{e\mu_e n} \tag{6.15}$$

where e is the electric charge, n is the concentration of majority carriers, μ_e is the electron mobility and r_H is the Hall-scattering factor. The Hall mobility is $\mu_H = r_H \mu_e$ which within a 20% due to the variation of r_H, is equal to the electron mobility. For a degenerate semiconductor, instead, the Hall mobility can be considered equal to the drift mobility ($r_H \simeq 1$) as already said in section 5.5.1.

6.3 Experimental Results of Non-Irradiated Samples

Temperature scans of ρ, R_H, μ_H were performed from 300 K down to 11 K for non-irradiated samples [102]. In addition we calculated the inverse of the Hall coefficient which gives the carriers concentration over the Hall scattering factor:

$$\frac{n}{r_H} = \frac{1}{e|R_H|} \tag{6.16}$$

Considering the values of r_H which were given in equations (5.158) and (5.159) for acoustic and ionized impurity scattering respectively, we can estimat the carriers concentration at $T = 300$ K :

$$\begin{aligned}
[0.01\ \Omega\ \text{cm}] \quad & p \simeq 8.24 \times 10^{18}\,\text{cm}^{-3} \\
[0.01\ \Omega\ \text{cm}] \quad & n \simeq 3.6 \times 10^{18}\,\text{cm}^{-3} \\
[56\ \Omega\ \text{cm}] \quad & n = (4\text{–}6.5) \times 10^{13}\,\text{cm}^{-3} \\
[157\ \Omega\ \text{cm}] \quad & n = (2.6\text{–}4.2) \times 10^{13}\,\text{cm}^{-3} \\
[2500\ \Omega\ \text{cm}] \quad & n = (2\text{–}3.3) \times 10^{12}\,\text{cm}^{-3} \\
[7000\ \Omega\ \text{cm}] \quad & n = (6.3\text{–}10) \times 10^{11}\,\text{cm}^{-3}
\end{aligned}$$

where it is considered that $r_H \simeq 1$ for degenerate samples.

The experimental results of R_H, n/r_H, ρ and μ_H are reported as a function of $1000/T$ in figure 6.3. As expected (see sections 5.1.3) for non-degenerate samples it is possible to identify two regions: the extrinsic region, where n/r_H is almost constant, and the freeze-out region where n/r_H decreases for increasing temperature. The Hall coefficient, which in the plot is reported with its sign, follows the same behavior but, in this case, its absolute value increases in the freeze-out region.

The Hall mobility increases with decreasing temperature from 300 K down to about 25 K. This behavior indicates that the acoustic scattering process dominates over the ionized impurity one (see sections 5.4.1 and 5.4.2). In the temperature interval from 11 K to 20 K, instead, it is almost constant.

From the $\rho = 1/(\mu_e n e)$ measurements it is possible to obtain that the electrons drift mobility follows a power low dependence on temperature which, in the interval [300-100] K, can be expressed as:

$$\mu_e \propto T^{-m} \tag{6.17}$$

where the exponent m is about 2, value in agreement with literature [95].

For very-low resistivity samples (which are degenerated) the freeze out region is absent. The carriers concentration n - p (in this case $r_H \simeq 1$), R_H and ρ values are almost constant in the entire energy range. The mobility for both types of samples (p and n) depends on the ratio of the relaxation time, which depends only on the Fermi energy level, and the effective mass (see equation (5.86)). As can be seen from this results the ratio doesn't change much from 300 K down to 11 K. For the n-type μ_e varies from about 224 cm^2/(Vs) at $T = 300$ K to 91 cm^2/(Vs) at $T = 11$ K (42%), while for the n-type μ_h varies from about 81 cm^2/(Vs) at $T = 300$ K to 26 cm^2/(Vs) at $T = 11$ K (51%).

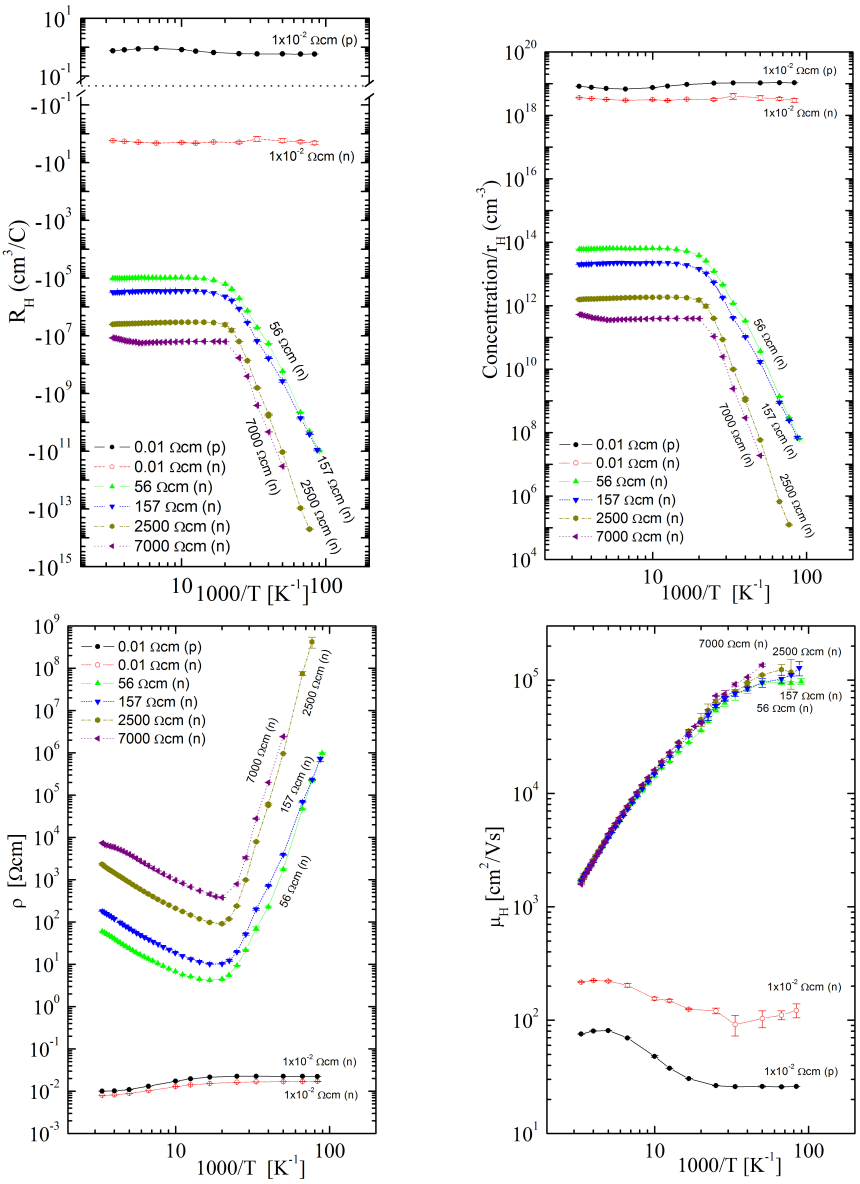

Figure 6.3: Experimental results of non-irradiated samples for different resistivities. Top left: Hall coefficient. Top right: carriers concentration over Hall scattering factor. Bottom left: resistivity. Bottom right: Hall mobility [102].

6.4 Temperature Scan of Irradiated Samples

Temperature scans of ρ, R_h and μ_H were also carried out on samples after irradiation with neutrons and carbon ions [102]. As can be seen from figure 6.5

for very-low resistivity samples (0.01 Ω cm), there are no relevant variations of these quantities after irradiation, even for the largest fluence.

For non-degenerate samples, instead, ρ and $|R_h|$ progressively increase with increasing fluence while μ_H decreases. In addition the Hall mobility dependence on temperature changes slope. This behavior is achieved at a lower absorbed NIEL-Dose with increasing sample resistivity i.e.:

$$\begin{aligned}
[56\ \Omega\ \text{cm}] \quad & D^{NIEL} \geq 235\,\text{Gy} \ \text{ or } \ FP \geq 5.5 \times 10^{16}\,\text{cm}^{-3} \\
[157\ \Omega\ \text{cm}] \quad & D^{NIEL} \geq 25.8\,\text{Gy} \ \text{ or } \ FP \geq 6.0 \times 10^{15}\,\text{cm}^{-3} \\
[2500\ \Omega\ \text{cm}] \quad & D^{NIEL} \geq 2.58\,\text{Gy} \ \text{ or } \ FP \geq 6.0 \times 10^{14}\,\text{cm}^{-3} \\
[7000\ \Omega\ \text{cm}] \quad & D^{NIEL} \geq 0.28\,\text{Gy} \ \text{ or } \ FP \geq 6.4 \times 10^{13}\,\text{cm}^{-3}
\end{aligned}$$

For low and medium resistivity samples (56 and 157 Ω cm), there is a progressive reduction of the extrinsic region with increasing irradiation fluence. This region is absent starting from a NIEL-Dose (or FP concentration) which depends on the resistivity:

$$\begin{aligned}
[56\ \Omega\ \text{cm}] \quad & D^{NIEL} \geq 25.8\,\text{Gy} \ \text{ or } \ FP \geq 6.0 \times 10^{15}\,\text{cm}^{-3} \\
[157\ \Omega\ \text{cm}] \quad & D^{NIEL} \geq 10.7\,\text{Gy} \ \text{ or } \ FP \geq 2.5 \times 10^{15}\,\text{cm}^{-3}
\end{aligned}$$

Also for high resistivity samples (2500 Ω cm) there is a progressive reduction of the extrinsic region with increasing fluence. For the very-high ones (7000 Ω cm) it is already absent at the first irradiation fluence. For these samples the extrinsic region is absent at a lower absorbed NIEL-Dose respect to the previous samples, i.e

$$\begin{aligned}
[2500\ \Omega\ \text{cm}] \quad & D^{NIEL} \geq 0.69\,\text{Gy} \ \text{ or } \ FP \geq 1.6 \times 10^{14}\,\text{cm}^{-3} \\
[7000\ \Omega\ \text{cm}] \quad & D^{NIEL} \geq 0.28\,\text{Gy} \ \text{ or } \ FP \geq 6.4 \times 10^{13}\,\text{cm}^{-3}
\end{aligned}$$

In addition, for these samples, the Hall coefficient changes sign starting from a NIEL-Dose of :

$$\begin{aligned}
[2500\ \Omega\ \text{cm}] \quad & D^{NIEL} \geq 25.8\,\text{Gy} \ \text{ or } \ FP \geq 6.0 \times 10^{15}\,\text{cm}^{-3} \\
[7000\ \Omega\ \text{cm}] \quad & D^{NIEL} \geq 2.71\,\text{Gy} \ \text{ or } \ FP \geq 6.3 \times 10^{14}\,\text{cm}^{-3}
\end{aligned}$$

It has to be noted that the change of the Hall coefficient sign, which was observed after irradiation for high and very-high resistivity sample, is very different from the one that can be observed in compensated semiconductors (see section 5.1.4). The level of compensation, in facts, is achieved during the fabrication process by adding the "desired" doping atoms concentrations. In

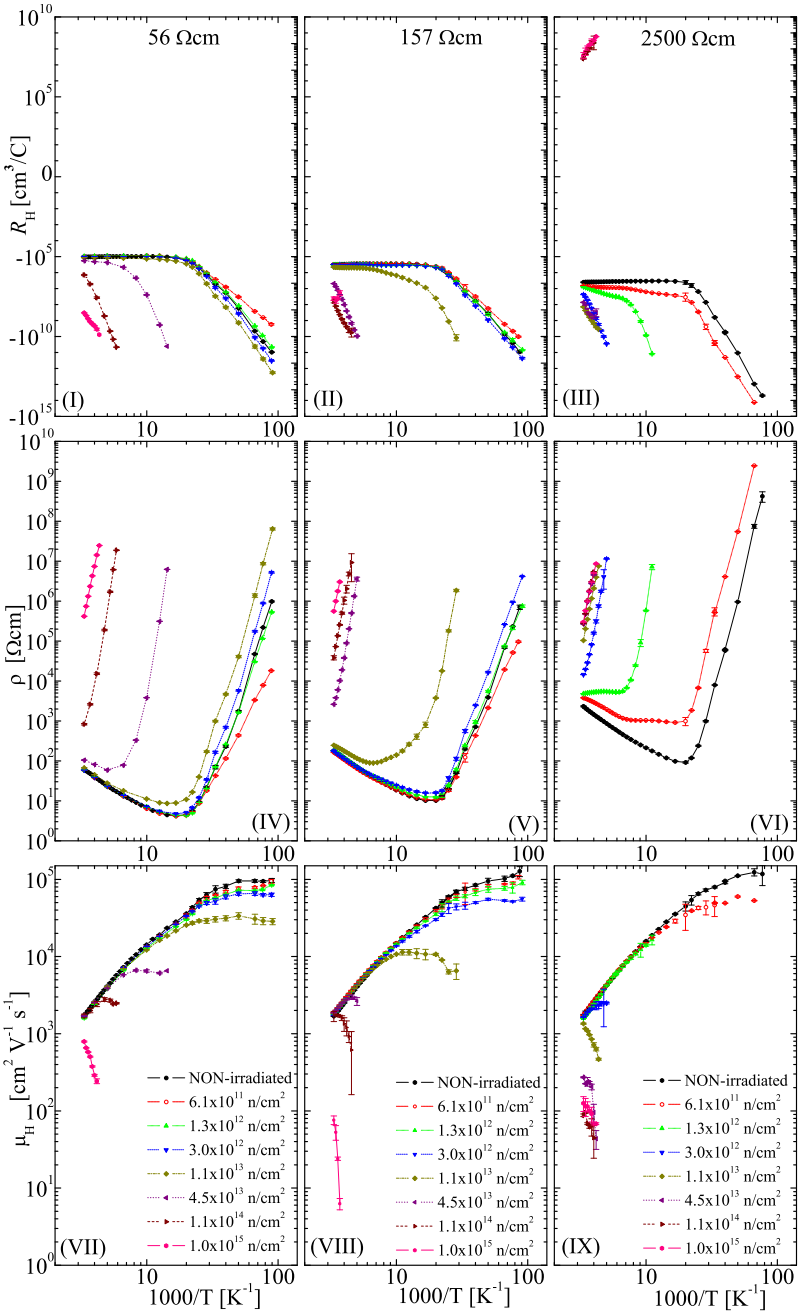

Figure 6.4: Temperature dependance of Hall coefficient [(I), (II), (III)], resistivity [(IV), (V), (VI)] and Hall mobility [(VII), (VIII), (IX)] for irradiated samples with neutrons. The sample-resistivities before irradiation are n-type of 56 Ω cm [(I), (IV), (VI)], n-type of 157 Ω cm [(II), (V), (VIII)] and n-type of 2500 Ω cm [(III), (VI), (IX)] [102].

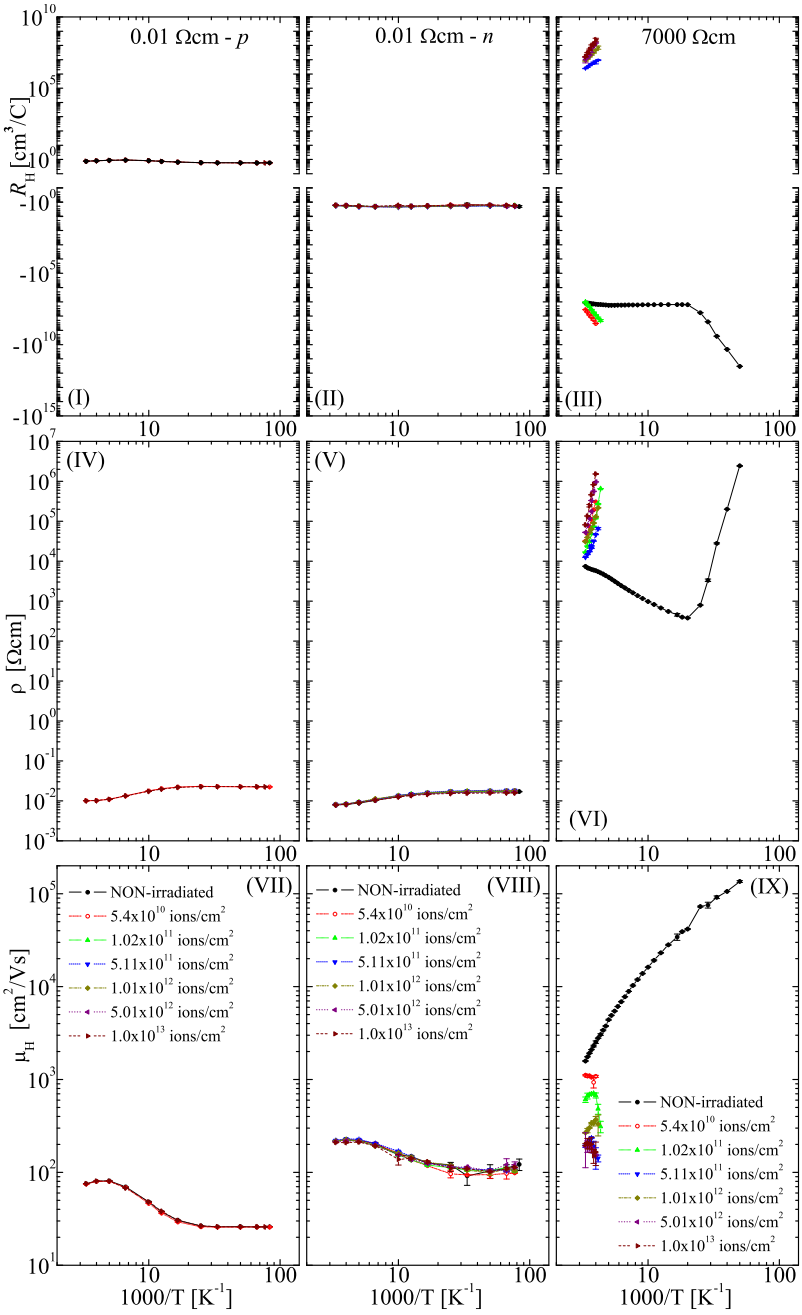

Figure 6.5: Temperature dependance of Hall coefficient [(I), (II), (III)], resistivity [(IV), (V), (VI)] and Hall mobility [(VII), (VIII), (IX)] for irradiated samples with carbon-ions. The sample-resistivities before irradiation are: p-type of 0.01 Ω cm [(I), (IV), (VI)], n-type of 0.01 Ω cm [(II), (V), (VIII)] and n-type of 7000 Ω cm [(III), (VI), (IX)] [102].

Sample resistivity in $\Omega\,$cm	0.01	56	157	2500	7000
Lack of extrinsic region	-	25.8	10.7	0.69	0.28
Change of Hall mobility slope	-	235	25.8	2.58	0.28
Reversed sign	-	-	-	25.8	2.71

Table 6.3: The displacement NIEL-Doses, in units of Gy, above which extrinsic region is absent, the slope of the Hall mobility changes and/or the Hall coefficient sign is reversed.

addition donors or acceptors, introduce shallow levels in the forbidden energy gap while the irradiation process introduce deep levels which have different characteristics. In irradiated samples free carriers are trapped in these deep levels: both the lifetime and the relaxation time (mean free time) diminish after irradiation. The lifetime diminishes because carriers are removed from the conduction band or the valance band according to the sample type (see section 3.3 on defect complexes). The relaxation time diminishes because carriers are subjected to more scattering processes with impurities created after irradiation (the ionized impurity scattering relaxation time is inversely proportional to the impurities concentration as can be seen from equation 5.95). The $|R_H|$ value increases because of carriers removal (n diminishes because they are trapped). The mobility decreases because the impurity scattering process increases. The resistivity increases because both μ_e and n decrease.

For each resistivity sample the major effects which arise after irradiation are listed in table 6.3 with the corresponding absorbed NIEL-Dose. In essence higher resistivity samples degrades with a lower absorbed NIEL-Dose i.e they are more affected by irradiation compared to the low resistivity ones.

Conclusions

With this work we were able to reproduce the Messenger's et al. [50] non-relativistic NIEL values for all nuclei in the low energy range of the space environment (1 keV -1 GeV) where screening effects are relevant. In addition we gave new information on the Coulomb NIEL fraction for heavy nuclei of the GCRs spectrum. We were able to modify the single scattering process of the GEANT4 simulation program in order to extend the use of this code to heavier nuclei. The modification essentially consists in the introduction of the reduced mass in the differential cross section for energy transfer. The so-modified code is able to properly reproduce the scattering probabilities. With the modified GEANT4 code it is possible to get the Coulomb NIEL fraction in agreement with those available in the non fully-relativistic regime for heavy ions and in the relativistic regime for protons. Furthermore, it adds new information about the heavy nuclei at relativistic energies. The simulation results are analogous to those obtained by a computational integration that we performed by the use of the Coulomb relativistic differential cross section proposed by Starusziewicz and Zalewski [40] (SZ). The modification was accepted by the GEANT4 team and it will be included in the GEANT4 9.3 release available from December 2009 [64].

In addition, we developed a code based on the ISO 15390 model for the generation of particles distributed according to the GCR fluxes. The results of the GEANT4 simulation well reproduce the expected values. This allows one to have a particle generator which is able to approximately reproduce the solar modulation effect for GCRs.

For instance, using the ISO model of GCRs fluxes and the NIEL for all the nuclei, we estimated the expected NIEL-Dose absorbed by a silicon sample during one year mission. The calculation was performed considering two different periods of the Sun activity for GCRs in the energy range from 50 MeV/nucleon up to 10 GeV/nucleon. For protons and alpha particles the NIEL-Dose computation includes both Coulomb and nuclear interactions [35], [34], [36], [57]. For all the other nuclei, we used the Coulomb NIEL fraction obtained from our computation. We estimated that the NIEL-Dose contribution of all the nuclei, from alpha to nickel, is about 40% of the proton one. For example, during a typical solar minimum period, the NIEL-Dose of the nuclei is ~ 10 μGy/yr, while the protons one is ~ 27 μGy/yr. During a maximum solar activity period, it is ~ 7 μGy/yr, and ~ 17 μGy/yr for nuclei

and protons respectively. Relative contributions, however, strongly depend on the ISO flux model which brings an uncertainty of about 27.5% for the protons NIEL-Dose, while for all the nuclei it is about 14.5%.

In addition Hall effect measurements were performed in our laboratory, on silicon samples of different resistivities which are usually used as substrates for the fabrication of detectors and devices employed in space missions [102]. The samples were irradiated with fast neutrons and high energy carbon ions. Temperature scans of the Hall coefficient, the resistivity and the Hall mobility were performed from 300 K down to 11 K. As expected, the resistivity increases while the Hall mobility decreases after irradiation. The Hall coefficient is inversely proportional to the effective number of majority carriers concentration and its absolute value was found to increase with increasing fluence. In addition, for high resistivity samples, it was observed a change of the Hall coefficient sign, which indicates the type of effective majority carries. To compare results of samples irradiated with different particles, it is convenient to express these measured quantities as a function of the FP concentration, which is directly related to the energy deposited by displacement processes. The main result of this work is that high initial resistivity samples are more affected by irradiation than the low resistivity ones. For very low resistivities (0.01 Ω cm) no relevant variations were observed after irradiation. For low resistivity (56 Ω cm) it was observed a lack of the extrinsic region starting from a FP concentration of 6×10^{15} cm^{-3}. The same phenomena occurs also for medium resistivity (157 Ω cm) but at a lower FP concentration, that is 2.5×10^{15} cm^{-3}. For high (2500 Ω cm) and very high (7000 Ω cm) resistivity this is found at 1.6×10^{14} cm^{-3} and at 6.4×10^{13} cm^{-3} respectively. In addition for these last two types of samples the change of the Hall coefficient signs occurs at a FP concentration of 6.0×10^{15} cm^{-3} for high resistivity, and at 6.3×10^{14} cm^{-3} for very high resistivity.

Appendix A

GEANT4 Coulomb NIEL

GEANT4 Coulomb NIEL fraction simulation results in units of MeV cm^2/g for every nucleus from proton to nickel in silicon target. NIEL values calculated by the use of the relativistic differential cross section SZ given by equation (4.7) are also listed. The energy E is given in units of MeV/nucleon. The threshold energy for displacement is $T_d = 21$ eV.

	Proton	(A,Z)=(1,1)	Alpha	(A,Z)=(4,2)
E	GEANT4	SZ	GEANT4	SZ
20	3.70×10^{-3}	3.24×10^{-3}	1.40×10^{-2}	1.31×10^{-2}
50	1.42×10^{-3}	1.37×10^{-3}	5.72×10^{-3}	5.50×10^{-3}
100	7.73×10^{-4}	7.38×10^{-4}	2.95×10^{-3}	2.96×10^{-3}
200	4.55×10^{-4}	4.23×10^{-4}	1.68×10^{-3}	1.69×10^{-3}
500	2.43×10^{-4}	2.37×10^{-4}	9.83×10^{-4}	9.47×10^{-4}
1000	1.86×10^{-4}	1.78×10^{-4}	7.40×10^{-4}	7.12×10^{-4}
2000	1.62×10^{-4}	1.52×10^{-4}	6.49×10^{-4}	6.08×10^{-4}
5000	1.49×10^{-4}	1.40×10^{-4}	6.00×10^{-4}	5.60×10^{-4}
10000	1.47×10^{-4}	1.38×10^{-4}	5.93×10^{-4}	5.50×10^{-4}
	Li	(A,Z)=(7,3)	Be	(A,Z)=(9,4)
E	GEANT4	SZ	GEANT4	SZ
20	3.03×10^{-2}	2.95×10^{-2}	5.44×10^{-2}	5.25×10^{-2}
50	1.30×10^{-2}	1.24×10^{-2}	2.33×10^{-2}	2.20×10^{-2}
100	6.80×10^{-3}	6.66×10^{-3}	1.19×10^{-2}	1.18×10^{-2}
200	3.91×10^{-3}	3.81×10^{-3}	7.25×10^{-3}	6.78×10^{-3}
500	2.16×10^{-3}	2.13×10^{-3}	3.86×10^{-3}	3.79×10^{-3}
1000	1.67×10^{-3}	1.60×10^{-3}	2.98×10^{-3}	2.85×10^{-3}
2000	1.41×10^{-3}	1.37×10^{-3}	2.50×10^{-3}	2.43×10^{-3}
5000	1.33×10^{-3}	1.26×10^{-3}	2.34×10^{-3}	2.24×10^{-3}
10000	1.31×10^{-3}	1.24×10^{-3}	2.32×10^{-3}	2.20×10^{-3}

	B	(A,Z)=(11,5)	C	(A,Z)=(12,6)
E	GEANT4	SZ	GEANT4	SZ
20	8.67×10^{-2}	8.21×10^{-2}	1.25×10^{-1}	1.18×10^{-1}
50	3.56×10^{-2}	3.44×10^{-2}	5.18×10^{-2}	4.95×10^{-2}
100	1.97×10^{-2}	1.85×10^{-2}	2.77×10^{-2}	2.66×10^{-2}
200	1.09×10^{-2}	1.06×10^{-2}	1.59×10^{-2}	1.53×10^{-2}
500	6.02×10^{-3}	5.92×10^{-3}	8.88×10^{-3}	8.53×10^{-3}
1000	4.61×10^{-3}	4.45×10^{-3}	6.49×10^{-3}	6.41×10^{-3}
2000	3.92×10^{-3}	3.80×10^{-3}	5.75×10^{-3}	5.47×10^{-3}
5000	3.69×10^{-3}	3.50×10^{-3}	5.35×10^{-3}	5.04×10^{-3}
10000	3.62×10^{-3}	3.44×10^{-3}	5.17×10^{-3}	4.95×10^{-3}
	N	(A,Z)=(14,7)	O	(A,Z)=(16,8)
E	GEANT4	SZ	GEANT4	SZ
20	1.65×10^{-1}	1.61×10^{-1}	2.18×10^{-1}	2.10×10^{-1}
50	7.12×10^{-2}	6.74×10^{-2}	9.42×10^{-2}	8.80×10^{-2}
100	3.67×10^{-2}	3.63×10^{-2}	4.85×10^{-2}	4.74×10^{-2}
200	2.14×10^{-2}	2.08×10^{-2}	2.83×10^{-2}	2.71×10^{-2}
500	1.17×10^{-2}	1.16×10^{-2}	1.55×10^{-2}	1.52×10^{-2}
1000	9.19×10^{-3}	8.72×10^{-3}	1.20×10^{-2}	1.14×10^{-2}
2000	7.84×10^{-3}	7.44×10^{-3}	1.04×10^{-2}	9.72×10^{-3}
5000	7.30×10^{-3}	6.86×10^{-3}	9.35×10^{-3}	8.96×10^{-3}
10000	7.05×10^{-3}	6.74×10^{-3}	9.18×10^{-3}	8.80×10^{-3}
	F	(A,Z)=(19,9)	Ne	(A,Z)=(20,10)
E	GEANT4	SZ	GEANT4	SZ
20	2.77×10^{-1}	2.66×10^{-1}	3.29×10^{-1}	3.28×10^{-1}
50	1.16×10^{-1}	1.11×10^{-1}	1.45×10^{-1}	1.38×10^{-1}
100	6.42×10^{-2}	6.00×10^{-2}	7.51×10^{-2}	7.40×10^{-2}
200	3.62×10^{-2}	3.43×10^{-2}	4.52×10^{-2}	4.24×10^{-2}
500	1.99×10^{-2}	1.92×10^{-2}	2.38×10^{-2}	2.37×10^{-2}
1000	1.53×10^{-2}	1.44×10^{-2}	1.91×10^{-2}	1.78×10^{-2}
2000	1.27×10^{-2}	1.23×10^{-2}	1.59×10^{-2}	1.52×10^{-2}
5000	1.18×10^{-2}	1.13×10^{-2}	1.45×10^{-2}	1.40×10^{-2}
10000	1.17×10^{-2}	1.11×10^{-2}	1.44×10^{-2}	1.38×10^{-2}

	Na	(A,Z)=(23,11)	Mg	(A,Z)=(24,12)
E	GEANT4	SZ	GEANT4	SZ
20	3.99×10^{-1}	3.97×10^{-1}	5.05×10^{-1}	4.73×10^{-1}
50	1.68×10^{-1}	1.66×10^{-1}	2.04×10^{-1}	1.98×10^{-1}
100	9.03×10^{-2}	8.96×10^{-2}	1.11×10^{-2}	1.07×10^{-2}
200	5.25×10^{-2}	5.13×10^{-2}	6.34×10^{-2}	6.10×10^{-2}
500	2.88×10^{-2}	2.87×10^{-2}	3.52×10^{-2}	3.41×10^{-2}
1000	2.27×10^{-2}	2.15×10^{-2}	2.69×10^{-2}	2.56×10^{-2}
2000	1.91×10^{-2}	1.84×10^{-2}	2.30×10^{-2}	2.19×10^{-2}
5000	1.75×10^{-2}	1.69×10^{-2}	2.08×10^{-2}	2.02×10^{-2}
10000	1.73×10^{-2}	1.66×10^{-2}	2.06×10^{-2}	1.98×10^{-2}
	Al	(A,Z)=(27,13)	Si	(A,Z)=(28,14)
E	GEANT4	SZ	GEANT4	SZ
20	5.64×10^{-1}	5.55×10^{-1}	6.66×10^{-1}	6.43×10^{-1}
50	2.41×10^{-1}	2.32×10^{-1}	2.79×10^{-1}	2.70×10^{-1}
100	1.35×10^{-1}	1.25×10^{-1}	1.51×10^{-1}	1.45×10^{-1}
200	7.46×10^{-2}	7.16×10^{-2}	8.43×10^{-2}	8.30×10^{-2}
500	4.24×10^{-2}	4.00×10^{-2}	4.82×10^{-2}	4.64×10^{-2}
1000	3.10×10^{-2}	3.01×10^{-2}	3.64×10^{-2}	3.49×10^{-2}
2000	2.65×10^{-2}	2.57×10^{-2}	3.13×10^{-2}	2.98×10^{-2}
5000	2.47×10^{-2}	2.37×10^{-2}	2.84×10^{-2}	2.74×10^{-2}
10000	2.43×10^{-2}	2.32×10^{-2}	2.82×10^{-2}	2.70×10^{-2}
	P	(A,Z)=(31,15)	S	(A,Z)=(32,16)
E	GEANT4	SZ	GEANT4	SZ
20	7.64×10^{-1}	7.39×10^{-1}	8.54×10^{-1}	8.40×10^{-1}
50	3.25×10^{-1}	3.09×10^{-1}	3.78×10^{-1}	3.52×10^{-1}
100	1.68×10^{-1}	1.67×10^{-1}	2.03×10^{-1}	1.89×10^{-1}
200	9.61×10^{-2}	9.53×10^{-2}	1.09×10^{-1}	1.08×10^{-1}
500	5.54×10^{-2}	5.33×10^{-2}	6.29×10^{-2}	6.06×10^{-2}
1000	4.12×10^{-2}	4.00×10^{-2}	4.73×10^{-2}	4.56×10^{-2}
2000	3.56×10^{-2}	3.42×10^{-2}	4.03×10^{-2}	3.89×10^{-2}
5000	3.24×10^{-2}	3.15×10^{-2}	3.68×10^{-2}	3.58×10^{-2}
10000	3.24×10^{-2}	3.09×10^{-2}	3.70×10^{-2}	3.52×10^{-2}

	Cl	(A,Z)=(35,17)	Ar	(A,Z)=(40,18)
E	GEANT4	SZ	GEANT4	SZ
20	9.53×10^{-1}	9.49×10^{-1}	1.15	1.06
50	4.06×10^{-1}	3.97×10^{-1}	4.58×10^{-1}	4.46×10^{-1}
100	2.24×10^{-1}	2.14×10^{-1}	2.56×10^{-1}	2.40×10^{-1}
200	1.21×10^{-1}	1.22×10^{-1}	1.38×10^{-1}	1.37×10^{-1}
500	7.07×10^{-2}	6.84×10^{-2}	7.92×10^{-2}	7.67×10^{-2}
1000	5.28×10^{-2}	5.14×10^{-2}	5.85×10^{-2}	5.77×10^{-2}
2000	4.49×10^{-2}	4.40×10^{-2}	5.02×10^{-2}	4.92×10^{-2}
5000	4.20×10^{-2}	4.05×10^{-2}	4.68×10^{-2}	4.54×10^{-2}
10000	4.17×10^{-2}	3.98×10^{-2}	4.66×10^{-2}	4.46×10^{-2}
	K	(A,Z)=(39,19)	Ca	(A,Z)=(40,20)
E	GEANT4	SZ	GEANT4	SZ
20	1.28	1.19	1.41	1.31
50	5.30×10^{-1}	4.96×10^{-1}	5.97×10^{-1}	5.50×10^{-1}
100	2.76×10^{-1}	2.67×10^{-1}	3.22×10^{-1}	2.96×10^{-1}
200	1.53×10^{-1}	1.53×10^{-1}	1.68×10^{-1}	1.69×10^{-1}
500	8.84×10^{-2}	8.55×10^{-2}	9.89×10^{-2}	9.47×10^{-2}
1000	6.53×10^{-2}	6.42×10^{-2}	7.26×10^{-2}	7.12×10^{-2}
2000	5.58×10^{-2}	5.48×10^{-2}	6.25×10^{-2}	6.08×10^{-2}
5000	5.23×10^{-2}	5.05×10^{-2}	5.80×10^{-2}	5.60×10^{-2}
10000	5.18×10^{-2}	4.97×10^{-2}	5.76×10^{-2}	5.50×10^{-2}
	Sc	(A,Z)=(45,21)	Ti	(A,Z)=(48,22)
E	GEANT4	SZ	GEANT4	SZ
20	1.49	1.45	1.61	1.59
50	6.42×10^{-1}	6.06×10^{-1}	6.75×10^{-1}	6.66×10^{-1}
100	3.28×10^{-1}	3.26×10^{-1}	3.62×10^{-1}	3.58×10^{-1}
200	1.88×10^{-1}	1.87×10^{-1}	2.04×10^{-1}	2.05×10^{-1}
500	1.10×10^{-1}	1.04×10^{-1}	1.20×10^{-1}	1.15×10^{-1}
1000	8.02×10^{-2}	7.85×10^{-2}	8.74×10^{-2}	8.61×10^{-2}
2000	6.81×10^{-2}	6.70×10^{-2}	7.52×10^{-2}	7.35×10^{-2}
5000	6.38×10^{-2}	6.17×10^{-2}	6.97×10^{-2}	6.78×10^{-2}
10000	6.33×10^{-2}	6.07×10^{-2}	6.94×10^{-2}	6.66×10^{-2}

	V	(A,Z)=(51,23)	Cr	(A,Z)=(52,24)
E	GEANT4	SZ	GEANT4	SZ
20	1.80	1.74	1.91	1.89
50	7.22×10^{-1}	7.28×10^{-1}	8.58×10^{-1}	7.92×10^{-1}
100	3.77×10^{-1}	3.92×10^{-1}	4.25×10^{-1}	4.26×10^{-1}
200	2.24×10^{-1}	2.24×10^{-1}	2.53×10^{-1}	2.44×10^{-1}
500	1.31×10^{-1}	1.25×10^{-1}	1.40×10^{-1}	1.36×10^{-1}
1000	9.58×10^{-2}	9.41×10^{-2}	1.05×10^{-1}	1.02×10^{-1}
2000	8.20×10^{-2}	8.03×10^{-2}	9.07×10^{-2}	8.75×10^{-2}
5000	7.61×10^{-2}	7.41×10^{-2}	8.29×10^{-2}	8.10×10^{-2}
10000	7.59×10^{-2}	7.28×10^{-2}	8.29×10^{-2}	7.92×10^{-2}
	Mn	(A,Z)=(55,25)	Fe	(A,Z)=(55,26)
E	GEANT4	SZ	GEANT4	SZ
20	2.18	2.05	2.33	2.22
50	9.06×10^{-1}	8.60×10^{-1}	9.46×10^{-1}	9.30×10^{-1}
100	5.09×10^{-1}	4.63×10^{-1}	5.11×10^{-1}	5.00×10^{-1}
200	2.68×10^{-1}	2.65×10^{-1}	2.90×10^{-1}	2.86×10^{-1}
500	1.54×10^{-1}	1.48×10^{-1}	1.67×10^{-1}	1.60×10^{-1}
1000	1.14×10^{-1}	1.11×10^{-1}	1.23×10^{-1}	1.20×10^{-1}
2000	9.73×10^{-2}	9.49×10^{-2}	1.0×10^{-1}	1.03×10^{-1}
5000	9.00×10^{-2}	8.75×10^{-2}	9.74×10^{-2}	9.46×10^{-2}
10000	8.97×10^{-2}	8.60×10^{-2}	9.69×10^{-2}	9.30×10^{-2}
	Co	(A,Z)=(59,27)	Ni	(A,Z)=(59,28)
E	GEANT4	SZ	GEANT4	SZ
20	2.51	2.39	2.74	2.57
50	1.04	1.00	1.06	1.08
100	5.54×10^{-1}	5.40×10^{-1}	5.81×10^{-1}	5.80×10^{-1}
200	3.23×10^{-1}	3.09×10^{-1}	3.25×10^{-1}	3.32×10^{-1}
500	1.75×10^{-1}	1.73×10^{-1}	1.93×10^{-1}	1.85×10^{-1}
1000	1.36×10^{-1}	1.30×10^{-1}	1.42×10^{-1}	1.40×10^{-1}
2000	1.14×10^{-1}	1.11×10^{-1}	1.21×10^{-1}	1.19×10^{-1}
5000	1.05×10^{-1}	1.02×10^{-1}	1.13×10^{-1}	1.10×10^{-1}
10000	1.04×10^{-1}	1.00×10^{-1}	1.12×10^{-1}	1.08×10^{-1}

Appendix B

The Silicon Structure

The fundamental structure of the silicon lattice crystal and an overview of the bands theory are given in B.1 and B.2 respectively. In addition the density of states is also reported in section B.5. The energy band structure provides information about the allowed energy and momentum states which are available to carriers inside the semiconductor. The motion of carriers under the influence of an external force, can be visualized in a quasi classical manner by the effective mass approximation given in section B.3.

B.1 Covalent Bound and Crystal Structure

Silicon is a IV group element in the Mendeleeve periodic table. The nucleon is made of $Z = 14$ protons and its atomic mass is $A = 28.0855$ express in atomic mass unit (amu). The electronic configuration of the single atom is given by $1s^2 2s^2 2p^6 3s^2 3p^2$. The $3s$ subshell has two allowed quantum states per atom and it is filled by two electrons. The $3p$ subshell has six allowed quantum states per atom and it is filled by two electrons. In the solid state, each silicon atom has energetic advantages in forming *covalent bound* with each of the four nearest silicon atoms, and so they arrange themselves in a tetrahedron configuration. This occurs through the sp^3 hybridization mechanism where one S-electron is brought in a p orbital. This configuration is favorite because the bonding with four other electrons of opposite spins forms a octet that fills the hybrid orbital.

To give a qualitatively understanding of the band formation, a monatomic material totally composed by N silicon atoms is considered: when atoms are far apart they don't interact and the atomic energy levels are N-fold degenerate (see fig B.1). As the N atoms are brought together to form a solid, each of the external $3s$ and $3p$ sub-shells overlap and interact with

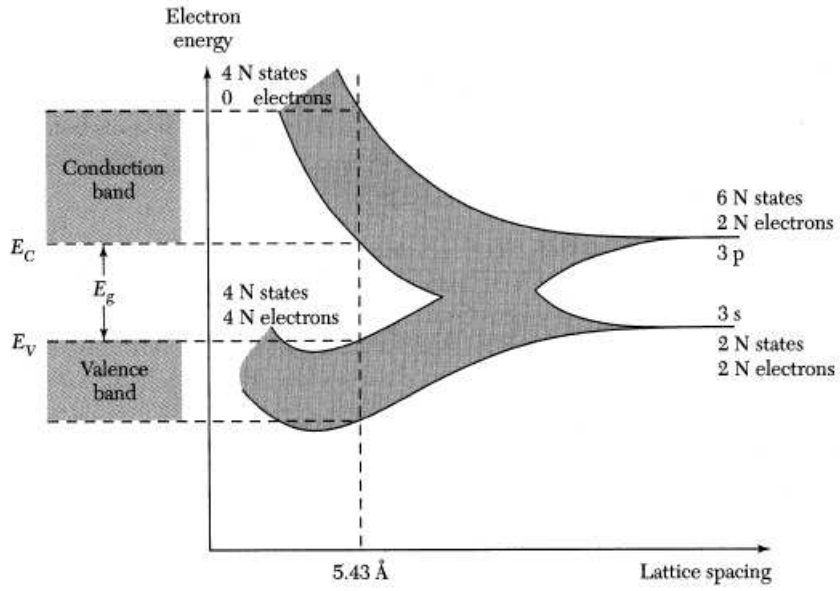

Figure B.1: Formation of energy bands as a diamond lattice crystal is formed by bringing N isolated silicon atoms together [77].

the others. The interaction consists in both attractive and repulsive forces which cause a shift in the energy levels. The degenerate levels split in N closely spaced levels and, if N is large, the result is a formation of an almost continuous *energy band*.
Coulomb repulsive forces between nuclei, prevent further decreasing of the atomic distances. At a certain distance, when attractive and repulsive forces are balanced, the configuration is stable. At the equilibrium interatomic distance the band energy will again spilt in two bands. Both the lower -*valence band*- and the upper -*conduction band* have four quantum states per atom. These two bands are separated by the forbidden *bandgap energy* which is equal to 1.124 eV in silicon at room temperature.

Silicon, as all semiconductors, has a crystal structure. The periodic arrangement of atoms in the crystal is called *lattice*. The lattice can be generated by three fundamentals translation vectors ($\mathbf{a}_1$, $\mathbf{a}_2$, $\mathbf{a}_3$) which are defined in order to reproduce the lattice periodicity. In this way every equivalent lattice point can be represented by a vector $\mathbf{R}$ as a linear combination of the translation vectors:

$$\mathbf{R} = n_1\mathbf{a}_1 + n_2\mathbf{a}_2 + n_3\mathbf{a}_3 \tag{B.1}$$

where n_i are integer numbers.
However, for more complicated lattice structures, the periodicity of the atoms

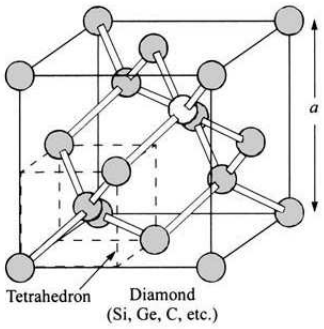

Figure B.2: Primitive cell of a diamond structure ; a is the lattice constant [76].

inside the crystal may not be simply reproduced by a translation. In these cases it is necessary to define a *base* inside the lattice which gives the exact position for all atoms. In silicon the base is given by two identical atoms which are in the fundamental positions $(0, 0, 0)$ and $(1/4, 1/4, 1/4)a$ where a is the *lattice constant* which gives the lattice dimensions. For silicon $a = 0.543$ nm [75].
By reproducing the primitive cell plus this base many times the whole crystal structure can be generated.

Silicon has the crystal *diamond* structure which is represented in fig B.2. The diamond structure can be seen as two interpenetrating face-centered cubes displaced one form the other by one quarter of a, along the diagonal direction. The volume enclosed in the parallelepiped defined by the translation vectors is called *primitive cell*. Since the choice of $\mathbf{a}_i$ is not unique the primitive cell is not unique too. The typical choice for the primitive cell is the *Wigner-Seitz* cell defined as the smallest volume around a point vector $\mathbf{R}$ equally spaced from its neighbors.

By dissecting the silicon diamond structure with planes in various directions, it is possible to see that different planes contain a different number of atoms. In fact, atoms are spaced one from the other at different distances depending on the lattice orientation. As a consequence, the crystal properties along various planes result to be different and the electrical characteristics may also depend on the crystal orientation.

A convenient method to define different planes is to use *Miller indices*. As an example, in fig B.3, three fundamental planes of a cubic crystal are reported in a Cartesian coordinate system. The planes are indicated by the notation (hkl) where the indexes h, k and l can assume a multiple value of the cube dimension (the fundamental value is one). The direction perpendicular to a particular plane is denoted by $[hkl]$ notation, for example [100]

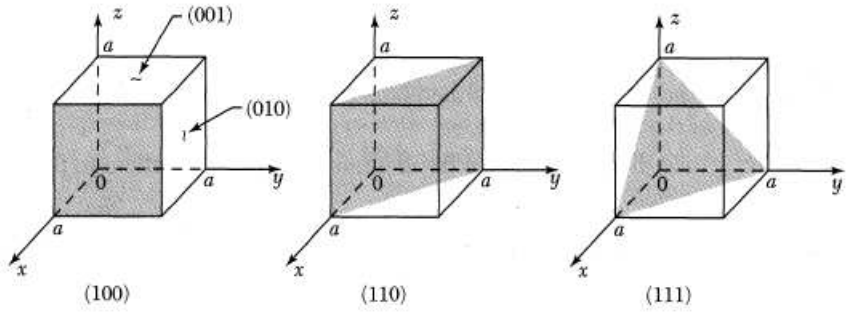

Figure B.3: Miller indices of some important planes in a cubic crystal [77].

denotes the x-axis direction. The notation $\langle hkl \rangle$ groups all set of equivalent directions, for example $\langle 100 \rangle$ denotes six different directions: they are the three positive directions of the Cartesian axes plus the three negative ones.

B.2 The Reciprocal Lattice and the Energy-Band Structure

The reciprocal lattice is the quasi-Fourier transformation of the crystal direct lattice. For each lattice vector $\mathbf{R}$, given by (B.1), the reciprocal $\mathbf{K}$ can be obtained by the condition:

$$\exp(\imath \mathbf{K} \cdot \mathbf{R}) = 1 \tag{B.2}$$

Similarly to the direct crystal lattice, the reciprocal one can be constructed from a set of translation vectors $\mathbf{b}_j$. These vectors, that span the reciprocal lattice, have to fulfill the condition $\mathbf{a}_i \cdot \mathbf{b}_j = 2\pi\delta_{ij}$ so that the (B.2) is guaranteed. The simplest way of doing it, is to choose this set of vectors:

$$\mathbf{b}_1 = \frac{2\pi}{V_a} \mathbf{a}_2 \times \mathbf{a}_3 \tag{B.3}$$

$$\mathbf{b}_2 = \frac{2\pi}{V_a} \mathbf{a}_3 \times \mathbf{a}_1 \tag{B.4}$$

$$\mathbf{b}_3 = \frac{2\pi}{V_a} \mathbf{a}_1 \times \mathbf{a}_2 \tag{B.5}$$

where $V_a = \mathbf{a}_1 \cdot (\mathbf{a}_2 \times \mathbf{a}_3)$ is the volume of the unit cell spanned by $\mathbf{a}_i$. By the definition of the set of vectors $\mathbf{b}_j$, every point in the reciprocal lattice can be

associated with a vector $\mathbf{K}$ which is defined by a linear combination of the given base:

$$\mathbf{K} = k_1\mathbf{b}_1 + k_2\mathbf{b}_2 + k_3\mathbf{b}_3 \tag{B.6}$$

where k_j coefficients are integer numbers.

The reciprocal lattice is useful in the description of the energy momentum relationship, when the coordinates of the wave vector $\mathbf{k}$ are given in the reciprocal lattice space.
The *E-k* relation gives information about the band structure of the lattice. It is obtained by the solution of the Schrödinger equation in the one-electron problem approximation:

$$\left(-\frac{\hbar^2}{2m^*}\nabla^2 + V(\mathbf{r}) \right)\psi(\mathbf{r},\mathbf{k}) = E(\mathbf{k})\psi(\mathbf{r},\mathbf{k}) \tag{B.7}$$

where m^* is the *effective mass* of the electron, $\psi(\mathbf{r},\mathbf{k})$ is the eigenstate of momentum $\mathbf{k}$ and $V(\mathbf{r})$ is the potential.

If the potential $V(\mathbf{r})$ is periodic in the direct lattice then the *Bloch* theorem states that the solution of the Schrödinger equation can be written as a product of plane waves $\exp(\imath\mathbf{k}\cdot\mathbf{r})$, and lattice-periodic functions $u_{n\mathbf{k}}(\mathbf{r})$, i.e:

$$\psi_{n\mathbf{k}}(\mathbf{r},\mathbf{k}) = \exp(\imath\mathbf{k}\cdot\mathbf{r})u_{n\mathbf{k}}(\mathbf{r}) \tag{B.8}$$

where n is a quantum number and $\mathbf{k}$ is the wavevector. Since the Bloch functions $u_{n\mathbf{k}}(\mathbf{r})$ are periodic, the wavefunctions are periodic as well in the direct lattice, that is:

$$\psi_{n\mathbf{k}}(\mathbf{r},\mathbf{k}) = \psi_{n\mathbf{k}}(\mathbf{r}+\mathbf{R},\mathbf{k}) \tag{B.9}$$

for all vectors $\mathbf{R}$.
Another consequence of the Bloch theorem is that if $E_{n\mathbf{k}}(\mathbf{k})$ is an eigenvalue then $E_{n\mathbf{k}}(\mathbf{k}+\mathbf{K})$ is an eigenvalue too for all vectors $\mathbf{K}$ of the reciprocal lattice, that is the Energy-momentum relationship is periodic in the reciprocal lattice:

$$E_n(\mathbf{k}) = E_n(\mathbf{k}+\mathbf{K}) \tag{B.10}$$

The Energy-momentum relation gives the Energy-band structure and can be displayed in various zone along different $\mathbf{k}$-directions. Each zone represents a different cell. The periodicity of the eigenvalues allows to deal only with one cell instead of considering the whole reciprocal lattice space. The reciprocal of the Wigner-Seitz cell which is called the *first Brillouin zone* is usually chosen. The first Brillouin zone is reported in figure B.4 for a diamond lattice structure, where some fundamental points and the $\mathbf{k}$-directions are

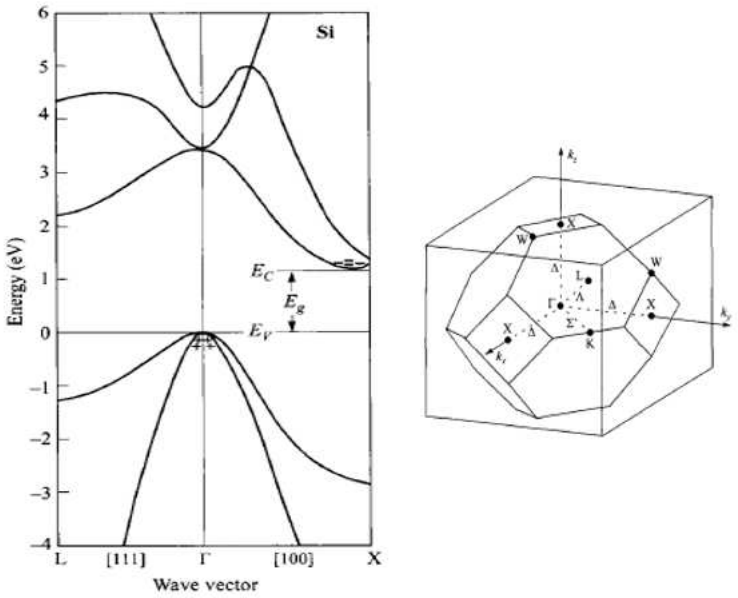

Figure B.4: (Left) Energy band structure of silicon where E_g is the energy bandgap; plus sign (+) indicates holes in the valance bands and minus sign (-) electron in the conduction band. (Right) Brillouin zone of diamond lattice [76].

also given. The Γ point always denotes the center zone, $\mathbf{k} = 0$. The X points denote the zone boundary in the $\langle 100 \rangle$ directions, located at a distance π/a from Γ; K are in the $\langle 110 \rangle$ directions at a distance $(3\sqrt{2}/4)\pi/a$; L are in the $\langle 111 \rangle$ directions at a distance $(\sqrt{3/4})\pi/a$.
The straight path from Γ to X, K, L are denoted by Δ, Σ, Λ respectively.

The energy-band diagram of silicon for the first Brillouin zone is shown in fig B.4. E_c denotes the bottom of the conduction band located in the Δ direction, while E_v is the top of the valance band located at the Γ point. Since there is a separation in momentum between the maximum of the valance band and the minimum of the conduction band, silicon is an *indirect* bandgap semiconductor. As a consequence when carriers move from one energy band to the other, there is also a change in momentum. The separation between those two energies corresponds to the energy gap E_g.

B.3 The Effective Mass Approximation

The energy-band structure gives the allowed energy and reduced momentum states of an electron inside the crystal. Under the influence of an external force, the equation of motion of the electron in the band structure is no

longer given by the classical Newton's second low. The external force might arise for example, by an electric or a magnetic field, or even from the electric potential of dopant and impurity atoms inside the crystal.

To describe the motion of the charges inside the crystal a superposition of wavefunctions must be used. The velocity of the whole wavepacket is given by the group velocity which, in the one dimensional case, has the form:

$$v_g = \frac{d\omega}{dk} = \frac{1}{\hbar}\frac{dE}{dk}. \tag{B.11}$$

This gives the dispersion relation which contains information about the crystal periodic potential which influences the motion of charges.
An external force F acting on a charge over a short distance dx will cause an increase of its wavepacket energy quantified by:

$$dE = Fdx = Fv_g dt = F\frac{1}{\hbar}\frac{dE}{dk}dt. \tag{B.12}$$

The equation of motion is written as:

$$\hbar\frac{dk}{dt} = F. \tag{B.13}$$

Differentiating the group velocity (B.11) respect to time, it is possible to obtain the charge acceleration:

$$a = \frac{dv_g}{dt} = \frac{dv_g}{dk}\frac{dk}{dt} = \frac{1}{\hbar}\frac{d^2E}{dk^2}\frac{dk}{dt} \tag{B.14}$$

and making use of the (B.13), the acceleration of the charge can be expressed by:

$$a = \frac{1}{\hbar^2}\frac{d^2E}{dk^2}F. \tag{B.15}$$

By this last expression it is possible to write the equation of motion of a charge inside the crystal in a quasi-classical manner i.e.:

$$F = m^* a \tag{B.16}$$

where m^* is the *effective mass* defined as:

$$m^* \equiv \left(\frac{1}{\hbar^2}\frac{d^2E}{dk^2}\right)^{-1} \tag{B.17}$$

which contains the information of the crystalline potential. The effective

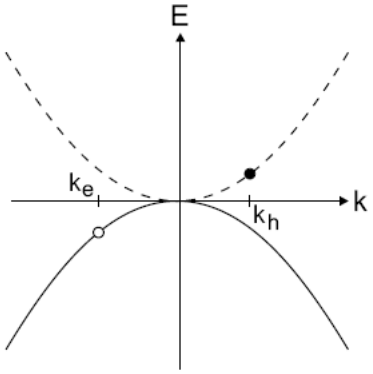

Figure B.5: Hole dispersion relation (dashed line) in relation to the electron one in the valance band (solid line). The hole is represented by the filled circle (•) , the electron by the empty one (◦) [75].

mass is inversely proportional to the curvature of the bands in the *E-k* diagram, and so it is positive ($m^* > 0$) near the band energy minimum -bottom of all bands- and negative ($m^* < 0$) near the band energy maximum -top of all bands.

With a negative effective mass the electron will accelerate in the opposite direction under the influence of an external force as if it were a positive charge. This can be explained considering that when an electron moves from the valance to the conduction band, it leaves a non-occupied valance bond which is called *hole*. Because of this free bond, all other valance electrons, subjected to the external force, will be free to move to the nearest non-occupied state: to an observer the hole seems to move in the opposite electrons direction. To model this situation it is simpler to consider the motion of the positive quasi-particle hole, instead of considering the transitions of all the valance electrons. The concept of holes is very useful to describe the properties of charge carriers at the top of the valance band. The dispersion relation of the hole is schematically sown in fig B.5 in relation to the dispersion of an electron in the valance band. The wavevector of the hole is related to that of the missing electron by $\mathbf{k}_h = -\mathbf{k}_e$ and the energy is larger for holes far from the top of the valance band $E(\mathbf{k}_h) = -E(\mathbf{k}_e)$ (if $E_v = 0$). The effective mass of the hole is positive at the top of the valance band and negative at the bottom, i.e. equal but opposite to the electron one $m_h^* = -m_e^*$ in the valance band. In addition, since the band diagram depends on the crystal orientation, the effective mass definition must be generalized in the three dimensional space. In this case the equation of motion is a tensor

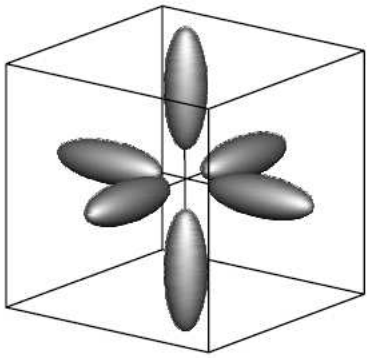

Figure B.6: Ellipsoid of constant energy in the vicinity of the conduction band minima for the six equivalent directions $\langle 100 \rangle$ in the first silicon Brillouin zone [75].

equation where the components of the force are given by $F_i = m^*_{ij} a_j$. The components of the effective mass tensor are then defined as:

$$m^*_{ij} \equiv \left(\frac{1}{\hbar^2} \frac{d^2 E}{dk_i dk_j} \right)^{-1}. \tag{B.18}$$

B.4 Constant Energy Surfaces

In a three dimensional space the E-k relation gives the allowed k-values which are represented by the edge surfaces in the $\mathbf{k}$-space. The geometrical shapes associated with these surfaces are called constant energy surfaces. In proximity of the band extreme points $\mathbf{k}_0$, the energy momentum relation can be expanded in series as:

$$E(\mathbf{k}) \simeq E(\mathbf{k}_0) + \alpha_x (\mathbf{k} - \mathbf{k}_0)_x^2 + \alpha_y (\mathbf{k} - \mathbf{k}_0)_y^2 + \alpha_z (\mathbf{k} - \mathbf{k}_0)_z^2 \tag{B.19}$$

where $\alpha_{x,y,z}$ are constants that can be fixed by equation (B.18). By an appropriate choice of the coordinate system, it is possible to choose $m^*_{ij} \neq 0$ only if $i = j$, and so the equation (B.19) becomes:

$$E - E_0 \simeq \frac{\hbar^2}{2} \left(\frac{k_x^2}{m_x^*} + \frac{k_y^2}{m_y^*} + \frac{k_z^2}{m_z^*} \right) \tag{B.20}$$

where E_0 is the energy value at the extreme point.

Since the silicon valance band is 3-folt degenerate in the Γ point ($\mathbf{k}_0$=0) (see figure B.4), the hole in the valance band can be characterized by one

effective mass parameter with three different values according to the specific sub-band. At the top of the band, these sub bands can be approximated by spherical symmetrical constant energy surfaces and so the (B.20) reduces to:

$$E - E_v \simeq \frac{\hbar^2 k^2}{2m_h^*}. \tag{B.21}$$

The three energy surfaces have different curvatures: the more bent is the *light hole band* with effective mass denoted by m_{lh}^*, while the less bent is the *heavy hole band* with effective mass m_{hh}^*. The third band is the *split-off* band with effective mass m_{so}^*. Since the split-off band is at only 0.044 eV below E_v, it is generally not considered.

The silicon conduction band minimum, instead, is located at $k_0 \simeq 0.8(2\pi/a)$ far apart from Γ along the $\langle 100 \rangle$ direction. It is not degenerate but the dispersion relation gives different values according to the reciprocal lattice orientation. In this case, the constant energy surface is not spherically symmetric but, around the minimum, can be represented by an ellipsoid as reported in fig B.6 where the six equivalent energy surfaces of the six equivalent directions Δ are represented. According to the ellipsoid orientation, the electron effective mass assumes different values. In the longitudinal direction the effective mass is denoted by m_l^*. In the other two transversal directions, the equivalent effective masses are denoted by m_t^*. The energy momentum relation can be expressed by:

$$E - E_c \simeq \frac{\hbar^2}{2}\left(\frac{k_x^2}{m_l^*} + \frac{k_y^2 + k_z^2}{m_t^*}\right) \tag{B.22}$$

Other minima in the conduction band are at much higher energies and are generally not considered.

B.5 Density of States

The density of states enables one to calculate the concentration of the free carriers inside the semiconductor. If it is integrated between two energy values it gives the number of allowed states in that energy range.
The complete calculation of the density of states is derived from the band theory, but an excellent approximation near the band edges, which are generally populated by carriers, can be obtained by a simpler approach.
Since electrons, near the bottom of the conduction band, have energies relative to E_c smaller than the surface barrier of the semiconductor, they can

be thought to be enclosed in a box where the band itself forms the pseudo-potential well. The density of states for a particle of mass m in a three-dimensional box is given by [75] [78]:

$$g(E) = \frac{m\sqrt{2mE}}{\pi^2\hbar^3}. \tag{B.23}$$

To obtain the conduction and the valance band density of states, m has to be replace with the appropriate effective mass, and the energy E with $E - E_c$ when the conduction band is considered or $E_v - E$ for the valance band. The density of states for the two cases become [75] [78]:

$$g_c(E) = \frac{m^*_{de}\sqrt{2m^*_{de}(E - E_c)}}{\pi^2\hbar^3} \tag{B.24}$$

$$g_v(E) = \frac{m^*_{dh}\sqrt{2m^*_{dh}(E_v - E)}}{\pi^2\hbar^3} \tag{B.25}$$

where m^*_{de} and m^*_{dh} are electron (e) and hole (h) *density of states effective masses*. Since carriers within a band are characterized by two or more effective masses, the effective mass which has to be used in the density of states must be an appropriate combination of the band structure effective masses.

To obtain the m^*_{dn} expression, the silicon conduction band structure has to be considered. The minimum of the conduction band is characterized by the ellipsoidal energy surface given by expression (B.22) that can be rewritten as:

$$\frac{k_x^2}{\alpha^2} + \frac{k_y^2 + k_z^2}{\beta^2} = 1 \tag{B.26}$$

$$\alpha = \sqrt{\frac{2m^*_l(E - E_c)}{\hbar^2}} \;\; ; \;\; \beta = \sqrt{\frac{2m^*_t(E - E_c)}{\hbar^2}} \tag{B.27}$$

The volume of the k-space enclosed by a single prolate spheroid is then equal to $(4/3)\pi\alpha\beta^2$. Since there are six ellipsoidal surfaces lying in the first Brillouin zone, the total volume is equal to $6(4/3)\pi\alpha\beta^2$. Instead of this volume an equivalent one is considered which is the one enclosed by a spherical effective energy surface of radius $k_{eff} = \sqrt{2m^*_{de}(E - E_c)/\hbar^2}$. The volume of this latter is then equal to $(4/3)\pi k^3_{eff}$. By equating these two volumes, it is possible to obtain the electron density of state effective mass [78]:

$$m^*_{de} = 6^{2/3}(m^*_l m^{*2}_t)^{1/3}. \tag{B.28}$$

To obtain the m^*_{dh} expression, the valance band structure has to be considered. It is characterized by the spherical constant energy surfaces given

by equation (B.21), and has two degenerate sub-bands. The total valance band density of state is then given by the sum of the two sub-bands density of states characterized by the light an the heavy hole effective masses:

$$g_v(E) = \frac{m^*_{lh}\sqrt{2m^*_{lh}(E_v - E)}}{\pi^2\hbar^3} + \frac{m^*_{hh}\sqrt{2m^*_{hh}(E_v - E)}}{\pi^2\hbar^3} \tag{B.29}$$

Form this latter expression and the (B.25), the hole density of state effective mass can be derived as:

$$m^*_{dh} = [(m^*_{lh})^{3/2} + (m^*_{hh})^{3/2}]^{2/3}. \tag{B.30}$$

For silicon the density of state effective masses are equal to $m^*_{de} = 1.06\ m_0$ and $m^*_{dh} = 0.58\ m_0$, where m_0 is the free electron mass.

List of Figures

1.1 Overall Galactic Cosmic Ray Energy Spectrum [21] [20] 9
1.2 Relative abundance of elements in Galactic Cosmic Rays (GCRs) and in the Solar System (SS). The abundance of silicon is defined as 100 [19]. . 11
1.3 Ratio of "secondary" over "primary" GCRs. Left: B/C ratio; right: (Sc+Ti+V)/Fe ratio. Details are available at [5] 12
1.4 AMS-02 expected sensitivity on Be10/Be9 ratio [6] 13
1.5 Mayor components of the primary cosmic rays [7] 14
1.6 Solar wind speed as a function of latitude for Ulysses' first two orbits. Bottom: sunspot number over the period 1992-2003, declining phase of the solar minimum to the solar maximum [22]. 15
1.7 Left: interplanetary magnetic field lines. [27]. Right: Coronal Magnetic field line configuration during solar minimum; dashed lines refers to a pure dipole magnetic field [25]. 16
1.8 Monthly averages (updated 2009/07/01) of the sunspot numbers [23]. . . 17
1.9 Schematic representation of the reversal magnetic field by the Babcock model. (a) Axis-symmetric poloidal magnetic field; (b) progressive growing of the toroidal magnetic field component due to the solar differential rotation; (c) formation of sunspots with closed magnetic field lines; (d) end of the cycle: the poloidal magnetic field is re-established with opposite polarity [24]. 18
1.10 Evolution of the current sheet during the solar cycle 22. Upper central part: synoptic maps of the magnetic field lines; red and blue points indicate outward and inward polarity respectively. Lower central part: red and blue lines are monthly and yearly averaged values of sunspot number respectively [26]. 19
1.11 Continuous line: long term Climax neutron monitor observation; dashed line: smoothed sunspot number. Under the abscissa axis the reversal magnetic field polarity is reported [14]. 20
1.12 Drift direction of a positive charge particle according to the solar polarity magnetic field [14]. 21
1.13 Artistic view of the Earth's magnetosphere. 23

1.14 Decomposition of the motion of a trapped particle in the Earth's magnetosphere. 24
1.15 South Atlantic Anomaly. From AP-8 MAX (SPENVIS)[1]. Proton integral flux ($E > 10$ MeV) at 500 km goes from 1 to $\sim 2\times10^3$ cm^{-2} s^{-1} [28]. . . 25
1.16 Trapped proton belt. From AP-8 MAX (SPENVIS)[1]. Proton integral fluxes ($E > 10$ MeV) go from 1 to $\sim 3\times10^5$ cm^{-2} s^{-1} [28]. 26
1.17 Trapped electron belt. From AE-8 MAX (SPENVIS)[1]. Electron integral fluxes ($E > 1$ MeV) go from 1 to $\sim 3\times 10^5$ cm^{-2} s^{-1} [28]. 26

2.1 Scattering process in the relative frame of reference. $v = v'$ initial and final velocities; $b = b'$ initial and final impact parameters; r, φ polar coordinates; r_m distance of closest approach; θ scattering angle; μ reduced mass; O origin of the scattering center. 30
2.2 Scattering process in the center of mass frame; $\mathbf{r}$ trajectory of the relative motion; $\mathbf{r}_{1CM}$, $\mathbf{r}_{2CM}$ trajectories of the projectile and target; $b_i = b'_i$ initial and final impact parameter ($i = 1, 2$); $b = b_1 + b_2$ impact parameter in the relative frame of reference; θ scattering angle in the relative system; θ_{CM} scattering angle in the CM system. 31
2.3 Scattering in the laboratory frame. $\mathbf{r}_1$, $\mathbf{r}_2$ projectile and target trajectories, b impact parameter; θ_1, θ_2 deflecting angles. 32
2.4 Schematic representation of the wave packet during a scattering process in the relative frame of reference. Δs width of the wave packet; $\Delta\theta$ uncertainty in the direction; $\mathbf{p}$ wave packet momentum; Δp uncertainty in the momentum; b impact parameter; $r_m(b, E_r)$ distance of closest approach; θ scattering angle. 41
2.5 Universal stopping cross section in reduced notation compared with four other non-relativistic calculations [33]. 51
2.6 Energy loss spectra of (a) 0.736 GeV/c and (b) 115 GeV/c protons. Continuous lines are the fitting curves of the experimental data. In figure (b) a magnification of the tail is reported [46]. 55

3.1 Schematic representation of the collision cascade caused by a PKA which was displaced by an incident particle [33]. 58
3.2 Total and elastic neutron cross section in silicon material [1]. 65
3.3 Damage function and corresponding NIEL values for neutrons in silicon material [1]. The HGK compilation is available on-line at [56] with $T_d =$ 25 eV. Van Ginneken $T_d = 25$ eV [59]. Huhtinen $T_d = 20$ eV [57] 67

3.4 Jun et al. [34] proton NIEL in silicon. Energy range 1keV-1 GeV, The Coulomb contribution is calculated by the use of the ZBL screened potential for $E < 50$ MeV and by the relativistic differential cross section (2.110) for $E \geq 50$ MeV. Nuclear elastic and inelastic contributions are included. Summers et al. [60] 68
3.5 Damage function and corresponding NIEL values for protons in the energy range from 2 eV to 24 GeV in silicon [1]. In the HGK compilation a threshold displacement energy equal to 20 eV is used [56]. Data taken from Jun et al. [34] assumed $T_d = 21$ eV. Huhtinen values are calculated with $T_d = 20$ eV [57]. 69
3.6 Results taken from Messenger et al. [50], of NIEL calculation for different incoming ions in the energy range 100 eV- 1 GeV in silicon material. . . 70
3.7 Kinetic energies at which the nuclear interactions are expected give the same NIEL contribution as the coulomb one as a function of the atomic mass number [1]. The upper curve is calculated considering 20 MeV equivalent proton kinetic energy, the lower is for 10 MeV. 71
3.8 Right: Alpha NIEL value where the header "This study" refers to non-relativistic screened Coulomb NIEL value plus nuclear interactions [36] and the heather "Ref. [10]" refers to [51] where the Coulomb potential is not screened. Left: Alpha NIEL due to nuclear interactions: nuclear elastic, inelastic and total [36]. 72
3.9 N_{eff} dependence on the accumulated 1 MeV neutron equivalent fluence for standard and oxygen enriched FZ silicon irradiated with reactor neutrons, 23 GeV protons and 192 MeV pions [62]. 75
3.10 Various current components in a *pnp* transistor under active mode of operation [76]. 79
3.11 (Left) Common emitter and (right) common base configuration of a *pnp* bipolar transistor. [76]. 80
3.12 Linear dependence of the quantity $\Delta(1/\beta)$ as a function of FP concentration for different type of bipolar transistors (**a**) small emitter area *npn* type; (**b**) large emitter area *npn* type; (**c**) vertical *pnp* type; (**d**) lateral *pnp* type. All measurements are performed with a constant current $I_C = 50$ μA [76]. 82
3.13 Top: Dependence of the parameter $k(I_C)$ on the collector current, I_C, for large and small emitter area region *npn* transistors; same parameter for vertical and lateral *pnp* transistors. Bottom: fitting coefficient of equation (3.79) [63]. 83
3.14 (Right) Collector current, I_C and (left) base current, I_B. Dependence on V_{BE} at 25 ^{o}C. The data are for *npn* transistor with large emitter area region of 50 μm $\times$ 50 μm before and after the irradiation with electrons [63]. 83

4.1 ZBL NIEL values for different incoming nuclei in a silicon material. The curves are obtained by the integration of the equation (4.1) while the dots are taken from [50]. 87
4.2 ZBL NIEL values from 1 keV/nucl up 1GeV/nucl (dashed lines) and NIEL values from 20 MeV/nucl to 10 GeV/nucl (solid lines) computed with the relativistic differential cross section (4.7). 89
4.3 Coulomb NIEL value results from the computational integration of equation 4.6. Solid lines are obtained by the use of the relativistic differential cross section of equation (4.7) while circles are with the equation (4.9) (Jun et al. (2004) [36] and Jun et al. (2003) [34]). 90
4.4 Total (Coulomb plus nuclear) NIEL for protons and alpha particles (for details se text in section (4.3)). Dotted lines are to guide the eye. . . . 91
4.5 Picture taken from [70]. Scattering of 172 MeV/c muons in 1.5 mm Aluminium foil. Data values [74] are black squares. Colored markers corresponds to different options of multiple scattering (Stand) and single scattering (Single Scat.). The bottom graphic represents the relative difference between GEANT4 simulation results and data values in percent; dashed areas are one standard deviation from data. 95
4.6 Probability of interaction as a function of the kinetic energy transferred to the target atom. Comparison of the GEANT4 simulation with the Classical Rutherford value calculated by equation (4.19). 96
4.7 Same as figure 4.6 after the introduction of the reduced mass μ_r as explained in section 4.4.3 98
4.8 GEANT4 upgraded simulation results of the Coulomb NIEL fraction for different incoming particles on a silicon target in comparison with the computational integration performed by the use of the SZ differential cross section (4.7). 100
4.9 Expected GCRs fluxes -ISO model- in two different periods of the solar activity for protons, alpha particle, carbon, and iron nuclei. The curves are obtained with the code based on the Nymmik's model [16] 103
4.10 Scatter plot of the (x, y, z) space coordinates of the GEANT4 particle generator. 103
4.11 Histogram reconstruction of the GCRs fluxes generated by GEANT4 in comparison with the Nymmik's spectrum performed in two different periods of the solar activity. 104
4.12 Spectral NIEL-Dose for protons (top) and alpha particles (bottom). Thick lines refers to a typical solar minimum period while thin lines to a maximum one. For each solar period the dashed lines are the $D^{NIEL}max(E)$, the solid ones are the mean spectral NIEL-Doses, while the dotted ones are the $D^{NIEL}_{min}(E)$ values. 105

5.1 Carrier distribution in respective bands when the Fermi level is (a) above (b) near and (c) below mid-gap respectively. In each case there are also shown: the energy-band diagram, the density of states and the occupancy factor [78]. 110
5.2 Ionization energy of various impurities atoms in silicon [76]. 114
5.3 (a) Temperature dependence of the majority carriers concentration for a n-type silicon doped with a phosphorus dopant concentration $N_D = 10^{15} cm^{-3}$. The dashed line n_i/N_D is included for comparison (b) Qualitative band gap diagram for different temperature regimes. [78]. 117
5.4 Fermi level for silicon as a function of temperature and impurity concentration [76]. 117
5.5 Formation of a (donor) impurity band. (a) with a small doping concentration the dopant energy level (E_D) is well defined, (b) increasing doping and development of an impurity band (c) the dopant band overlaps to the conduction band for high impurity concentration. The shaded areas indicate populated states at $T = 0$ K. $D(E)$ is the density of states [75]. . 120
5.6 The temperature behavior of the electron mobility in a silicon sample for different donor concentrations 129
5.7 Scheme of the Hall effect geometry for electrons moving carriers inside an ideal infinite sample. Positive (+) and negative (-) signs refer to charge accumulation on the y sample direction. 135
5.8 Hall scattering factor (γ) versus temperature (T) for n-type silicon. Experimental data (N_I is the ionized impurity concentration):$\triangle$ ($N_I = 2 \times 10^{13}$ cm^{-3}); $\circ$ ($N_I = 1.5 \times 10^{14}$ cm^{-3}); $\bullet$ ($N_I = 4.6 \times 10^{15}$ cm^{-3}). Theoretical lines: 1 ($N_I = 1 \times 10^{13}$ cm^{-3}); 2 ($N_I = 1 \times 10^{14}$ cm^{-3}); 3 ($N_I = 1 \times 10^{15}$ cm^{-3}); 4 ($N_I = 1 \times 10^{16}$ cm^{-3});5 ($N_I = 1 \times 10^{17}$ cm^{-3}) [85], [96] 141
5.9 Hall scattering factor (γ) versus impurity concentration N_D for n-type silicon. Experimental data:$\bullet$ ($T = 77$ K); $\circ$ ($T = 300$ K); $\triangle$ ($T = 77$ K, low mobility sample). Theoretical lines: I ($T = 300$ K); II ($T = 77$ K); III ($T = 77$ K, additional neutral impurities with 6×10^{16} cm^{-3}) [95] [94] 141

6.1 Top: schematic representation of the Hall effect setup. Bottom: Pictures of instruments. 147
6.2 Schematically representation of voltages and currents for resistivity and Hall coefficient measurements. 148
6.3 Experimental results of non-irradiated samples for different resistivities. Top left: Hall coefficient. Top right: carriers concentration over Hall scattering factor. Bottom left: resistivity. Bottom right: Hall mobility [102]. 151

6.4 Temperature dependance of Hall coefficient [(I), (II), (III)], resistivity [(IV), (V), (VI)] and Hall mobility [(VII), (VIII), (IX)] for irradiated samples with neutrons. The sample-resistivities before irradiation are n-type of $56\,\Omega\,\mathrm{cm}$ [(I), (IV), (VI)], n-type of $157\,\Omega\,\mathrm{cm}$ [(II), (V), (VIII)] and n-type of $2500\,\Omega\,\mathrm{cm}$ [(III), (VI), (IX)] [102]. 153
6.5 Temperature dependance of Hall coefficient [(I), (II), (III)], resistivity [(IV), (V), (VI)] and Hall mobility [(VII), (VIII), (IX)] for irradiated samples with carbon-ions. The sample-resistivities before irradiation are: p-type of $0.01\,\Omega\,\mathrm{cm}$ [(I), (IV), (VI)], n-type of $0.01\,\Omega\,\mathrm{cm}$ [(II), (V), (VIII)] and n-type of $7000\,\Omega\,\mathrm{cm}$ [(III), (VI), (IX)] [102]. 154

B.1 Formation of energy bands as a diamond lattice crystal is formed by bringing N isolated silicon atoms together [77]. 164
B.2 Primitive cell of a diamond structure ; a is the lattice constant [76]. . . 165
B.3 Miller indices of some important planes in a cubic crystal [77]. 166
B.4 (Left) Energy band structure of silicon where E_g is the energy bandgap; plus sign (+) indicates holes in the valance bands and minus sign (-) electron in the conduction band. (Right) Brillouin zone of diamond lattice [76]. 168
B.5 Hole dispersion relation (dashed line) in relation to the electron one in the valance band (solid line). The hole is represented by the filled circle (•) , the electron by the empty one (○) [75]. 170
B.6 Ellipsoid of constant energy in the vicinity of the conduction band minima for the six equivalent directions ⟨100⟩ in the first silicon Brillouin zone [75]. 171

List of Tables

4.1 NIEL-Dose values D^{NIEL} and uncertainties $\sigma_{D^{NIEL}}$, in units of μGy/yr, for all the nuclei of the GCRs spectrum. Values are obtained for typical solar minimum (3-th and 4-th columns) and solar maximum periods (5-th and 6-th columns). The integration was performed from 50 MeV/nucleon up to 10 GeV/nucleon. 107

6.1 Type, doping concentration and resistivity of the silicon bulk samples before irradiation with the corresponding irradiation particles. The resistivity ρ is given in units of Ω cm; the doping concentration N_{dopant} is given in units of cm^{-3}. 144

6.2 Fluences, FP concentrations and absorbed NIEL-Doses induced by neutrons and carbon ions. 146

6.3 The displacement NIEL-Doses, in units of Gy, above which extrinsic region is absent, the slope of the Hall mobility changes and/or the Hall coefficient sign is reversed. 155

Bibliography

[1] C. Leroy, P. G. Rancoita, Principles of Radiation Interaction in Matter and Detection, 2nd Edition World Scientific (2008).

[2] T. I. Gomgosy "Physics of the space environment" Cambrige University Press (1998).

[3] C. Grupen "Astroparticle Physics" Springer (2005)

[4] T. K. Gaisser "Cosmic Rays and Particles Physics" Cambrige University Press (1990).

[5] A. W. Strong and I.V. Moskalenko "Models for Galactic Cosmic-Ray propagation", *Adv. Space Res.* Vol 27 No. 4, pp 717-727, 2001.

[6] F. Barao "AMS-Alpha Magnetic Spectrometer on the International Space Station", Nucl. Instr. Meth. in Phys. Res. A 535 (2004) 134-138.

[7] C. Amsler et al., Physics Letters B667, 1 (2008) available on the PDG WWW pages (URL: http://pdg.lbl.gov/)

[8] K. Greisen "End to the Cosmic-Ray Spectrum?", *Phys. Rev. Lett.* 16, 748 - 750 (1966)

[9] H. W. Babcock "The topology of the Sun's magnetic field and the 22-years cycle" Astrophys. J. 133,572, 1961.

[10] E.N. Parker, 1965 P&SS 13,9.

[11] L.J. Gleeson, W.I. Axford 1967 ApJ 149, L115.

[12] M. A. Forman , L. J. Gleeeson 1975 Ap&SS 32,77

[13] P.A. Isemberg J.R. Kokipii 1979 ApJ 234, 746.

[14] M. L. Dulgin "Australian Cosmic Ray Modulation Research" Publ. Astron. Soc. Aust., 2001, 18, 1240.

[15] Space Environment (Natural and Artificial) - Galactic Cosmic Rays Model, Ref. no. ISO 15390:2004(E).

[16] R. A. Nymmik et al. "A Model of Galactic Cosmic Ray Fluxes" Nuclear Track Radiation Measurements Vol. 20. No.3, pp 427-429, 1991.

[17] G. W. Pölss, "Physics of the Earth's space environment, an introduction." Springer (2004)

[18] D. Hastings, H. Garrett, "Spacecraft-Environment interaction" Cambrige University Press (1996)

[19] Based on data from Astrophysics Science Division, NASA Goddard Space Flight Center Web site, available at `http://helios.gsfc.nasa.gov/ace/abund\_plot.html`;

[20] S. Swordy s-swordy@uchicago.edu Picture available at: `http://astroparticle.uchicago.edu/cosmic\_ray\_spectrum\_picture.htm`

[21] J. Cronin, T.K. Gaisser, and S.P. Swordy, Sci. Amer. v276, p44 (1997)

[22] Picture available at: `http://sci.esa.int/science-e/www/object/index.cfm?fobjectid=33482`

[23] Picture available at: `http://solarscience.msfc.nasa.gov/SunspotCycle.shtml`

[24] Picture available at: `http://iipegasistarspots.googlepages.com/theory`

[25] G.W. Pneumann and R. A. Kopp "Gas-Magnetic Field Interactions in the Solar Corona", Solar Physics, Volume 18, Issue 2, pp.258-270

[26] Pete Riley, J. A. Linker, and Z. Mikić "Modelling the heliospheric current sheet: Solar cycle variations" Journal of Geophysical Research, Vol. 107, No. A7, 2002

[27] J. Vallèe, Fundamentals of Cosmic Physics, Vol. 19, pp. 319-422, 1998

[28] Picture aveilable at: `http://radbelts.gsfc.nasa.gov/outreach/`

[29] Vette, J. I., The NASA/National Space Science Data Center Trapped Radiation Environment Model Program (1964-1991), NSSDC/WDC-A-R&S 91-29, 1991.

[30] Chr. Lehmann *"Interaction of radiation with solids"*, North-Holland Publishing Company 1977.

[31] J. Lindhard, V. Nielsen and M. Scharff. Mat. Fys. Medd. Dan. Vid. Selsk., 36 No. 10 (1968).

[32] U. Littmark and J.F. Ziegler, Phys. Rev. 23A, 64 (1981).

[33] M. Nastasi, J. Mayer, J. Hirvonen "Ion-Solid interactions: fundamentals and applications", Cambrige University Press 1996.

[34] I. Jun et al. "Proton Energy loss (NIEL) for device applications" IEEE Transactions on Nuclear Science, Vol 50, N 6, 2003.

[35] I. Jun et al. "Effects of secondary particles on total dose and displacement damage in Space Proton Environments" IEEE Transactions on Nuclear Science, Vol 48, N 1, 2001.

[36] I. Jun et al. "Alpha particle Nonionizing Energy Loss (NIEL)" IEEE Transactions on Nuclear Science, Vol 51, N 6, 2004.

[37] D.Braunig F. Wulf Radiat. Phys. Chem. Vol. 43, No. 1/2, pp. 105127, 1994.

[38] F. Seitz, D. Turnbull, "Solid State Physisc: Advances in research and applications" Volume 2, New York Academic Press (1956).

[39] P.P Fiziev and I.T Todorov, *Physical Review* D, 63, (2001) 104007.

[40] A. Starusziewicz and K. Zalewski, *Acta Physica Poloncia*, B8, 10 (1977) 815.

[41] A.P. Martynenko and R.N. Faustov, "Relativistic reduced mass and quasipotential" Theoretical and Mathematical Physics Vol 64. N 2 , 1985.

[42] A. Allisy et al, "Stopping Powers and Ranges for Protons and Alpha Particles", ICRU Report 49, 1993.

[43] Geant4 Physics Reference Manual, available on line at: `http://geant4.web.cern.ch/geant4/`

[44] L. Landau "On the Energy loss of fast particles by ionization" J. Phys. U.S.S.R. 8, 201 (1944).

[45] P. V. Vavilov "Ionization Losses of High Energy Heavy particles", Soviet Physics Jetp, Vol. 5 N.4 (1957)

[46] S. Hancock el al, "Energy loss and energy straggling of protons and pions in the momentum range 0.7 to 115 GeV", Phys. Rev. Vol. 28, N. 2 (1983).

[47] G. H. Kinchin, R.S. Pease "The displacement of atoms in solids by radiation" *Report on Progress in Physics, Vol* 18 (1955)

[48] M. T. Robinson, I. M. Torrens " Computer simulation of atomic-displacement cascades in solids in the binary-collision approximation" Physical Review B, Vol. 9, N. 12 (1974)

[49] M. J. Norgett, M. T. Robinson, I. M. Torrens "A proposed method of calculation displacement dose rates" *Nuclear engineering and design* 33, (1975) 50-54, North-Holand Publishing Company.

[50] S. R. Messenger et al. "NIEL for Heavy Ions: An Analytical Approach" IEEE Transaction on Nuclear Science Vol, 50, N. 6 (2003).

[51] S. R. Messenger, G. P. Summers, E. A. Burke, M. A. Xapsos, R. J.Walters, E. M. Jackson, and B. D.Weaver, Nonionizing energy loss (NIEL) for heavy ions, IEEE Trans. Nucl. Sci., vol. 46, pp. 1595-1602, Dec. (1999).

[52] A. Vasilescu "The NIEL scaling hypotesis applied to neutron spectra of irradiation facilities in the ATLAS and CMS SCT" *ROSE/TN/97-2*, 1997.

[53] ECSS-E-10-12 Draft 0.11 20/10/05 (European Cooperation for Space Standardization), "Space Engineering: Methods for the calculation of radiation received and its effects, and policy for design margins".

[54] E. A. Burke "Energy Dependence of Proton-induced displacememt damage in silicon" *IEEE* Transaction on Nuclear Science, Vol. NS-33, No.6, 1986.

[55] V. S. Barashenko and A. Polanski "Electronic Guide for Nuclear Cross-Sections" *JINR E-2-94-417*, Dubna 1994.

[56] A. Vasilescu and G. Lindstroem, Displacement Damage in silicon, on-line compilation available at:
`http://sesam.desy.de/members/gunnar/Si-dfuncs.html`

[57] M. Huhtinen "Simulation of non-ionizing energy loss and defect formation in silicon" Nuclear Instruments and Methods in Physics Research A 491, 194-215, 2002.

[58] G. Lutz "Semiconductors Radiation Detectors" Springer 1999.

[59] A. Van Ginneken "Non ionizing energy deposit in silicon for radiation damage studies" *FN-522*, Fermi National Accelerator Laboratory.

[60] G. P. Summers et al. "Damage correlation in semiconductors exposed to gamma, electron and proton radiation" IEEE Transactions on Nuclear Science, Vol. 40, pp. 1372-1379, 1993.

[61] C. Leroy and P.G.Rancoita "Particle interaction and displacement damage in silicon devices operated in radiation environments" Reports on Progress in Physics, Vol 70, No 4, 2007.

[62] The ROSE Collaboration, 3rd RD48 Status Report, CERN/LHCC 2000-009, 2000.

[63] C. Consolandi et al."Systematic investigation of monolithic bipolar transistors irradiated with neutrons, heavy ions and electrons for space applications", Nucl. Instr. and Meth. B 252 (2006), 276-284

[64] M.J. Boschini et al., GEANT4-*Based Application Development for NIEL Calculation in the Space Radiation Environment*, Proc. of the 11th International Conference on Particle Physics and Advanced Technology, Como 5–9/10/2009, World Scientific (Singapore) 2010.

[65] S. Agostinelli et al., Nuclear Instruments and Methods in Physics Research A 506 (2003) 250-303

[66] J. Allison et al.,IEEE Transactions on Nuclear Science 53 No. 1 (2006) 270-278.

[67] J. Apostolakis et al. Published in J. Phys.: Conf. Ser. 119: 032004, 2008.

[68] S. Elles et al., Published in J. Phys.: Conf. Ser. 102: 012009, 2008.

[69] `http://geant4.web.cern.ch/geant4/`

[70] [Geant4] Physics Reference Manual Version: geant4 9.2 (19 December, 2008), available at:
`http://geant4.web.cern.ch/geant4/UserDocumentation/UsersGuides/PhysicsReferenceManual/fo/PhysicsReferenceManual.pdf`

[71] G. Wentzel, *Z. Phys. 40 (1927) 590.*

[72] H. A. Behte, *Phys. Rev. 98 (1953) 1256.*

[73] A. V. Butkevick, *Nucl. Instr. and Meth. in Phys. Res. A 488 (2002) 282-194.*

[74] D. Attwood et al., *NIM B 251 (2006) 41.*

[75] Grundmann M. 2006 *The Physics of Semiconductors* (Springer).

[76] Sze S. M. , Kwok K. Ng 2007 *Physics of Semiconductor Devices* (John Wiely & Sons) 3rd Edition.

[77] Sze S. M. 2001 *Semiconductors Devices, physics and technology.* (John Wiely & Sons) 2nd Edition.

[78] Pierret Robert F.,*Advanced Semiconductor Fundamentals* second edition, Person Education inc. Upper Saddle River, New Jersey.

[79] Hamaguchi C. (Springer) *Basic Semiconductor Physics*

[80] E. A. Gutierrez, M. J. Deen, C. Cleays (ACADEMIC PRESS) *Low Temperature Electronics: Physics, Devices, Circuits and Applications.*

[81] E. Conwell *et al.* "Theory of impurity scattering in semiconductors", *Phys. Rev.* 77(3), 388-390 (1950)

[82] H. Brooks, "Scattering by ionized impurities in semiconductors", *Phys. Rev.* 83, 879-885 (1951).

[83] B. K. Ridley "Quantum processes in semiconductors" CLARENDON PRESS OXFORD (1999)

[84] Erginsoy, C. (1950). Phys. Rev. 79, 1013

[85] S. Adaki *Handbook on physical Properties of Semiconductors*, Kluwer Academic Publishers (2004).

[86] N. D. Arora, J. R. Hauser and D.J. Roulston, *IEEE Trans. Electron Dev.* ED-29, 292 (1982).

[87] D. M. Caughey and R. E. Thomas, "Carrier mobilities in silicon empirically related to doping and field", *Proc. IEEE* 52, 2192-2193 (1967).

[88] C.T. Sha *et al.* "Effect of zinc impurity scattering in semiconductors", *IEEE Trans. Electron Devicec* ED-28(3),304-313 (1981).

[89] P. Blood and J. W. Orton "The electrical characterization of semiconductors", *Rep. Prog. Phys.* Vol. 41, 1978.

[90] P. Blood and J. W. Orton "The electrical characterization of semiconductors: majority carriers and electron states", Academic Press (1982)

[91] N. Croitoru et al., Nucl. Instr. And Meth. B 124 (1997) 542.

[92] T.Angelescu et al.,Nucl. Instr. And Meth. A 345 (1994) 303-307

[93] C. Hamaguchi. *Basic Semiconductor Physics.* Spinger-Verlang Berlin Heidelberg 2001.

[94] Kirnas, I. G., P. M. Kurilo, P. G. Litovchenko, V. S. Lutsyak, and V. M. Nitsovich, Phys. Status Solidi (A) 23, 2 (1974) K123-K127.

[95] S. Adachi *Handbook on physical Properties of Semiconductors* Kluwer Academic Publishers 2004.

[96] N. N. Dmitrenko et al., Physica Status Solidi A 26, 1, 1974, K45-K48 (182K)

[97] U. Biggeri et al., Nucl. Instr. And Meth. A 400 (1997) 113.

[98] J.F. Ziegler, J.P. Biersack and U. Littmark, *The Stopping Range of Ions in Solids*, Vol. 1, Pergamon Press (New York) 1985.

[99] *ASTM* E722-85.

[100] T. Angelescu et al., *Nucl. Instr. and Meth. in Phys. Res. A* 345 (1994) 303-307

[101] D. Codegoni et al., *Nucl. Instr. and Meth.in Phys. Res. B* 217 (2004) 65.

[102] C. Consolandi et al., *Hall coefficient dependence on resistivity down to cryogenics temperatures in silicon samples irradiated with neutrons and* ^{12}*C-ions*, Proc. of the 11th International Conference on Particle Physics and Advanced Technology, Como 5–9/10/2009, World Scientific (Singapore) 2010.